
**JOURNAL OF CRYSTAL
GROWTH**

VOLUME 246, Nos. 1-2, pp. 1-176
DECEMBER 1 (2002)

DISTRIBUTION STATEMENT A
Approved for Public Release
Distribution Unlimited

EDITORS:

G.B. STRINGFELLOW (Principal Editor),
University of Utah

M. SCHIEBER (Founding Editor),
Hebrew University

R.S. FEIGELSON, Stanford University

D.T.J. HURLE, University of Bristol

R. KERN, Univ. Aix-Marseille

K. NAKAJIMA, Tohoku University

20021231 145

CO-FOUNDERS: N. CABRERA, B. CHALMERS, F.C. FRANK

FORMER ADVISOR: R.A. LAUDISE[†]

North-Holland

Also available on

SCIENCE  DIRECT®

www.sciencedirect.com

Journal of Crystal Growth

<http://www.elsevier.com/locate/jcrysgro>

Scope of the journal

Experimental and theoretical contributions are invited in the following fields: Theory of nucleation and growth, molecular kinetics and transport phenomena, crystallization in viscous media such as polymers and glasses. Crystal growth of metals, minerals, semiconductors, magnetics, inorganic, organic and biological substances in bulk or as thin films. Apparatus, instrumentation and techniques for crystal growth, and purification methods. Characterization of single crystals by physical and chemical methods.

EDITORIAL BOARD

G.B. STRINGFELLOW (Principal Editor)

College of Engineering, University of Utah, 1495 E. 100 S., Room 214,
Salt Lake City, UT 84112-1109, USA

Fax: +1 801 581 8692; e-mail: stringfellow@eng.utah.edu

M. SCHIEBER (Founding Editor)

The Fredy and Nadine Herrmann Graduate School of Applied Science,
Hebrew University, Jerusalem 91904, Israel

Fax: +972 2 566 3878; e-mail: schieber@vms.huji.ac.il

R.S. FEIGELSON

Center for Materials Research, Press Warehouse,
Stanford University, Stanford, CA 94305-4045, USA

Fax: +1 650 723 3752/3044; e-mail: feigel@soc.stanford.edu

D.T.J. HURLE

H.H. Wills Physics Laboratory, University of Bristol,
Tyndall Avenue, Bristol BS8 1TL, UK

E-mail: donhurle@iname.com

R. KERN

CRMC², CNRS, Campus Luminy, Case 913,
F-13288 Marseille Cedex 9, France

Fax: +33 4 91 418 916; e-mail: kern@crmc2.univ-mrs.fr

K. NAKAJIMA

Institute of Materials Research, Tohoku University,
Katahira 2-1-1, Sendai 980-8577, Japan

Fax: +81 22 215 2011; e-mail: nakajima@imr.tohoku.ac.jp

ASSOCIATE EDITORS

C.R. ABERNATHY (*Chemical beam epitaxy, III-nitrides, Novel dielectrics*)

Fax: +1 352 846 1182; e-mail: caber@mse.ufl.edu

K.W. BENZ (*Microgravity, Electronic materials*)

Fax: +49 761 203 4369; e-mail: benz@ruf.uni-freiburg.de

C.D. BRANDLE (*Oxides*)

E-mail: cdb@agere.com

N.E. CHAYEN (*Crystallization of biological macromolecules*)

Fax: +44 171 594 3169; e-mail: n.chayen@ic.ac.uk

A.A. CHERNOV (*Kinetics of crystallization, Protein crystallization*)

Fax: +7 095 135 1011, +1 205 544 8762; e-mail: alex.chernov@msfc.nasa.gov

A.Y. CHO (*Molecular beam epitaxy*)

Fax: +1 908 582 2043; e-mail: ayc@lucent.com

J.J. DERBY (*Computational models*)

Fax: +1 612 626 7246; e-mail: derby@umn.edu

R. GIEGÉ (*Biocrystallization*)

Fax: +33 3 8860 2218; e-mail: r.giege@ibmc.u-strasbg.fr

M.E. GLICKSMAN (*Solidification*)

Fax: +1 518 276 2198; e-mail: glickm@rpi.edu

M.S. GOORSKY (*XRD characterization, Epitaxy for devices*)

Fax: +1 310 206 7353; e-mail: goorsky@scas.ucla.edu

T. HIBIYA (*Oxides, Melt thermophysical properties, microgravity*)

Tel.: +81 42 585 8654; e-mail: hibiya@cc.tmit.ac.jp

S. HIYAMIZU (*Molecular beam epitaxy*)

Fax: +81 6 845 4632; e-mail: hiyamizu@mp.cs.osaka-u.ac.jp

R. JAMES (*II-VI semiconductors, Radiation sensors*)

Fax: +1 631 344 5584; e-mail: rjames@bnl.gov

T.M. KAWASAKI (*Oxide thin films and epitaxy*)

Fax: +81 22 215 2086; e-mail: kawasaki@imr.tohoku.ac.jp

T.F. KUECH (*Thin films, Electronic and optical devices*)

Fax: +1 608 265 3782; e-mail: kuech@engr.wisc.edu

G.B. McFADDEN (*Theory*)

Fax: +1 301 990 4127; e-mail: mcfadden@nist.gov

A. McPHERSON (*Protein growth*)

Fax: +1 949 824 1954; e-mail: amcphers@uci.edu

G. MÜLLER (*Bulk semiconductors*)

Fax: +49 9131 852 8495; e-mail: georg.mueller@ww.uni-erlangen.de

J.B. MULLIN (*Semiconductors*)

Fax: +44 1202 759 835; e-mail: brian.mullin@btinternet.com

D.N. NORTON (*Oxide thin films and epitaxy*)

Fax: +1 352 846 1182; e-mail: dnort@msc.ufl.edu

H. OHNO (*Epitaxy*)

Fax: +81 22 217 5553; e-mail: ohno@rice.tohoku.ac.jp

K. ONABE (*MOVPE, MBE of III-V, III-nitride compounds*)

Fax: +81 3 5841 8884; e-mail: onabe@k.u-tokyo.ac.jp

K.H. PLOOG (*Molecular beam epitaxy*)

Fax: +49 30 203 77201; e-mail: ploog@pdi-berlin.de

M. ROTH (*Nonlinear optical and electro-optical materials*)

Fax: +972 2 566 3878; e-mail: mroth@vms.huji.ac.il

K. SATO (*Biocrystallization and organic crystals*)

Fax: +81 824 227 062; e-mail: kyosato@hiroshima-u.ac.jp

L.F. SCHNEEMEYER (*Superconductivity, Oxides, Novel materials, Priority communications*)

Fax: +1 908 582 3609; e-mail: schneemeyer@agere.com

D.W. SHAW (*Semiconductors, Epitaxy, Devices*)

Fax: +1 972 883 6839; e-mail: dshaw@utdallas.edu

J. SHERWOOD (*Industrial crystallization*)

Fax: +44 141 548 4822; e-mail: j.n.sherwood@strath.ac.uk

M. UWABA (*Growth kinetics*)

Fax: +81 52 789 2928; e-mail: uwaba@phys.nagoya-u.ac.jp

A. ZANGWILL (*Theory (epitaxy)*)

Fax: +1 404 894 9958; e-mail: andrew.zangwill@physics.gatech.edu

Abstracted/indexed in

Aluminium Industry Abstracts; Chemical Abstracts; Current Contents: Physical, Chemical and Earth Sciences; Ei Compendex Plus; Engineered Materials Abstracts; Engineering Index; INSPEC; Metals Abstracts

Publication information

Journal of Crystal Growth (ISSN 0022-0248). For 2002, volumes 234-246 are scheduled for publication. Subscription prices are available upon request from the Publisher or from the Regional Sales Office nearest you or from this journal's website (<http://www.elsevier.com/locate/jcrysgro>). Further information on this journal and other Elsevier Science products is available through Elsevier's website (<http://www.elsevier.com>).

Subscriptions are accepted on a prepaid basis only and are entered on a calendar year basis. Issues are sent by standard mail (surface within Europe, air delivery outside Europe). Priority rates are available upon request. Claims for missing issues should be made within six months of the date of dispatch.

USA mailing notice: Journal of Crystal Growth (ISSN 0022-0248) is published semimonthly by Elsevier Science B.V. (P.O. Box 211, 1000 AE Amsterdam, The Netherlands). Annual subscription price in the USA is US\$ 9220 (valid in North, Central and South America), including air speed delivery Periodicals postage rate paid at Jamaica, NY 11431.

USA Postmaster: Send address changes to Journal of Crystal Growth, Publications Expediting Inc., 200 Meacham Ave., Elmont, NY 11003.

Airfreight and mailing in the USA by Publications Expediting Inc., 200 Meacham Ave., Elmont, NY 11003.

PRINTED IN THE NETHERLANDS

North-Holland, an imprint of Elsevier Science

JOURNAL OF CRYSTAL GROWTH

EDITORIAL BOARD

G.B. STRINGFELLOW (*Principal Editor*)
College of Engineering, University of Utah, 1495 E. 100 S., Room 214,
Salt Lake City, UT 84112-1109, USA
Fax: +1 801 581 8692; e-mail: stringfellow@eng.utah.edu

M. SCHIEBER (*Founding Editor*)
The Fredy and Nadine Herrmann Graduate School of Applied Science,
Hebrew University, Jerusalem 91904, Israel
Fax: +972 2 566 3878; e-mail: schieber@vms.huji.ac.il

R.S. FEIGELSON
Center for Materials Research, Press Warehouse,
Stanford University, Stanford, CA 94305-4045, USA
Fax: +1 650 723 3752/3044; e-mail: feigel@soc.stanford.edu

D.T.J. HURLE
H.H. Wills Physics Laboratory, University of Bristol,
Tyndall Avenue, Bristol BS8 1TL, UK
E-mail: donhurle@iname.com

R. KERN
CRMC², CNRS, Campus Luminy, Case 913,
F-13288 Marseille Cedex 9, France
Fax: +33 4 91 418 916; e-mail: kern@crmc2.univ-mrs.fr

K. NAKAJIMA
Institute of Materials Research, Tohoku University,
Katahira 2-1-1, Sendai 980-8577, Japan
Fax: +81 22 215 2011; e-mail: nakajima@imr.tohoku.ac.jp

ASSOCIATE EDITORS

C.R. ABERNATHY (*Chemical beam epitaxy, III-nitrides, Novel dielectrics*)
Dept. of Materials Science and Engineering, University of Florida,
Rhines Hall, Gainesville, FL 32606, USA
Fax: +1 352 846 1182; e-mail: caber@mse.ufl.edu

K.W. BENZ (*Microgravity, Electronic materials*)
Kristallographisches Institut, Universität,
Hebelstr. 25, D-79104 Freiburg, Germany
Fax: +49 761 203 4369; e-mail: benz@ruf.uni-freiburg.de

C.D. BRANDLE (*Oxides*)
Room 7D-414, Agere Systems, 600 Mountain Ave.,
Murray Hill, NJ 07974, USA
E-mail: cdb@agere.com

N.E. CHAYEN (*Crystallization of biological macromolecules*)
Biological Structure and Function Group, Div. of Biomedical Sciences,
Alexander Fleming Building, Imperial College, London SW7 2AZ, UK
Fax: +44 171 594 3169; e-mail: n.chayen@ic.ac.uk

A.A. CHERNOV (*Kinetics of crystallization, Protein crystallization*)
Institute of Crystallography, Academy of Sciences,
Leninskii Prospekt, Moscow 117333, Russian Federation
Fax: +7 095 135 1011;
University of Space Research Assoc.,
4950 Corp. Dr., Suite 100, Huntsville, AL 35805, USA
Fax: +1 205 544 8762; e-mail: alex.chernov@msfc.nasa.gov

A.Y. CHO (*Molecular beam epitaxy*)
Lucent Technology, Room 6H-422, 600 Mountain Avenue,
Murray Hill, NJ 07974-0636, USA
Fax: +1 908 582 2043; e-mail: ayc@lucent.com

J.J. DERBY (*Computational models*)
Dept. of Chemical Engineering and Materials Science,
University of Minnesota, 151 Amundson Hall, 421 Washington Ave. S.E.,
Minneapolis, MN 55455-0132, USA
Fax: +1 612 626 7246; e-mail: derby@umn.edu

R. GIEGE (*Biocrystallization*)
UPR 9002 du CNRS, Inst. de Biologie Molec. et Cellulaire,
15, rue René Descartes, F-67084 Strasbourg Cx, France
Fax: +33 3 8860 2218; e-mail: r.giege@ibmc.u-strasbg.fr

M.E. GLICKSMAN (*Solidification*)
School of Engineering, Materials Engineering Dept.,
Rensselaer Polytechnic Institute, Troy, NY 12180-3590, USA
Fax: +1 518 276 2198; e-mail: glickm@rpi.edu

M.S. GOORSKY (*XRD characterization, Epitaxy for devices*)
Dept. of Materials Science Engineering, University of California,
Los Angeles, CA 90095-1595, USA
Fax: +1 310 206 7353; e-mail: goorsky@seas.ucla.edu

T. HIBIYA (*Oxides, Melt thermophysical properties, Microgravity*)
Tokyo Metropolitan Institute of Technology, Dept. of Aerospace
Engineering, 6-6, Asahigaoka, Hino 191-0065, Japan
Tel.: +81 42 585 8654; e-mail: hibiya@cc.tmit.ac.jp

S. HIYAMIZU (*Molecular beam epitaxy*)
Dept. of Physical Sciences, Graduate School of Engineering Science,
Osaka University, Toyonaka, Osaka 560, Japan
Fax: +81 6 845 4632; e-mail: hiyamizu@mp.es.osaka-u.ac.jp

R. JAMES (*II-VI semiconductors, Radiation sensors*)
Associate Laboratory Director, Energy, Environment and National
Security, Brookhaven National Laboratory, Building 460, Upton, L.I.,
NY 11973, USA
Fax: +1 631 344 5584; e-mail: rjames@bnl.gov

T.M. KAWASAKI (*Oxide thin films and epitaxy*)
Tohoku University, Inst. of Materials Research,
2-1-1 Katahira, Aoba, Sendai 980-8577, Japan
Fax: +81 22 215 2086; e-mail: kawasaki@imr.tohoku.ac.jp

T.F. KUECH (*Thin films, Electronic and optical devices*)
Dept. of Chemical Engineering, University of Wisconsin-Madison,
Madison, WI 53706, USA
Fax: +1 608 265 3782; e-mail: kuech@engr.wisc.edu

G.B. McFADDEN (*Theory*)
National Institute of Standards and Technology,
Bldg. 820, Room 365, 100 Bureau Drive, Stop 8910,
Gaithersburg, MD 20899-8910, USA
Fax: +1 301 990 4127; e-mail: mcfadden@nist.gov

A. McPHERSON (*Protein growth*)
Dept. of Molecular Biology and Biochemistry, University of California,
Irvine, CA 92697-3900, USA
Fax: +1 949 824 1954; e-mail: amcphe@uci.edu

G. MÜLLER (*Bulk semiconductors*)
Crystal Laboratory, Dept. of Materials Science (WW6), University
Erlangen-Nürnberg, Martensstr. 7, D-91058 Erlangen,
Germany
Fax: +49 9131 852 8495; e-mail: georg.mueller@ww.uni-erlangen.de

J.B. MULLIN (*Semiconductors*)
EMC-HooTwo, 22 Branksome Towers, Westminster Road,
Poole, Dorset, BH13 6JT, UK
Fax: +44 1202 759 835; e-mail: brian.mullin@btinternet.com

D.N. NORTON (*Oxide thin films and epitaxy*)
University of Florida, Dept. Materials Science and Engrg.,
100 Rhines Hall, P.O.B. 116400, Gainesville, FL 32611-6400, USA
Fax: +1 352 846 1182; e-mail: dnort@mse.ufl.edu

H. OHNO (*Epitaxy*)
Research Institute of Electrical Communication, Tohoku University,
2-1-1 Katahira, Aoba-ku, Sendai 980-8577, Japan
Fax: +81 22 217 5553; e-mail: ohno@iec.tohoku.ac.jp

K. ONABE (*MOVPE, MBE of III-V, III-nitride compounds*)
Univ. of Tokyo, Dept. Advanced Materials Science and Dept. of Applied
Physics, 7-3-1 Hongo, Bunkyo-ku, Tokyo 113-8656, Japan
Fax: +81 3 5841 8884; e-mail: onabe@k.u-tokyo.ac.jp

K.H. PLOOG (*Molecular beam epitaxy*)
Paul-Drude-Institut für Festkörperelektronik,
Hausvogteiplatz 5-7, D-10117 Berlin, Germany
Fax: +49 30 203 77201; e-mail: ploog@pdi-berlin.de

M. ROTH (*Nonlinear optical and electro-optical materials*)
Graduate School of Applied Science, Hebrew University,
Jerusalem 91904, Israel
Fax: +972 2 566 3878; e-mail: mroth@vms.huji.ac.il

K. SATO (*Biocrystallization and organic crystals*)
Faculty of Applied Biological Science, Hiroshima University,
Higashi-Hiroshima 724, Japan
Fax: +81 824 227 062; e-mail: kyosato@hiroshima-u.ac.jp

L.F. SCHNEEMEYER (*Superconductivity, Oxides, Novel materials, Priority communications*)
Room 1T-304, Agere Systems, Murray Hill, NJ 07974-2070, USA
Fax: +1 908 582 3609; e-mail: schneemeyer@agere.com

D.W. SHAW (*Semiconductors, Epitaxy, Devices*)
University of Texas, 503 Potomac Pl., Southlake, TX 76002, USA
Fax: +1 972 883-6839; e-mail: dshaw@utdallas.edu

J. SHERWOOD (*Industrial crystallization*)
Dept. of Pure and Applied Chemistry, University of Strathclyde,
295 Cathedral street, Glasgow G1 1XL, Scotland, UK
Fax: +44 141 548 4822; e-mail: j.n.sherwood@strath.ac.uk

M. UWABA (*Growth kinetics*)
Dept. of Physics, Nagoya University,
Furo-cho, Chikusa-ku, Nagoya 464-8602, Japan
Fax: +81 52 789 2928; e-mail: uwaha@phys.nagoya-u.ac.jp

A. ZANGWILL (*Theory (epitaxy)*)
School of Physics, Georgia Institute of Technology,
Atlanta, GA 30332, USA
Fax: +1 404 894 9958; e-mail: andrew.zangwill@physics.gatech.edu

JOURNAL OF CRYSTAL GROWTH

EDITORS

G.B. STRINGFELLOW
Principal Editor

M. SCHIEBER
Founding Editor

R.S. FEIGELSON

D.T.J. HURLE

R. KERN

K. NAKAJIMA

VOLUME 246 (2002)



ELSEVIER

Amsterdam – London – New York – Oxford – Paris – Shannon – Tokyo

© 2002 Elsevier Science B.V. All rights reserved

This journal and the individual contributions contained in it are protected under copyright by Elsevier Science B.V., and the following terms and conditions apply to their use:

Photocopying

Single photocopies of single articles may be made for personal use as allowed by national copyright laws. Permission of the Publisher and payment of a fee is required for all other photocopying, including multiple or systematic copying, copying for advertising or promotional purposes, resale, and all forms of document delivery. Special rates are available for educational institutions that wish to make photocopies for non-profit educational classroom use. Permissions may be sought directly from Elsevier Science via their homepage: (<http://www.elsevier.com>) by selecting "Customer support" and then "Permissions". Alternatively you can send an e-mail to: permissions@elsevier.co.uk, or fax to: (+44) 1865 853333.

In the USA, users may clear permissions and make payments through the Copyright Clearing Center, Inc., 222 Rose Wood Drive, Danvers, MA 01923, USA; tel.: +1 978 7508400, fax: +1 978 7504744.

In the UK through the Copyright Licensing Agency Rapid Clearance Service (CLARCS), 90 Tottenham Court Road, London W1P 0LP, UK; tel.: +44 20 7631 5555, fax: +44 20 7631 5500.

Other countries may have a local reprographic rights agency for payments.

Derivative works

Subscribers may reproduce tables of contents or prepare lists of articles including abstracts for internal circulation within their institutions. Permission of the Publisher is required for resale or distribution outside the institution. Permission of the Publisher is required for all other derivative works, including compilations and translations.

Electronic storage or usage

Permission of the Publisher is required to store or use electronically any material contained in this journal, including any article or part of a article. Except as outlined above, or part of this publication may be reproduced, stored in a retrieval system or transmitted in any form or by any means, electronic, mechanical, photocopying, recording or other wise, without prior written permission of the Publisher.

Address permissions requests to: Elsevier Science Global Rights Department, at the mail, fax and e-mail addresses quoted above.

Notice

No responsibility is assumed by the Publisher for any injury and/or damage to persons or property as a matter of products liability, negligence or other wise, or from any use or operation of any methods, products, instructions or ideas contained in the material herein.

Because of rapid advances in the medical sciences, in particular, independent verification of diagnoses and drug dosages should be made. Although all advertising material is expected to conform to ethical (medical) standards, inclusion in this publication does not constitute a guarantee or endorsement of the quality of such product or of the claims made of it by its manufacturer.

Orders, claims, and product enquiries

Please contact the Customer Support Department at the Regional Sales Office nearest you:

New York: Elsevier Science, P.O. Box 945, New York, NY 10159-0945, USA; tel.: +1 212 633 3730 [toll free number for North American customers: +1-888-4ES-INFO (437-4636)]; fax: +1 212 633 3680; e-mail: usinfo-f@elsevier.com.

Amsterdam: Elsevier Science, P.O. Box 211, 1000 AE Amsterdam, The Netherlands; tel.: +31 20 485 3757; fax: +31 20 485 3432; e-mail: nlinfo-f@elsevier.com

Tokyo: Elsevier Science, 9-15 Higashi-Azabu, 1-chome, Minato-ku, Tokyo 106-0044, Japan; tel.: +81 3 5561 5033; fax: +81 3 5561 5047; e-mail: info@elsevier.co.jp.

Singapore: Elsevier Science, 3 Killiney Road, #08-01 Winsland House I, Singapore 239519; phone: (+65) 6349 0200; fax: (+65) 6733 1510; e-mail: asiainfo@elsevier.com.sg.

Rio de Janeiro: Elsevier Science, Rua Sete de Setembro 111/16 Andar, 20050-002 Centro, Rio de Janeiro - RJ, Brazil; tel.: +55 21 509 5340; fax: +55 21 507 1991; e-mail: elsevier@campus.com.br.

[Note: (Latin America): for orders, claims and help desk information, please contact the Regional Sales Office in New York as listed above.]

Advertising information

Advertising orders and enquiries can be sent to:

USA, Canada and South America: Mr Tino de Carlo, The Advertising Department, Elsevier Science Inc., 360 Park Avenue South, New York, NY 10010-1710, USA; tel.: +1 212 633 3815; fax: +1 212 633 3820; e-mail: t.decarlo@elsevier.com.

Japan: The Advertising Department, Elsevier Science K.K., 9-15 Higashi-Azabu, 1-chome, Minato-ku, Tokyo 106-0044, Japan; tel.: +81 3 5561 5033; fax: +81 3 5561 5047

Europe and rest of the world: Commercial Sales Department, Elsevier Science Ltd., The Boulevard, Langford Lane, Kidlington, Oxford OX5 1 B, UK; tel.: +44 1865 843016; fax: +44 1865 843976; e-mail: media@elsevier.com

⊗ The paper used in this publication meets the requirements of ANSI/NISO Z39.48-1992 (Permanence of Paper)

PRINTED IN THE NETHERLANDS



ELSEVIER

Available online at www.sciencedirect.com

SCIENCE @ DIRECT®

Journal of Crystal Growth 246 (2002) 1–8

JOURNAL OF
**CRYSTAL
GROWTH**

www.elsevier.com/locate/jcrysgro

Temperature control in InGaAs-based quantum well structures grown by molecular beam epitaxy on GaAs (100) and GaAs (111)B substrates

J. Hernando^{a,*}, J.M.G. Tijero^b, J.L. Sánchez de Rojas^a

^a *Departamento de Ingeniería Electrónica, ETSI Telecomunicación, Universidad Politécnica de Madrid, Ciudad Universitaria, s/n, 28040, Madrid, Spain*

^b *Departamento de Física Aplicada, ETS Arquitectura, Universidad Politécnica de Madrid, Avd. Juan Herrera, s/n, 28040, Madrid, Spain*

Received 11 April 2002; accepted 25 July 2002

Communicated by A.Y. Cho

Abstract

A molecular beam epitaxy (MBE) growth procedure for InGaAs-based structures on GaAs (100) and (111)B substrates is presented and discussed. The main objective of the procedure is to gain an accurate control over the growth temperature in order to ensure its precise setting and reproducibility in any MBE reactor. Growth temperature is set relative to the temperature of a system-independent reference. The reference is the transition between two static surface reconstructions as shown by the reflection high-energy electron diffraction patterns. The reference temperature is checked whenever the temperature has to be changed all over the growth of the structure. The reliability of the procedure is demonstrated by the systematic studies of the influence of the growth conditions on test samples and the reproducibility of the optimum conditions for the growth of high-quality InGaAs-based quantum well devices on both GaAs (100) and (111)B substrates.

© 2002 Elsevier Science B.V. All rights reserved.

PACS: 81.15.Hi

Keywords: A3. Molecular beam epitaxy; A3. Quantum wells; B1. Arsenates; B2. Semiconducting III–V materials; B3. Infrared devices; B3. Laser diodes

1. Introduction

Molecular beam epitaxy (MBE) is a well-developed technology for the growth of quantum devices. This physical vapour deposition technique

makes use of an ultra-high vacuum environment to preserve the beam nature of mass transport, to minimise the incorporation of unintentional impurities and to analyse in situ the wafer surface with the help of reflection high-energy electron diffraction (RHEED). In addition, the precise shutter control over the source fluxes provides more abrupt interfaces than those obtained by

*Corresponding author.

E-mail address: hernando@die.upm.es (J. Hernando).

other growth techniques. All these features have contributed to the application of MBE to commercial production [1].

At this stage, economically minded MBE production requires the establishment of a procedure that ensures the reproducibility of the growth conditions from run-to-run and from campaign-to-campaign in the same reactor, as well as from system-to-system. This goal of reproducibility much relies on an extremely precise control over the growth conditions. Moreover, this control would allow the performance of reliable studies of the influence of growth conditions on material quality and the application of the optimised growth conditions to the fabrication of nominally identical structures, which actually show the same operating characteristics. However, this control is not easily achievable in an MBE system. The main difficulty is the lack of a precise knowledge of the real temperature of the wafer all along the growth. This is due to the difference between the real temperature of the wafer and the temperature reading provided by a thermocouple or an infrared optical pyrometer, which are the most common thermometers in any MBE system. This difficulty would be overcome if growth temperature could be set relative to the temperature of a system-independent reference, for example, some easily observable phase transition of the material. A number of authors have already suggested or made use of this kind of references in the control of the growth temperature in MBE reactors [2–8]. However, to the best of our knowledge, there is no comprehensive report on the details and subtleties of the procedure, which can be critical in the final degree of control obtained.

The objective of this paper is to describe a systematic procedure for the control of the growth temperature of InGaAs-based quantum well structures on GaAs (100) and (111)B substrates. We use the reference temperature provided by the sharply defined reversible transition between two static surface reconstructions of the substrates, as shown by the RHEED pattern. In Section 2, a comprehensive description of our growth procedure is presented and discussed, with specific emphasis on the requirement of some intermediate checks of the reference temperature for the

accurate setting and reproducibility of the growth temperature. In Section 3, the reliability of the procedure is proven through the analysis of the effect of the change of growth conditions on the properties of test structures and the successful reproducibility of the optimum conditions for the fabrication of two InGaAs-based devices of great interest in the literature, namely, quantum well infrared photodetectors on GaAs (100) and quantum well lasers on misoriented GaAs (111)B substrates.

2. Growth procedure

The growth of As-related compounds is controlled by three parameters, namely growth rate, flux ratio and growth temperature. Growth rates of GaAs and InAs are determined by RHEED intensity oscillations on GaAs (100) and InAs (100) substrates, respectively. The flux of arsenic is indirectly specified by the As_4/Ga flux ratio and the corresponding GaAs growth rate. The As_4/Ga flux ratio is calibrated by finding the RHEED boundary between the (2×4) As- and the (4×2) Ga-stabilised dynamic reconstructions on GaAs (100) [3]. The As_4/Ga flux ratio at this boundary is equal to 0.5.

Growth temperature is the most critical condition. The key point of our procedure is the selection of an intrinsic reference and the checking and correction of the growth temperature with respect to the temperature of this reference all along the growth. The reference temperature chosen is the temperature of the transition between two of the static surface reconstructions of the substrate at a fixed arsenic flux, as revealed by the RHEED pattern. For GaAs (100) substrates, the most convenient reference is the $(2 \times 4) \rightleftharpoons c(4 \times 4)$ transition [3]. For GaAs (111)B substrates, two transitions can be used as references: the $(1 \times 1)HT \rightleftharpoons (\sqrt{19} \times \sqrt{19})R23.4^\circ$ [hereafter referred to as $(\sqrt{19} \times \sqrt{19})$] for the high-temperature range and the $(\sqrt{19} \times \sqrt{19}) \rightleftharpoons (1 \times 1)LT$ for the low-temperature range (we follow the nomenclature defined by Woolf et al. [4]). Since they are intrinsic properties of the material, at a given arsenic flux, each of these transitions appears

always at the same temperature, no matter the different temperature readings which may be displayed by the thermometers in each MBE system. The reference temperature will be called T_R , while the temperature reading at this temperature will be referred to as T_m . Any temperature along the growth will be denoted by its difference ΔT with respect to T_R . It is assumed that a change ΔT in the temperature reading corresponds to an identical change ΔT in the real temperature of the substrate. Therefore, if a temperature reading $T_m + \Delta T$ is set, the corresponding substrate temperature will be assumed to be $T_R + \Delta T$.

It is a rather common practice for temperature control to check the temperature reading T_m just before starting the growth and to set all the subsequent temperatures along the growth relative to this initial reading. In our case, the transitions can be observed under static conditions whenever the temperature is changed for the growth of the different regions of the structure. This allows us to check the reference temperature not only before growth but also every time the temperature has to be changed for the growth of the next region. As explained below, these additional checks have been extremely important in the high degree of control achieved over the growth temperature.

Next, the details of the procedure are illustrated by means of the description of all the steps in the growth of a typical InGaAs/GaAs (100) quantum well structure. The structure consists of a low-temperature intrinsic active region (with one or more quantum wells), embedded within two contacts grown at the same high growth temperature. The flux of As_4 molecules is kept constant all along the growth. Fig. 1 shows the evolution of both the real temperature (dashed line) and the corresponding thermocouple reading (solid line) along the growth. We use the thermocouple reading because the low growth temperature required for the active region is below the range of our pyrometer (500–1500°C). Moreover, the thermocouple is connected to a controller that allows us to change the temperature with the help of ramps. The steps of the growth are as follows:

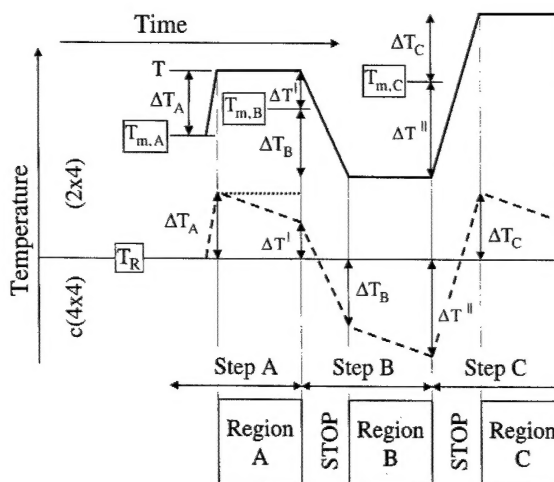


Fig. 1. Evolution of the real temperature (dashed line) and the temperature reading (solid line) along the growth on GaAs (100) substrates. The structures are formed by a low-temperature active region (region B) between two contacts grown at high temperature (regions A and C). The temperature of the $(2 \times 4) \leftrightarrow c(4 \times 4)$ transition is called T_R . The different temperature readings at T_R are indicated by T_m in each region.

Step A: After the surface oxide removal and the growth of some mono-layers of GaAs to smooth the surface, the temperature is decreased down to the observation of the $(2 \times 4) \leftrightarrow c(4 \times 4)$ transition and the corresponding thermocouple reading $T_{m,A}$ is noted down. $T_{m,A}$ is the same no matter the transition is observed either decreasing or increasing the temperature and independent of the ramping rate used (from 20°C/min to 60°C/min). Then, the temperature is increased at a rate of 20°C/min and set at a thermocouple reading $T = T_{m,A} + \Delta T_A$ with $\Delta T_A = 75^\circ\text{C}$. The bottom GaAs contact is subsequently grown at this constant reading. By keeping the thermocouple reading constant, the growth temperature was also expected to be constant. A dotted line in the region A of Fig. 1 indicates this assumption.

Step B: 200 Å before the end of the bottom contact, the growth is stopped for 180 s to ramp the temperature down (60°C/min) for the growth of the InGaAs-based active region. At the $(2 \times 4) \leftrightarrow c(4 \times 4)$ transition, a new thermocouple reading $T_{m,B}$ is registered. This new reading $T_{m,B}$ was expected to be similar to $T_{m,A}$. However, the readings can be significantly different. In our

system, $T_{m,B}$ is observed to be higher than $T_{m,A}$. This discrepancy cannot be related to changes in the arsenic flux, and consequently in the temperature of the transition, T_R , since the checking of this flux at the end of the growth does not reveal any significant change. Therefore, $T_{m,A}$ and $T_{m,B}$ are different thermocouple readings corresponding to the same temperature T_R and we have to conclude that, even if the thermocouple is kept constant, the growth temperature changes as the growth progresses from an initial value $T_R + \Delta T_A$ to a final value of $T_R + \Delta T^I$ with $\Delta T^I = \Delta T_A - [T_{m,B} - T_{m,A}]$. Then, $T_{m,B} - T_{m,A}$ represents the overall change of the growth temperature along the bottom contact layer. In our case, the temperature decreases at a rate of about $0.2^\circ\text{C}/\text{min}$. This is indicated by the dashed line in the region A of Fig. 1.

The growth temperature of the active region is set by decreasing the thermocouple reading by an amount ΔT_B with respect to the new thermocouple reading at the transition $T_{m,B}$. In this way, the growth temperature can be assumed to be $T_R - \Delta T_B$. It is important to emphasise here that if a new checking of the reference temperature had not been performed after growing the bottom contact layer, the growth temperature would have been $T_R - \Delta T_B - [T_{m,B} - T_{m,A}]$. The value of $T_{m,B} - T_{m,A}$ can be as high as 20°C for thick contacts grown at low growth rates and may be crucial for the growth of structures in which the growth temperature is a critical parameter. This is the case of InGaAs layers on GaAs (100), where a variation in the growth temperature of 10°C changes the growth mode (see Section 3). This sensitivity to the growth temperature proves the usefulness of making a new checking of the reference temperature for achieving an accurate control over the real growth temperature of the active region. As in the bottom contact, a significant decrease in the temperature is expected along the growth of this region, as indicated in Fig. 1. It is also worth pointing out that the growth interruptions required did not have any detrimental effect on the quality of the samples.

Step C: After the last InGaAs quantum well plus 200 \AA of GaAs, the growth is stopped again for

180 s to rise the temperature ($60^\circ\text{C}/\text{min}$) for the growth of the top GaAs contact. A new checking of the thermocouple reading is performed at the $(2 \times 4) \Leftrightarrow c(4 \times 4)$ transition. In our system, the new reading $T_{m,C}$ is again higher than $T_{m,B}$, as a consequence of the decrease of the temperature of the wafer during the growth of the active region. The temperature dropping is observed to be about $0.2^\circ\text{C}/\text{min}$. The top contact is finally grown at a constant thermocouple reading $T_{m,C} + \Delta T_C$ with $\Delta T_C = \Delta T_A = 75^\circ\text{C}$. Therefore, we have ensured that the bottom and top contacts are grown at the same temperature. After finishing the growth, the reference temperature is checked again. Once more, the growth temperature is observed to have decreased at a similar rate ($0.2^\circ\text{C}/\text{min}$) during the growth of the top contact.

Having observed in our system a systematic decrease of the temperature of the wafer (about $0.2^\circ\text{C}/\text{min}$ at a constant thermocouple reading), the procedure was corrected by heating the substrate such that the thermocouple reading continuously rises at a $0.2^\circ\text{C}/\text{min}$ rate along the growth of each region. With this increasing ramp, the temperature decrease observed is negligible.

The procedure for growing on GaAs (111)B substrates is similar. In this case, we consider two surface reconstruction transitions: $(1 \times 1)\text{HT} \Leftrightarrow (\sqrt{19} \times \sqrt{19})$ and $(\sqrt{19} \times \sqrt{19}) \Leftrightarrow (1 \times 1)\text{LT}$. The difference in temperature between these two transitions is found to be about 80°C in the entire range of arsenic fluxes used, in accordance with previous works [4]. For the growth of the bottom contact, the thermocouple reading is set at $\Delta T_A = -20^\circ\text{C}$ with respect to the $(1 \times 1)\text{HT} \Leftrightarrow (\sqrt{19} \times \sqrt{19})$ transition. The top contact is grown at $\Delta T_C = 60^\circ\text{C}$ with respect to the $(\sqrt{19} \times \sqrt{19}) \Leftrightarrow (1 \times 1)\text{LT}$ transition. Therefore, both contacts are grown at about the same growth temperature. For the active region, the transition from $(\sqrt{19} \times \sqrt{19})$ to $(1 \times 1)\text{LT}$ is used to fix the growth temperature.

It is very important to point out that this procedure does not require the knowledge of the temperature T_R to achieve reproducible growths. The difference in temperature ΔT is the only parameter needed to reproduce the growth temperature, once the flux of arsenic is given.

3. Application of the procedure and results

The procedure described in the previous section was used for the growth of InGaAs-based quantum wells devices on both GaAs (100) and (111)B. For each substrate, in all the samples, the growth temperature of the contact layers was $T_R + \Delta T$ (ΔT having the values reported in Section 2), no matter the As_4 flux. Since T_R depends on the arsenic flux, the real growth temperature of the contacts was different for each As_4 flux, as shown later in Fig. 3. Nevertheless, no significant effect of this variable temperature was observed on the final quality of the devices.

3.1. InGaAs quantum wells on GaAs (100)

As a preliminary study, InGaAs single layers of various compositions and thicknesses were grown on on-axis GaAs (100). RHEED allowed us to observe the transition from bidimensional (2D) growth mode to three-dimensional (3D) growth mode [9] under several growth conditions.

In Table 1 we show the growth conditions for various InGaAs layers, along with the RHEED pattern just at the end of the layer and 30 s after the indium and the gallium shutters were closed (static conditions). Indium contents of 25%, 30% and 35% and the corresponding thickness of 55, 40 and 30 Å were used. The GaAs growth rate of the InGaAs alloys was 1 µm/h and the As_4/Ga flux ratio was calculated based on this growth rate.

No evidence of 3D growth appeared for the 25% indium content layers. For the 30% indium

content layers, 3D growth occurred at the highest temperature, i.e., $\Delta T = -30^\circ\text{C}$ with respect to the $(2 \times 4) \Leftrightarrow c(4 \times 4)$ transition, while at the lowest substrate temperature ($\Delta T = -60^\circ\text{C}$), islands formation was avoided. In the case of the 35% indium content layer, the growth mode should be close to the onset of 3D growth at the lowest temperature ($\Delta T = -60^\circ\text{C}$) and just at the end of layer, since the formation of islands was readily observed after waiting for 30 s in static conditions, as well as when the temperature was increased by only 10°C . The evolution of the layer towards thermodynamic equilibrium could explain the appearance of 3D growth at the lowest temperature under static conditions [10].

We applied our procedure to the growth of three n-i-n quantum well infrared photodetector (QWIP) structures. The intrinsic active region was formed by ten silicon doped $\text{In}_x\text{Ga}_{1-x}\text{As}$ quantum wells separated by 500 Å GaAs barriers. The indium content and thickness of the quantum wells of each QWIP correspond to one of the combinations of indium content and well thickness in Table 1. The growth conditions given in Table 1 with $\Delta T = -60^\circ\text{C}$ were used for the active region of each QWIP in order to ensure 2D growth. The multiple quantum well structure was sandwiched between n-type silicon-doped GaAs contacts, grown with the same GaAs growth rate and As_4/Ga flux ratio as the active region. In Fig. 2, we show the low-temperature photoluminescence (PL) of the QWIP structures. The intensity and full-width at half-maximum (FWHM) of the PL measurements confirms the structures high optical

Table 1

Growth conditions of the different InGaAs layers on GaAs (100) to check the presence or absence of 3D growth in the RHEED pattern just at the end of the layer and 30 s after the end of the layer under static conditions

Indium content (%)	Well thickness (Å)	Flux ratio As_4/Ga	ΔT with respect to $(2 \times 4) \Leftrightarrow c(4 \times 4)$	RHEED just at the end of layer	RHEED 30 s after the end of layer
25	55	2.0	-30	NO 3D	NO 3D
25	55	2.0	-60	NO 3D	NO 3D
30	40	2.0	-30	3D	3D
30	40	2.0	-60	NO 3D	NO 3D
35	30	2.3	-50	3D	3D
35	30	2.3	-60	NO 3D	3D

The GaAs growth rate is 1 µm/h.

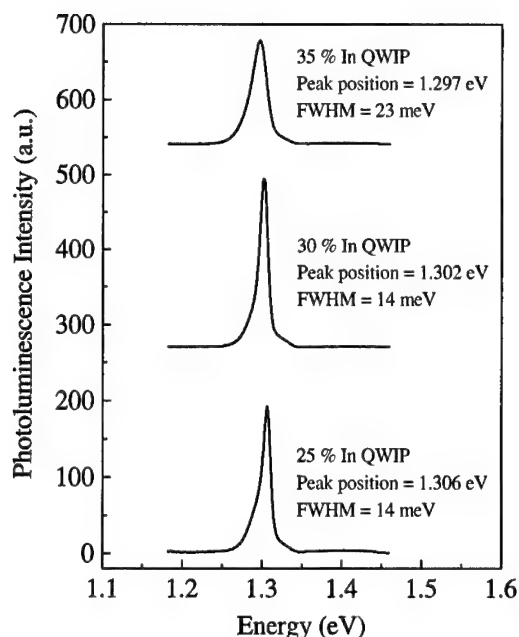


Fig. 2. Low-temperature (25 K) photoluminescence spectra of the InGaAs/GaAs QWIPs with different indium contents. The excitation source was a He–Ne laser ($\lambda = 632.8$ nm) and the optical power was 1 mW.

quality, which has been demonstrated by the analysis of device performance [11]. The PL peak of the 35% indium content QWIP is much broader than others (23 meV instead of 14 meV). This can be attributed to a rougher interface because of the proximity of the 3D growth onset.

3.2. InGaAs quantum wells on GaAs (111)B

A series of InGaAs single quantum wells embedded within the intrinsic region of a p–i–n structure were grown on GaAs (111)B substrates misoriented 1° towards $[2\ 1\ 1]$. The indium content in the wells was 20% and the thickness 100 Å. The objective of these growths was to optimise the growth conditions of this type of structure. Fig. 3 shows the boundaries of the static surface phase diagram of a GaAs (111)B substrate. In the vertical axis, we report the As_4/Ga flux ratio for a GaAs growth rate of $0.4\ \mu\text{m/h}$. The $(1 \times 1)\text{HT} \Leftrightarrow (\sqrt{19} \times \sqrt{19})$ boundary was drawn based on the pyrometer readings in different growths (circles in Fig. 3). The

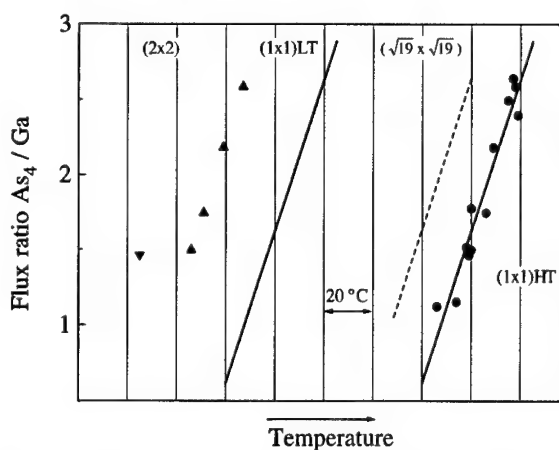


Fig. 3. Static surface phase diagram of GaAs (111)B substrates. The triangles describe the growth conditions of various $100\ \text{\AA}$ $\text{In}_{0.2}\text{Ga}_{0.8}\text{As}$ quantum wells of the p–i–n structures. The growth temperature is decreased by 32°C and 52°C with respect to the $(\sqrt{19} \times \sqrt{19}) \Leftrightarrow (1 \times 1)\text{LT}$ transition for the up and down triangles, respectively. The As_4/Ga flux ratio is related to a growth rate of $0.4\ \mu\text{m/h}$.

$(\sqrt{19} \times \sqrt{19}) \Leftrightarrow (1 \times 1)\text{LT}$ boundary is almost parallel but 80°C below for the range of As_4/Ga flux ratios used in this work. Solid black lines are drawn as a guide to the eyes. The change from $(1 \times 1)\text{LT}$ to (2×2) is not shown as it is not sufficiently sharp, but it is around 20°C below the $(\sqrt{19} \times \sqrt{19}) \Leftrightarrow (1 \times 1)\text{LT}$ transition.

The triangles represent the growth conditions of several quantum wells. The GaAs growth rate was $0.4\ \mu\text{m/h}$ for the InGaAs quantum wells. The growth temperature was decreased by 32°C and 52°C with respect to the $(\sqrt{19} \times \sqrt{19}) \Leftrightarrow (1 \times 1)\text{LT}$ transition for the up and down triangles, respectively.

The dashed line in Fig. 3 is 20°C below the $(1 \times 1)\text{HT} \Leftrightarrow (\sqrt{19} \times \sqrt{19})$ boundary. It represents the growth conditions of the bottom and top GaAs contacts, grown along this line with the same GaAs growth rate and As_4/Ga flux ratio as the intrinsic region. As mentioned before, the growth temperature of the contacts was different depending on the As_4/Ga flux ratio.

In Fig. 4, we plot the low-temperature PL FWHM of the samples versus the As_4/Ga flux ratio. A clear improvement in the FWHM was observed as the As_4/Ga flux ratio was decreased

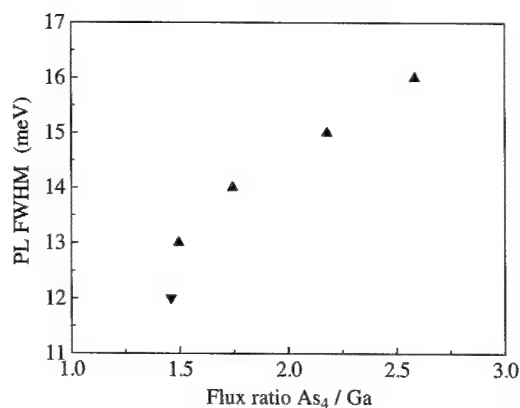


Fig. 4. Low-temperature (25 K) photoluminescence full-width at half-maximum versus the As_4/Ga flux ratio for the 100 \AA $In_{0.2}Ga_{0.8}As$ -based p-i-n structures.

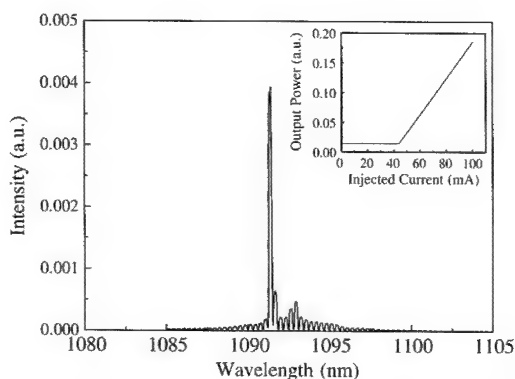


Fig. 5. Room temperature CW emission spectrum of a 100 \AA $In_{0.28}Ga_{0.72}As$ quantum well laser grown on GaAs (111)B under an injection current slightly above threshold. The inset shows the output power versus the injected current.

for $\Delta T_B = -32^\circ\text{C}$. As the arsenic flux was being changed, the thermal energy of the adatoms on the surface was modified. But the constancy of ΔT_B guaranteed a similar arsenic surface coverage over the wafer. The FWHM further improved for $\Delta T_B = -52^\circ\text{C}$, for the best As_4/Ga flux ratio at the previous ΔT_B . All these samples were grown showing a clear (2×2) reconstruction under static conditions, with no evidence of a $(\sqrt{19} \times \sqrt{19})$ reconstruction on dynamic conditions. The optimised growth conditions have been applied to p-i-n structures with higher indium contents as well as to GaAs/AlGaAs/InGaAs quantum well lasers on GaAs (111)B. The $(1 \times 1)HT \Leftrightarrow (\sqrt{19} \times \sqrt{19})$

transition was taken as the reference point when changing the temperature for the growth of the AlGaAs layers. Fig. 5 shows the CW emission spectrum of a 100 \AA $In_{0.28}Ga_{0.72}As$ quantum well laser at room temperature under an injection current slightly above threshold. The wavelength emission is about $1.09 \mu\text{m}$ with a threshold current of 160 A/cm^2 for a $1000 \mu\text{m}$ cavity. These values are among the best when compared with the data reported in the literature for InGaAs-based lasers on GaAs (111)B with emission above $1.06 \mu\text{m}$ [12,13]. These lasers are difficult to achieve because of the proximity of the onset of strain relaxation for the high indium content and thick quantum wells required and its achievement demonstrates the reliability of our procedure for the growth of critical structures.

4. Conclusion

An MBE growth procedure for GaAs (100) and (111)B substrates has been described. The procedure is especially focussed on the control over the growth temperature. This control is achieved by fixing the growth temperature with respect to the temperature of a system-independent reference. The reference is the boundary between two static surface reconstructions at a fixed flux of arsenic, as evidenced by the RHEED pattern. The thermocouple readings are used as a measurement of the difference of the growth temperature with respect to the reference temperature. To accurately set this difference, the checking of the reference temperature is made whenever the growth temperature has to be changed along the growth. The procedure does not require assuming that the growth temperature keeps constant as long as the temperature reading does, which is a rather common practice in MBE. This procedure has allowed us to achieve a high degree of control over the growth temperature, to perform systematic studies of the influence of the growth conditions on the characteristics of test samples and to reproduce the optimum growth conditions for the fabrication of high-quality, high indium content, InGaAs-based devices on GaAs (100) and (111)B substrates. These results prove the reliability of the procedure.

Acknowledgements

This work is supported by the Spanish Naval Research Office (CIDA), the Spanish CICYT Project No. TIC2000-0380-C03-02, the Spanish Project HB1999-0028 and the Office of Naval Research (NICOP) Project No. N00014-00-1-0366. Thanks are due to José María Ulloa for laser emission measurements.

References

- [1] J.M. Fastenau, W.K. Liu, X.M. Fang, D.I. Lubyshev, R.I. Pelzel, T.R. Yurasits, T.R. Stewart, J.H. Lee, S.S. Li, M.Z. Tidrow, *Infrared Phys. Technol.* 42 (2001) 407.
- [2] J.M. Van Hove, P.I. Cohen, *J. Vac. Sci. Technol.* 20 (1982) 726.
- [3] S.M. Newstead, R.A.A. Kubiak, E.H.C. Parker, *J. Crystal Growth* 81 (1987) 49.
- [4] D.A. Woolf, Z. Sobiesierski, D.I. Westwood, R.H. Williams, *J. Appl. Phys.* 71 (1992) 4908.
- [5] A.M. Dabiran, P.I. Cohen, J.E. Angelo, W.W. Gerberich, *Thin Solid Films* 231 (1993) 1.
- [6] R. Grey, J.P.R. David, G. Hill, A.S. Pabla, M.A. Pate, G.J. Rees, P.N. Robson, P.J. Rodriguez-Girones, T.E. Sale, J. Woodhead, T.A. Fisher, R.A. Hogg, D.J. Mowbray, M.S. Skolnick, D.M. Whittaker, A.R.K. Willcox, *Microelectron. J.* 26 (1995) 811.
- [7] K. Pak, M.R. Fahy, X.-M. Zhang, B.A. Joyce, *J. Crystal Growth* 186 (1998) 21.
- [8] V.P. LaBella, D.W. Bullock, C. Emery, Z. Ding, P.M. Thibado, *Appl. Phys. Lett.* 79 (2001) 3065.
- [9] R.P. Mirin, J.P. Ibbeston, K. Nishi, A.C. Gossard, J.E. Bowers, *Appl. Phys. Lett.* 67 (1995) 3795.
- [10] O. Dehaese, X. Wallart, F. Molloy, *Appl. Phys. Lett.* 66 (1995) 52.
- [11] J. Hernando, J.L. Sánchez-Rojas, A. Guzmán, E. Muñoz, J.M.G. Tijero, D. González, G. Aragón, R. García, *Appl. Phys. Lett.* 78 (2001) 2390.
- [12] T. Fleischmann, M. Moran, M. Hopkinson, H. Meidia, G.J. Rees, A.G. Cullis, J.L. Sánchez-Rojas, I. Izpura, *J. Appl. Phys.* 89 (2001) 4689.
- [13] L. Borruel, J.M. Ulloa, J.J. Sánchez, B. Romero, J. Temmyo, J.M.G. Tijero, J.L. Sánchez-Rojas, I. Esquivias, *Photonics West 2001, Integrated Optoelectronic Devices*, paper 4283-28, San Jose, CA, 2001.



ELSEVIER

Available online at www.sciencedirect.com

SCIENCE @ DIRECT®

Journal of Crystal Growth 246 (2002) 9–14

JOURNAL OF
**CRYSTAL
GROWTH**

www.elsevier.com/locate/jcrysgro

Atomic depth distribution and growth modes of Sn on Si(1 1 1)- 4×1 -In and α - $\sqrt{3} \times \sqrt{3}$ -Au surfaces at room temperature

T. Yamanaka^{a,*}, S. Ino^b

^a *Catalysis Research Center, Hokkaido University, Kita11-Nishi10, Kita-ku, Sapporo 060-0811, Japan*

^b *Department of Electronics, Faculty of Engineering, Utsunomiya University, Utsunomiya 321-8585, Japan*

Received 14 August 2002; accepted 22 August 2002

Communicated by R. Kern

Abstract

Atomic depth distribution and growth modes of Sn on 4×1 -In and α - $\sqrt{3} \times \sqrt{3}$ -Au surfaces were studied at room temperature by using reflection high-energy electron diffraction and characteristic X-ray spectroscopy measurements as functions of glancing angle θ_g of the incident electron beam. In the growth of Sn on an α - $\sqrt{3} \times \sqrt{3}$ -Au surface, partial alloying between Au and Sn occurred after deposition of 1 ML of Sn. During further deposition of Sn, alloying between Au and Sn became more significant. During growth of Sn on a 4×1 -In surface, alloying between Sn and In occurred, and a part of In segregated to the upper parts of the film.

© 2002 Elsevier Science B.V. All rights reserved.

PACS: 81.15.-z; 61.14.Hg; 68.55.-a

Keywords: A1. Reflection high energy electron diffraction; A1. Segregation; A1. Surface structure; A3. Molecular beam epitaxy; B1. Metals

1. Introduction

The growth of a material on a substrate precovered by another element and interdiffusion of preadsorbed atoms during such growth processes have been studied extensively for technical reasons. The electronic properties of delta-doped semiconductors, for example, change significantly

depending on the degree of diffusion of the dopant. In addition, the morphology of a grown film is drastically altered from islands to a flat layer when preadsorbed atoms segregate to the uppermost layer during growth, and the surface energy is reduced by this segregation, a phenomenon called surfactant-mediated epitaxy (SME) [1–3]. Elucidation of growth processes on an atomic scale in both lateral and perpendicular directions is required for controlling quality and morphology of thin films. By using scanning tunneling microscopy, behaviors of adsorbates

*Corresponding author. Tel.: +81-117063687; fax: +81-117094748.

E-mail address: yama@cat.hokudai.ac.jp (T. Yamanaka).

can be studied in lateral direction on surfaces. However, behaviors of grown elements in the direction perpendicular to the surface in monolayer resolution are more difficult to determine.

We have developed a method for analysis of atomic depth distribution by using reflection angle electron diffraction and total reflection angle X-ray spectroscopy (TRAXS) [4]. By this method, resolution of depth better than 1 ML can be attained for very shallow regions of the first to about the third layer for both well-ordered and disordered films. By using this method, some growth processes of Ag [4,5], Au [4,5], Ga [6], and In [7] on Si(111) surfaces precovered by another metal were studied, and various growth motions of elements were observed.

In this paper, growth modes of Sn at room temperature on Si(111)- $\alpha\sqrt{3} \times \sqrt{3}$ -Au and 4×1 -In surfaces are described. The morphology of grown films was characterized by reflection high-energy X-ray diffraction (RHEED) and the atomic depth distribution of elements was determined by characteristic X-rays excited by RHEED beam, as functions of incident glancing angle θ_g . During growth of Sn on a 4×1 -In surface, alloying between Sn and In occurred. In the growth of Sn on an $\alpha\sqrt{3} \times \sqrt{3}$ -Au surface, after deposition of 1 ML of Sn, partial alloying between Au and Sn occurred. During further deposition of Sn, alloying between Au and Sn became more significant.

2. Experimental procedure

In this study, surface structures during growth were monitored by RHEED observation, and θ_g dependencies of intensities of characteristic X-rays emitted from the surfaces excited by the RHEED beam were measured to determine the atomic depth distribution of elements. X-ray spectroscopy is not surface-sensitive since a significant amount of X-rays from deep regions is detected in addition to the signals from the surface. However, when the X-ray detector is placed at an angle near the critical angle for total reflection, the signals from deep regions can be reduced, and X-ray spectroscopy becomes a surface sensitive method [8,9], which is called TRAXS [9]. The apparatus used in

this study is described in detail in a previous paper [10]. The width of the take-off angle was 0.4° , and it was set in the range of 0.5 – 0.9° . A small electron gun on a turntable was then rotated around an axis that lies on the sample surface in a UHV chamber, during which time the positions of the sample and detector were fixed. The glancing angle θ_g could be changed from 0 to 180° , with an angular resolution of 0.036° , by using a stepping motor. The electron gun was operated at an acceleration voltage of 10 keV. The X-rays emitted from the sample surface propagated successively, through the first beryllium window for the UHV seal, 5 mm of air, and the second beryllium window of the vacuum seal of an solid state detector (SSD), finally reaching an Si(Li) detector. The sample was cut in a circular shape of 12 mm in diameter from an Si(111) wafer. Cleaning of the Si(111) surface was performed by heating above 1200°C by electron bombardment until a clear 7×7 RHEED pattern was observed. Si(111)- 4×1 -In and $\alpha\sqrt{3} \times \sqrt{3}$ -Au structures were prepared by deposition of metals from coiled tungsten filaments.

3. Results

3.1. Growth of Sn on an Si(111)- $\sqrt{3} \times \sqrt{3}$ -Au surface

An Si(111)- $\alpha\sqrt{3} \times \sqrt{3}$ -Au surface was formed by $\frac{2}{3}$ ML of Au deposition on an Si(111)- 7×7 surface at 500°C [11]. The surface was cooled to room temperature and Sn was grown on this surface. As shown in Fig. 1a, the RHEED pattern taken after deposition of 1 ML of Sn showed diffuse 1×1 streaks, indicating a flat surface. θ_g dependencies of InL, AuM and SiK are shown in Fig. 2a. Since the diameters of the incident electron beam and the sample were about 0.15 and 12 mm, respectively, the entire beam fell on the sample at θ_g above 0.7° . The rapid decreases in X-ray yields below $\theta_g = 0.7^\circ$ are due to the finite size of the sample. SnL and AuM showed maxima at 1° and 2° , respectively. SiK showed a broad maximum at 15° . After deposition of 1 ML of additional Sn, a RHEED pattern showed

transmitted spots, and similar patterns were observed during further deposition of Sn, as shown in Fig. 1b (in the case of $\Theta_{\text{Sn}} = 4$). θ_g

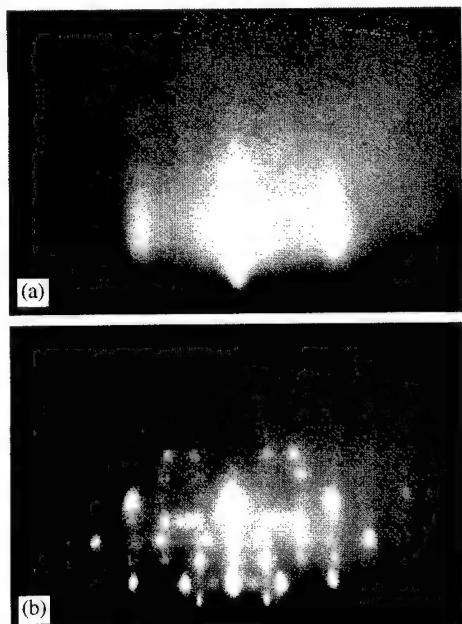


Fig. 1. (a) and (b) show RHEED patterns obtained from a surface after deposition of Sn on an $\text{Si}(111)\text{-}\sqrt{3} \times \sqrt{3}\text{-Au}$ surface at room temperature at $\Theta_{\text{Sn}} = 1$ and 4, respectively.

dependencies taken at $\Theta_{\text{Sn}} = 4$ are shown in Fig. 2b. θ_g dependencies of SnL and AuM are very similar, showing maxima at 2° , and their intensities decrease more slowly with increases in θ_g compared with the results obtained at $\Theta_{\text{Sn}} = 1$ (Fig. 2a).

3.2. Growth of Sn on an $\text{Si}(111)\text{-}4 \times 1\text{-In}$ surface

An $\text{Si}(111)\text{-}4 \times 1\text{-In}$ surface was formed by deposition of 1 ML of In on an $\text{Si}(111)\text{-}7 \times 7$ surface at 500°C [12]. The surface was cooled to room temperature and Sn was grown on this surface. During deposition of Sn, a RHEED pattern showed transmitted spots, as shown in Fig. 3 (in the case of $\Theta_{\text{Sn}} = 4$). θ_g dependencies of SnL, InL and SiK are shown in Fig. 4. At $\Theta_{\text{Sn}} = 1$, SnL and InL showed a maximum at 1° , and decreased with increases in θ_g . SiK showed a broad maximum at 12° . After deposition of 3 ML of additional Sn ($\Theta_{\text{Sn}} = 4$), θ_g dependencies of InL still showed maxima at 1° while θ_g dependencies of SnL showed a maximum at 2° . Both θ_g dependencies of SnL and InL decreased more slowly with increases in θ_g compared with the results obtained at $\Theta_{\text{Sn}} = 1$ (Fig. 4a). The maximum of SiK slightly shifted to a higher θ_g of 13° .

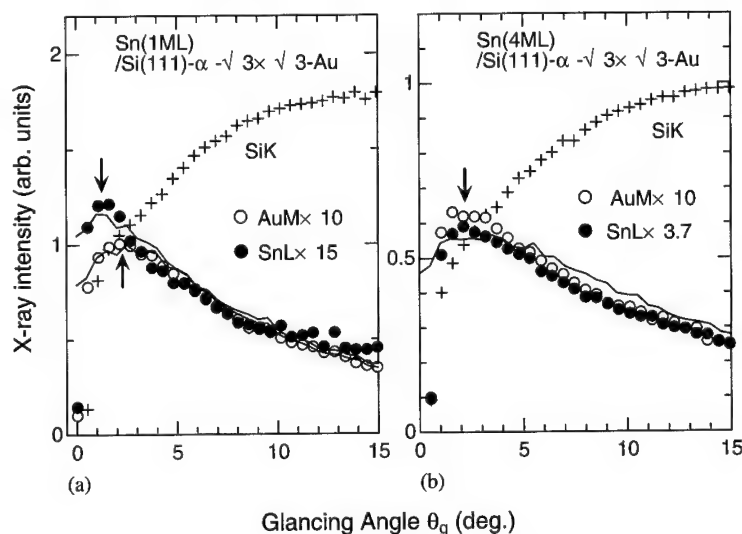


Fig. 2. θ_g dependencies of characteristic X-rays SnL, AuM and SiK measured during growth of Sn on an $\text{Si}(111)\text{-}\sqrt{3} \times \sqrt{3}\text{-Au}$ surface at room temperature. Peak positions of the θ_g dependencies are indicated by arrows. (a) and (b) are results at $\Theta_{\text{Sn}} = 1, 4$, respectively. Solid lines are θ_g dependencies of SnL and AuM calculated by Monte Carlo method assuming the growth model (see the text).

4. Discussion

During growth processes of Sn on Si(111)- 4×1 -In and $\alpha\text{-}\sqrt{3} \times \sqrt{3}$ -Au surfaces, θ_g dependencies of characteristic X-rays from adsorbed metals and SiK showed different behaviors, as shown in Figs. 2 and 4. These dependencies changed as the coverage of grown metals increased. This is because θ_g dependence changes according to the depths of elements. Therefore, atomic depth distribution can be analyzed from θ_g dependence of characteristic X-rays. We calculated



Fig. 3. A RHEED pattern obtained from a surface after deposition of 4 ML of Sn on an Si(111)- 4×1 -In surface at room temperature.

θ_g dependencies of characteristic X-ray emissions from various layers in a 5-ML Sn film on a Si surface calculated by the Monte Carlo method [13,14] for incident electron energy of 10 keV. The calculation is described in detail in a previous paper [4]. The results are shown in Fig. 5. θ_g dependence calculated for each layer has a maximum, and the position of the maximum shifts to higher θ_g as the depth of the layer increases. The experimental results of θ_g dependence can be explained as a summation of contributions from specific layers.

In the growth of Sn on an Si(111)- $\alpha\text{-}\sqrt{3} \times \sqrt{3}$ -Au surface, a RHEED pattern at $\Theta_{\text{Sn}} = 1$ showed streaks, indicating a flat surface (Fig. 1a). SnL and AuM had peaks at 1° and 2° at $\Theta_{\text{Sn}} = 1$, respectively, and θ_g dependencies of SnL and AuM were similar above $\theta_g = 2^\circ$, as shown in Fig. 2a. This means that alloying between Sn and Au had occurred but that the concentration of Sn in the first layer was greater than that in the second layer. At $\Theta_{\text{Sn}} = 4$, a RHEED pattern showed transmitted spots (Fig. 1b), indicating the formation of islands. As shown in Fig. 2b, θ_g dependencies of SnL and AuM became very similar, indicating that alloying between Sn and Au had become more significant.

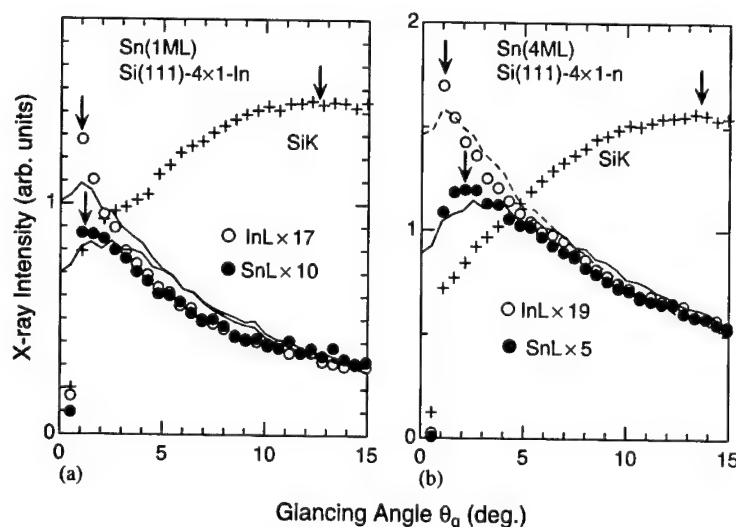


Fig. 4. θ_g dependencies of characteristic X-rays InL, SnL and SiK measured during growth of Sn on an Si(111)- 4×1 -In surface at room temperature. Peak positions of the θ_g dependencies are indicated by arrows. (a) and (b) are results at $\Theta_{\text{Sn}} = 1, 4$, respectively. Solid lines are θ_g dependencies of InL and SnL calculated by Monte Carlo method assuming the growth model (see the text).

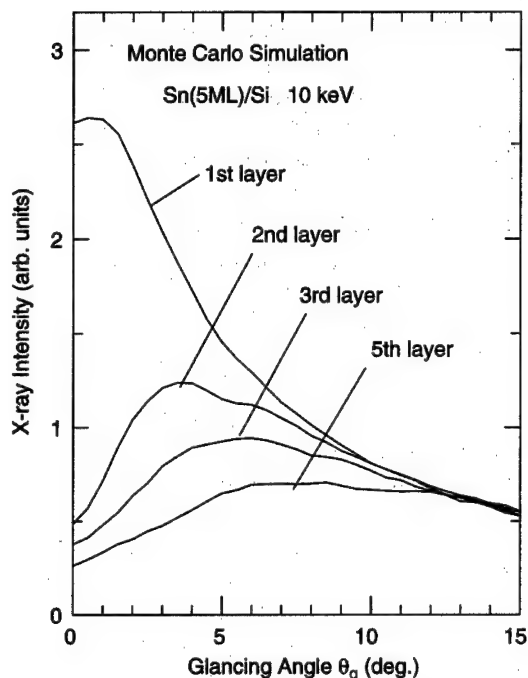


Fig. 5. θ_g dependencies of characteristic X-ray emission from various layers in a 5-ML Sn film on an Si surface calculated by Monte Carlo simulation. The position of maximum shifts to higher θ_g as the depth of layer increases.

In the growth of Sn on an Si(111)- 4×1 -In surface, a RHEED pattern showed transmitted spots, as shown in Fig. 3. At $\theta_{Sn} = 1$, both θ_g dependencies of SnL and InL had peaks at 1° , but the ratio of intensity of InL to that of SnL increased at low θ_g , as shown in Fig. 4a. At $\theta_{Sn} = 4$, θ_g dependencies of SnL and InL had peaks at 1° and 2° , respectively. These results mean that alloying between Sn and In had occurred but that the concentration of In in the upper layers was greater than that in deeper layers.

We tried to fit the experimental results of θ_g dependencies by those calculated by Monte Carlo simulation, assuming flat layers of Sn, Au and In. The results are shown by solid lines in Figs. 2 and 4. For the growth of Sn on an Si(111)- $\alpha\sqrt{3} \times \sqrt{3}$ -Au surface at $\theta_{Sn} = 1$, it was assumed that 0.46 ML of Sn and 0.2 ML of Au existed in the first layer and that 0.54 ML of Sn and 0.46 ML existed in the second layer, resulting in a total Sn coverage of 1 ML and a total Au coverage of 2/3 ML. At $\theta_{Sn} = 4$, it was assumed that Sn and Au

were completely mixed. The calculated results agree with the experimental results, as shown in Figs. 2a and b.

For the growth of Sn on an Si(111)- 4×1 -In, the results obtained at $\theta_{Sn} = 1$ are shown by a solid line in Fig. 4a. It was assumed that 0.35 ML of Sn and 0.65 ML of In existed in the first layer and that 0.65 ML of Sn and 0.35 ML of In existed in the second layer. The calculated results roughly explain the experimental results, but the agreement was not very good. The solid line in Fig. 4b shows results obtained at $\theta_{Sn} = 4$ calculated with the assumption that the first layer consisted of 0.6 ML of Sn and 0.4 ML of In and that each of second to fifth layers consisted of 0.85 ML of Sn and 0.15 ML of In. The agreement between experimental and calculated results is good. The disagreement between experimental and calculated results is thought to be due to the formation of island structures, in contrast to the assumption of flat layers in the calculation.

It is interesting to compare the growth of Sn on an Si(111)- $\alpha\sqrt{3} \times \sqrt{3}$ -Au surface to the growth of Au on an Si(111)- $2\sqrt{3} \times 2\sqrt{3}$ -Sn surface reported previously [5]. During the latter growth, substitution between Au and Sn was also observed, and substitution cannot therefore be explained simply in terms of strength of Si-Au and Si-Sn bondings. In addition, in the growth of Au on an Si(111)- $2\sqrt{3} \times 2\sqrt{3}$ -Sn surface, a flat Au film was formed by the surfactant effect of In, while islands were found to be formed in the growth of Sn on an $\alpha\sqrt{3} \times \sqrt{3}$ -Au surface in the present study. These results indicate that the morphology of the film sensitively depends on the order of deposition in the co-adsorption of two metals, suggesting various possibilities for control of the morphology of films.

5. Summary

Growth modes of Sn on Si(111)- $\alpha\sqrt{3} \times \sqrt{3}$ -Au and -4×1 -In surfaces at room temperature were studied by using reflection high-energy electron diffraction (RHEED) and characteristic X-ray spectroscopy measurements as functions of glancing angle θ_g of the incident electron beam. In the

growth of Sn on an $\alpha\text{-}\sqrt{3} \times \sqrt{3}$ -Au surface, after deposition of 1 ML of Sn, alloying between Au and Sn partially occurred, and a flat Au–Sn layer was formed. The first layer of this film was rather rich in Sn. During further deposition of Sn, the formation of islands was observed and alloying between Au and Sn became more significant. During growth of Sn on a 4×1 -In surface, alloying between Sn and In occurred, but a part of In segregated in the upper parts of the film.

References

- [1] M. Copel, M.C. Reuter, E. Kaxiras, R.M. Tromp, *Phys. Rev. Lett.* 63 (1989) 632.
- [2] M. Horn-von Hoegen, F.K. LeGoues, M. Copel, M.C. Reuter, R.M. Tromp, *Phys. Rev. Lett.* 67 (1991) 1130.
- [3] H.A. van der Vegt, H.M. van Pinxteren, M. Lohmeier, E. Vlieg, J.M.C. Thornton, *Phys. Rev. Lett.* 68 (1992) 3335.
- [4] T. Yamanaka, A. Endo, S. Ino, *Surf. Sci.* 294 (1993) 53.
- [5] T. Yamanaka, S. Ino, *Phys. Rev. B* (2002) 085316.
- [6] T. Yamanaka, S. Ino, *Surf. Sci.* 330 (1995) 126.
- [7] T. Yamanaka, S. Ino, *Jpn. J. Appl. Phys.* 35 (1996) 3991.
- [8] R.S. Becker, J.A. Golovchenko, J.R. Patel, *Phys. Rev. Lett.* 50 (1982) 153.
- [9] S. Hasegawa, S. Ino, Y. Yamamoto, H. Daimon, *Jpn. J. Appl. Phys.* 24 (1985) L387.
- [10] T. Yamanaka, S. Ino, *Rev. Sci. Instr.* 72 (2001) 1477.
- [11] M. Chester, T. Gustafsson, *Surf. Sci.* 256 (1991) 135.
- [12] J. Nogami, S.-I. Park, C.F. Quate, *Phys. Rev. B* 36 (1987) 6221.
- [13] K. Murata, T. Matsukawa, R. Shimizu, *Jpn. J. Appl. Phys.* 10 (1971) 678.
- [14] D.E. Newbury, in: D.E. Newbury, D.C. Joy, P. Echlin, C.E. Fiori, J.I. Goldstein (Eds.), *Advanced Scanning Electron Microscopy and X-ray Microanalysis*, Plenum, New York, 1986, p. 3.



ELSEVIER

Available online at www.sciencedirect.com

SCIENCE @ DIRECT®

Journal of Crystal Growth 246 (2002) 15–20

JOURNAL OF CRYSTAL GROWTH

www.elsevier.com/locate/jcrysgro

Enhanced impurity incorporation by alternate Te and S doping in GaAs prepared by intermittent injection of triethylgallium and arsine in ultra high vacuum

Yutaka Oyama^{a,b}, Kenji Tezuka^a, Ken Suto^{a,b}, Jun-Ichi Nishizawa^{b,*}

^a *Department of Materials Science and Engineering, Graduate School of Engineering, Tohoku University, Aramaki Aza Aoba 02, Sendai 980-8579, Japan*

^b *Semiconductor Research Foundation, Semiconductor Research Institute, Kawauchi Aoba, Sendai 980-0862, Japan*

Received 24 May 2002; accepted 21 August 2002

Communicated by H. Ohno

Abstract

Enhanced incorporation of doped impurity in GaAs by alternate doping of Te and S is reported. When diethyltelluride (DETe) was injected on GaAs surface covered with S, the incorporation of Te was enhanced and it is shown that the Te concentration was increased according to the S coverage. Mechanism of enhanced impurity incorporation is discussed in view of the charge distribution in the molecules and the electronegativity difference.

© 2002 Elsevier Science B.V. All rights reserved.

Keywords: A1. Doping; A1. Impurities; A3. Atomic layer epitaxy; B1. Gallium compounds; B2. Semiconducting gallium arsenide; B2. Semiconducting III–V materials

1. Introduction

Novel semiconductor devices require the control of layer thickness with atomic accuracy and extreme steep impurity profile with very heavily doping concentration. Molecular layer epitaxy (MLE) is one of the most promising epitaxial growth methods to realize such multi-thin layered structure devices. MLE is the method to grow a mono-molecular GaAs epitaxial layer by applying intermittent injection of TMGa/AsH₃ onto GaAs

substrate, which has been achieved in 1984 by Nishizawa [1], after the idea of atomic layer epitaxy (ALE) of II–VI compounds on glass substrates by Suntola [2,3]. In this epitaxial process, GaAs layers are grown in a mono-molecular unit by the surface reaction. Nowadays, MLE method is extensively applied to various kinds of material systems.

In our previous study of X-ray multi-crystal diffractometry analysis [4], the differential strain has been observed in the homo-epitaxial layers doped with Te in the range of 10^{19} – 10^{20} cm^{−3}. This is because the covalent radius of Te is larger than that of Ga, As, and Te atoms may exist as lattice defect or form aggregation in the heavily doped

*Corresponding author. Tel.: +81-22-223-7287; fax: +81-22-223-7289.

E-mail address: nishizawa@hanken.jp (J.-I. Nishizawa).

region. However, in the case of S-doped GaAs, the differential strain hardly occurred in the epitaxial layer doped with S even in the range of 10^{19} – 10^{20} cm $^{-3}$, though the covalent radius of S is smaller than that of Ga, As (covalent radius R : $R_{\text{Ga}} = 1.24 \text{ \AA}$, $R_{\text{As}} = 1.21 \text{ \AA}$, $R_{\text{Te}} = 1.37 \text{ \AA}$, $R_{\text{S}} = 1.04 \text{ \AA}$ [5,6]). In accordance with these results, it is expected that the Te and S co-doping is unable to reduce the lattice strain, and then the enhanced incorporation of impurity will be expected due to the effect of strain compensation, which has been reported in Si vapor phase epitaxy [7].

In view of the steep impurity profile, the diffusion coefficient of Te ($D_{0,\text{Te}} = 1 \times 10^{-13}$ cm 2 /s at 1000°C [8]) is one of the smallest one in n-type dopant impurities. Thus, it is considered that Te atoms hardly diffuse during growth and an extreme steep impurity profile is expected. The diffusion coefficient of S ($D_{0,\text{S}} = 2.6 \times 10^{-5}$ cm 2 /s at 900–1000°C [7]) is also smaller than that of Se, Si ($D_{0,\text{Se}} = 3.0 \times 10^{-3}$ cm 2 /s at 727°C [9], $D_{0,\text{Si}} = 0.11$ cm 2 /s at 1150°C [10]). Thus, it is considered that S is also suitable to obtain an extreme steep impurity profile. The difference of the diffusion length of Te and S is expected to be about 10 Å in the case of MLE growth at 360°C.

Within our knowledge, co-doping of the different n-type gas dopant has never been intentionally conducted in the epitaxial growth by taking advantage of characteristics of two dopants. In this study, our purpose is to obtain a high-quality n-type GaAs thin layers with co-doping of Te and S. This is applicable to the fabrication of ideal SIT [11] and TUNNETT [12,13], which require multi-layered structures with atomic accuracy.

2. Experimental procedure

The substrates used were undoped semi-insulating (SI) (001) oriented GaAs by the liquid-encapsulated Czochralski (LEC) method. GaAs substrates were degreased by acetone, dichloroethane, iso-propylalcohol (IPA). Then, GaAs substrates were chemically etched by SEMICO-CLEAN[®] followed by dipping in HCl for 15 s for the removal of the thin oxide layer. After drying

IPA, substrates were set on a quartz pedestal with glassy carbon in the MLE growth chamber through a high-vacuum loading chamber. The pre-treatments of substrates were carried out in a growth chamber at 450°C under AsH $_3$ exposure whose pressure is 8.0×10^{-4} Torr [14].

Te and S heavily co-doped epitaxial layer were grown on GaAs substrate. Arsine (AsH $_3$) and triethylgallium (TEG) were used as precursors for the epitaxial growth of GaAs. Diethylsulfide (DES) and diethyltelluride (DETe) were used for the impurity doping source gases as donor dopants. The supplied pressures P of AsH $_3$, TEG, DETe, DES were 8.0×10^{-4} , 7.2×10^{-6} , 2.0×10^{-6} , 1.3×10^{-5} Torr, respectively.

In this experiment, two sorts of impurity doping sequences were applied. First, the impurity gas is exposed after the GaAs surface is terminated by the exposure of TEG followed by evacuation. This is denoted to be mode AG (after gallium). Second, the impurity gas is exposed after AsH $_3$ is exposed. This is denoted as mode AA (after AsH $_3$). The substrate temperature used in these experiments was 360°C where the doped impurity concentration difference between mode AA and AG shows maximum. As the growth temperature raised, the impurity concentration difference decreases in the temperature range of 320–450°C. A schematic drawing of the MLE growth sequence is shown in Fig. 1.

Secondary ion mass spectroscopy (SIMS) measurements were applied to determine the concentration of doped impurities with 1 keV, 10 nA Cs $^+$ as primary ions. The Te concentration was

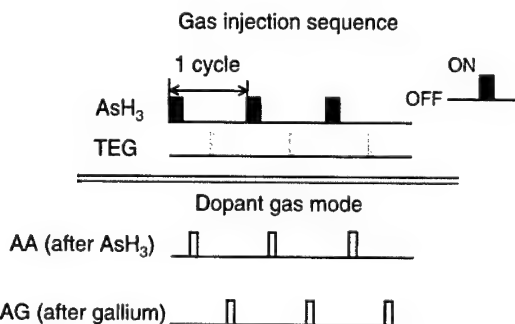


Fig. 1. A schematic drawing of the MLE growth sequence by the intermittent injection of TEG and AsH $_3$ in an ultra high vacuum.

calibrated by using horizontal Bridgman-grown bulk GaAs crystals doped with various concentration of Te grown under appropriate arsenic vapor pressure. S concentration was also calibrated by using S-implanted GaAs. In order to remove the effects of the side-wall region of sputtered 500 μm crater during SIMS measurements, only 9% area gating was used to retrieve the negative ions from the crater.

In order to investigate the lattice strain in heavily impurity-doped GaAs epitaxial layer, X-ray multi-crystals diffractometry analysis is

applied using $g = 004, 224$ diffraction plane with prefixed Ge(2 2 0) asymmetric configuration monochromator.

3. Results and discussion

Fig. 2(a) shows the SIMS depth profiles of multi-layered structure, in which each layer was grown subsequently only by changing the impurity doping sequences in one epitaxial process. Layered structure and impurity doping sequences are

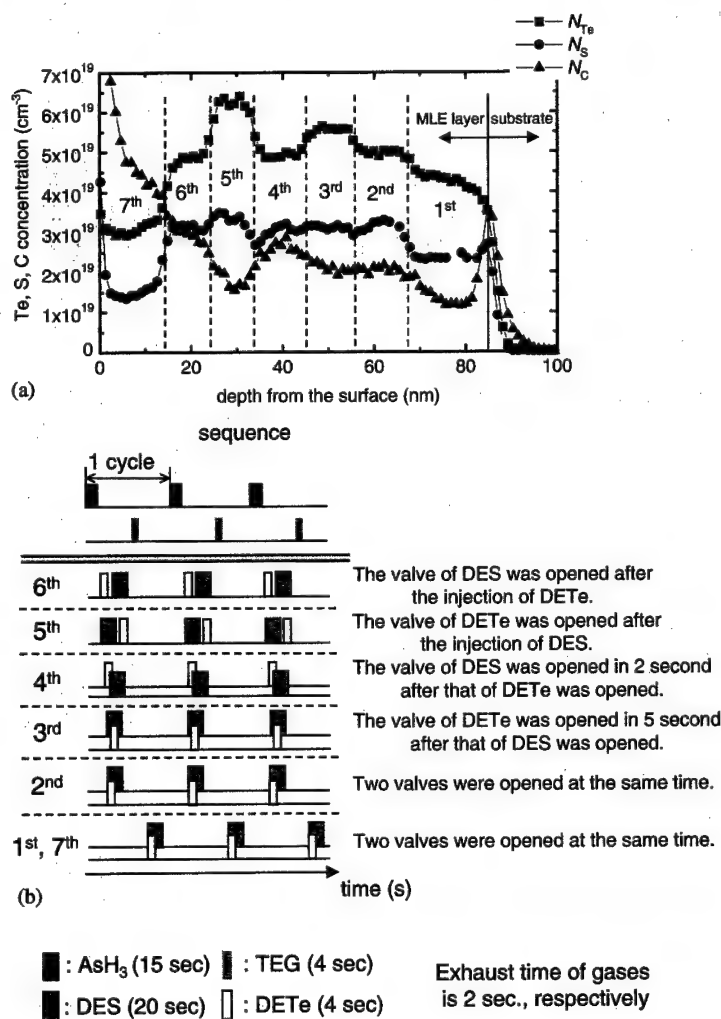


Fig. 2. (a) SIMS depth profiles of Te, S and Carbon in multi-layered structure, in which each layer was grown subsequently only by changing the impurity doping sequences in one epitaxial process. Carbon concentration is not calibrated and this is the relative value. (b) Layer structure and impurity doping sequences for SIMS measurement.

shown in Fig. 2(b). In Fig. 2(a), the doping sequences of 1st and 7th layers are the same. In these layers, DETe and DES were supplied at the same time after TEG was supplied on the surface (mode AG). Whereas 2nd layer was doped with DETe and DES at the same time also, the impurity doping sequence of 2nd layer is different and it is mode AA, in which the impurity source was supplied after AsH₃ is supplied on the surface. To compare the Te and S concentration between 1st/7th and 2nd layers, it is clearly shown that the incorporation of impurity is enhanced when the impurity source was exposed after AsH₃ is supplied on the surface. It is shown from the comparison between 2nd and 3rd layers that the Te concentration is enhanced when the DETe introduction is delayed after DES supply. This continues to the results of 5th layer with alternate supply of DES and DETe. It is also noticed that the impurity concentration of 1st and 7th layer, which were grown by the same doping sequence, shows difference. This reason is not clear, but may be due to the effect of interface in the 1st layer and the gradual change of source supply conditions during epitaxial growth.

In order to investigate the effect of S underlayer before the introduction of DETe in mode AA, it is clearly shown from Fig. 2(a) that the Te concentration of 5th layer, in which DETe is introduced after DES is supplied on the surface, is enhanced compared with that of 2nd and 3rd layers. It is also noticed that the residual C concentration is reduced in the 5th layer.

On the contrary, when we see the effect of Te underlayer on the incorporation of S in mode AA, it is shown that both Te and S concentration is almost the same as seen in 4th and 6th layers in Fig. 2(a) in this experimental conditions.

In order to investigate the S coverage dependences on incorporated Te concentration in mode AA, multi-layered structures were grown by changing the DES exposure time before DETe introduction. Fig. 3(a) shows the change of Te concentration as a function of S concentration. Doping sequences used in Fig. 3(a) is shown in Fig. 3(b). It is shown that Te concentration is increased monotonically according to the increase of S coverage, then shows a saturating tendency.

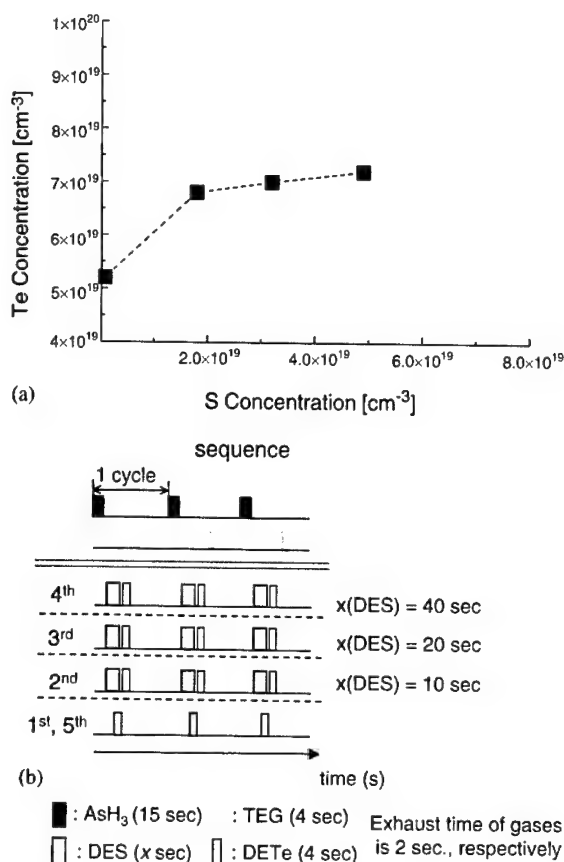


Fig. 3. Change of incorporated Te concentration as a function of S concentration when DES is exposed before DETe injection. (b) Doping sequences and layered structure for SIMS measurements.

Next, in order to investigate the effect of Te coverage on S concentration, the Te coverage was changed in order of the following written layers (Fig. 4(b)) by changing DES injection time before DETe injection in the similar sequences of 2nd layer, 4th layer and 6th layer in Fig. 2(b). Fig. 4(a) shows the Te concentration dependence on the S concentration. As shown in Fig. 4(a), S concentration decreased monotonically as a function of Te concentration.

The effect of underlying S layer on the enhanced incorporation of Te will be explained in view of the large electronegativity of S with respect to Te, As and C, and its relation with the charge distribution in DES and DETe molecules near the surface. The effect of underlying Te layer on the reduced

incorporation of S will be also explained by the small electronegativity of Te compared with those of S and C. Similar calculations [15,16] and observations based on the electronegativity difference have been reported in various kinds of surface

systems such as the initial reaction process of the HBO molecule on the Si (111)- 7×7 surface [17], oxygen on Si [18], monolayer graphite on Si-terminated SiC(111) [19], submonolayer coverages of In and Sb on Ge(100)- 2×1 surface [20], etc.

The electrical and crystallographic features were investigated by the Hall effect measurements and the X-ray multi-crystal diffractometry analysis. Table 1 shows the summary of the impurity concentration, carrier concentration, differential strain and the full-width at half-maximum (FWHM) value of X-ray rocking curves. All samples were grown at the same growth temperature of 360°C and the thickness of the epitaxial layer was almost the same. It is shown that the S-doped layer (sample A) with the impurity concentration of $4.5 \times 10^{19} \text{ cm}^{-3}$ has shown no double peaks in X-ray rocking curve, meaning that no serious strain is induced by S-doping. On the other hand, in the case of Te doped layer with almost the same impurity concentration of $4.2 \times 10^{19} \text{ cm}^{-3}$ has shown a differential strain ($\Delta a/a$) of 3.1×10^{-3} with FWHM of 165 arcsec. When sample B (Te doping) and D (Te and S doping) were compared, in which the Te concentration is almost the same and the total impurity concentration of D is larger than that of B, it is noticed that the differential strain is almost the same value of $3.1\text{--}3.6 \times 10^{-3}$. However, FWHM value of X-ray rocking curve for sample D (co-doping) is much narrower than that of sample B, meaning that the crystal quality was improved by the co-doping of Te and S presumably due to the strain compensation in the lattice.

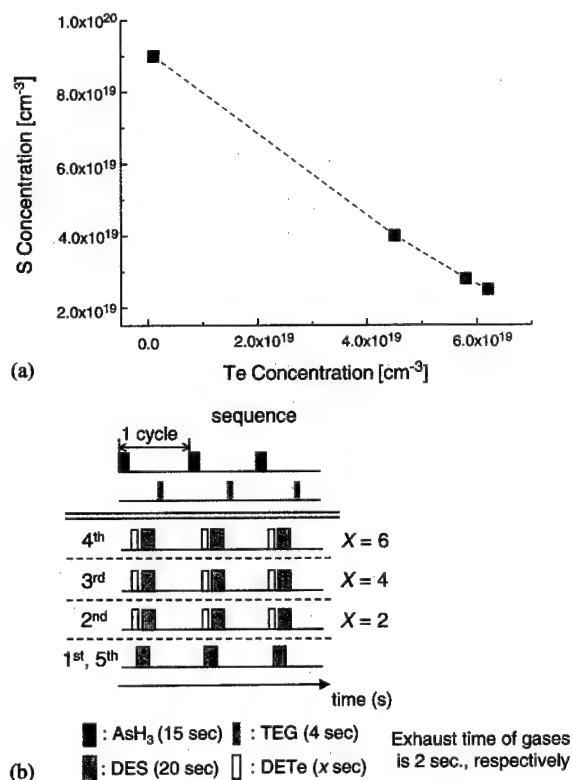


Fig. 4. (a) Te concentration dependence on the S concentration when DETe is exposed before DES injection, (b) Doping sequences and layered structure for SIMS measurements.

Table 1

Electrical and crystallographic characteristics of Te/S co-doped GaAs by the intermittent injection of TEG and AsH₃ with alternate doping of Te and S

Sample	Thickness (nm)	N_S (10^{19} cm^{-3})	N_{Te} (10^{19} cm^{-3})	$n(RT)$ (10^{19} cm^{-3})	$(\Delta a/a)$ ($\times 10^{-3}$)	FWHM (arcsec)
A (S-doped)	77	4.5	—	1.6	—	—
B (Te doped)	110	—	4.2	1.7	3.1	165
C (Te-doped)	101	—	6.0	0.54	2.3	582
D (Te and S co-doped)	118	2.3	4.5	1.6	3.6	137

4. Conclusion

In the GaAs epitaxial process by the intermittent injection of TEG and AsH₃ in an ultra high vacuum, the effects of alternate co-doping of Te and S on the incorporation of donor impurities were investigated. It was found that the incorporation of donor impurity Te is enhanced when the DES is exposed on (001) oriented GaAs surface before the introduction of DETe. Sulfur coverage dependence on the incorporated Te concentration is also shown. On the other hand, it is shown that the Te-related products on the surface prevent the incorporation of S in the epitaxial layer. These results are presumably closely related with the electronegativity difference between surface adatoms and polarized molecules. From the precise X-ray diffraction results, it is shown that the crystal quality was improved by the co-doping of Te and S presumably due to the strain compensation in the lattice.

Acknowledgements

The authors are grateful to Mr. Tomoyuki Hamano and Mr. Hideyuki Kikuchi of Semiconductor Research Institute for their technical support of MLE growth, and Kyoza Suda of Tohoku University for his technical support of SIMS measurements.

References

- [1] J. Nishizawa, Y. Kokubun, in: Extended Abstracts of the 16th Conference on Solid State Device and Materials, The Japan Society of Applied Physics, Kobe, Japan, 1984.
- [2] T. Suntola, J. Antson, Finnish Patent No. 52395, 1974, and US Patent No. 4058430, 1977.
- [3] M. Ahonen, M. Sessa, T. Suntola, *Thin Solid Films* 65 (1980) 301.
- [4] Y. Oyama, J.-I. Nishizawa, K. Seo, K. Suto, *J. Crystal Growth* 213 (2000) 221.
- [5] M. Leszczynski, J. Bak-Misiuk, J. Domagala, J. Muszalski, M. Kaniewska, J. Marczewski, *Appl. Phys. Lett.* 67 (1995) 539.
- [6] L. Pauling, *The Chemical Bond: A Brief Introduction to Modern Structural Chemistry*, Cornell University Press, Ithaca, NY, 1967, p. 136.
- [7] J. Nishizawa, in: C.H.L. Goodman (Ed.), *Crystal Growth*, Vol. 2, Plenum Press, New York, 1978.
- [8] H.C. Casey, G.L. Pearson, in: J.H. Crawford, L.M. Slifkin (Eds.), *Point Defects in Solids*, (Vol. 2), Plenum Press, New York, 1975, p. 203.
- [9] B. Goldstein, *Phys. Rev.* 121 (1961) 1305.
- [10] M.E. Greiner, J.F. Gibbons, *Appl. Phys. Lett.* 44 (1984) 750.
- [11] J. Nishizawa, *Proceedings of 11th Conference on Solid State Devices 1979*, *Jpn. J. Appl. Phys.* 19 (Suppl.) (1980) 3.
- [12] T. Okabe, S. Takamiya, K. Okamoto, J. Nishizawa, *IEEE Electron Device Meeting*, 1968.
- [13] Motoya, J. Nishizawa, *Topics in Millimeter Wave Technology*, Vol. 2, Academic Press, Boston, 1988, pp. 1–46 (Chapter 1).
- [14] J. Nishizawa, Y. Oyama, P. Plotka, H. Sakuraba, *Surf. Sci.* 348 (1996) 105.
- [15] M. Menon, R.E. Allen, *J. Vac. Sci. Technol. A* 6 (3) (1988) 1491.
- [16] J.J. Barton, C.A. Swarts, W.A. Goddard, T.C. Macgill, *J. Vac. Sci. Technol.* 17 (1) (1980) 164.
- [17] T. Kaikoh, K. Miyake, Y.J. Li, R. Morita, M. Yamashita, H. Shigekawa, *J. Vac. Sci. Technol. A* 18 (4) (2000) 1469.
- [18] T. Uchiyama, M. Tsukada, *Phys. Rev. B: Condens. Matter* 53 (12) (1996) 7914.
- [19] J. Nakamura, H. Konogi, T. Osaka, *Phys. Rev. B: Condens. Matter* 51 (8) (1995) 5344.
- [20] D.H. Rich, T. Miller, T.-C. Chiang, *Phys. Rev. B: Condens. Matter* 41 (5) (1990) 3004.



ELSEVIER

Available online at www.sciencedirect.com

SCIENCE @ DIRECT®

JOURNAL OF CRYSTAL GROWTH

Journal of Crystal Growth 246 (2002) 21–24

www.elsevier.com/locate/jcrysgro

Defect-selective etching of GaN in a modified molten bases system

G. Kamler^{a,*}, J.L. Weyher^{a,b}, I. Grzegory^a, E. Jezierska^c, T. Wosiński^d

^a High Pressure Research Center of the Polish Academy of Sciences, Sokolowska 29, 01-142 Warsaw, Poland

^b University of Nijmegen, RIM, Exp. Solid State Physics III, Toernooiveld 1, 6525 ED Nijmegen, The Netherlands

^c Faculty of Materials Science and Engineering, Warsaw University of Technology, Narbutta 85, 02-524 Warsaw, Poland

^d Institute of Physics, Polish Academy of Sciences, Al Lotników 32/46, 00-668 Warsaw, Poland

Received 24 April 2002; accepted 23 August 2002

Communicated by J.B. Mullin

Abstract

The method of defect-selective etching of Ga polar (0001) surface of GaN single crystals and epitaxial layers is presented. Etching is performed in molten KOH–NaOH eutectic (E) with an addition of 10 wt% of MgO powder (E+M). At temperatures above the melting point of E, a sticky droplet of etch is formed, which allows revealing of defects on one side of the crystal only, leaving the other side intact. This method is advantageous for defect study on Ga-polar surface of GaN single crystals, because the much higher temperature required for etching of this surface will not result in the fast dissolution of N-polar side. The reliability of the method has been confirmed by: (i) revealing of the indentation-induced dislocations in the GaN single crystals and (ii) comparison of the results of (E+M) etching with photoelectrochemical etching and transmission electron microscopy on hetero-epitaxial layers.

© 2002 Elsevier Science B.V. All rights reserved.

PACS: 81.65.C; 61.72.H

Keywords: A1. Etching; A1. Line defects; B1. Gallium nitride

Etching in molten NaOH–KOH eutectic has been successfully used for revealing dislocations in Ga-polar GaN hetero-epitaxial layers and N-polar surfaces of bulk GaN single crystals [1,2]. However, high etching rate anisotropy [3] makes etching of the Ga-polar surface of a bulk crystal difficult without protecting the much more reactive N-polar surface. The optimal temperature for

revealing dislocations on the Ga-polar surface is at least 100°C higher than that for the opposite surface, resulting in undesirable rapid dissolution of the GaN crystal (on the N-polar surface). In this communication a simple modification of the NaOH–KOH by addition of 10 wt% of MgO powder is presented, which allows revealing of dislocations on Ga-polar surfaces without attacking N-polar surfaces of GaN single crystals. The method is also suitable for well-controlled and/or local etching of hetero-epitaxial layers. The reliability of this method for revealing dislocations

*Corresponding author. Tel.: +48-22-632-1635; fax: +48-22-632-4218.

E-mail address: grzemler@o2.pl (G. Kamler).

is demonstrated by comparison with: (i) E-etch used on GaN hetero-epitaxial layers, (ii) plane view transmission electron microscopy (TEM) of this layer, (iii) photoelectrochemical (PEC) etching and (iv) formation of etch pits on dislocations introduced by indentation into GaN single crystals.

Etching studies were performed on high pressure grown GaN single crystals [4] and hetero-epitaxial GaN layers grown on sapphire by metal organic chemical vapor deposition (MOCVD). All experiments have been carried out on the (0001) Ga-polar surface. The Ga-polar surface of GaN single crystals was prepared by mechanical polishing using 0.1 μm diamond paste followed by reactive ion etching (RIE) in chlorine-argon radio frequency plasma. The reference N-polar surface was polished mechano-chemically [5]. Indentations were performed at 370°C under the load of 2 N for 10 min. Etching experiments were carried out in the temperature range of 300–500°C for 1–3 min in NaOH–KOH–MgO (labeled further E + M) mixture (53.6–37.3–9.1 at%, respectively). This composition corresponds to the NaOH–KOH eutectic with 10 wt% MgO addition. A piece of solid E + M was placed on the top of GaN sample, which was subsequently placed on an aluminum plate and heated on a hot plate. MgO hindered running out of molten bases from the etched surface. The thermocouple was placed next to the sample and the whole set was covered with a quartz evaporating dish in order to stabilize the temperature. For the purpose of calibration, the hetero-epitaxial layers were photo-etched (PEC etching method [6]) using the conditions described in Ref. [7] and etched in molten E in a Pt crucible [1]. After etching, the samples were studied by differential interference contrast (DIC) optical microscopy and scanning electron microscopy (SEM).

Etching in molten E + M of the Ga-polar surface of a low dislocation density GaN single crystal revealed characteristic star-like pattern on indentation-induced dislocations, Fig. 1a (as the reference, see “rosettes” revealed on N-polar surfaces by E etch in Refs. [1,2]). The only recognizable difference between the etch pits formed on Ga- and N-polar surfaces is their shape: the pits on Ga-polar surface are hexagonal (as shown in Fig. 1b),

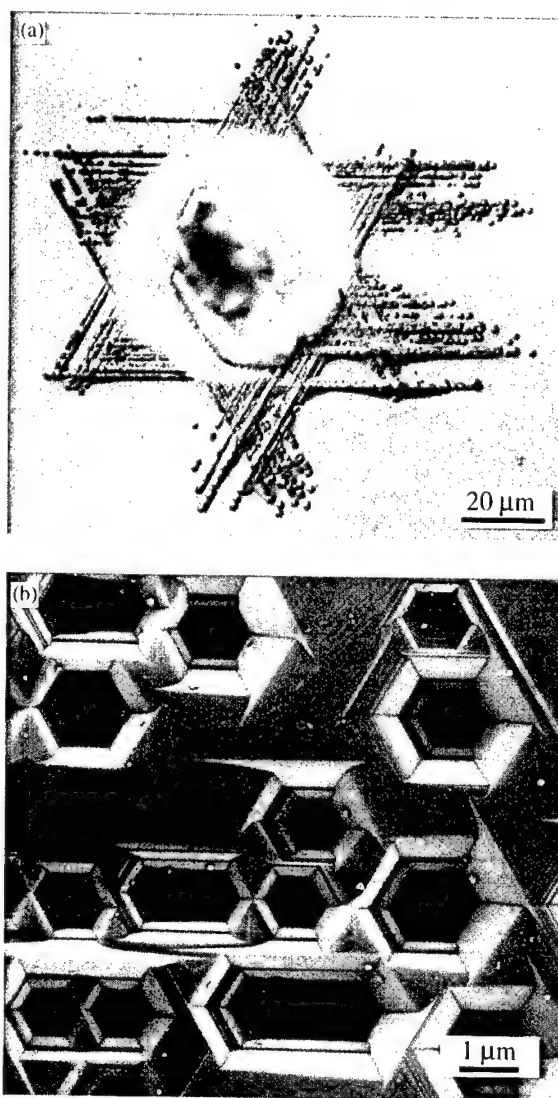


Fig. 1. (a) DIC optical image of dislocations introduced by indentation and revealed by E + M etching at 470°C. (b) SEM image of one arm of the rosette from (a).

while the ones on N-polar are rounded. This refers both to the pits on dislocations introduced by indentation and to the grown-in dislocations. The density of the latter was of the order of $4 \times 10^2 \text{ cm}^{-2}$, which remains in agreement with the previously reported density of dislocations in the GaN single crystals [1]. As a matter of example, Fig. 2a shows a single dislocation-related etch pit formed during E + M etching on Ga-polar

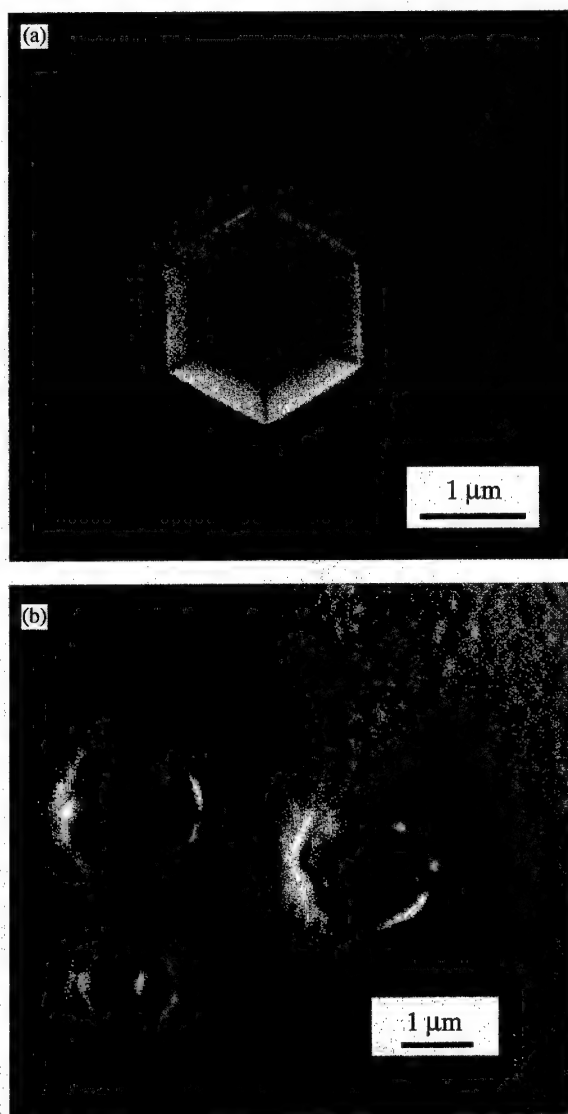


Fig. 2. SEM (a) and DIC optical (b) images of the grown-in dislocations revealed by E+M etch on (a) Ga-polar and (b) N-polar surfaces of GaN single crystals. The etching temperatures were 470°C and 250°C, respectively.

surface and Fig. 2b a group of dislocations revealed by the same etch on the N-polar surface.

Despite the use of MgO addition, some amount of molten E+M etch could get to the bottom N-polar surface of the GaN single crystal. No remarkable etching occurred, however, on this surface due to the use of the Al plate, which instantly reacts with molten E+M.

Typical image of the Ga-polar GaN hetero-epitaxial layer after E+M etching is shown in Fig. 3a. Similar results have been obtained by etching in molten E without the addition of MgO powder. Two grades of etch pits can be distinguished after this selective etching, namely the larger, less dense and the smaller ones. The latter often form linear or cell patterns. The density of the small pits is in the range $3\text{--}8 \times 10^9 \text{ cm}^{-2}$ and correlates well with the density of dislocations established from plane-view TEM examination of the same GaN layer. Similarly, the density of whisker-like etch features, which are formed during PEC etching (see Fig. 3b), is in the same range and their distribution often also assumes a cell-like pattern.

The same TEM study also revealed the presence of nano-pipes of density one to two orders of magnitude lower than the density of dislocations (see Fig. 3c). From the fact that nano-pipes can be considered as dislocations of the largest Burgers vector (i.e. of the largest energy) together with the previously established correlation between the larger etch pits and the nano-pipes [1], we conclude that the large pits in Fig. 3a were formed on the nano-pipes.

Concluding remarks: The E+M etching method presented in this communication is suitable for revealing dislocations on both Ga- and N-polar {0001} surfaces of epitaxial and single crystal GaN. An important advantage of the E+M over the E etch is that it can be used at high temperature for revealing dislocations on the Ga-polar surface of the GaN single crystals without dissolution of the N-polar side, despite it being much less resistant to any chemical attack. By comparison with PEC etching method and TEM examination of the plane-view epitaxial material, it can be concluded that the E+M etch constitutes a reliable etch for revealing dislocations and nano-pipes in GaN.

The authors would like to thank A. Presz for the SEM assistance, P.R. Hageman for the MOCVD-grown GaN sample and G. Nowak for RIE etching of the GaN single crystals. One of the authors (J.L.W.) wishes to thank Stichting voor Fundamenteel Onderzoek der Materie (FOM) and NATO (Linkage Grant) for financial support.

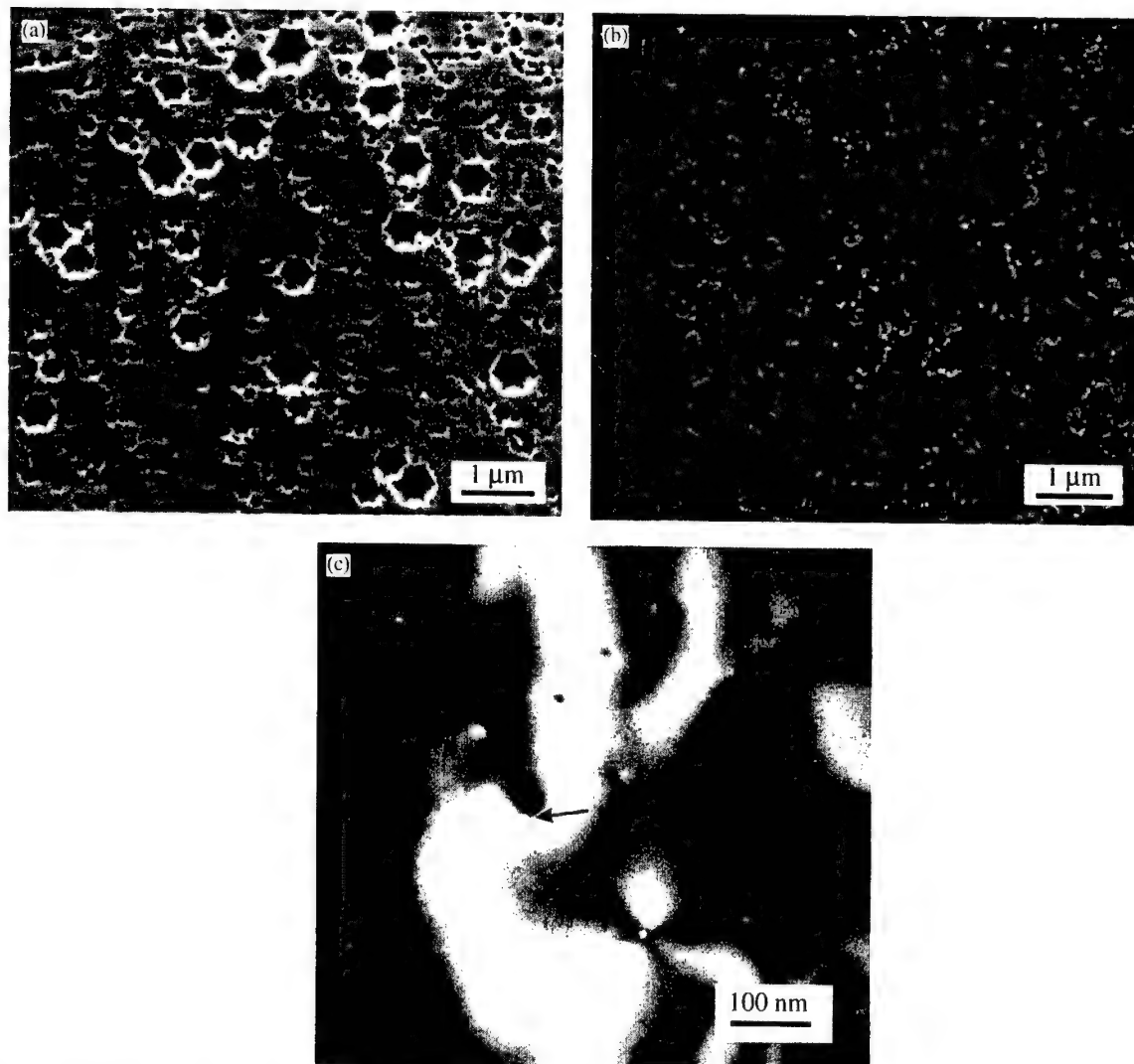


Fig. 3. SEM images of defect-related etch pits formed during E+M etching (a) and PEC etching (b) of two GaN hetero-epitaxial samples taken from the same 2" wafer. (c) Plane view TEM image of dislocations and nanopipes in the same material. The arrows point at the nanopipes.

References

- [1] J.L. Weyher, P.D. Brown, J.L. Rouviere, T. Wosinski, A.R.A. Zauner, I. Grzegory, *J. Crystal Growth* 210 (2000) 151.
- [2] J.L. Weyher, M. Albrecht, T. Wosiński, G. Nowak, H.P. Strunk, S. Porowski, *Mater. Sci. Eng. B* 80 (2001) 318.
- [3] J.L. Rouvière, J.L. Weyher, M. Seelmann-Eggebert, S. Porowski, *Appl. Phys. Lett.* 73 (1998) 668.
- [4] S. Porowski, I. Grzegory, *J. Crystal Growth* 178 (1997) 174.
- [5] J.L. Weyher, S. Muller, I. Grzegory, S. Porowski, *J. Crystal Growth* 182 (1997) 17.
- [6] C. Youtsey, L.T. Romano, I. Adesida, *Appl. Phys. Lett.* 73 (1998) 797.
- [7] J.L. Weyher, F.D. Tichelaar, H.W. Zandbergen, L. Macht, P.R. Hageman, *J. Appl. Phys.* 90 (2001) 6105.



ELSEVIER

Available online at www.sciencedirect.com

SCIENCE @ DIRECT®

Journal of Crystal Growth 246 (2002) 25–30

JOURNAL OF
CRYSTAL
GROWTH

www.elsevier.com/locate/jcrysgr

N-type doping behavior of $\text{Al}_{0.15}\text{Ga}_{0.85}\text{N}:\text{Si}$ with various Si incorporations

Cheul-Ro Lee

School of Advanced Materials Engineering, Research Center of Advanced Materials, Development (RCAMD), Engineering College, Chonbuk National University, Chonju 561-756, Chonbuk, South Korea

Received 12 August 2002; accepted 29 August 2002

Communicated by M. Schieber

Abstract

The n-type doping characteristics such as crystallinity, electronic and optical properties of $\text{Al}_{0.15}\text{Ga}_{0.85}\text{N}:\text{Si}$ epitaxial layers grown by MOCVD with various Si incorporations have been investigated. While the mirror-like surface without any defects such as cracks and hillocks can be seen in the undoped $\text{Al}_{0.15}\text{Ga}_{0.85}\text{N}$ epilayer which was grown without any intentional doping of Si, many cross hatch patterned cracks are observed in the n- $\text{Al}_{0.15}\text{Ga}_{0.85}\text{N}:\text{Si}$ which was grown with Si incorporation rate of 1.0 nmol/min. The N-type $\text{Al}_{0.15}\text{Ga}_{0.85}\text{N}:\text{Si}$ exhibits consistent increase in the electron concentration and decrease in the mobility with raising doping level of Si. The CL spectra of every Si-doped layer show that the donor-to-valence band transition is dominated at 350 nm, which is red shifted by 7 nm against the band edge luminescence emission of the undoped $\text{Al}_{0.15}\text{Ga}_{0.85}\text{N}$ layer. By calculating the relative intensity between donor-to-band transition of Si-doped $\text{Al}_{0.15}\text{Ga}_{0.85}\text{N}$ and band edge emission of the undoped compound, the change of optical characteristics with different Si doping levels were evaluated. This result suggested that the cross hatch patterned cracks of the layer which was highly doped by Si are responsible for the abrupt decrease of optical luminescence characteristics. © 2002 Elsevier Science B.V. All rights reserved.

PACS: 81.05.Ea; 81.15.Gh; 68.55.-a

Keywords: A1. CL; A3. Metalorganic chemical vapor deposition; B1. $\text{AlGaIn}:\text{Si}$; B1. n- AlGaIn

1. Introduction

Among III-nitride semiconductor alloys, the ternary $\text{Al}_x\text{Ga}_{1-x}\text{N}$ is an important material in nitride-based optoelectronic devices such as light emitters and detectors operating in the ultraviolet wavelength range [1–5]. Undoped and doped $\text{Al}_x\text{Ga}_{1-x}\text{N}$ films are commonly used for carrier

confinement as barrier layers in quantum well light emitting and laser diodes. And, this ternary semiconductor material is also needed for fabricating electronic devices such as $\text{Al}_x\text{Ga}_{1-x}\text{N}/\text{GaN}$ heterostructure field effect transistor (HFET), high-power electronic devices, high-speed electronic devices, and to allow operation at high temperature and in hostile environments [6–9].

But, so far, there have been relatively few publications on the growth characteristics and

E-mail address: crlee7@moak.chonbuk.ac.kr (C.-R. Lee).

doping properties of the $\text{Al}_x\text{Ga}_{1-x}\text{N}$ alloy system [10,11]. Most of these papers are dedicated to studies on the growth characteristics of this material system with the variation of Al content. Lee et al. [12] studied $\text{Al}_x\text{Ga}_{1-x}\text{N}$ for x between 0 and 0.75 and found that there was an abrupt decrease in bulk electron concentration and mobility for x in the range of 0.4–0.6, beyond which the crystal became semi-insulating. Bremser et al. [13] observed a rapid decrease in the net ionized donor concentration with increasing Al content. Until now, only a few researchers studied the optical and electronic properties related n- and p-type doping [12,14] notwithstanding the successful doping of $\text{Al}_x\text{Ga}_{1-x}\text{N}$ alloys is a great major requirement for the development of high efficiency wide-band-gap devices. Stampfl et al. [15] have investigated theoretically the doping characteristics of this alloy on the basis of density-functional-pseudopotentials calculations for native point defects and dopant impurities. Peter Kozodoy et al. have also calculated and demonstrated the polarization effect in p-type $\text{Al}_x\text{Ga}_{1-x}\text{N}$ alloy which enhances the ionization of deep acceptors and leads to the accumulation of carriers in hole sheets [16].

In this paper, the n-type doping behaviors of $\text{Al}_{0.15}\text{Ga}_{0.85}\text{N}:\text{Si}/\text{GaN}$ epilayers grown by MOCVD with various Si incorporations is reported. Double crystal diffractometry (DCXRD), atomic force microscope (AFM), van der Pauw technique (Hall effect measurement) and cathodoluminescence (CL) measurement were used to evaluate the doping characteristics of these epilayers.

2. Experimental procedures

The epitaxial films were grown in a horizontal MOCVD reactor at a reduced pressure of 300 Torr. NH_3 and MO-sources flow were separated to reduce undesirable parasitic reaction. The reactor was also modified for prevention of pre-reaction, reduction of convection and full mixing of all sources and gases in front of the susceptor [17]. Trimethylgallium (TMG), trimethylaluminum (TMA), NH_3 (ammonia) and SiH_4 (silane)

were used as Ga, Al, N and Si sources, respectively.

Fig. 1 is a schematic diagram of the structure of $\text{Al}_{0.15}\text{Ga}_{0.85}\text{N}:\text{Si}/\text{GaN}$ grown on sapphire (0001). The GaN epilayers of about $1.7\text{ }\mu\text{m}$ thick were grown on sapphire (0001) for 40 min at 1100°C after growing GaN nucleation layers of about 30 nm thick at 520°C . During the growth of GaN, the flow rates of NH_3 , TMG and H_2 were 1500 SCCM, 50 mol/min and 3000 SCCM, respectively. The background electron concentration and carrier mobility of GaN epilayers are $4 \times 10^{17}/\text{cm}^3$ and $220\text{ cm}^2/\text{Vs}$, respectively, with sharp band edge emission whose FWHM was 23 meV at room temperature (RT) and bound exciton emission whose FWHM was 5 meV at 10 K. The surface morphology observed with optical microscope and SEM was featureless and smooth without any defects such as hillocks or truncated hexagonals and so on.

After growing the undoped GaN epilayers mentioned above, Si-doped $\text{Al}_{0.15}\text{Ga}_{0.85}\text{N}$ epilayers of 150 nm thick were grown at 1100°C with increasing the flow rate of SiH_4 . During the growth of $\text{Al}_{0.15}\text{Ga}_{0.85}\text{N}:\text{Si}$, the flow rates of NH_3 , TMG, TMA and H_2 were 1500 SCCM, 20 mol/min, 7 mol/min and 3000 SCCM, respectively. And the flow rates of SiH_4 (50 ppm) were changed with 0 (sample A), 0.5 (sample B), 0.8 (sample C) and 1.0 nmol/min (sample D) in order to increase electron concentration in $\text{Al}_{0.15}\text{Ga}_{0.85}\text{N}$. Finally, each sample was evaluated by various tools for characterizing the crystallinity, electronic and optical properties of $\text{Al}_{0.15}\text{Ga}_{0.85}\text{N}:$

$\text{Al}_{0.15}\text{Ga}_{0.85}\text{N}:\text{Si}$ (t=150nm) (Tg=1100 °C)
Undoped GaN Layer (Tg=1100 °C, 1.7 μm)
GaN Nucleation Layer (Tg=520 °C, 30 nm)
Sapphire (0001)

Fig. 1. $\text{Al}_{0.15}\text{Ga}_{0.85}\text{N}:\text{Si}/\text{GaN}$ structure grown with various Si incorporations.

Si layer with various incorporation rates of the Si donor.

3. Results and discussion

Fig. 2 shows the surface morphologies observed by an optical microscope of Si-doped $\text{Al}_{0.15}\text{Ga}_{0.85}\text{N}$ epilayers A–D grown with various flow rates of SiH_4 . The mirror-like surface without any defect such as cracks and hillocks can be seen in the undoped $\text{Al}_{0.15}\text{Ga}_{0.85}\text{N}$ epilayer (sample A) which was grown without any intentional flow of SiH_4 . However, the surfaces of the $\text{Al}_{0.15}\text{Ga}_{0.85}\text{N}:\text{Si}$ epilayers become rough as the flow rate of SiH_4 during growth increases. Finally, the surface having many cross hatch patterned cracks is shown in sample D, which was grown with the highest Si incorporation. The rough surface means that the epilayer is partially grown three dimensionally instead of two-dimensional lateral growth. It is considered that the rough surface results from the large difference of the atomic size between Ga and Si. And also, it is believed that the cross hatch patterned cracks on the surface originate from the internal stress due to the large mismatch between GaN and highly Si-doped $\text{Al}_{0.15}\text{Ga}_{0.85}\text{N}$. In

general, the atomic size of Si which is the substitutional element for Ga in $\text{Al}_{0.15}\text{Ga}_{0.85}\text{N}$ is much smaller than that of Ga. This difference makes the lattice distort. And, the lattice distortion generates dislocations and cross hatch patterned cracks [18]. So, it can be supposed that the lattice distortion and dislocation density of $\text{Al}_{0.15}\text{Ga}_{0.85}\text{N}:\text{Si}$ epilayers increase with the increase of Si incorporation.

Fig. 3 shows AFM scan of Si-doped $\text{Al}_{0.15}\text{Ga}_{0.85}\text{N}$ epilayers A–D. The average RMS values of $\text{Al}_{0.15}\text{Ga}_{0.85}\text{N}:\text{Si}$ epilayers A–D are 0.524, 2.248, 2.748 and 1.295 nm, respectively. Although the surface morphology becomes rough with the increase of Si incorporation ranging from 0.0 to 0.8 nmol/min, the surface becomes flat again with Si rising from 0.8 to 1.0 nmol/min. This discontinuity means that the roughness of the surface within cross hatch patterned cracks becomes small as the cracks are generated. Therefore, the cracks are believed to play a role in releasing the internal stress of the $\text{Al}_{0.15}\text{Ga}_{0.85}\text{N}:\text{Si}$ epilayer. From the data of these AFM scans, it can be seen that the tendency for three-dimensional (3D) growth becomes stronger than that for a two-dimensional (2D) lateral growth with increasing Si incorporation in an $\text{Al}_{0.15}\text{Ga}_{0.85}\text{N}:\text{Si}$ epilayer.

Fig. 4 shows representative rocking curve for the (0002) diffraction of undoped $\text{Al}_{0.15}\text{Ga}_{0.85}\text{N}$ (A) and FWHMs of the DCXRD for (0002) diffraction from the Si-doped $\text{Al}_{0.15}\text{Ga}_{0.85}\text{N}$ epilayers grown with different flow rates of SiH_4 . The rocking curve shows two peaks. One of the two curves is the (0002) peak of GaN, the other is that of $\text{Al}_{0.15}\text{Ga}_{0.85}\text{N}$. The Al mole fraction of the $\text{Al}_x\text{Ga}_{1-x}\text{N}$ was determined by calculating the difference of peak positions between $\text{Al}_x\text{Ga}_{1-x}\text{N}$ and GaN peaks assuming the (0002) peak of GaN is constant at $2\theta = 34.53^\circ$ and Vegard's law is valid. The FWHMs of samples A, B, C and D are 472, 480, 505 and 518 arcsec, respectively. As the incorporation rate of Si in $\text{Al}_{0.15}\text{Ga}_{0.85}\text{N}$ increases, the crystallinity becomes worse. Therefore, it is possible to conclude that the dislocation density, which results from the difference of atomic size between Ga and Si, of the Si-doped $\text{Al}_{0.15}\text{Ga}_{0.85}\text{N}$ epilayers increases continuously with the raising of Si incorporation.

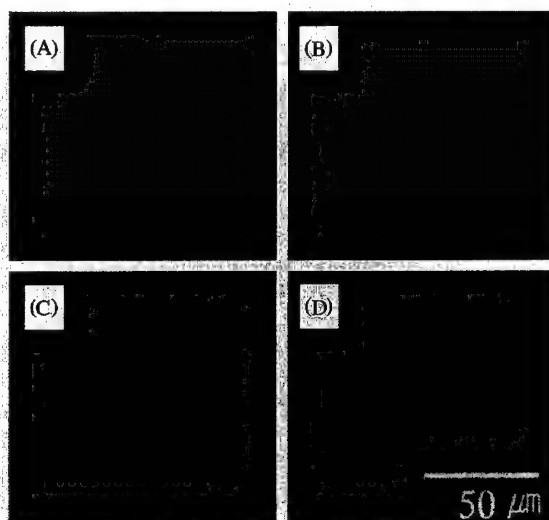


Fig. 2. Surface morphologies observed by optical microscope of Si-doped $\text{Al}_{0.15}\text{Ga}_{0.85}\text{N}$ epilayers A–D grown with various Si incorporations.

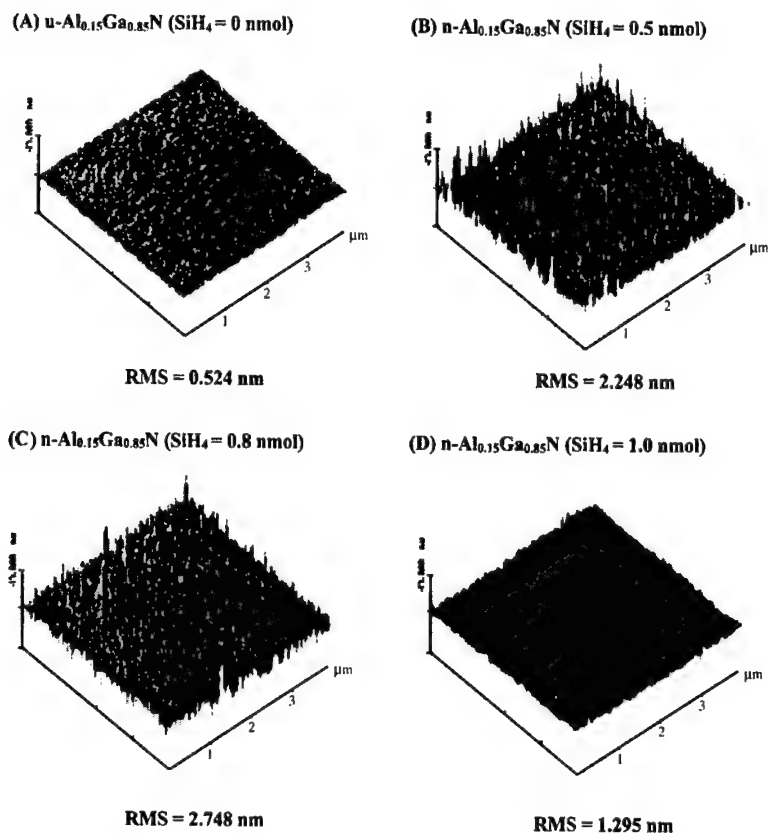


Fig. 3. DCXRD pattern for (0002) diffraction of undoped Al_{0.15}Ga_{0.85}N and crystallinity of Si-doped Al_{0.15}Ga_{0.85}N layers grown with various Si incorporations.

The electron concentration and carrier mobility of Si-doped Al_{0.15}Ga_{0.85}N epilayers were measured at RT by Hall effect measurement using the van der Pauw technique. Fig. 5 shows the results of Hall effect measurement on the Si-doped Al_{0.15}Ga_{0.85}N epilayers. Every Si-doped Al_{0.15}Ga_{0.85}N layer showed an n-type conduction. The carrier concentration and mobility of sample A grown without intentional Si doping are $2.0 \times 10^{18}/\text{cm}^3$ and $80 \text{ cm}^2/\text{Vs}$, of sample B are $3.2 \times 10^{18}/\text{cm}^3$ and $77 \text{ cm}^2/\text{Vs}$, of sample C are $6.0 \times 10^{18}/\text{cm}^3$ and $53 \text{ cm}^2/\text{Vs}$ and of sample D grown with the highest Si incorporation are $1.2 \times 10^{19}/\text{cm}^3$ and $50 \text{ cm}^2/\text{Vs}$, respectively. While the carrier concentration increased, the carrier mobility decreased with the increase of Si incorporation, which is believed to result from the increase of defect density illustrated in Fig. 4.

Fig. 6 exhibits the RT CL spectra of the Si-doped Al_{0.15}Ga_{0.85}N epitaxial layers at different levels of Si incorporation. For the undoped Al_{0.15}Ga_{0.85}N (sample A), the CL spectrum is dominated by band edge emission at 343 nm, while the band emission of undoped GaN are weakly shown at 365 nm. When the Si is introduced into the Al_{0.15}Ga_{0.85}N film (sample B), band edge emission peak disappears and the peak of donor-to-valence band transition at 350 nm begins to appear. This red shift of 7 nm is shown at every Si-doped Al_{0.15}Ga_{0.85}N sample (B, C, D) independent of the level of Si incorporation rate ranging from 0.5 to 1.0 nmol/min. Judging from these CL spectra in Fig. 6, it is considered that the donor element Si is easily activated in Al_{0.15}Ga_{0.85}N at any doping concentration and its activation energy is about 0.11 eV which is nearly the same as the

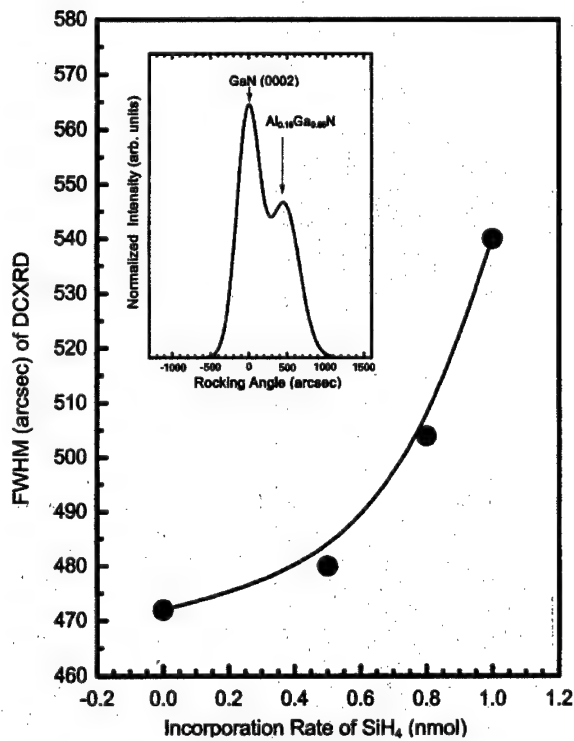


Fig. 4. AFM scan of Si-doped $\text{Al}_{0.15}\text{Ga}_{0.85}\text{N}$ epilayers A–D grown with various Si incorporations.

value in GaN layer [19]. Meanwhile, the emission of undoped GaN at 365 nm cannot be clearly discriminated for the samples B, C and D due to the red shifted peaks of Si-doped $\text{Al}_{0.15}\text{Ga}_{0.85}\text{N}$ layers.

Fig. 7 shows the relative intensity ratio ($I_{\text{DB}}/I_{\text{BE}}$) between I_{DB} (donor-to-valence band transition of Si-doped $\text{Al}_{0.15}\text{Ga}_{0.85}\text{N}$) and I_{BE} (band edge emission of undoped $\text{Al}_{0.15}\text{Ga}_{0.85}\text{N}$) peaks of the CL spectra measured at RT, which was calculated from Fig. 6. The calculated ratio of $I_{\text{DB}}/I_{\text{BE}}$ decreases by Si doping in $\text{Al}_{0.15}\text{Ga}_{0.85}\text{N}$ independent of the samples. This behavior is nearly similar to the change of crystallinity as shown in Fig. 4 and electrical characteristics as seen in Fig. 5, which maybe due to the increase of various non-radiation centers by Si doping such as vacancy, dislocation and cross hatch patterned cracks on the surface. While the relative intensity of donor-to-band transition is almost a constant value in spite of the increase of Si incorporation rate from 0.5 to 0.8 nmol/min, the intensity

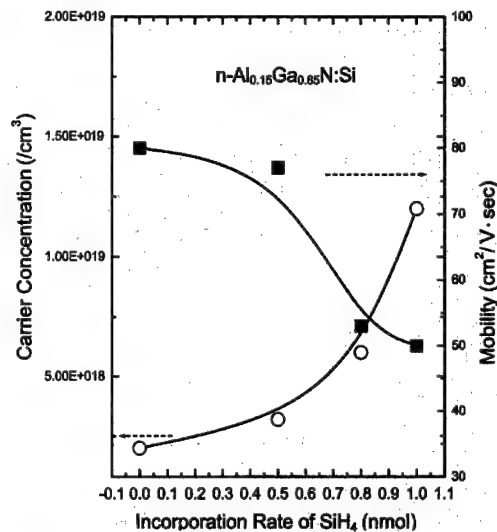


Fig. 5. Variation of electron concentrations and mobilities of $\text{Al}_{0.15}\text{Ga}_{0.85}\text{N}:\text{Si}$ layers grown with various doping level of Si.

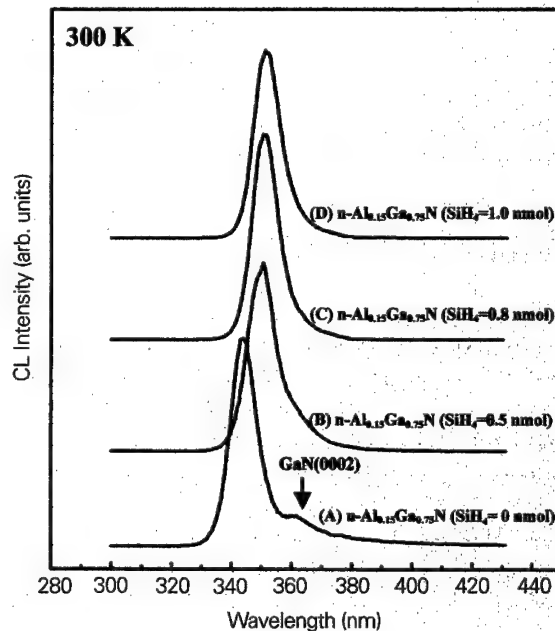


Fig. 6. CL spectra at room temperature of Si-doped $\text{Al}_{0.15}\text{Ga}_{0.85}\text{N}$ epilayers A–D grown with various Si incorporations.

decreases abruptly above the rate of 1.0 nmol/min (sample D). Therefore, it is considered that the reason why this abrupt decrement of intensity takes place from 1.0 nmol/min of SiH_4 probably results from the many cross hatch patterned cracks

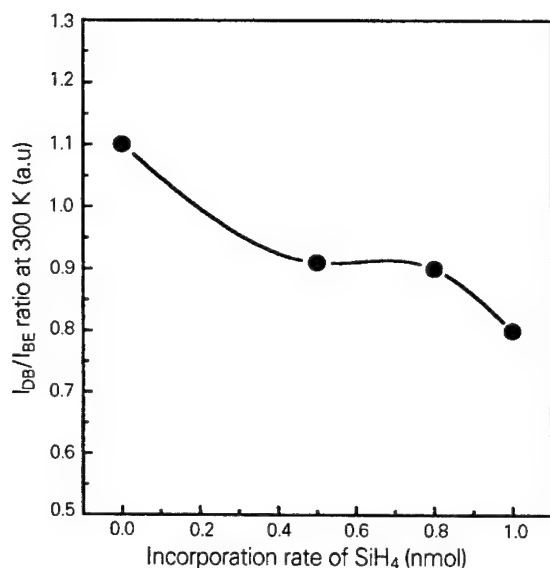


Fig. 7. CL intensity ratio (I_{DB}/I_{BE}) calculated from Fig. 6 of Si-doped $Al_{0.15}Ga_{0.85}N$ epilayers A–D grown with various Si incorporations.

on the surface as shown in Fig. 2(D), which is largely responsible for the non-radiation in optoelectronic materials.

4. Summary

The n-type doping behaviors of $Al_{0.15}Ga_{0.85}N:Si$ grown by MOCVD with different doping level of Si were evaluated.

Judging from experimental results, it can be concluded that the increase of Si incorporation roughens the surface and worsens the crystallinity of n- $Al_{0.15}Ga_{0.85}N:Si$ epilayers due to the increment of internal lattice distortion which generates dislocations and cross hatch patterned cracks. However, the generation of cross hatch patterned cracks makes flat the surface of local area within the cracks by releasing internal stress.

Meanwhile, the electron concentration increases and the mobility decreases nearly in proportion to the raising of Si incorporation. The donor-to-valence band transition of every Si-doped layer is dominated at 350 nm, which is red shifted by 7 nm against band edge emission of the undoped $Al_{0.15}Ga_{0.85}N$. And, the cracks of highly Si-doped

$Al_{0.15}Ga_{0.85}N$ are believed to take part in the abrupt decreasing of its optical luminescence characteristics.

Acknowledgements

This paper was supported by Korea Research Foundation Grant (2000-003-E00472).

References

- [1] S. Nakamura, J. Vac. Sci. Technol. A 13 (1995) 705.
- [2] S. Nakamura, M. Senoh, S. Nagahama, N. Iwasa, T. Yamada, Jpn. J. Appl. Phys. Part 2 35 (1996) L74.
- [3] K. Itaya, M. Onomura, J. Nishio, L. Sugiura, S. Saito, M. Suzuki, J. Rennie, Jpn. J. Appl. Phys. Part 2 35 (1996) L1315.
- [4] I. Akasaki, S. Sota, H. Sakai, T. Tanaka, M. Koike, H. Amano, Electron. Lett. 32 (1996) 1105.
- [5] S. Nakamura, M. Senoh, S. Nagahama, N. Iwasa, T. Yamada, T. Matsushida, Y. Sugimoto, H. Kiyoku, Appl. Phys. Lett. 69 (1996) 3034.
- [6] G. Yu, H. Ishikawa, M. Umeno, T. Egawa, J. Watanabe, T. Jimbo, T. Soga, Appl. Phys. Lett. 72 (1998) 2202.
- [7] J.A. Garrido, J.L. Sanchez-Rojas, A. Jimenez, E. Munoz, F. Omnes, P. Gibart, Appl. Phys. Lett. 75 (1999) 2407.
- [8] N. Dyakonova, A. Dickens, M.S. Shur, R. Gaska, J.W. Yang, Appl. Phys. Lett. 72 (1998) 2562.
- [9] J.P. Bergman, T. Lundstrom, B. Monemer, Appl. Phys. Lett. 74 (1998) 3456.
- [10] Tzu-fang Huang, J.S. Harris, Appl. Phys. Lett. 72 (1998) 1158.
- [11] J.B. Webb, H. Tang, S. Rolfe, J.A. Bardwell, Appl. Phys. Lett. 75 (1999) 953.
- [12] H.G. Lee, M. Gershenson, B.L. Goldenberg, J. Electron. Mater. 20 (1991) 621.
- [13] M.D. Bremser, W.G. Perry, T. Zheleva, N.V. Edwards, O.H. Nam, N. Parihh, D.E. Aspnes, R.F. Davis, MRS Internet J. Nitride Semicond. Res. 1 (1996) 8.
- [14] M.A. Khan, R.A. Skogman, R.G. Schulze, M. Gershenson, Appl. Phys. Lett. 43 (1983) 492.
- [15] C. Stampfl, J. Neugebauer, Chris G. Van de Walle, Mater. Sci. Eng. B 29 (1999) 253.
- [16] P. Kozodoy, M. Hansen, S.P. Danbaars, U.K. Mishra, Appl. Phys. Lett. 74 (1999) 3681.
- [17] C.R. Lee, S.J. Son, I.H. Lee, J.Y. Lee, S.K. Noh, J. Crystal Growth 182 (1997) 11.
- [18] A. Cros, R. Dimitrov, H. Angerer, O. Ambacher, M. Stutzmann, S. Christiansen, M. Albrecht, H.P. Strunk, J. Crystal Growth 181 (1997) 197.
- [19] I.H. Lee, I.H. Choi, S.K. Noh, Appl. Phys. Lett. 71 (10) (1997) 1359.



ELSEVIER

Available online at www.sciencedirect.com

SCIENCE @ DIRECT®

Journal of Crystal Growth 246 (2002) 31–36

JOURNAL OF
**CRYSTAL
GROWTH**

www.elsevier.com/locate/jcrysgr

On mass transport and surface morphology of sublimation grown 4H silicon carbide

D. Schulz^{a,*}, J. Doerschel^a, M. Lechner^b, H.-J. Rost^a, D. Siche^a, J. Wollweber^a

^a *Institut für Kristallzüchtung, Max-Born-Strasse 2, 12489 Berlin, Germany*

^b *SiCrystal AG, Paul, Paul-Gossen-Str. 100, 91052 Erlangen, Germany*

Received 13 June 2002; accepted 3 September 2002

Communicated by K.W. Benz

Abstract

Physical vapor transport experiments have been done with regard to mass transport and the morphology of 4H silicon carbide layers. Especially the very early stages of crystal growth were investigated. It was found that the growth rate is hardly influenced by the seed thickness. By using seeds of different off-orientations, morphological features of the grown surfaces could be revealed, which can be attributed to the formation of macrodefects. Two types of growth defects are discussed, which arise from the disturbance of the step flow either by step bunching or by micropipes.

© 2002 Elsevier Science B.V. All rights reserved.

PACS: 81.10.Bk; 68.35.Ct

Keywords: A1. Mass transfer; A1. Surfaces; A2. Growth from vapor; A2. Single crystal growth; B2. Semiconducting silicon compounds

1. Introduction

4H-SiC single crystal growth is challenging due to the poor polytype stability. The variety of parameters and processes which influence the occurrence of different polytypes during sublimation growth lead to a limited understanding of this phenomenon. In this context, special attention has to be paid on the early crystal growth stages, because normally the conditions are far from equilibrium. Not only temperature and pressure

but also the pressure reduction rate should have an influence on the polytype stability as has been first reported by Tairov et al. [1].

Different polytypes of SiC can be regarded as different stacking sequences of Si–C bilayers perpendicular to the *c*-axis. Therefore it can be assumed, that the desired polytype could be perfectly reproduced by using off-oriented seeds leading to the appearance of the special sequence directly at the surface. In the case of chemical vapor deposition, this is a common way to grow 4H-SiC layers free of other polytypes [2].

In the present paper we investigate the early stages of sublimation growth. Mass transfer as well as the surface morphology has been studied.

*Corresponding author. Tel.: +49-30-6392-2844; fax: +49-30-6392-3003.

E-mail address: dschulz@ikz-berlin.de (D. Schulz).

Surface features of layers grown on seeds with different off-orientations were examined by optical microscopy (OM), scanning electron microscopy in electron beam induced current (EBIC) mode and surface profiling. Two features of the surfaces will be discussed. In one case, the disturbance of the step flow is related to step bunching whereas in the other case it is induced by micropipes.

2. Experimental procedure

Growth experiments have been carried out in an inductively heated graphite crucible. A special set-up was created to provide both, the chance to be freely distributed in terms of the design as well as to be capable of growing single crystals at least up to 35 mm in diameter. The details of this arrangement are published in Ref. [3]. The temperature range of $2010 \leq T_G(^{\circ}\text{C}) \leq 2100$ has been applied. Growth pressures in the range of $300 \leq p_G(\text{Pa}) \leq 5000$ have been used to evaluate different stages, in particular at the very beginning of growth.

A growth sequence consisted of a heating phase while maintaining nearly atmospheric pressure, followed by an exponential pressure reduction down to the growth pressure p_G . According to the expression $p = p_0 \exp(-t/\tau) + p_G$, the time constant was set to $\tau = 15$ min (p_0 —starting pressure, t —time). Usually growth was stopped when reaching the final pressure p_G . In addition, in some experiments, both T_G and p_G were kept constant for a specified time before backfilling with inert gas and decreasing the temperature simultaneously. This is assumed to preserve the final growth state.

4G-SiC seeds with off-orientations of 2° , 5° and 8° , respectively, have been used for the study of the

off-orientation influence on the step flow pattern. The seed diameter was 35 mm.

3. Mass transport

To determine the growth rate in more detail, experiments of different final pressures and subsequent growth were done. The values are listed in Table 1. The growth time is estimated to be the difference between the reaching of 1800°C during the heating phase and the beginning of the backfilling process. Based on previous experiments, it was concluded that growth already occurs at temperatures as low as 1900°C [4]. The percentage is based on the total weight grown after the third step. It can be seen, that the crystallization rate increases by a factor of about 2.5 in the second phase. Obviously most of the material is grown during the third phase.

Another series of experiments was performed using the same growth sequence including all the three phases. After each growth run, the transport rate has been examined. The temperature was fixed at 2030°C and the growth duration was approximately 4.3 h. Basically only the seed thickness was varied between the growth runs. The growth rate remained nearly unchanged (Fig. 1).

Although the seed thickness increases from run to run by about $250 \mu\text{m}$, there is almost no change in the transport rate. Before experiment no. 8, the seed thickness reached about 5 times the thickness of the original seed.

A decrease of the growth rate with time has been described by different authors, e.g. Refs. [5,6]. By comparing experimental data with numerical simulations, this effect was attributed to heat transfer limitations [7,8]. Both heat transfer resistance of the growing crystal and the latent

Table 1

Mass increase during different growth stages (t_G growth time, R_{tot} growth rate corresponding to t_G , $T_G = 2085^{\circ}\text{C}$)

No.	Phase	t_G (h)	Mass increase (%)	R_{tot} (g/h)
(1)	Pressure reduction from atmospheric to 5000 Pa	1.04	2.6	0.009
(2)	Pressure reduction from 5000 to 500 Pa	1.42	6.6	0.028
(3)	2 h crystal growth at 500 Pa	3.42	90.8	0.17

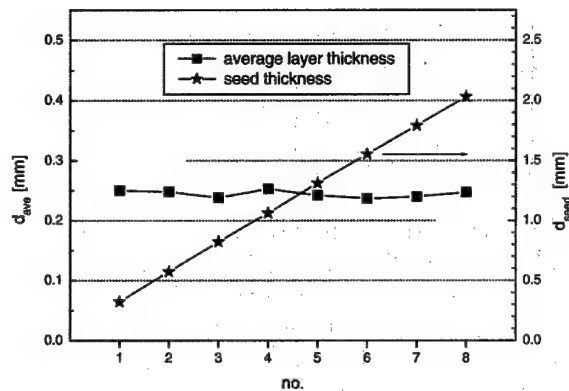


Fig. 1. Average thickness of the grown layer and seed thickness vs. subsequent growth runs.

heat of crystallization were assumed to cause an increase in the interface temperature and a decrease of the axial temperature gradient.

Since in the present analysis the differences in the growth rate can be neglected, the influence of the growing crystal on heat transfer was not detected. It has to be noted that the crystals were undoped. The doping level should have an influence on the radiative heat transfer conditions through the crystal.

4. Surface morphology

Three different kinds of seeds have been used for the study of the surface morphology. While maintaining the $[11.0]$ direction of the off-orientation, the angle has been varied between 2° , 5° and 8° .

In the case of 8° off-orientation, the surface is basically free of any steps and looks mirror-like. Disregarding the features connected with micropipes, there are several pits visible on the surface. In most cases they can be related to dislocations.

By decreasing the off-orientation to 5° a new type of growth steps occur. The terraces can be described as $(000\bar{1})$ planes surrounded by a circular segment (Fig. 2) which in the following will be referred to as growth defects. Surface profiling revealed a depth up to $0.5\mu\text{m}$ and the angle of the terraces coincides with the off-orientation of the substrate.



Fig. 2. Growth defect of a layer grown on 5° off-oriented seed (step flow direction downwards, optical micrograph).

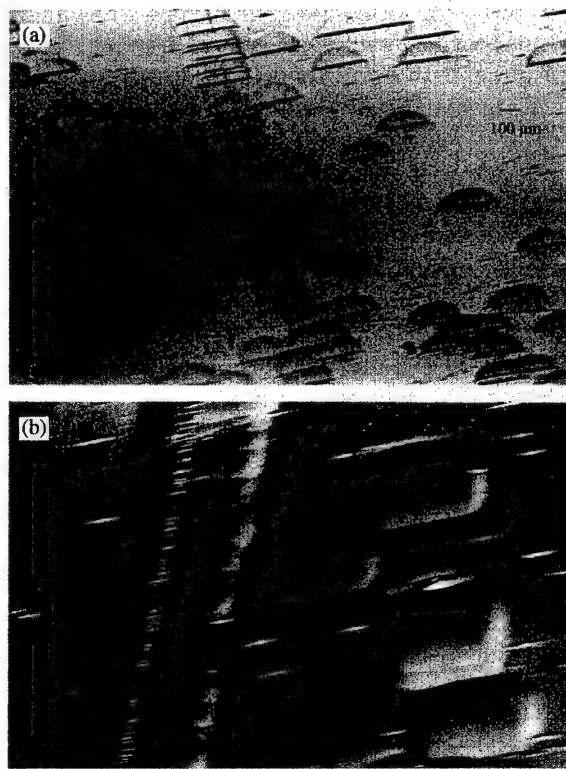


Fig. 3. Optical micrographs of layers on 5° off-oriented seeds: (a) layer thickness $\approx 5\mu\text{m}$ and (b) layer thickness $\approx 18\mu\text{m}$ (step flow direction is almost downwards).

These growth defects are often generated along artefacts of the mechanical polishing of the seeds. Scratches are assumed to be regions of higher dislocation density due to a subsurface damage layer. With increasing layer thickness, the growth defects tend to vanish, while leaving a depression on the surface (Fig. 3). Furthermore, the small pits which also occur on 8° layers are still present in smooth regions. In order to examine the origin of

the terraces, EBIC investigations have been carried out.

In the left-hand top corner of Fig. 4, a typical image of a micropipe can be seen, whereas there is no indication of dislocations connected with the growth defect. Consequently they may preferably form at defects, e.g. dislocations, but not necessarily.

When decreasing the off-orientation to 2° the growth defects enlarge even more in the lateral direction up to several millimetres. Then the circular segments interfere with each other.

Although the growth defects described above have not been found on 8° off-oriented seeds, the step flow may also be disturbed. Because micropipes act as obstacles with respect to the movement of a step, they can lead to open-volume defects recently reported by Siche et al. [9] to occur in bulk crystals. One type of these macrodefects could be attributed to polytype changes during sublimation growth, whereas the second type was assumed to be related to micropipe agglomeration.

The early stage of the second type of open-volume defects has been studied on 8° off-oriented layers. As can be seen in Fig. 5, the disturbance of the step flow leads to an elongation defect where crystallization is prohibited. The actual defect is even longer than visible from the figure. While the open-volume region vanishes, there still exists a surface depression. This shows, that the step flow has been disturbed in earlier stages as well. In

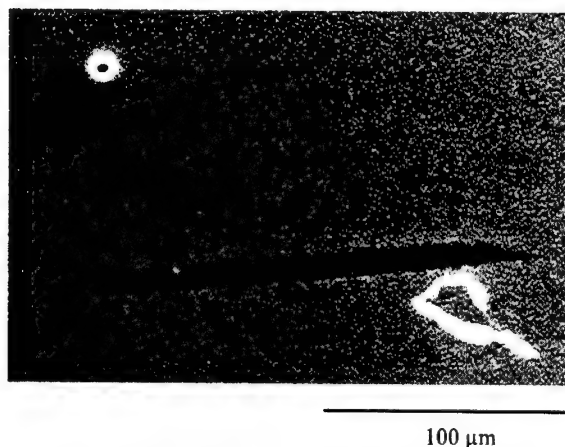


Fig. 4. Scanning electron micrograph in EBIC mode.

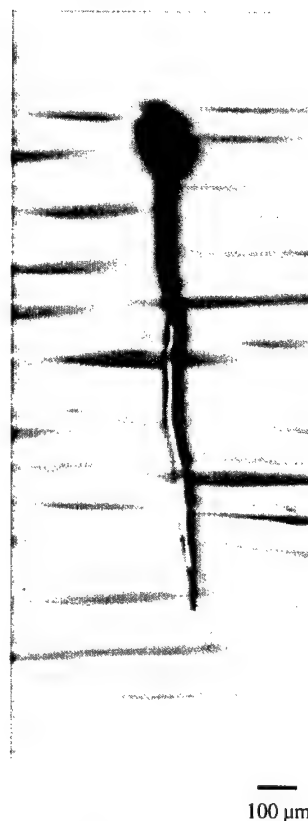


Fig. 5. Open-volume defect caused by a micropipe (8° off-oriented seed, step flow direction downwards, optical micrograph).

some cases, the depression bridges distances up to 10 mm. Part of this depression can be open while others stay closed. Open and close parts may also alternate with one another.

5. Conclusions

During the early crystal growth stages, especially in the pressure reduction phase, there are processes, which cannot adequately be described by steady-state physics. Most important changes in terms of the growth rate have been found in the pressure range between 5000 and 500 Pa. But also effects on surface morphology and polytype stability have to be expected.

A series of growth runs of high reproducibility indicate a constant crystallization rate on seeds of

different thickness. Consequently, heat transfer through the growing crystal does not influence mass transport conditions at least up to a crystal length of 2 mm. It can be concluded that a decrease of the growth rate during silicon carbide sublimation is mainly caused by the altering of the source material. In the case of a crucible inductively heated by only one coil, the highest temperature in the source material is usually at the periphery. Therefore graphitization most probably occurs in these regions, leading to both a decrease of the evaporation temperature and a diffusion barrier for the crystal-forming species coming from colder regions. As a consequence, the actual temperature difference between source and seed decreases.

The surface morphology of grown layers exhibit new features when decreasing the off-angle from 8° to 2° . In addition to the main facet, a large number of small (000 $\bar{1}$) planes associated with a circular depression form randomly distributed all over the layer surface. In some cases, the occurrence can be attributed to defects, such as artefacts of the mechanical treatment of the seed. EBIC investigations have shown that these depressions may be generated without interacting with dislocations. Assuming that step bunching is responsible for the built-up of the large basal planes, the random distribution could be explained. With increasing layer thickness also the facet size perpendicular to the step flow direction increases leaving a trace at both ends of the facet. This leads to the circular segment. After having reached a critical layer thickness, these facets start to decrease in size and therefore the depressions disappear. It is supposed that the occurrence is also connected with the interface curvature, because these growth defects have not been observed on the surface of bulk single crystals. Usually at first the interface is flat and starts to become convex within a few millimeters of growth.

Open-volume defects have been observed on layers grown on 8° off-oriented seed. In all cases these macrodefects are correlated to a micropipe. Similar defects were also reported for layers grown by sublimation epitaxy at temperatures of about 1800°C [10]. Their layers had a thickness up to $100\text{ }\mu\text{m}$ and the effect was more pronounced when increasing the growth rate above $50\text{ }\mu\text{m/h}$. The

steps even continued in the trench. In the present study, the layer thickness was typically $250\text{ }\mu\text{m}$ and the growth rate was about as twice as high. In contrast to the results of sublimation epitaxy step flow is even more disturbed, leading to an open volume behind the micropipe. This shows, that rather the step flow conditions on 8° off-oriented substrates than micropipe agglomeration can cause the generation of short open-volume defects in bulk crystals.

Moreover, an influence of nitrogen doping on step kinetics could be found. In run no. 7 of the

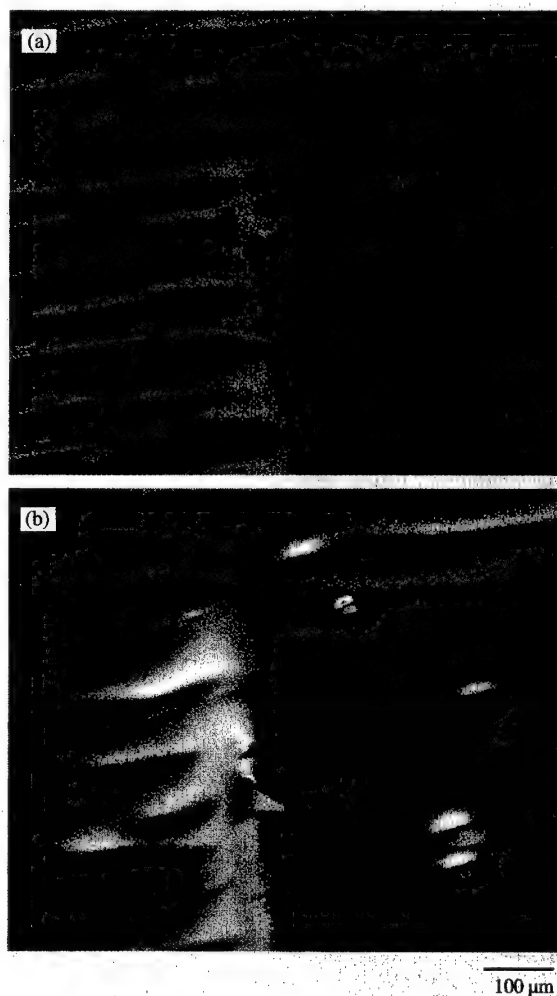


Fig. 6. Optical micrographs of layers grown on 8° off-oriented seed, open-volume defect (a) without doping, layer thickness $\approx 1\text{ mm}$, (b) with nitrogen doping, layer thickness $\approx 1.75\text{ mm}$ (step flow direction downwards).

eight subsequent experiments (Fig. 1) nitrogen was added to the inert gas atmosphere. The seed for these experiments already possessed an extended open-volume defect of several millimeters in length. From run to run, a hollow slit could be observed, showing that no crystallization took place inside the defect. By adding nitrogen to the atmosphere, the open volume began to close (Fig. 6). Similar to sublimation epitaxy [11] steps are found inside the depressed region. This clearly gives a hint of the influence of impurities on surface energy and therefore step kinetics. In addition, nitrogen is capable of stabilizing growth of the 4H polytype.

Acknowledgements

This work was financially supported by the Bundesministerium für Bildung und Forschung under the project number 01BM071.

References

- [1] Yu.M. Tairov, *Mater. Sci. Eng. B* 29 (1995) 83.
- [2] H. Matsunami, T. Kimoto, *Mater. Sci. Eng. R* 20 (1997) 125.
- [3] K. Böttcher, D. Schulz, *Mater. Sci. Forum* (2002), submitted for publication.
- [4] D. Schulz, G. Wagner, J. Doerschel, J. Dolle, W. Eiserbeck, T. Müller, H.-J. Rost, D. Siche, J. Wollweber, *Mater. Sci. Eng. B* 61, 62 (1999) 86.
- [5] Yu.M. Tairov, V.F. Tsvetkov, in: R.C. Marshall, J.W. Faust Jr., C.E. Ryan (Eds.), *Silicon Carbide-1973*, University of South Carolina Press, South Carolina, 1973, pp. 146–160.
- [6] S.Yu. Karpov, A.V. Kulik, I.A. Zhmakin, Yu.N. Makarov, E.N. Mokhov, M.G. Ramm, M.S. Ramm, A.D. Roenkov, Yu.A. Vodakov, *J. Crystal Growth* 211, 347.
- [7] R. Eckstein, D. Hofmann, Y. Makarov, St.G. Müller, G. Pensl, E. Schmitt, A. Winnacker, *Mater. Res. Soc. Symp. Proc.* 423 (1996) 215.
- [8] St.G. Müller, R. Eckstein, D. Hofmann, L. Kadinski, P. Kaufmann, M. Kölbl, E. Schmitt, *Mater. Sci. Forum* 264–268 (1998) 264.
- [9] D. Siche, J.-J. Rost, J. Doerschel, D. Schulz, J. Wollweber, *J. Crystal Growth* 287 (2002) 237.
- [10] R. Yakimova, M. Syväjärvi, T. Iakimov, H. Jacobsson, A. Kakanakova-Georgieva, P. Raback, E. Janzen, *Appl. Surf. Sci.* 184 (2001) 27.
- [11] N. Vouroutzis, R. Yakimova, M. Syväjärvi, H. Jacobson, J. Stoemenos, E. Janzen, *Mater. Sci. Forum* 389–393 (2001) 395.

A global thermal analysis of multizone resistance furnaces with specular and diffuse samples

Isabel Pérez-Grande, Damián Rivas*, Valentín de Pablo

E.T.S.I. Aeronáuticos, Universidad Politécnica de Madrid, Plaza Cardenal Cisneros 3, 28040 Madrid, Spain

Received 16 July 2002; accepted 3 September 2002

Communicated by K.W. Benz

Abstract

The heating process in multizone resistance furnaces, as applied to floating-zone crystal growth, is analyzed. A global model is formulated, where the temperature fields in the sample, the furnace and the insulation are coupled; the input thermal data is the electric power supplied to the heaters; the thermal conductivity of the insulation is modeled with the aid of experimental results. The radiation heat exchange between the sample and the furnace is formulated analytically, taking into account specular reflections on the sample; in general, for solid samples the reflectance is both diffuse and specular, and for some melts it is mostly specular. This behavior is modeled through the exchange view factors, which depend on whether the sample is solid or liquid, and, therefore, they are not known a priori. The effect of this specular behavior on the temperature field is analyzed, and compared with the case of diffuse samples; this effect is shown to be important in the analysis of the melt zone, for instance, differences of the order of 100% are obtained in parameters like the melt length or the maximum temperature difference in the melt when specular reflections are neglected. The model is used to simulate the heating process in the floating-zone technique in microgravity conditions; parameters like the Marangoni number or the temperature gradient at the melt–crystal interface are estimated. The model is validated comparing with experimental data.

© 2002 Elsevier Science B.V. All rights reserved.

PACS: 81.10.Mx; 44.40.+a

Keywords: A1. Computer simulation; A1. Heat transfer; A1. Radiation; A2. Floating zone technique; A2. Microgravity conditions; A2. Multizone resistance furnaces

1. Introduction

Resistance furnaces have been commonly used in microgravity experimental programmes for

directional solidification (see the monograph facilities for microgravity investigation in physical sciences supported by ESA, ESA SP-1116, revision 2, 1995). Presently, a resistance furnace (FMF) is being developed to be used in the International Space Station (ISS) for the floating-zone technique [1,2]. This method for crystal growth is widely used in microgravity since it is a container-free method,

*Corresponding author. Tel.: +34-91-336-6308; fax: +34-91-336-6307.

E-mail address: damian@fmetsia.upm.es (Damián Rivas).

which allows to obtain crystals of high quality. A predecessor of this furnace has been presented and tested in Refs. [3,4]; it is a 10-zone resistance furnace (ZMF), designed for high-temperature floating-zone or travelling-heater growth. Another laboratory model is considered in Ref. [5]; this is a three-zone resistance furnace, which is designed for growth experiments under the influence of magnetic fields (in the present work we will model this furnace and reproduce results obtained with it).

The temperature distribution during the growth process must be carefully controlled to improve the quality of the grown crystal; for example, the growth of compound semiconductors requires the control of the temperature gradients at the growing interface to avoid constitutional supercooling [6]. Therefore, a good knowledge of the temperature field is necessary in order to design the μg experiments properly. Along with on-ground experimentation, an important tool is the numerical simulation of the process. Thus, the mathematical modeling of the problem becomes a necessary task. Different models of the heating process in resistance furnaces have been developed. Crochet et al. [7] present a mathematical model for the case of crystal growth by the vertical Bridgman method; they consider important factors like the semitransparency of the melt container. Adornato and Brown [8] analyze segregation effects in directional solidification by the vertical Bridgman method, considering a three-zone furnace; in their model the furnace temperature is given and fixed. Brandon and Derby [9] consider a furnace model similar to that of [8], and apply it to the growth of semitransparent crystals. Amon et al. [10] consider the vertical gradient-freeze technique; they use a multizone furnace that is optimized by the computer package developed by Kurz et al. [11]. Boschert et al. [5] and Lin et al. [1] simulate the heating process using the FIDAP commercial code; they analyze the effect on the design of devices like magnets to produce magnetic fields or the visualization optical system. In all these works, the models of the radiation problem do not consider specular reflections (that is, they assume that the radiation is only diffuse).

In the case of floating-zone growth, the melt surface in many crystals (like Si or Ge) has a

mirror-like character and the reflectance of the solid sample has a specular component, therefore, a priori, a proper model of the radiation process must include both specular and diffuse reflections, if one is to obtain the temperature field in the sample accurately. The specular behavior of surfaces has been considered in configurations different from the floating zone, for instance, Maruyama and Aihara [12] and Hann et al. [13] analyze the radiation heat transfer with specular and diffuse surfaces in a Czochralski furnace (for the radiative interaction they use a ray-tracing method). To the best of our knowledge, specular reflections on the sample have not been taken into account previously in the analytical formulation of the radiation problem in the floating-zone method. The main task of this work is the formulation of the radiative heat exchange in resistance furnaces with specular and diffuse reflecting samples in the floating-zone technique. From the formulation point of view, the main consequence of considering specular reflections is that the exchange factors (needed to describe the radiative interaction) change as the melt zone changes; hence, they cannot be calculated beforehand, but they are part of the solution (just as the extent of the melt is). We will show that the effect of these specular reflections on the results is quite important, parameters like the melt length or the Marangoni number (that drives the thermocapillary flow in the melt) change considerably.

The description of the heating process in this kind of furnaces requires a global formulation; indeed, the radiation problem is coupled to the conduction heat transfer in the sample (including the phase change), in the furnace (including the heat generation by the heaters), and in the insulation. Thus, in this work we formulate a global model where the heat input is the electric power supplied to the heaters. For concreteness, we consider a three-zone furnace like the one described in Boschert et al. [5]. We seek the steady state, and at this stage we do not consider convection effects in the melt. We will perform a parametric study to determine the influence of different factors on the temperature fields. A parameter that happens to be very important is the thermal conductivity of the insulation material,

on which the temperature field depends strongly. A precise characterization of the insulation is difficult to make, due to the inhomogeneities that it has; in this work it will be made with the aid of experimental results, in such a way that the model becomes adjusted for that particular furnace. These experiments will also serve to validate the model. Finally, we will use the model to estimate important parameters for the floating-zone growth in μg conditions, like the Marangoni number or the temperature gradient at the melt–crystal interface.

2. Problem geometry

The sample is modeled by a solid cylinder of radius R_1 and length $2L$, and the furnace by a hollow cylinder of length $2L$ as well, concentric with the sample. The furnace consists of two layers made of different materials, as shown in Fig. 1. The inner layer, of thickness t_c , is made of ceramic material. The heaters are wrapped around this layer and covered by a layer of insulation material.

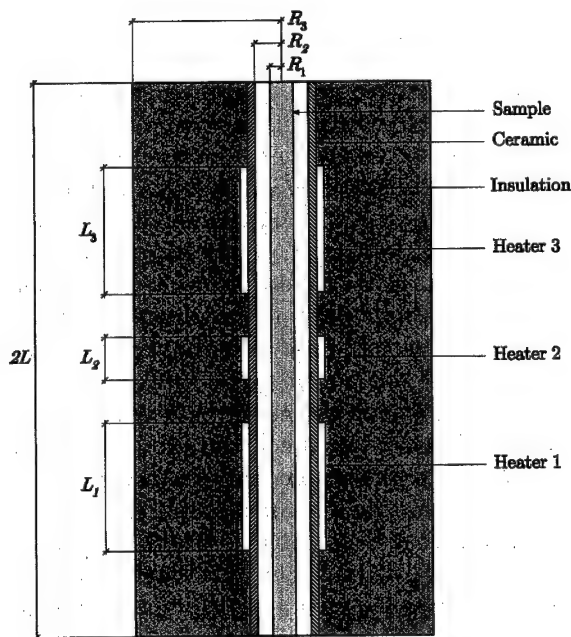


Fig. 1. Sample and furnace geometry.

The inner radius of the furnace is R_2 and the outer radius of the insulation layer is R_3 . In this work we consider a furnace powered by three heaters placed symmetrically. The length of the two outer heaters is $L_1 = L_3$ and that of the central heater is L_2 , the separation between heaters is d and their thickness is t_h .

In the following the furnace used in Ref. [5] will be considered. Thus, the geometrical parameters take the following values: $2L = 330$ mm, $R_2 = 15$ mm, $R_3 = 80$ mm, $t_c = 5$ mm, $L_1 = L_3 = 79$ mm, $L_2 = 22$ mm, $d = 21$ mm, $t_h = 2$ mm. The radius of the sample and the power of the heaters will depend on the application. The ceramic and insulation materials are corundum and keratherm, respectively. The furnace interior will be filled with air, and the two ends will be closed.

Notice that for simplicity we have considered the same length for the sample and the furnace, which leads to quite long samples. This is in fact the case to be considered in the FMF furnace in the ISS, where a sample of length 250 mm is envisaged [2].

3. Problem formulation

The temperature fields in the sample and in the furnace are coupled through the radiative interaction between the cylindrical surface of the sample and the inner surface of the furnace (and also to a lower extent through the furnace atmosphere). Therefore, we formulate the conduction problem in the sample and in the furnace (including the insulation), and the radiation problem in the furnace interior. The effect of the furnace atmosphere is taken into account, in a simplified manner, in the boundary conditions at both the inner surface of the furnace and the surface of the sample: heat fluxes proportional to the temperature difference between the two surfaces are considered, these fluxes are determined using an effective thermal conductivity for the gas, as defined in Ref. [14], and assuming one-dimensional heat transfer across the gas layer.

In the formulation of the problem we consider the following hypothesis in respect of the interaction with the environment: (a) the two annular

bases of the furnace are thermally isolated; (b) the external cylindrical surface of the furnace is at a constant temperature, set by the external cooling water circuit; (c) the two bases of the sample are at constant temperatures, defined experimentally, and (d) the effect of the two annular closing ends of the furnace interior is neglected altogether.

The problem is supposed to be axisymmetric, thus, only a meridian section needs to be studied. We consider a cylindrical coordinate system (\hat{r}, \hat{z}) centered in the center of the sample. In the formulation of the radiative interaction, one must take a point of the sample's surface, say with axial coordinate \hat{z} , and another point of the furnace's surface with a different axial coordinate, say $\hat{\eta}$ (see Eqs. (11)–(12)). Thus, for clarity, in the following general formulation we consider the axial variable \hat{z} for points in the sample and the axial variable $\hat{\eta}$ for points in the furnace. The dimensionless coordinates are $r = \hat{r}/R_1$, $z = \hat{z}/L$ (along the sample) and $\eta = \hat{\eta}/L$ (along the furnace). The dimensionless temperatures are $\theta_1 = T_1/T_m$ (sample) and $\theta_2 = T_2/T_m$ (furnace), T_m being the sample's melting temperature. For the radiation problem, the dimensionless heat fluxes are $q_1 = Q_1/\sigma T_m^4$ (sample) and $q_2 = Q_2/\sigma T_m^4$ (furnace), where σ is the Stefan–Boltzmann constant.

In dimensionless form, the steady, axisymmetric sample temperature field, $\theta_1(r, z)$, is given by the conduction equation and boundary conditions as follows:

$$\frac{\partial}{\partial z} \left(k_1(\theta_1) \frac{\partial \theta_1}{\partial z} \right) + A^2 \frac{1}{r} \frac{\partial}{\partial r} \left(r k_1(\theta_1) \frac{\partial \theta_1}{\partial r} \right) = 0, \quad (1)$$

$$\theta_1(r, -1) = \theta_{b1}, \quad (2)$$

$$\theta_1(r, 1) = \theta_{b2}, \quad (3)$$

$$\frac{\partial \theta_1}{\partial r}(0, z) = 0, \quad (4)$$

$$k_1(\theta_1) \frac{\partial \theta_1}{\partial r}(1, z) = -Ra_1 q_1(z) - Bi_1(\theta_1 - \theta_2) \quad (5)$$

and, likewise, the furnace temperature field, $\theta_2(r, \eta)$, by

$$\frac{\partial}{\partial \eta} \left(k_2(\theta_2) \frac{\partial \theta_2}{\partial \eta} \right) + A^2 \frac{1}{r} \frac{\partial}{\partial r} \left(r k_2(\theta_2) \frac{\partial \theta_2}{\partial r} \right) + \tilde{q}_h(r, \eta) = 0, \quad (6)$$

$$\frac{\partial \theta_2}{\partial \eta}(r, -1) = 0, \quad (7)$$

$$\frac{\partial \theta_2}{\partial \eta}(r, 1) = 0, \quad (8)$$

$$\theta_2 \left(\frac{R_3}{R_1}, \eta \right) = \theta_0, \quad (9)$$

$$k_2(\theta_2) \frac{\partial \theta_2}{\partial r} \left(\frac{R_2}{R_1}, \eta \right) = Ra_2 q_2(\eta) + Bi_2(\theta_2 - \theta_1), \quad (10)$$

where $\tilde{q}_h(r, \eta)$ is the dimensionless volumetric heat generation (by the heaters), made dimensionless as

$$\tilde{q}_h = \frac{\tilde{Q}_h L^2}{k_f T_m},$$

where k_f is the reference thermal conductivity of the furnace. The function \tilde{Q}_h is null except in the three regions occupied by the heaters. In each of these regions, it is uniform and given by (power per unit volume)

$$\tilde{Q}_h = \frac{W_i}{2\pi t_h L_i (R_h + t_h/2)},$$

where W_i is the power of the corresponding heater, and $R_h = R_2 + t_c$ is the inner radius of the heaters.

In these equations $\theta_{b1} = T_{b1}/T_m$ and $\theta_{b2} = T_{b2}/T_m$ are the known temperatures at the bases of the sample, $\theta_0 = T_0/T_m$ is the known temperature at the furnace cylindrical outer surface. The thermal conductivities of the sample and the furnace are defined by the dimensionless functions $k_1(\theta_1) = \hat{k}_1(T_1)/k_s$ and $k_2(\theta_2) = \hat{k}_2(T_2)/k_f$, where k_s is the reference thermal conductivity of the sample. These two functions are in general discontinuous: the former as a consequence of the phase change in the sample, and the latter due to the various materials that form the furnace.

The functions $q_1(z)$ and $q_2(\eta)$ in Eqs. (5) and (10) are the net *outgoing* radiation heat fluxes along the sample and the furnace, respectively. The formulation of the radiation problem for these two heat

fluxes is the main task of this work; this is done in the next section. For convenience we include here the final set of equations

$$\frac{q_1(z)}{\varepsilon_1(\theta_1)} - \int_{-1}^1 \frac{1 - \varepsilon_2(\theta_2)}{\varepsilon_2(\theta_2)} q_2(\eta) \frac{R_2}{R_1} K_1(z, \eta) d\eta = \theta_1^4(z) - \int_{-1}^1 \theta_2^4(\eta) \frac{R_2}{R_1} K_1(z, \eta) d\eta, \quad (11)$$

$$\begin{aligned} \frac{q_2(\eta)}{\varepsilon_2(\theta_2)} - \int_{-1}^1 \frac{\rho_1^d(\theta_1)}{\varepsilon_1(\theta_1)} q_1(z) K_1(z, \eta) dz \\ - \int_{-1}^1 \frac{1 - \varepsilon_2(\theta_2)}{\varepsilon_2(\theta_2)} q_2(\eta') K^e(\eta, \eta') d\eta' \\ = \theta_2^4(\eta) - \int_{-1}^1 (1 - \rho_1^s(\theta_1)) \theta_1^4(z) K_1(z, \eta) dz \\ - \int_{-1}^1 \theta_2^4(\eta') K^e(\eta, \eta') d\eta', \end{aligned} \quad (12)$$

where $\varepsilon_1(\theta_1)$ and $\varepsilon_2(\theta_2)$ are the emissivities of the sample and furnace radiating surfaces, respectively, and $\rho_1^d(\theta_1)$ and $\rho_1^s(\theta_1)$ are the diffuse and specular components of the sample's reflectance; the sample properties are, in general, discontinuous, as a consequence of the phase change. The dimensionless kernel functions $K_1(z, \eta)$ and $K^e(\eta, \eta')$ define the exchange factors sample–furnace and furnace–furnace, respectively, these two functions are analyzed in the next section.

The dimensionless parameters that appear in the problem are the following: the radiation parameters $Ra_1 = \sigma T_m^3 R_1 / k_s$ and $Ra_2 = \sigma T_m^3 R_1 / k_f$, the Biot parameters $Bi_1 = k_g / (k_s \ln(R_2/R_1))$, $Bi_2 = k_g / (k_f (R_2/R_1) \ln(R_2/R_1))$, where k_g is the effective thermal conductivity of the furnace gas (evaluated at $T = (T_1 + T_2)/2$), and the geometrical parameters $\Lambda = L/R_1$ (slenderness), R_2/R_1 and R_3/R_1 .

3.1. Numerical procedure

The solution of Eqs. (1)–(12) is obtained numerically by means of an iterative method (which is a generalization of the method used in Ref. [15]). At each iteration step, $\theta_1(r, z)$ is obtained from Eqs. (1)–(5) and $\theta_2(r, \eta)$ from Eqs. (6)–(10), with $k_1(\theta_1)$, $q_1(z)$ and $\theta_2(R_2/R_1, z)$, and $k_2(\theta_2)$, $q_2(\eta)$ and $\theta_1(1, \eta)$, respectively, known from the previous step. Likewise, $q_1(z)$ and $q_2(\eta)$ are obtained from

Eqs. (11)–(12), with all the functions depending on temperature known from the previous step.

The two conduction problems are solved by a finite difference method. The computational domains are discretized using uniform grids; the domain $[-1, 1] \times [0, 1]$ for θ_1 is divided into 330×40 grid intervals, and the domain $[-1, 1] \times [R_2/R_1, R_3/R_1]$ for θ_2 into 330×65 . In the discretizations a central difference scheme is used; the resulting systems of linear equations, for θ_1 and θ_2 , are solved by a block-line Gauss–Seidel iterative method. In the radiation problem, the two integral equations are discretized, dividing the one-dimensional domains into 330 intervals of equal length, and using the Simpson method. The resulting system of linear equations for q_1 and q_2 is solved by a direct LU method.

The iterative process is started using linear temperature distributions for θ_1 and θ_2 as the initial step, and is stopped when $\sum |\theta_{ij} - \tilde{\theta}_{ij}| / \sum |\theta_{ij}| < 10^{-6}$ for θ_1 and for θ_2 , where the summations are extended over all grid points in each case ($\tilde{\theta}$ represents the temperature from the previous step).

4. Radiative exchange between sample and furnace

In this section we develop a model for the radiative interaction between the sample and the furnace based on the following assumptions: (a) all the solid surfaces are considered opaque gray; (b) all the surfaces emit diffusely; (c) the furnace reflects radiation diffusely, whereas the sample reflects both diffuse and specularly; (d) the furnace gas is considered transparent; (e) the temperature dependence of properties is taken into account, and (f) the effect of both ends of the furnace cavity is neglected. A radiation enclosure composed of two finite areas, the sample and the furnace surfaces, is considered. For this geometry, it can be seen that all the radiation leaving the sample will arrive at the furnace, whereas the furnace will radiate both to the sample and to itself (directly or by specular reflection on the sample).

In general, if we consider an enclosure composed of N finite areas ($N = 2$ in our case), the *net radiation method* provides the following

dimensional integral equation, for surface k , relating the temperatures and the heat fluxes (see Ref. [16])

$$\begin{aligned} \frac{Q_k(\vec{r}_k)}{\varepsilon_k(T_k)} - \sum_{j=1}^N \int_{A_j} \frac{\rho_j^d(T_j)}{\varepsilon_j(T_j)} Q_j(\vec{r}_j) dF_{dA_k \rightarrow dA_j}^c(\vec{r}_j, \vec{r}_k) \\ = \sigma T_k^4(\vec{r}_k) - \sum_{j=1}^N \int_{A_j} (1 - \rho_j^s(T_j)) \sigma T_j^4(\vec{r}_j) \\ \times dF_{dA_k \rightarrow dA_j}^c(\vec{r}_j, \vec{r}_k). \end{aligned} \quad (13)$$

The complete formulation is formed by N such equations, one for each surface, where \vec{r}_k defines the location of surface k , T_k and Q_k are the temperature and the net *outgoing* heat flux on surface k , respectively, $\varepsilon_k(T_k)$, $\rho_k^d(T_k)$ and $\rho_k^s(T_k)$ are the emissivity, and the diffuse and specular components of the reflectance of surface k , respectively, and $dF_{dA_k \rightarrow dA_j}^c$ is the *exchange view factor* between the surface elements dA_k and dA_j , that is, the ratio between the *diffuse* radiation that leaves dA_k and reaches dA_j , either directly or by specular reflection on other surfaces, and the total *diffuse* radiation that leaves dA_k . In Eq. (13), we have taken into account the following relations:

$$\varepsilon_k(T_k) = \alpha_k(T_k) = 1 - (\rho_k^d(T_k) + \rho_k^s(T_k)) \quad (14)$$

corresponding to partially-specular opaque gray surfaces (see Ref. [16]).

In our problem let $k = 1$ represent the sample and $k = 2$ the furnace. The differential surface elements are reduced in our axisymmetric problem to ring elements defined by the differential length elements dz (sample) and $d\eta$ (furnace). Since the furnace is diffuse gray, $\rho_2^s = 0$ and then $\rho_2^d = 1 - \varepsilon_2$. Moreover, the sample does not radiate to itself, neither directly (which is geometrically obvious) nor by specular reflection on the furnace (since $\rho_1^s = 0$); that is, the exchange view factor between two sample elements is null ($dF_{dz \rightarrow dz}^c = 0$). Consequently, the equations for our sample–furnace system in dimensionless form are

$$\begin{aligned} \frac{q_1(z)}{\varepsilon_1(\theta_1)} - \int_{A_2} \frac{1 - \varepsilon_2(\theta_2)}{\varepsilon_2(\theta_2)} q_2(\eta) dF_{dz \rightarrow d\eta}^c \\ = \theta_1^4(z) - \int_{A_2} \theta_2^4(\eta) dF_{dz \rightarrow d\eta}^c \end{aligned} \quad (15)$$

$$\begin{aligned} \frac{q_2(\eta)}{\varepsilon_2(\theta_2)} - \int_{A_1} \frac{\rho_1^d(\theta_1)}{\varepsilon_1(\theta_1)} q_1(z) dF_{d\eta \rightarrow dz}^c \\ - \int_{A_2} \frac{1 - \varepsilon_2(\theta_2)}{\varepsilon_2(\theta_2)} q_2(\eta') dF_{d\eta \rightarrow d\eta'}^c \\ = \theta_2^4(\eta) - \int_{A_1} (1 - \rho_1^s(\theta_1)) \theta_1^4(z) dF_{d\eta \rightarrow dz}^c \\ - \int_{A_2} \theta_2^4(\eta') dF_{d\eta \rightarrow d\eta'}^c. \end{aligned} \quad (16)$$

In these equations $dF_{dz \rightarrow d\eta}^c$, $dF_{d\eta \rightarrow dz}^c$ and $dF_{d\eta \rightarrow d\eta'}^c$ are the exchange view factors that appear in the problem, which are analyzed in the following.

4.1. Exchange view factors

Since the furnace inner surface is a diffuse reflector, the exchange view factor $dF_{dz \rightarrow d\eta}^c$ between a differential ring on the sample and a differential ring on the furnace will just be the *diffuse* view factor $dF_{dz \rightarrow d\eta}$ (which represents the fraction of energy emitted by one ring that reaches the other); its determination is a geometrical problem, which is formulated in the appendix. This view factor can be written as (Eq. (A.4))

$$dF_{dz \rightarrow d\eta} = \frac{R_2}{R_1} K_1(z, \eta) d\eta, \quad (17)$$

where the kernel function $K_1(z, \eta)$ is given by (Eq. (A.5))

$$\begin{aligned} K_1(z, \eta) = A \int_{-c}^c \frac{\left(-1 + \frac{R_2}{R_1} \cos \psi\right) \left(\frac{R_2}{R_1} - \cos \psi\right)}{\pi \left[1 + \left(\frac{R_2}{R_1}\right)^2 - 2 \frac{R_2}{R_1} \cos \psi + A^2 (\eta - z)^2\right]^2} d\psi, \end{aligned} \quad (18)$$

where $c = \cos^{-1}(R_1/R_2)$.

Next, the exchange view factor $dF_{d\eta \rightarrow dz}^c$ coincides again with the *diffuse* view factor $dF_{d\eta \rightarrow dz}$, which can be determined from $dF_{dz \rightarrow d\eta}$ (Eq. (17)) by the reciprocity relation (see the appendix). One has (Eq. (A.6))

$$dF_{d\eta \rightarrow dz} = K_1(z, \eta) dz. \quad (19)$$

As it can be observed, K_1 depends on the difference $\eta - z$, that is, the distance between the rings. This function $K_1(\eta - z)$ is plotted in Fig. 2a for $L = 165$ mm, $R_2 = 15$ mm and different values of R_1 . From this figure one can see that the value of K_1 is appreciable only for very small values of $\eta - z$ (it is practically null for $0.2 < \eta - z \leq 2$), which means that the influence of a furnace ring is only important on that part of the sample just in front of it. Also, we see that, for a given furnace, the bigger the radius of the sample, the bigger the influence of the furnace ring defined by $\eta = z$ on the sample ring defined by z .

Finally, the exchange view factor $dF_{d\eta \rightarrow d\eta'}^e$ between two furnace rings consists of two terms:

$$dF_{d\eta \rightarrow d\eta'}^e = dF_{d\eta \rightarrow d\eta'} + dF_{d\eta \rightarrow d\eta'}^s. \quad (20)$$

The first one is the *diffuse* view factor which accounts for the diffuse radiation that leaves $d\eta$ and directly intercepts $d\eta'$. This view factor is derived in the appendix; it can be written as

(Eq. (A.9))

$$dF_{d\eta \rightarrow d\eta'} = K_2(\eta, \eta') d\eta', \quad (21)$$

where the kernel function $K_2(\eta, \eta')$ is given by (Eq. (A.10))

$$K_2(\eta, \eta') = \frac{L}{R_2} \int_{-2c}^{2c} \frac{(1 - \cos \psi)^2}{\pi \left[2(1 - \cos \psi) + \left(\frac{L}{R_2} \right)^2 (\eta' - \eta)^2 \right]^2} d\psi. \quad (22)$$

Again, this is a function of $\eta' - \eta$, that is, the distance between the two furnace rings. This function $K_2(\eta' - \eta)$ is plotted in Fig. 2b for $L = 165$ mm, $R_2 = 15$ mm and different values of R_1 (that appears in c). We also include, for comparison, the theoretical result corresponding to $R_1 = 0$ (see Ref. [16]). As in the case of K_1 , the influence of a furnace ring is only important on that part of the furnace nearby (for $0.4 < \eta' - \eta \leq 2$ K_2 is practically null). Also, obviously, the bigger the radius of the sample (which intercepts the furnace radiation), the smaller the influence.

The second part of the exchange view factor, $dF_{d\eta \rightarrow d\eta'}^s$, accounts for the radiation that leaves $d\eta$ and intercepts $d\eta'$ by *specular reflection* on the sample. This term will be non-zero only if the sample element located at $\xi = (\eta + \eta')/2$ reflects specularly (see Fig. 3); in fact, it is given by the *diffuse* view factor between the furnace ring and the sample ring where the radiation is reflected,

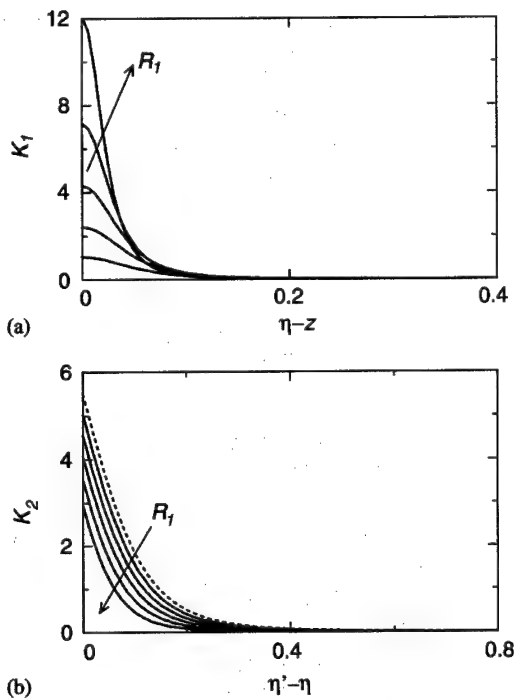


Fig. 2. View-factor kernels: (a) $K_1(z, \eta)$ and (b) $K_2(\eta, \eta')$. $R_1 = 2, 4, 6, 8$ and 10 mm. Dotted line: $R_1 = 0$. $R_2 = 15$ mm, $L = 165$ mm.

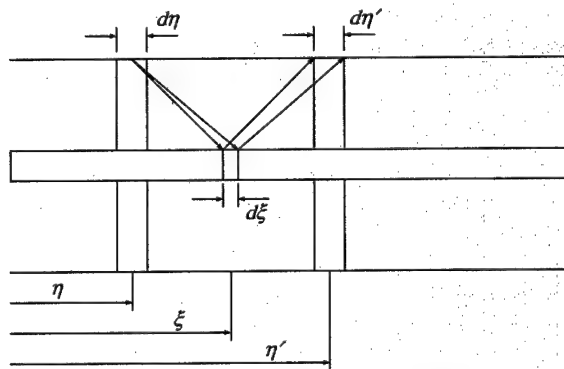


Fig. 3. Specular reflection on the sample.

multiplied by the corresponding specular reflectance, that is

$$dF_{d\eta \rightarrow d\eta'}^s = \rho_1^s(\xi) dF_{d\eta \rightarrow d\xi} = \rho_1^s(\xi) K_1(\xi, \eta) d\xi$$

(after using Eq. (19)) and, since $d\xi = \frac{1}{2}d\eta'$, one has

$$dF_{d\eta \rightarrow d\eta'}^s = \frac{1}{2}\rho_1^s\left(\frac{\eta + \eta'}{2}\right) K_1\left(\frac{\eta + \eta'}{2}, \eta\right) d\eta'. \quad (23)$$

In conclusion we can write

$$dF_{d\eta \rightarrow d\eta'}^c = K^c(\eta, \eta') d\eta', \quad (24)$$

where the kernel function K^c is given by (after using Eqs. (21) and (23))

$$K^c(\eta, \eta') = K_2(\eta, \eta') + \frac{1}{2}\rho_1^s\left(\frac{\eta + \eta'}{2}\right) K_1\left(\frac{\eta + \eta'}{2}, \eta\right). \quad (25)$$

In Fig. 4 we represent this kernel K^c for two different emitting points, defined by $\eta = 0$ and -0.6 (depicted in the figure by the two circular dots). We have considered a specular-diffuse silicon sample, with $R_1 = 8$ mm, part of which is liquid, namely, a zone 20 mm long in the middle of the sample; its specular reflectance is defined by $\rho_1^s = 0.2$ for the solid (50% of the solid reflectance) and 0.63 for the liquid (90% of the liquid reflectance). This is the kind of sample considered in Section 6 in the analysis of our model. Also, for comparison, we have plotted the kernel K_2 (dotted

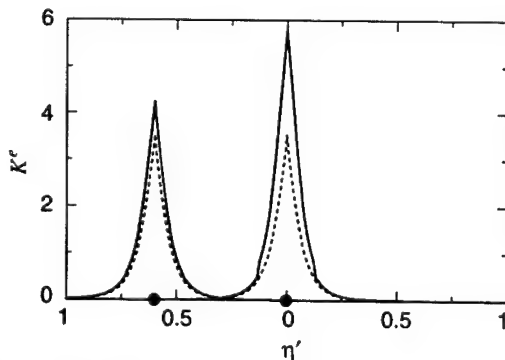


Fig. 4. Exchange-factor kernel $K^c(\eta, \eta')$, for two emitting points at $\eta = 0$ and -0.6 , for a specular-diffuse sample ($\rho_{1,s}^s/\rho_{1,s} = 0.5$, $\rho_{1,l}^s/\rho_{1,l} = 0.9$). Melt zone length: 20 mm. Circular dots: location of emitting points. Dotted lines: view-factor kernel $K_2(\eta, \eta')$ (for a diffuse sample). $R_1 = 8$ mm, $R_2 = 15$ mm, $L = 165$ mm.

lines in Fig. 4), for the same two emitting points, which corresponds to the case of diffuse samples (that is, $\rho_1^s = 0$). The differences are clear, and their effect on the results is analyzed below in Section 6.

Once the view factors have been derived, the radiation equations (15)–(16), with Eqs. (17), (19) and (24) lead to Eqs. (11) and (12) of the general formulation, with K_1 and K^c given by Eqs. (18), (22) and (25).

5. Model validation

The model we have just formulated is validated now by comparing with experimental data. We simulate the experiments performed in Ref. [5] for a quartz sample of radius $R_1 = 2$ mm; in fact, we consider eight different runs, the four reported in Ref. [5], plus another four provided by the same authors. The powers supplied to the heaters and the temperatures of the bases of the sample (taken from the experiments) are listed in Table 1. As in Ref. [5], some losses in the power inputs are considered: we take 10% of losses for the three heaters (they take 20% for the central heater and 10% for the other two).

The physical properties of the different materials are as follows (Ref. [5]):

- Quartz: Thermal conductivity ($\text{W m}^{-1} \text{K}^{-1}$),
 $\hat{k}_1(T_1) = 1.55 + 1.51 \times 10^{-3} (T_1 - 473)$
 emissivity, $\varepsilon_1(T_1) = 0.76$, reflectance, $\rho_1^d(T_1) + \rho_1^s(T_1) = 0.24$ (it can be shown that the effect of

Table 1

Data defining the experimental runs in the case of a quartz sample.

Run	W_1 (W)	W_2 (W)	W_3 (W)	T_{b1} (K)	T_{b2} (K)	W_T (W)	kfact
#1	53	136	47	400	451	236	4.8
#2	73	116	81	393	509	270	4.8
#3	126	90	120	423	556	336	4.5
#4	125	83	150	421	582	358	4.5
#5	150	147	141	446	605	438	4.3
#6	152	197	168	494	689	517	4.0
#7	182	198	139	481	656	519	4.0
#8	184	193	169	478	684	546	4.0

the specular reflectance in the overall temperature distribution is very small, thus for concreteness we take $\rho_1^d = 0.24$ and $\rho_1^s = 0$.

- Air: Thermal conductivity ($\text{W m}^{-1} \text{K}^{-1}$),

$$k_a(T) = 0.0456 + 0.054 \times 10^{-3} (T - 600).$$

- Corundum: Thermal conductivity ($\text{W m}^{-1} \text{K}^{-1}$),

$$\hat{k}_2(T_2) = 4.4 - 10^{-3} (T_2 - 523) \\ \times [3.2 - 1.6 \times 10^{-3} (T_2 - 1023)]$$

emissivity, $\varepsilon_2(T_2) = 0.8$ (diffuse surface).

- Insulation (keratherm): Thermal conductivity ($\text{W m}^{-1} \text{K}^{-1}$),

$$\hat{k}_{\text{ins}}(T_2) = \text{kfact} \{ 0.09 + 10^{-3} (T_2 - 473) \\ \times [0.15 + 0.094 \times 10^{-3} (T_2 - 873)] \}.$$

As it was already shown by Crochet et al. [7] for a vertical Bridgman furnace, the thermal conductivity of the insulation materials, \hat{k}_{ins} , has a strong influence on the electric power required to attain the melting temperature in the sample. The existing inhomogeneities in the insulation material, both those typical of the material and those due to the necessary wiring for the heaters and the temperature sensors, make the analytical characterization of the insulation material a difficult task. For this reason, for each particular furnace it is necessary to determine this property experimentally. In our case we have included the multiplicative factor kfact, which must be adjusted for each run so that the experimental data are fit. For reference, in Ref. [7] they increase the thermal conductivity of their insulation material from 0.13 to 0.72, that is a factor of 5.5, and in Ref. [5] they consider an overall factor ranging from 1.6 to 1.9.

The eight runs considered can be grouped in four sets according to the total power W_T supplied to the heaters: Runs #1 and 2, 3 and 4, 5, and 6, 7 and 8 (see Table 1). The values of kfact that best fit the experimental results are also listed in Table 1. We can see that the same kfact is obtained for the runs in each set, that is, kfact depends on the total power and not on the power distribution among the heaters. This dependence turns out to be linear,

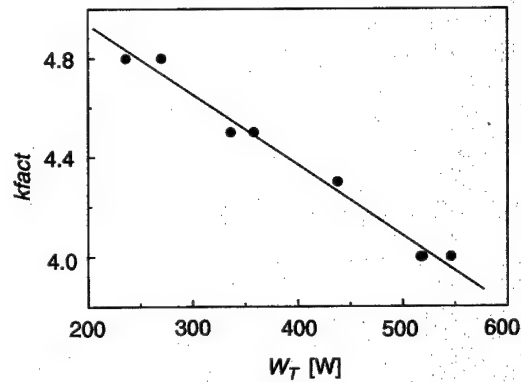


Fig. 5. kfact vs. W_T for the three-heater furnace. Solid circles: values adjusted for the experimental runs with a quartz sample (see Table 1). Solid line: least-squares fit.

as shown in Fig. 5. The least-squares fit is

$$\text{kfact} = 5.503 - 2.834 \times 10^{-3} W_T \quad (26)$$

with the total power W_T measured in watts.

The results are shown in Fig. 6 (for the reference properties we have taken $k_f = 1.2 \text{ W m}^{-1} \text{K}^{-1}$, $k_s = 2.5 \text{ W m}^{-1} \text{K}^{-1}$ and $T_m = 1000 \text{ K}$). We can see that the overall qualitative agreement is very good, which allows us to validate our model.

The quantitative differences can be explained as follows. First, the two plugs fixing the quartz sample are not included in our model (since they are not used in a general configuration); thus, differences at the ends of the sample are to be expected. Second, as the effect of the annular ends of the furnace cavity on the radiation problem has been neglected, this simplification also contributes to the differences observed at the ends of the sample. Third, the boundary conditions in our furnace model are symmetrical (at top and bottom), whereas in the experimental runs are not; this can explain why the asymmetry in our results is smaller. Finally, we have not pursued a better quantitative agreement by introducing some effects considered by Boschert et al. [5], namely, additional heating close to the outer part of the inner insulation, accounting for the heat generated in the internal cables; enhanced heat transport in the furnace gas parallel to the furnace axis; and double heat losses for the central heater.

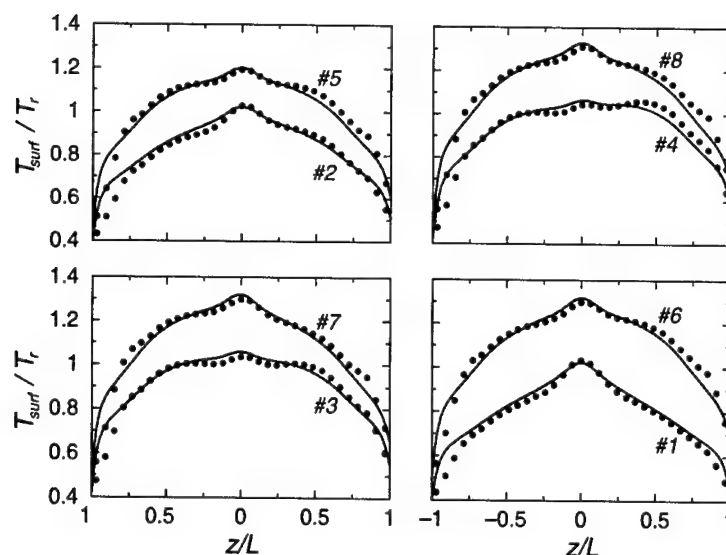


Fig. 6. Surface temperature distributions for a quartz sample. See Table 1 for the description of the 8 runs. Solid circles: experimental data. Reference temperature, $T_r = 1000$ K. $R_1 = 2$ mm, $R_2 = 15$ mm, $L = 165$ mm.

Expression (26) for k_{fact} defines the behavior of the insulation for this particular furnace. It is used below when we obtain results for silicon samples.

6. Results

In this section we analyze our model. We consider now a silicon sample of radius $R_1 = 8$ mm. The temperatures of the sample bases are taken as $T_{b1} = T_{b2} = 1000$ K (for simplicity, the same values for all the runs considered). The physical properties of solid and liquid silicon (supposed constant for each phase) are [13,17]: thermal conductivities, $\hat{k}_{1,s} = 22 \text{ W m}^{-1} \text{ K}^{-1}$, $\hat{k}_{1,l} = 64 \text{ W m}^{-1} \text{ K}^{-1}$; emissivities, $\varepsilon_{1,s} = 0.6$, $\varepsilon_{1,l} = 0.3$; reflectances, $\rho_{1,s}^d = 0.2$, $\rho_{1,s}^s = 0.2$, $\rho_{1,l}^d = 0.07$, $\rho_{1,l}^s = 0.63$, that is, a specular-diffuse sample defined by a specular component of 50% for the solid, and of 90% for the liquid silicon. (For the reference properties we take $k_r = 1.2 \text{ W m}^{-1} \text{ K}^{-1}$, $k_s = 22 \text{ W m}^{-1} \text{ K}^{-1}$ and $T_m = 1683$ K.)

As indicated in the Introduction, the main objective of this work is to study the influence of the specular reflections on the temperature field in the sample. Another important parameter, as already mentioned, is the thermal conductivity of

the insulation material, on which the sample's temperature depends strongly. These two factors are analyzed below. Lastly in this section, we will use the model to make predictions about the operation of the furnace in microgravity conditions.

In what follows we only seek symmetric temperature distributions, hence we always take the same power for the lateral heaters ($W_1 = W_3$).

6.1. Thermal conductivity of the insulation material

As indicated in the previous section, the thermal conductivity of the insulation is affected by a factor k_{fact} , which for the present furnace has been estimated as a function of the total power with the help of experimental results. We are going to show that the temperature field in the sample depends strongly on this factor and, hence, it becomes quite important to estimate it accurately.

In Fig. 7 we represent the variation with k_{fact} of the maximum temperature difference in the melt ($T_{\text{max}} - T_m$), the melt length at the free surface (L_{melt}), and the Marangoni number, defined as

$$Ma = \frac{\sigma_T(T_{\text{max}} - T_m)L_{\text{melt}}/2}{\rho\nu\chi}, \quad (27)$$

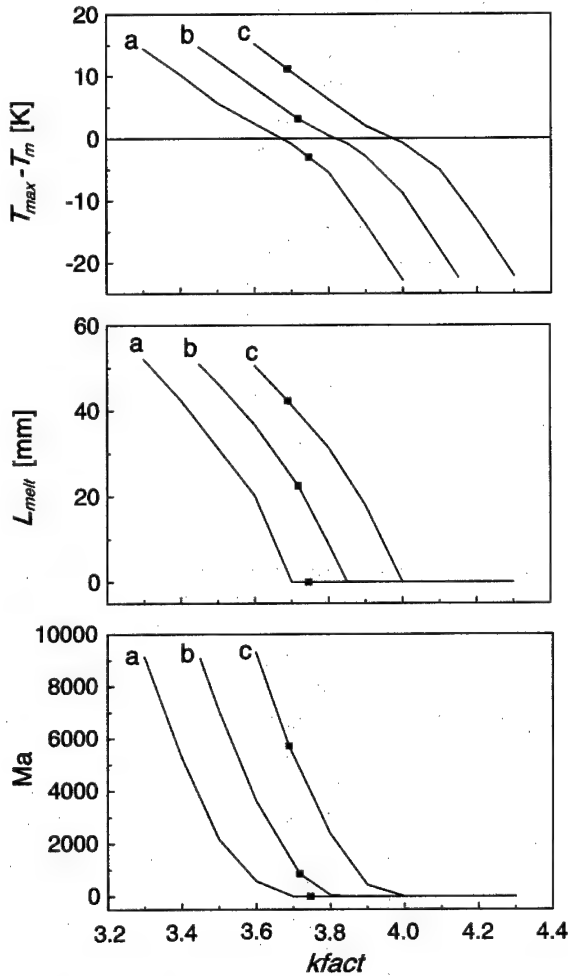


Fig. 7. Maximum temperature difference in the melt, melt length at the free surface and Marangoni number, for silicon samples, vs. k_{fact} . $W_1 = W_3 = 190$ W: (a) $W_2 = 240$ W, (b) $W_2 = 250$ W and (c) $W_2 = 260$ W. Square dots: nominal values of k_{fact} . $R_1 = 8$ mm, $R_2 = 15$ mm, $L = 165$ mm.

where $\rho = 2.5 \times 10^3 \text{ kg m}^{-3}$ is the density of the liquid Si, $\nu = 0.35 \times 10^{-6} \text{ m}^2 \text{ s}^{-1}$ the dynamic viscosity, $\chi = 0.13 \times 10^{-4} \text{ m}^2 \text{ s}^{-1}$ the thermal diffusivity and $\sigma_T = 0.28 \times 10^{-3} \text{ N m}^{-1} \text{ K}^{-1}$ the negative of the coefficient of variation of surface tension with temperature [18]. We consider three different values of total power: $W_T = 620, 630$ and 640 W, distributed among the three heaters as follows: $W_1 = W_3 = 190$ W (lateral heaters) and $W_2 = 240, 250$ and 260 W (central heater). The square dots in these graphs represent the nominal

values of k_{fact} according to Eq. (26) for each value of W_T .

We can see that, for a given power, small variations in k_{fact} lead to very large changes in the results, especially in L_{melt} , and as a consequence in Ma . For instance, for $W_T = 640$ W, $k_{\text{fact, nominal}} \approx 3.7$ and the results are $T_{\text{max}} - T_{\text{m}} \approx 11$ K, $L_{\text{melt}} \approx 42$ mm and $Ma \approx 5720$. However, if we take $k_{\text{fact}} = 3.6$ or 3.8 , the results become 15 K, 50 mm and 9310 , or 6 K, 31 mm and 2380 , respectively. This represents variations in Ma of $+63\%$ or -58% , respectively.

6.2. Influence of the specular reflections

In order to quantify this effect, results obtained with the specular-diffuse silicon sample are compared with results obtained when only diffuse surfaces are involved. The integral Eqs. (11) and (12) are still valid when only diffuse reflections are considered, just taking $\rho_1^s = 0$, $\rho_1^d = 1 - \epsilon_1$ and $K^e(\eta, \eta') = K_2(\eta, \eta')$. The coefficients and the exchange view factors appearing in the first equation are the same in the two problems, whereas, in the second equation, they change significantly due to the values of the sample's specular reflectance.

In Fig. 8 we represent $T_{\text{max}} - T_{\text{m}}$, L_{melt} and Ma as functions of the total power for both cases, specular-diffuse and diffuse. The total power is distributed among the heaters as follows: $W_1 = W_3$ and $W_2 = 1.5W_1$ (the influence of the power distribution is analyzed in the next subsection). We can see that, for a given power, when specular reflections on the sample are not taken into account, the model predicts larger values of $T_{\text{max}} - T_{\text{m}}$, L_{melt} and as consequence of Ma . For example, for $W_T = 620$ W the results obtained in the specular-diffuse case are $T_{\text{max}} - T_{\text{m}} \approx 4$ K, $L_{\text{melt}} \approx 23$ mm and $Ma \approx 1000$, whereas for a diffuse sample they increase to $T_{\text{max}} - T_{\text{m}} \approx 8$ K, $L_{\text{melt}} \approx 34$ mm and $Ma \approx 3490$. We can see that the Marangoni number predicted without specular reflections is roughly three and a half times higher, and L_{melt} 48% higher.

We must conclude that, with respect to the melt, the effect of the specular reflections predicted by the model is quite important; if one is to obtain accurate results, specular reflections must be taken

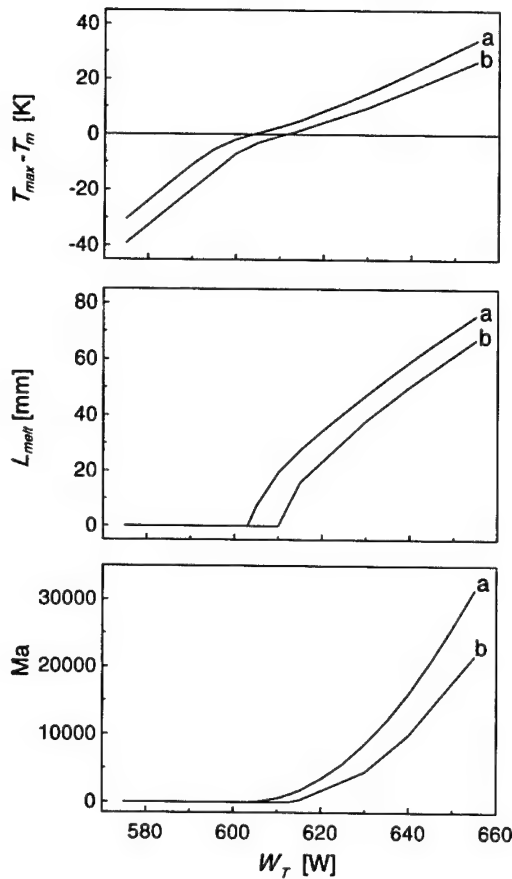


Fig. 8. Maximum temperature difference in the melt, melt length at the free surface and Marangoni number, for silicon samples, vs. W_T . $W_1 = W_3$, $W_2 = 1.5W_1$: (a) Diffuse sample and (b) specular-diffuse sample ($\rho_{1,s}^s/\rho_{1,s} = 0.5$, $\rho_{1,l}^s/\rho_{1,l} = 0.9$). $R_1 = 8$ mm, $R_2 = 15$ mm, $L = 165$ mm.

into account. Notice, however, that if one considers the overall temperature distribution (where a representative temperature difference can be up to the order of 1000 K), the relative effect of the specular reflections is much smaller.

In the previous analysis we have considered that the specular component of the reflectance of solid silicon is 50%. This figure is meant to be a representative value. In order to see the effect of this parameter on the results, in Fig. 9 we present the variation of $T_{max} - T_m$, L_{melt} and Ma with $\rho_{1,s}^s/\rho_{1,s}$ (ratio of specular reflectance to total reflectance for the solid sample); we have considered $W_T = 620$ W and $\rho_{1,l}^s/\rho_{1,l} = 0.9$ (that is,

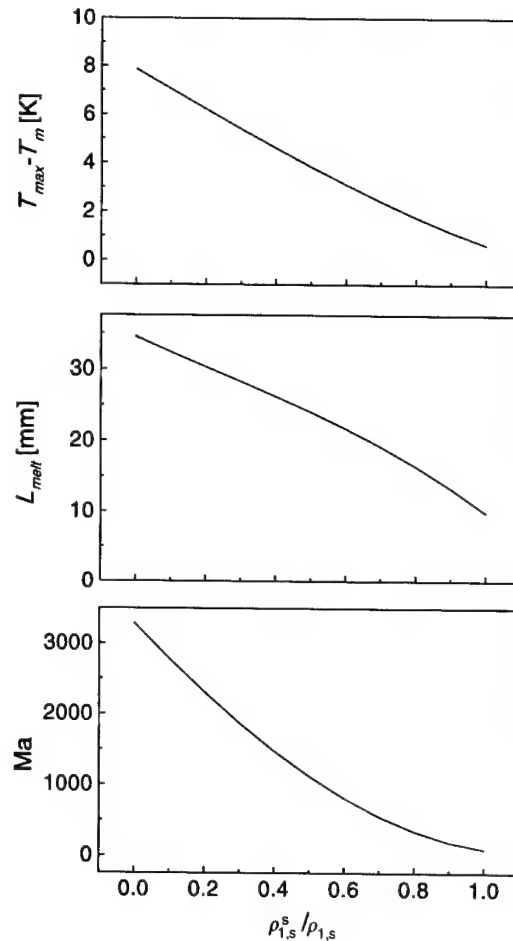


Fig. 9. Maximum temperature difference in the melt, melt length at the free surface and Marangoni number, for silicon samples, vs. $\rho_{1,s}^s/\rho_{1,s}$. $W_T = 620$ W; $W_1 = W_3$, $W_2 = 1.5W_1$. $\rho_{1,l}^s/\rho_{1,l} = 0.9$. $R_1 = 8$ mm, $R_2 = 15$ mm, $L = 165$ mm.

90% specular reflectance for liquid silicon). We can see that the effect is quite large: L_{melt} goes from 34 mm for $\rho_{1,s}^s/\rho_{1,s} = 0$ (diffuse solid sample) to 9 mm for $\rho_{1,s}^s/\rho_{1,s} = 1$ (specular solid sample); likewise, $T_{max} - T_m$ and Ma go from 8 K and 3240, respectively, to almost 0. We conclude that also this physical property must be determined precisely in order to predict accurate results. On the other hand, it can be shown that the effect of the specular component of the reflectance of liquid silicon is very small in cases of interest where $L_{melt} \ll L$.

6.3. Furnace operation

We are going to analyze first the influence of the distribution of power among the three heaters (for a given total power). We consider three cases: even distribution, $W_1 = W_2 = W_3$; central heater with 50% more power than the other two, $W_1 = W_3$, $W_2 = 1.5W_1$; and double power for the central heater, $W_1 = W_3$, $W_2 = 2W_1$. In the following we consider again $\rho_{1,s}^s/\rho_{1,s} = 0.5$ and $\rho_{1,l}^s/\rho_{1,l} = 0.9$.

In Fig. 10 we represent $T_{\max} - T_m$, L_{melt} and Ma as functions of the total power, for the three distributions. We can see that uneven distributions are more efficient, in the sense that they require

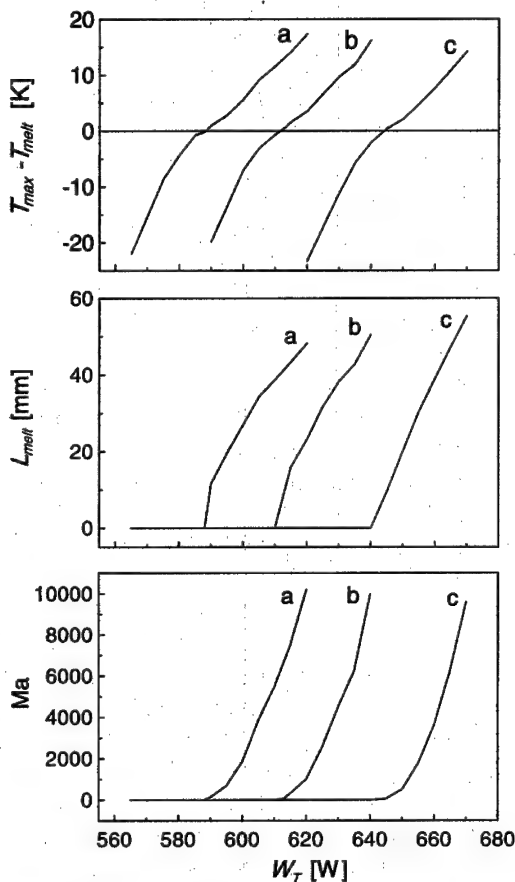


Fig. 10. Maximum temperature difference in the melt, melt length at the free surface and Marangoni number, for silicon samples, vs. W_T , for different power distributions. $W_1 = W_3$: (a) $W_2 = 2W_1$, (b) $W_2 = 1.5W_1$ and (c) $W_2 = W_1$. $\rho_{1,s}^s/\rho_{1,s} = 0.5$, $\rho_{1,l}^s/\rho_{1,l} = 0.9$. $R_1 = 8$ mm, $R_2 = 15$ mm, $L = 165$ mm.

less power for a given length of melt. For example, to obtain $L_{\text{melt}} = 20$ mm, the total power increases from 595 to 650 W (an increase of 9%).

We notice also the steep variation of L_{melt} with W_T . For example, if we consider the distribution $W_1 = W_3$, $W_2 = 1.5W_1$, an increase in power of only 5 W, from 620 to 625 W (less than 1%), leads to an increase of L_{melt} from 23 to 32 mm (an increase of 39%), and an increase of Ma from 1000 to 2570 (roughly, two and a half times higher).

In Fig. 11 we represent $T_{\max} - T_m$, Ma and the temperature gradients at the solid–liquid interface,

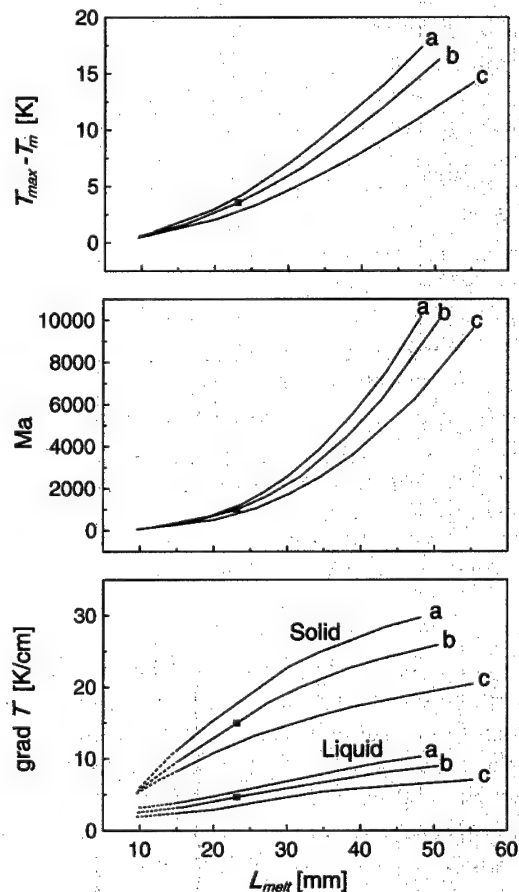


Fig. 11. Maximum temperature difference in the melt, Marangoni number and temperature gradients at the solid–liquid interface, for silicon samples, vs. L_{melt} . $W_1 = W_3$: (a) $W_2 = 2W_1$, (b) $W_2 = 1.5W_1$ and (c) $W_2 = W_1$. Square dots correspond to $W_T = 620$ W and $W_2 = 1.5W_1$. $\rho_{1,s}^s/\rho_{1,s} = 0.5$, $\rho_{1,l}^s/\rho_{1,l} = 0.9$. $R_1 = 8$ mm, $R_2 = 15$ mm, $L = 165$ mm. Dotted lines: extrapolated values.

as functions of L_{melt} , for the three power distributions. For instance, for the case $W_T = 620$ W and $W_2 = 1.5W_1$ (represented in Fig. 11 by square dots), the results are $L_{\text{melt}} \approx 23$ mm, $T_{\text{max}} - T_m \approx 4$ K, $Ma \approx 1000$, $(\nabla T)_{\text{solid}} \approx 15$ K cm⁻¹ and $(\nabla T)_{\text{liquid}} \approx 5$ K cm⁻¹. We can compare these results with those corresponding to mirror furnaces: for a similar value of L_{melt} one expects $Ma \sim 4000$ and $(\nabla T)_{\text{liquid}} \sim 35$ K cm⁻¹ [18]; that is, the model predicts considerably smaller values of these parameters in resistance furnaces. The influence of the power distribution is clear: the more concentrated in the central heater, the larger those parameters. (For small values of L_{melt} the measurement of the temperature gradients is quite inaccurate, hence, the values shown in the figure by dotted lines have been extrapolated.)

We can see that the model also predicts very small values of the temperature difference $T_{\text{max}} - T_m$, which correspond to very flat surface temperature distributions in the Si melt. Examples of such distributions are represented in Fig. 12, for $W_2 = 1.5W_1$, corresponding to $W_T = 620$ and 640 W; we have also plotted the case $W_T = 590$ W where the sample does not melt. The corresponding temperature distributions along the furnace surface are also represented in Fig. 12 (dotted lines). We can see that, in each case, the temperature profiles for the sample and

the furnace are very close, except in the zone that corresponds to the central heater. This difference is due to the very high value of the heat flux generated (per unit volume) in this central heater, caused by the larger power supplied and its smaller size (as compared to the other two heaters).

7. Conclusions

A global model of the heating process in multizone resistance furnaces, as applied to floating-zone crystal growth, has been formulated, where the temperature fields in the sample, the furnace and the insulation are coupled; the input data is the electric power supplied to the heaters. The conduction problem includes the phase change of the sample and the heat generation by the heaters. The radiation problem takes into account specular reflections on the sample. For samples like silicon, the reflection is both specular and diffuse in the solid, and mostly specular in the melt. Since the location and extent of the melt are part of the solution, the exchange view factors, necessary to model the radiative interaction, are not known a priori, contrary to cases where only diffuse surfaces are considered.

The model has been validated comparing with experimental results obtained with a furnace composed of three heaters; the comparison of our theoretical results with the experimental data has been very good. We have shown that the temperature field in the sample depends strongly on the thermal conductivity of the insulation, which happens to be very difficult to characterize analytically, due to all the inhomogeneities associated to the heaters and sensors necessary to operate the furnace. This characterization seems to be a primary task; we have made it with the help of experimental data for the particular furnace under consideration. We have introduced a factor multiplying the thermal conductivity of the insulation material, which has been adjusted experimentally; the results show a linear dependence of this factor with the total power supplied to the heaters, irrespective of how this power is distributed among the heaters. This kind of characterization, namely, depending on an external parameter,

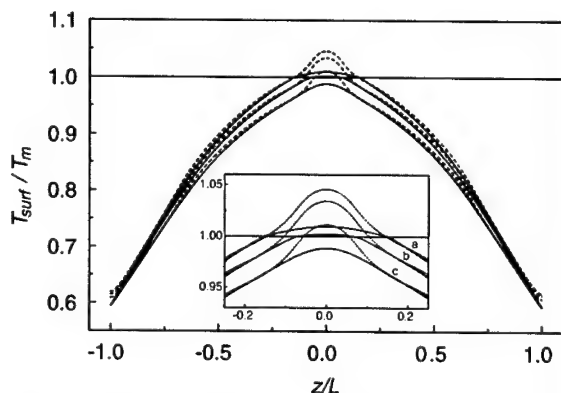


Fig. 12. Surface temperature distributions. $W_1 = W_3$, $W_2 = 1.5W_1$: (a) $W_T = 640$ W, (b) $W_T = 620$ W and (c) $W_T = 590$ W. Solid lines: silicon sample distribution. Dotted lines: furnace distribution. $\rho_{1,s}^s/\rho_{1,s} = 0.5$, $\rho_{1,l}^s/\rho_{1,l} = 0.9$. $R_1 = 8$ mm, $R_2 = 15$ mm, $L = 165$ mm.

facilitates its application to any other simulation, but for that particular furnace. To apply the model to other furnaces, similar experimental characterizations must be made, if one is to perform accurate simulations; in conclusion, the model must be adjusted to each particular furnace.

We have applied the model, adjusted for the three-heater furnace, to the case of specular-diffuse silicon samples, and simulated the heating process in the floating-zone method; important parameters like the maximum temperature difference in the melt and the melt length at the free surface, which in turn define the Marangoni number, that drives the thermocapillary flow in the melt, have been estimated. The results show that neglecting the specular reflections leads to an overestimation of those parameters: differences of the order of 100% are obtained in the temperature difference and in the melt length, giving values of the Marangoni number up to 4 times higher. It has been also shown that the effect of the percentage of specular reflectance of the solid sample is as important, so that this parameter must be determined accurately as well. We conclude that the effect of the specular reflections on the melt parameters is quite important and must be taken into account.

We have shown that the dependence of the melt length on power is very steep: changes in power or the order of 1% induce changes in this parameter of the order of 50%, giving values of the Marangoni number up to 3 times higher. This result predicted by the model seems to indicate that the controllability of the process should be difficult; for instance, to obtain a melt zone of a given length should be difficult, which may require active control of the process. Another important parameter, the temperature gradient at the solid-liquid interface, has been shown to be quite small (and smaller than in the case of operating in mirror furnaces). If larger values were required, one way to increase the gradient would be, according to our model, to increase the concentration of the supplied power in the central heater. In the ZMF and FMF furnaces this is accomplished by increasing the power supplied to the central heater and by actively extracting power by cooling zones which are adjacent to the central zone.

A problem of great interest is the study of the thermocapillary flow in the melt, since it is the cause of defects in the grown crystal [19]. To carry out that study the heating process must be formulated properly, which in our case leads to taking specular reflections on the sample into account. We propose to couple our radiation model with the convection problem in the melt to analyze the thermocapillary flows in μg conditions, in the case of crystal growth in resistance furnaces using the floating-zone method. We leave this coupling for future work. Likewise, we also leave for future work some improvements to our model; for example, the analysis of the effect of the ampoule that in practice may hold the sample.

Acknowledgements

This work has been supported by the Spanish Comisión Interministerial de Ciencia y Tecnología (CICYT) under Grant PB-98-0726. The authors are grateful to Dr. P. Dold for fruitful discussions and for providing the experimental data.

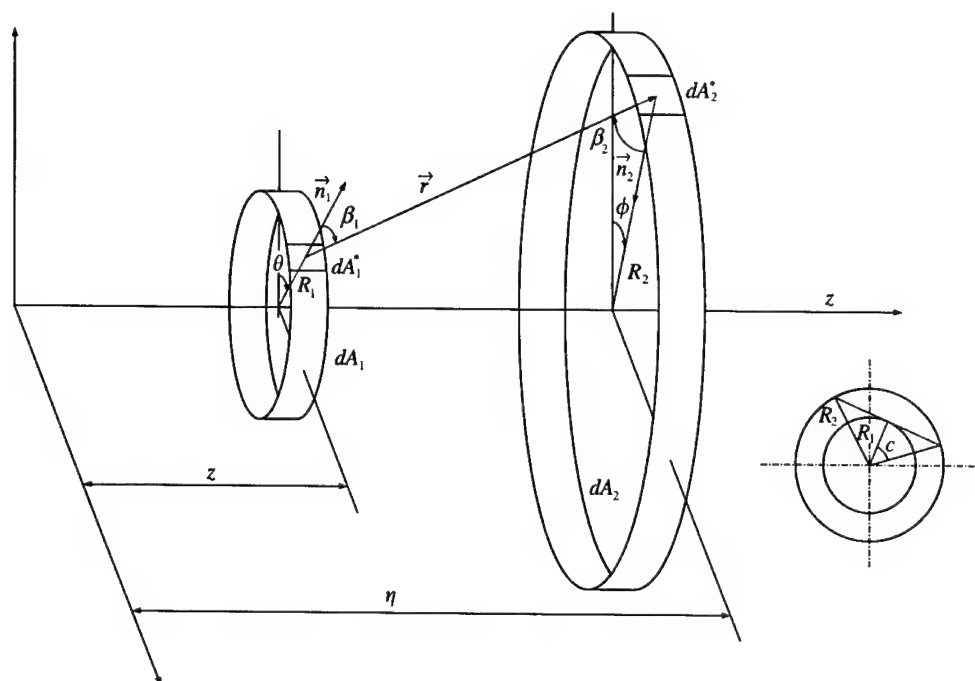
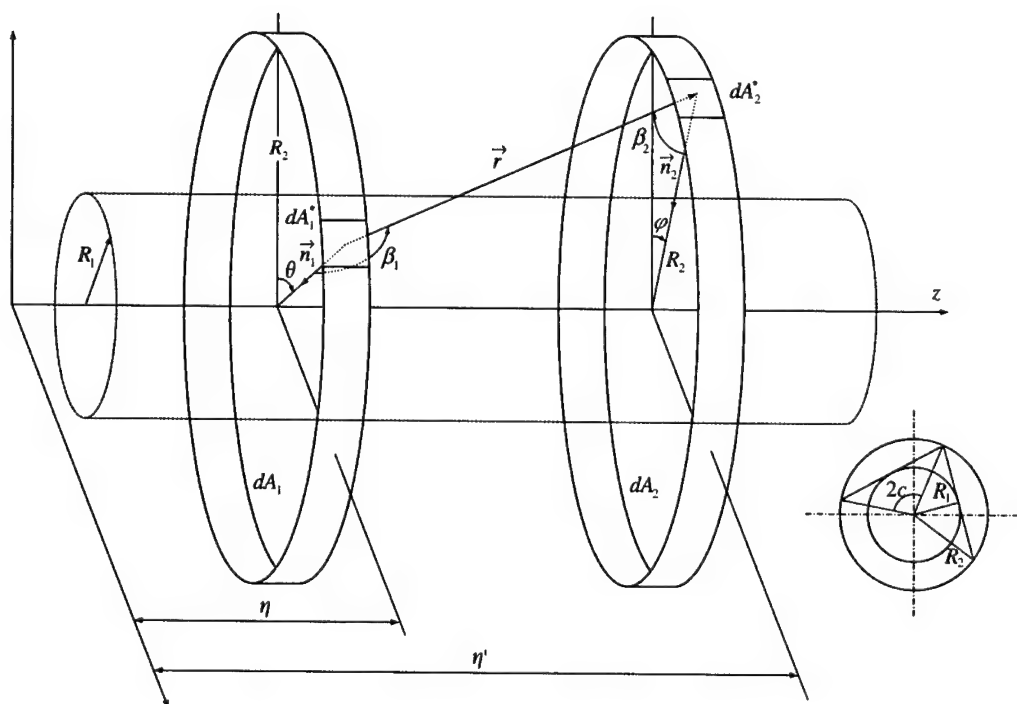
Appendix

The three diffuse view factors needed in Eqs. (15)–(16) are calculated here. The diffuse view factor between two infinitesimal surfaces dA_1^* and dA_2^* is defined as (see Ref. [20])

$$dF_{dA_1^* \rightarrow dA_2^*} = \frac{\cos \beta_1 \cos \beta_2}{\pi |\vec{r}|^2} dA_2^*, \quad (\text{A.1})$$

where \vec{r} is the position vector between both elemental surfaces, $\cos \beta_1 = \vec{n}_1 \cdot \vec{r}/|\vec{r}|$ and $\cos \beta_2 = -\vec{n}_2 \cdot \vec{r}/|\vec{r}|$, \vec{n}_1 and \vec{n}_2 being the normal unit vectors to both surfaces (see Figs. 13 and 14).

(A) *View factor between a differential ring on the sample and a differential ring on the furnace:* $dF_{dz \rightarrow d\eta}$. Consider the surface elements dA_1^* and dA_2^* , on the sample and on the furnace, respectively, shown in Fig. 13. The position vectors in the coordinate system shown in the figure are $\vec{r}_1 = (R_1 \cos \theta, R_1 \sin \theta, \hat{z})$ and $\vec{r}_2 = (R_2 \cos \phi, R_2 \sin \phi, \hat{\eta})$, hence, $\vec{r} = \vec{r}_2 - \vec{r}_1 = (R_2 \cos \phi - R_1 \cos \theta, R_2 \sin \phi - R_1 \sin \theta, \hat{\eta} - \hat{z})$, and the normal

Fig. 13. View-factor geometry. Case sample-furnace: $dF_{dz \rightarrow d\eta}$.Fig. 14. View-factor geometry. Case furnace-furnace: $dF_{d\eta \rightarrow d\eta'}$.

unit vectors are $\vec{n}_1 = (\cos \theta, \sin \theta, 0)$ and $\vec{n}_2 = (-\cos \phi, -\sin \phi, 0)$.

Consider now the sample and furnace ring elements, dA_1 and dA_2 , on which the surface elements dA_1^* and dA_2^* lay. The view factor between the infinitesimal surface element dA_1^* and the infinitesimal ring element dA_2 is

$$dF_{dA_1^* \rightarrow dA_2} = \int_{dA_2} dF_{dA_1^* \rightarrow dA_2^*} = R_2 \int_{-c}^c \frac{(-R_1 + R_2 \cos \psi)(R_2 - R_1 \cos \psi)}{\pi [R_1^2 + R_2^2 - 2R_1 R_2 \cos \psi + (\hat{\eta} - \hat{z})^2]^2} d\psi d\hat{\eta} \quad (\text{A.2})$$

after using Eq. (A.1) and the differential surface area $dA_2^* = R_2 d\phi d\hat{\eta}$, where $\psi = \phi - \theta$ and $c = \cos^{-1}(R_1/R_2)$. Since the problem is axisymmetric, the view factor is the same for all the elements of the sample ring, that is,

$$dF_{dA_1 \rightarrow dA_2} = dF_{dA_1^* \rightarrow dA_2}. \quad (\text{A.3})$$

If we consider the dimensionless variables $z = \hat{z}/L$ and $\eta = \hat{\eta}/L$, and change the nomenclature, we can write

$$dF_{dz \rightarrow d\eta} = \frac{R_2}{R_1} K_1(z, \eta) d\eta, \quad (\text{A.4})$$

where the dimensionless kernel function $K_1(z, \eta)$ is given by

$$K_1(z, \eta) = \frac{1}{\pi} \int_{-c}^c \frac{\left(-1 + \frac{R_2}{R_1} \cos \psi\right) \left(\frac{R_2}{R_1} - \cos \psi\right)}{\left[1 + \left(\frac{R_2}{R_1}\right)^2 - 2\frac{R_2}{R_1} \cos \psi + \Lambda^2 (\eta - z)^2\right]^2} d\psi. \quad (\text{A.5})$$

(B) View factor between a differential ring on the furnace and a differential ring on the sample: $dF_{d\eta \rightarrow dz}$. Using the reciprocity relation $dA_1 dF_{dA_1 \rightarrow dA_2} = dA_2 dF_{dA_2 \rightarrow dA_1}$ we obtain $R_1 dz dF_{dz \rightarrow d\eta} = R_2 d\eta dF_{d\eta \rightarrow dz}$, which after using Eq. (A.4) gives

$$dF_{d\eta \rightarrow dz} = K_1(z, \eta) dz. \quad (\text{A.6})$$

(C) View factor between two differential rings on the furnace: $dF_{d\eta \rightarrow d\eta'}$. Consider in this case the surface elements dA_1^* and dA_2^* , both on the furnace

surface, shown in Fig. 14. The position vectors are now $\vec{r}_1 = (R_2 \cos \theta, R_2 \sin \theta, \hat{\eta})$ and $\vec{r}_2 = (R_2 \cos \phi, R_2 \sin \phi, \hat{\eta}')$, hence, $\vec{r} = \vec{r}_2 - \vec{r}_1 = R_2(\cos \phi - \cos \theta, \sin \phi - \sin \theta, (\hat{\eta}' - \hat{\eta})/R_2)$ and the normal unit vectors are $\vec{n}_1 = (-\cos \theta, -\sin \theta, 0)$ and $\vec{n}_2 = (-\cos \phi, -\sin \phi, 0)$.

Consider now the two furnace ring elements dA_1 and dA_2 , on which dA_1^* and dA_2^* are located. The view factor between the infinitesimal furnace element dA_1^* and the infinitesimal furnace ring dA_2 is

$$dF_{dA_1^* \rightarrow dA_2} = \int_{dA_2} dF_{dA_1^* \rightarrow dA_2^*} = \int_{-2c}^{2c} \frac{(1 - \cos \psi)^2}{\pi \left[2(1 - \cos \psi) + \left(\frac{\hat{\eta}' - \hat{\eta}}{R_2}\right)^2\right]^2} d\psi \frac{d\hat{\eta}'}{R_2} \quad (\text{A.7})$$

after using Eq. (A.1) and the differential surface area given by $dA_2^* = R_2 d\phi d\hat{\eta}'$, where $\psi = \phi - \theta$. The problem is axisymmetric, and therefore the view factor is the same for all the elements of the furnace ring, that is,

$$dF_{dA_1 \rightarrow dA_2} = dF_{dA_1^* \rightarrow dA_2}. \quad (\text{A.8})$$

In terms of the dimensionless variables $\eta = \hat{\eta}/L$ and $\eta' = \hat{\eta}'/L$, and changing the nomenclature, we can write

$$dF_{d\eta \rightarrow d\eta'} = K_2(\eta, \eta') d\eta', \quad (\text{A.9})$$

where the dimensionless kernel function $K_2(\eta, \eta')$ is given by

$$K_2(\eta, \eta') = \frac{L}{R_2} \int_{-2c}^{2c} \frac{(1 - \cos \psi)^2}{\pi \left[2(1 - \cos \psi) + \left(\frac{L}{R_2}\right)^2 (\eta' - \eta)^2\right]^2} d\psi. \quad (\text{A.10})$$

References

- [1] K. Lin, P. Dold, Cryst. Res. Technol. 36 (2001) 629.
- [2] Ch. Stenzel, J. Stapelmann, H. Krause, A. Aead, Proceedings of the Sixth European Conference on Industrial Furnaces and Boilers, Estoril, Portugal, 2–5 April 2002.

- [3] R.J. Behrle, H. Figgemeier, A. Danilewsky, K.W. Benz, ESA SP-295 (1990) 673.
- [4] R. Schwarz, A.N. Danilewsky, G. Bischofink, K.W. Benz, ESA SP-333 (1992) 702.
- [5] St. Boschert, P. Dold, K.W. Benz, *J. Crystal Growth* 187 (1998) 140.
- [6] P. Dold, A. Barz, et al., *J. Crystal Growth* 192 (1998) 125.
- [7] M.J. Crochet, F. Dupret, et al., *J. Crystal Growth* 97 (1989) 173.
- [8] P.M. Adornato, R.A. Brown, *J. Crystal Growth* 80 (1987) 155.
- [9] S. Brandon, J.J. Derby, *J. Crystal Growth* 121 (1992) 473.
- [10] J. Amon, P. Berwian, G. Müller, *J. Crystal Growth* 198/199 (1999) 361.
- [11] M. Kurz, A. Pusztai, G. Müller, *J. Crystal Growth* 198/199 (1999) 101.
- [12] S. Maruyama, T. Aihara, *Int. J. Heat Mass Transfer* 37 (1994) 1723.
- [13] S.-H. Hahn, T. Tsukada, et al., *J. Crystal Growth* 191 (1998) 413.
- [14] G.D. Raithby, K.G.T. Hollands, *Adv. Heat Transfer* 11 (1975) 265.
- [15] D. Rivas, R. Haya, *J. Crystal Growth* 206 (1999) 230.
- [16] M.F. Modest, *Radiative Heat Transfer*, McGraw-Hill, New York, 1993, pp. 234, 241, 783.
- [17] P. Dold, Ph.D. Thesis, Albert-Ludwigs-Universität Freiburg, 1994.
- [18] A. Cröll, W. Müller-Sebert, K.W. Benz, R. Nitsche, *Microgravity Sci. Technol.* III/4 (1991) 204.
- [19] A. Cröll, P. Dold, K.W. Benz, *J. Crystal Growth* 137 (1994) 95.
- [20] R. Siegel, J.R. Howell, *Thermal Radiation Heat Transfer*, Hemisphere Publishing Corporation, Washington, 1992, p. 195.



ELSEVIER

Available online at www.sciencedirect.com

SCIENCE @ DIRECT®

JOURNAL OF CRYSTAL GROWTH

Journal of Crystal Growth 246 (2002) 55–63

www.elsevier.com/locate/jcrysgro

The role of growth conditions on the p-doping of GaN by plasma-assisted molecular beam epitaxy

E. Haus^{a,*}, I.P. Smorchkova^{b,1}, B. Heying^{a,1}, P. Fini^a, C. Poblenz^a,
T. Mates^a, U.K. Mishra^b, J.S. Speck^a

^a Materials Department, University of California, Santa Barbara, CA 93106, USA

^b Electrical and Computer Engineering Department, University of California, Santa Barbara, CA 93106, USA

Received 28 December 2001; accepted 22 June 2002

Communicated by M.S. Goorsky

Abstract

Mg-doped GaN layers were grown by plasma-assisted molecular beam epitaxy under a range of conditions. The growth temperatures and III/V ratio were altered and the resultant films were analyzed using atomic force microscopy, Hall effect measurements, and secondary ion mass spectroscopy (SIMS). The growth temperatures ranged from 600°C to 700°C. The III/V ratios were varied from N-rich (less than unity) to Ga-rich conditions (greater than unity). AFM showed that N-rich (III/V ratio < 1) conditions yielded rough surface morphologies and room temperature Hall measurements show they were not measurably p-type. Ga-rich conditions (III/V ratio > 1) yielded smoother morphologies and exhibited p-type conductivity. The trend in morphology with changing III/V ratio is consistent with previous studies of the MBE growth of unintentionally doped GaN. SIMS measurements show that Mg incorporation was negligibly affected by the III/V ratio but exponentially decreased with increasing growth temperature.

© 2002 Published by Elsevier Science B.V.

Keywords: A1. Morphology; A1. P-doping; A3. Molecular beam epitaxy; B1. Gallium nitride

1. Introduction

Achieving high-quality p-type GaN layers is crucial for the development of many nitride-based optoelectronic and electronic semiconductor devices, such as short-wavelength light-emitting diodes (LEDs), lasers, and heterojunction bipolar transistors (HBTs). For these devices, precise

doping levels and profiles are needed, which has sparked much interest in developing p-type GaN. Magnesium is the most promising acceptor for nitrides despite its large thermal activation energy of ~200 meV [1].

There has been much interest recently in p-type doping of GaN with the recent progress in short wavelength optoelectronics [2]. The initial development of gallium nitride and currently commercially available nitride devices are grown via metal organic chemical vapor deposition (MOCVD). However, MOCVD-grown, Mg-doped GaN films

*Corresponding author.

¹ Current address: TRW, Semiconductor Products Center, Redondo Beach, CA.

suffer from hydrogen passivation and memory effects. Hydrogen passivation causes Mg-doped films to be resistive after growth [3]. A post-growth activation is required to drive off the hydrogen to achieve conductive p-type GaN. Memory effects are caused by the long transient times for the Mg in MOCVD reactors. These transient times do not allow for abrupt doping profiles, often a requirement in optoelectronic materials. Device performance is often very sensitive to the depletion region positioning and thus broad doping profiles can severely degrade performance. MBE-grown GaN avoids these two issues. MBE growth occurs in a hydrogen-free environment, and thus post-growth Mg activation is unnecessary. Moreover, sharp doping profiles have been achieved in MBE-grown GaN:Mg films [4], thus making MBE an attractive, alternative means for growing device quality p-type GaN.

Recent studies of unintentionally doped MBE-grown GaN have produced growth diagrams or surface phase diagrams for a range of conditions [5]. These growth diagrams help to identify optimum growth conditions, and to develop high-quality films. Under typical growth temperatures (600–800°C), MBE-grown GaN exhibits three distinct growth regimes [5]. These regimes are determined by the III/V ratio and substrate temperature, resulting in a $\text{III/V} > 1$ (Ga-rich) regime, a $\text{III/V} < 1$ (N-rich) regime, and $\text{III/V} \sim 1$ “intermediate” regime. Fig. 1 shows the three distinct growth regimes for substrate temperatures 550–750°C, which assumes a constant flux of active nitrogen. Structural, electrical and morphological properties can vary greatly between films grown in these different regimes.

GaN films grown in the Ga-rich regime often exhibit surface morphologies that are quite smooth, which correlate with the streaky reflection high-energy electron diffraction (RHEED) patterns observed during growth. Typically, in this regime, the surface shows terraces separated by monolayer steps. Films grown in the Ga-rich regime have a two-monolayer thick Ga-wetting layer and Ga droplets after growth. These films typically have the lowest defect densities, smoothest morphologies, and good electrical transport properties. Films grown in the intermediate or

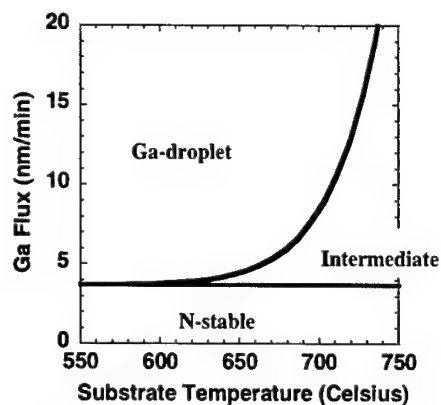


Fig. 1. Growth diagram for GaN, depicting Ga-flux and substrate temperatures for the three growth regimes—Ga-rich ($\text{III/V} > 1$), intermediate “crossover”, and N-rich ($\text{III/V} < 1$) for a constant N-flux of 2.8 nm/min.

“crossover” regime for GaN are somewhat similar to the Ga-rich regime. The surface is still relatively smooth, but pit-terminated threading dislocations (TDs) or trenches break up the surface. Films grown in the N-stable regime have the roughest morphologies and exhibit pit-terminated TDs. This correlates to the typical, bright, spotty RHEED patterns seen during growth. This regime produces films with the highest defect densities, the worst transport properties, and at low temperatures, columnar microstructures with a high density of stacking faults [6,7].

The transition between the N-rich regime and the Ga-rich regime is due to a change in adatom surface diffusion caused by a change in Ga-adlayer coverage. In the N-rich regime, the surface is saturated with N causing low adatom surface diffusion. The kinetically limited growth leads to poor morphology and an increase in TD terminated pits. As the Ga-flux is increased, Ga-adatom surface coverage increases leading to an increase in surface diffusion which reduced the formation of pits. It has been proposed that compensating centers due to point defect are decreased from the N- to Ga-rich regime, which improves the transport properties [8].

While great progress has been made in the growth and optimization of bulk GaN, Mg-doped GaN still remains as a barrier to device applications. There has been much research in Mg-doped

GaN, such as codoping, substrate polarity, and growth rate dependence on Mg-flux [9–12]. However, Mg-doping and its effects on GaN growth are still not fully understood. In addition, other complications arise when trying to grow p-type GaN with optimum bulk GaN growth conditions. Heying et al. report their best transport properties for GaN films grown over 700°C, but obtaining p-type conductivity at high growth temperatures remains elusive due to limited Mg incorporation. Others have even reported n-type conductivity for GaN:Mg grown over 600°C [13].

In this paper, we demonstrate the effects of growth temperature and III/V ratio on the surface morphology, transport properties and Mg incorporation in Mg-doped GaN films. We present optimized growth conditions that yield the best transport properties and smoothest surface morphologies.

2. Experimental procedure

Bulk GaN:Mg films were grown by plasma-assisted molecular beam epitaxy in a Varian Gen II MBE system. Active nitrogen was supplied by an EPI Unibulb nitrogen plasma source. Conventional effusion cells were used for Ga and Mg. The layers were grown on top of ~1–3 µm thick unintentionally doped *n*-GaN templates [$n \sim (3-5) \times 10^{16} \text{ cm}^{-3}$] grown by MOCVD on (0001) sapphire substrates, with a 30 nm undoped, MBE-grown spacer layer. All samples were grown at a constant N-flux with an RF power of 150 W and a nitrogen flow rate of 0.05 sccm. The Ga-flux and growth temperature were then varied for the different growths.

Three sets of Mg-doped GaN films were grown to systematically investigate the effects of III/V ratio and growth temperature on surface morphology, Mg incorporation, and hole mobility. The resulting films were then characterized with atomic force microscopy (AFM), secondary ion mass spectroscopy (SIMS), and Hall mobility measurements. For Hall measurements, 250 nm Pd and 2500 nm Au were deposited on the surface. To make the Hall measurements more reliable and to circumvent possible leakage or shorts from our

MBE-grown material to the conductive, underlying MOCVD-grown template, ~200 µm wide van der Pauw patterns were lithographically defined and the neighboring material was etched away. The remaining “pillars” of material served as our contacts. Fig. 2 shows these van der Pauw patterns.

The first set of samples investigated the effects of the III/V ratio on surface morphology, hole concentration and mobility. The Mg-flux, N-flux, and growth temperature were held constant, while the Ga-flux was altered to span the III/V ratio from less than unity to greater than unity. We investigated the effects of the III/V ratio at both 650°C and 600°C. Table 1 shows the growth conditions for this series of samples.

The Ga-rich samples had visible Ga buildup and droplets on the surface, as shown in Fig. 3. The N-rich samples did not exhibit any visible Ga buildup. All samples were etched in HCl to remove any excess Ga and were then imaged with AFM. The transport properties were then characterized with Hall effect mobility measurements.

The second set of samples investigated the effects of growth of temperature on the transport properties, surface morphology and Mg incorporation. All samples were grown in the upper intermediate regime (III/V slightly greater than

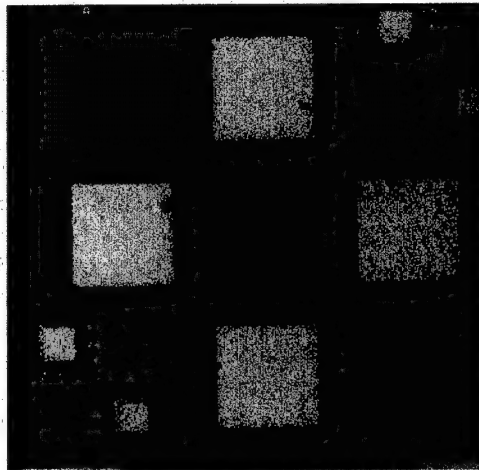


Fig. 2. Image of gold/palladium contacts and etched van der Pauw patterns for Hall effect measurements. The contact pads are 110 µm × 110 µm.

Table 1

Growth conditions for samples investigating the effects of altered III/V ratio. All samples were grown with constant N-flux (150 W rf plasma power, 0.05 sccm N₂ flow)

Temperature (°C)	Ga-flux (Torr)	Mg-flux (Torr)	III/V
650	1.4×10^{-7}	5×10^{-9}	<1
	1.8×10^{-7}		<1
	2.2×10^{-7}		~1
	2.6×10^{-7}		>1
	3.0×10^{-7}		>1
600	1.0×10^{-7}	2.3×10^{-9}	<1
	1.4×10^{-7}		>1

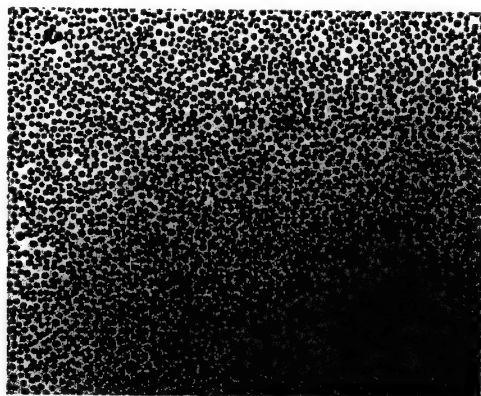


Fig. 3. Optical image of Ga droplets on MBE-grown GaN:Mg under Ga-rich conditions. The actual image size is 2.5 mm wide \times 2 mm high.

unity), while the growth temperature was varied. Growth conditions for these samples are given in Table 2. AFM, Hall effect measurements and SIMS were used to characterize these films. To eliminate possible changes in conditions between growths and to best determine temperature effects on Mg incorporation, another film was grown under constant III/V ratio and Mg-flux, but the growth temperature was abruptly changed twice. The temperature was changed from 650°C to 675°C, and then from 675°C to 700°C. The film was then analyzed with SIMS to determine Mg incorporation as a function of substrate temperature.

The final sample set studied the effects of III/V ratio on Mg incorporation. The impinging Ga-flux was abruptly changed twice throughout the

Table 2

Growth conditions for samples investigating the effects of growth temperature. All samples were grown with constant N-flux (150 W rf plasma power, 0.05 sccm N₂ flow) and in the upper crossover (III/V slightly greater than unity)

Temperature (°C)	Ga-flux (Torr)	Mg-flux (Torr)	III/V
650	2.4×10^{-8}	1.0×10^{-8}	≥ 1
675	2.5×10^{-8}		≥ 1
685	2.7×10^{-8}		≥ 1
700	3.3×10^{-8}		≥ 1

growth while N-flux, Mg-flux, and growth temperature were kept constant. These changes roughly coincide with three regimes: N-rich, III/V ≈ 1 , and Ga-rich. The transition from N- to Ga-rich was marked by the RHEED pattern changing from bright and spotty for N-rich to dim and streaky for Ga-rich. For these samples, one started N-rich and the III/V ratio was increased, while the other started Ga-rich and the III/V ratio was decreased. Since excess Ga can remain on the surface, the transition from Ga- to N-rich may not be abrupt even though the impinging flux can change abruptly. With increasing III/V ratio during growth, this potential problem can be circumvented. Mg distributions were obtained from SIMS analysis of these films.

3. Results

The III/V ratio had a tremendous effect on surface morphology. Figs. 4a–d show AFM images of films that were grown at 650°C, and Figs. 5a and b show AFM images of samples grown at 600°C. The surface morphologies of the Ga-rich and crossover samples grown at 650°C were much smoother than the N-rich sample and showed a stepped surface indicative of two-dimensional growth. The surface of N-rich sample was rougher and had a columnar surface indicative of three-dimensional growth. The variation in height was three times larger for the most N-rich sample (Fig. 4a) than was for the Ga-rich sample (Fig. 4d). Hall effect measurements were performed on these samples. The Ga-rich and

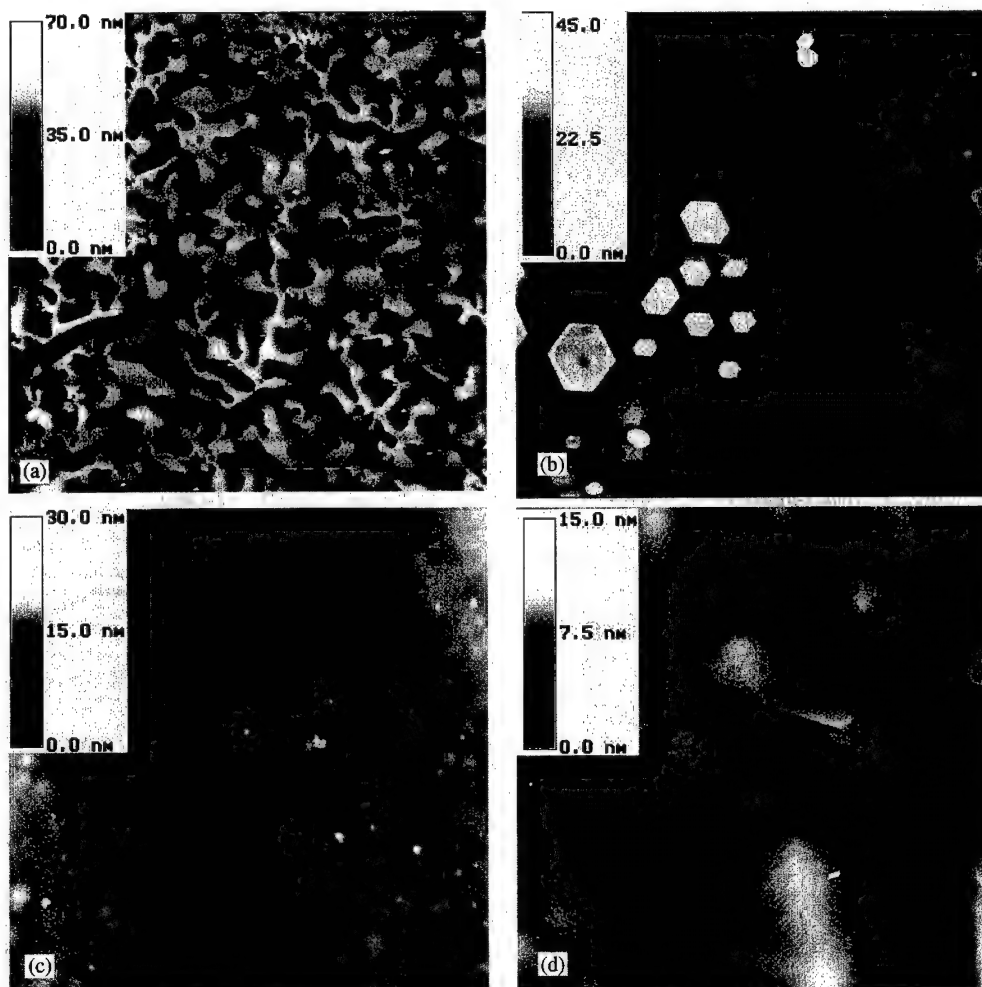


Fig. 4. AFM images of MBE-grown GaN:Mg with grown (a) in the N-rich regime, (b) in the N-rich regime near the crossover, (c) in the intermediate crossover regime, and (d) in Ga-rich regime near the crossover. The Ga-rich regime sample exhibited similar surface morphology to (d).

crossover samples had measurable hole concentration and mobilities while the N-rich samples were too resistive to make reliable Hall effect measurements. The hole concentrations ranged from 4.8×10^{17} to $5.7 \times 10^{17} \text{ cm}^{-3}$ and the mobilities ranged from 11 to $13 \text{ cm}^2/\text{Vs}$, as shown in Fig. 6.

For the samples grown at 600°C , the surface morphology was considerably smoother for the Ga-rich sample. However, neither sample demonstrated p-type conductivity. The surface morphology for the Ga-rich sample at 600°C (Fig. 5a) was markedly rougher than that of the Ga-rich sample grown at 650°C (Fig. 4d). The Ga-rich did not

yield reliable Hall effect measurements, while the N-rich sample was measurably n-type, with $n \sim 2.2 \times 10^{17} \text{ cm}^{-3}$ and $\mu \sim 80 \text{ cm}^2/\text{Vs}$.

Temperature also had a marked effect on surface morphology and transport properties. The samples grown at 675°C , 685°C , and 700°C had surface morphologies that were similar to the film grown at 650°C in the Ga-rich or crossover regime. However, these samples proved difficult to make reliable Hall effect measurements. Fig. 7 shows the SIMS analysis of the "control" sample where the temperature was abruptly changed from 650°C to 675°C , and from 675°C to 700°C .

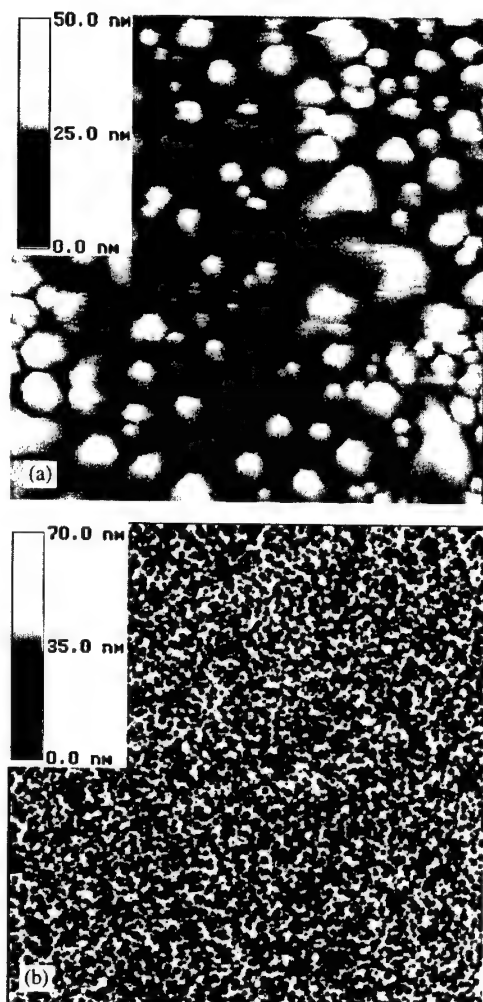


Fig. 5. AFM images GaN samples grown at 600°C (a) in the Ga-rich regime and (b) in the N-rich regime.

Increased growth temperature clearly reduced the Mg incorporation—the Mg concentration appears to decrease exponentially with increasing temperature. An Arrhenius plot shown in Fig. 8 more clearly shows the dependence, with the activation energy for Mg desorption from a Ga surface of GaN to be about 2.7 eV.

While III/V ratio had tremendous effect on the surface and electrical transport properties, it appears to have negligible effect on Mg incorporation. Figs. 9a and b show the SIMS analysis of the two films where the Ga-flux was abruptly changed during growth, while the N-flux, Mg-flux and

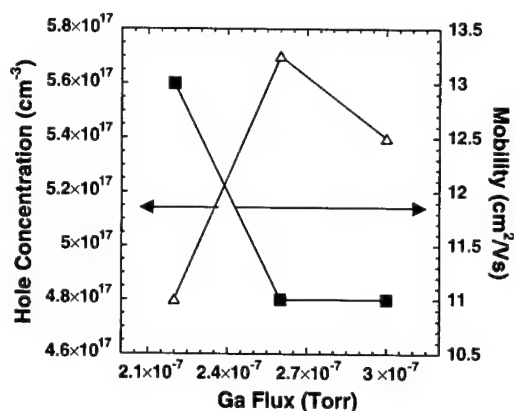


Fig. 6. A plot of hole mobilities and hole concentrations for three samples grown at 650°C. All samples plotted were grown with the III/V ratio ≥ 1 .

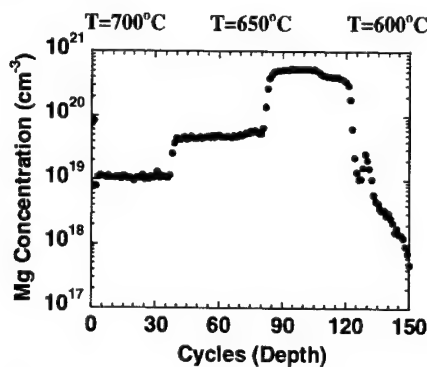


Fig. 7. SIMS analysis of a sample grown under constant N-flux, Mg-flux and Ga-Flux, but with abrupt temperature changes, from 600°C to 650°C and from 650°C to 700°C.

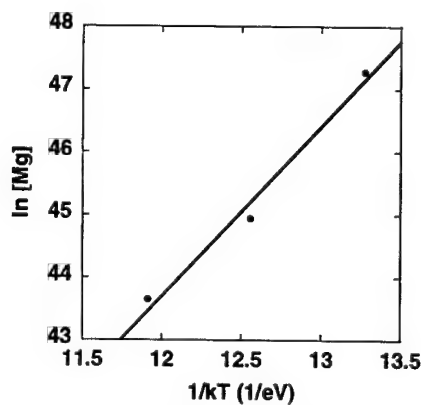


Fig. 8. Arrhenius plot showing the exponential decrease of Mg incorporation of MBE-grown GaN:Mg with increasing substrate temperature. Calculations were performed with Mg concentrations in units of cm^{-3} .

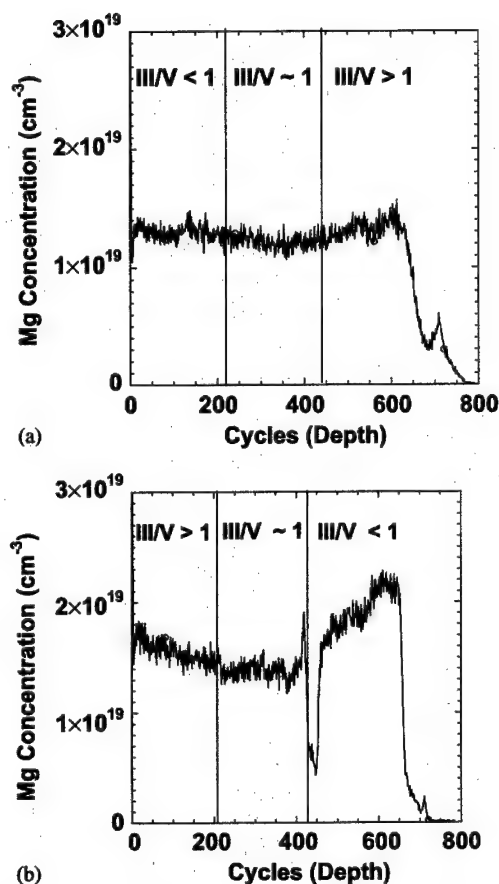


Fig. 9. SIMS analysis of GaN:Mg with (a) III/V ratio decreasing from left to right and (b) III/V ratio increasing from left to right. The sudden drop and increase in Mg concentration for (b) is a measurement artifact.

growth temperature were kept constant. In both the Ga- to N-rich transition and N- to Ga-rich transition, the Mg level appears constant. These results clearly show that Mg incorporation exponentially decreases with increasing growth temperature and is independent of III/V ratio. This implies that the resistivity of our N-rich samples is not due to lack of Mg but rather is due to either inactive or compensated Mg acceptors.

4. Discussion

Our results show that the surface morphologies and transport properties of Mg-doped GaN

depend on both growth temperature and the III/V ratio. However, the Mg incorporation is sensitive only to substrate temperature and is insensitive to the III/V ratio.

At higher growth temperatures, we realized smoother morphologies but observed an exponential decrease in Mg incorporation. These two competing effects determined the optimum growth temperature. At growth temperatures greater than 650°C, we were unable to make reliable Hall measurements with our films. We believe the difficulties are due to insufficient Mg incorporation to overcome unintentional background n-doping and to fill all hole traps. From our SIMS analysis, we observed an exponential decrease in Mg incorporation with growth temperature, which is consistent with the results of Ptak et al. [14]. This decrease follows an Arrhenius relationship, with a desorption energy of 2.7 eV.

Different effects come into play for the lower-temperature growth of Mg-doped GaN. Our SIMS analysis shows that Mg incorporation is not an issue for films grown at and below 650°C, but rather point defect formation and unintentional oxygen incorporation become the dominant obstacles in achieving p-type conductivity. Previous SIMS studies of bulk MBE GaN films at UCSB have shown increased oxygen incorporation and increased background electron concentrations for lower growth temperatures. Furthermore, it is possible that the decreased crystal quality at lower growth temperatures induces compensating defects and physically reduces p-type contact quality on the surface. We therefore believe that the Mg acceptors are compensated by oxygen donors and possibly by other point defects for our films grown below 650°C.

The III/V ratio had the most pronounced effect on the properties of our films. At III/V ratios greater than unity, we observed smooth surface morphologies and p-type conductivity with reasonable hole mobilities. As the III/V ratio was decreased, we observed a marked increase in surface roughness and a decrease in conductivity resulting in semi-insulating films. We believe that the increased surface roughness is due to kinetically limited growth caused by a lack of available

Ga on the surface. The trend in morphology with changing III/V ratio is consistent with previous studies of the MBE growth of unintentionally doped GaN [5]. Elsass et al. have observed increased oxygen incorporation with decreasing III/V ratio for AlGaIn [15]. We believe that oxygen may be a compensating donor for our films grown in the N-rich regime. Moreover, we also believe that our compensation is due to point defects since the TD density in the MBE GaN films is fixed by the MOCVD template.

Hierro et al. have shown a correlation of increasing acceptor-like point defects in n-type GaN with decreasing III/V ratio [16]. Using deep level transient spectroscopy (DLTS), they have shown an order of magnitude increase in the density of electron traps for GaN grown under N-rich conditions compared to Ga-rich conditions. Since these are acceptor-like traps, they are obviously not the source of compensation for our Mg-doped films. However, we speculate that a similar mechanism may be the cause of our compensation. These point defects or complexes would still be deep level traps, but would be donor-like traps that compensate our holes and increase the Fermi level resulting in semi-insulating films. Further research into p-type films is needed to fully understand the compensation that occurs in the III/V ratio.

To account for the measured n-type conductivity, we observed in the N-rich regime at 600°C, we believe that we were most likely measuring the underlying MOCVD-grown template background carriers. We suspect that the isolation between our Mg-doped layer and the underlying n-type region was weak due to a lack of holes in our Mg-doped layer. As hole concentration decreases, the Fermi level increases. This in turn decreases the built-in voltage across the junction. We suspect we overcome this built-in voltage and measured parallel conduction of the two films, with the template being the dominant transport region.

5. Conclusion

In summary, N-rich GaN:Mg layers yield very rough surface morphologies and were not measur-

ably p-type even with significant Mg incorporation. Decreasing growth temperature below 650°C degraded the surface morphology for both Ga- and N-rich films and resulted in n-type material for the N-rich material, which we believe to be defect induced. The Ga-rich growth regime resulted in much smoother morphologies and p-type conductivity. Mobility, carrier (hole) concentrations and Mg incorporation appear to be negligibly affected by increasing III/V ratio for III/V > 1 (intermediate and Ga-droplet regimes). Temperature seems to improve surface morphologies, especially for heavily doped GaN films, but Mg incorporation decreases exponentially with increasing growth temperature. For Mg-doped films to be measurably p-type, growth temperatures of around 650°C should be used in RF-plasma MBE growth. At lower temperatures, we believe increased defects will compensate the active Mg.

Acknowledgements

This work was supported through the ONR IMPACT and POLARIS MURI programs at UCSB (Colin Wood and John Zolper program managers).

References

- [1] W. Götz, N.M. Johnson, J. Walker, D.P. Bour, R.A. Street, *Appl. Phys. Lett.* 68 (1996) 667.
- [2] S. Nakamura, G. Fasol, *The Blue Laser Diode*, Springer, Berlin, 1997.
- [3] H. Amano, M. Kito, K. Hiramatsu, I. Akasaki, *Jpn. J. Appl. Phys.* 28 (1989) L2112.
- [4] I.P. Smorchkova, E. Haus, B. Heying, P. Kozodoy, P. Fini, J.P. Ibbetson, S. Keller, S.P. DenBaars, J.S. Speck, U.K. Mishra, *Appl. Phys. Lett.* 79 (2000) 718.
- [5] B. Heying, R. Averbeck, L.F. Chen, E. Haus, H. Riechert, J.S. Speck, *J. Appl. Phys.* 88 (2000) 1856.
- [6] E.J. Tarsa, B. Heying, X.H. Wu, P. Fini, S.P. DenBaars, J.S. Speck, *J. Appl. Phys.* 82 (1997) 5472.
- [7] T. Zywiets, J. Neugebauer, M. Scheffler, *Appl. Phys. Lett.* 73 (1998) 487.
- [8] B. Heying, I. Smorchkova, C. Poblenz, C. Elsass, P. Fini, S. DenBaars, U. Mishra, J.S. Speck, *Appl. Phys. Lett.* 77 (2000) 2886.
- [9] J.A. Van Vechten, J.D. Zook, R.D. Horning, B. Goldenberg, *Jpn. J. Appl. Phys. (Part 1)* 31 (1992) 3662.

- [10] S. Nakamura, N. Iwasa, M. Senoh, T. Mukai, *Jpn. J. Appl. Phys. (Part 1)* 31 (1992) 1258.
- [11] C.G. Van de Walle, C. Stampfl, J. Neugebauer, *J. Crystal Growth* 189–190 (1998) 508.
- [12] B. Daudin, G. Mula, P. Peyla, *Phys. Rev. B* 61 (2000) 10335.
- [13] J.M. Myoung, K. Kim, *J. Vac. Sci. Technol. A* 18 (2000) 455.
- [14] A.J. Ptak, T.H. Myers, L.T. Romano, C.G. Van de Wall, J.E. Northrup, *Appl. Phys. Lett.* 78 (2001) 286.
- [15] C.R. Elsass, T. mates, B. Heying, C. Poblentz, P. Fini, P.M. Petroff, S.P. Den Baars, J.S. Speck, *Appl. Phys. Lett.* 77 (2000) 3167.
- [16] A. Hierro, A.R. Arehart, B. Heying, M. Hansen, J.S. Speck, U.K. Mishra, S.P. DenBaars, S.A. Ringel, *Appl. Phys. Lett.* 80 (2002) 805.

A new phenomenon in the floating-zone (FZ) growth of Si nanowires

Quanli Hu*, Guoqing Li, Hiroshi Suzuki, Hiroshi Araki, Nobuhiro Ishikawa,
Wen Yang, Tetsuji Noda

National Institute for Materials Science, Nano-materials Laboratory, 1-2-1 Sengen, Tsukuba, Ibaraki 305-0047, Japan

Received 2 May 2002; accepted 10 September 2002

Communicated by R.S. Feigelson

Abstract

Silicon nanowires have been fabricated with the floating-zone melt-vapor method. The growth-time dependence of the size and morphology of Si nanowires was shown to reflect the dynamic behavior of nanowire growth with an oxide-assisted growth mechanism. A new long-time growth phenomenon for silicon nanowires was discovered and a related model was proposed.

© 2002 Elsevier Science B.V. All rights reserved.

Keywords: A2. Growth from vapor; B1. Nanomaterials; B2. Semiconducting silicon

1. Introduction

Si nanowires have been grown using the VLS mechanism [1,2], STM [3], and laser ablation or thermal evaporation [4–6]. Lee et al. reported that the thermal evaporation method is useful for the large-scale synthesis of Si nanowires, which can be explained by a new oxide-assisted growth mechanism that involves the use of an oxide to promote nanowire growth. The oxide-assisted growth mechanism seems to be suitable to the initial stages of nanowire formation. On the other hand, the dynamic behavior of nanowire growth that has already been formed should also be given more

attention because it is closely related with the future application of silicon nanowires. For example, according to classic defect physics, surface defects could develop or accumulate in some nanowires in the case of long-time growth, and the dynamic behavior of these defects would then influence any further growth of the nanowires. Unfortunately, until now, related research has not been reported.

In the present work, a new and simple method for growing Si nanowires was introduced. With this new method for the fabrication of silicon nanowires, the influence of growth time on the size, morphology, and crystallinity of silicon nanowires was investigated in order to obtain an in-depth understanding of the growth mechanisms of silicon nanowires. As a result, we developed a new model for the growth of silicon nanowires.

*Corresponding author. Tel.: +81-298592736; fax: +81-298592701.

E-mail address: hu.quanli@nims.go.jp (Q. Hu).

2. Experimental procedure

Silicon powders (purity: 99.999 at%; grain size: 300 mesh) were used as a starting material and placed into a rubber tube (diameter: 0.8 cm; length: 7–10 cm); they were then shaped with a hydraulic press at a pressure of 170 MPa. The bars of raw material were sintered in vacuum (1.33×10^{-5} Pa) at 1450 K for 3 h. Although the silicon oxides (SiO_2 or SiO) were not artificially doped, about 40–100 ppm oxygen was still detected by the chemical analysis; and also the concentration of the major metallic impurities (Fe, Mg, Al and Cu) introduced by sintering process was less than 19 ppm from the sintered silicon bar mentioned above. The sintered bar was then melted using the floating-zone (FZ) method inside a quartz tube at 1673 K to fabricate silicon nanowires under an atmosphere of pure flowing argon ($> 10 \text{ cm}^3/\text{min}$). The schematic drawing of the FZ furnace used for the growth of silicon nanowires was described elsewhere [7]. The floating zone was formed by a 2 kW Xe lamp and a water-cooled copper concave reflector outside a quartz tube. The width of the floating zone was about 2 mm. During the melting process of the floating zone at the bottom of silicon bar, the silicon nanowires were grown on the surface of the raw material bar, 1.5–2 cm from

the FZ center. After 5–300 min of melting, silicon nanowires, a sponge-like web of dark-yellow material, were collected, as shown in Fig. 1. The structure of silicon nanowires was examined by field-emission scanning electron microscope (FESEM, JSM-6700F), transmission electron microscope (TEM, JEM-2010) and high-resolution transmission electron microscope (HRTEM, JEM-3000F).

3. Results and discussion

Fig. 2 shows an FESEM image of silicon nanowires with a growth time of 10 min. Generally, these nanowires can be divided into two groups according to the diameter, i.e., (1) thin nanowires with an average diameter of 20–30 nm; and (2) large nanowires with an average diameter of 200–400 nm. Each nanowire consists of a wire body and a spherical or half-spherical ball at its tip. The growth-time dependence of the average diameter of thin silicon nanowires is shown in Fig. 3. As can be seen in this figure, there is no obvious variation on the diameter of thin silicon nanowires. Similarly, TEM observations do not reveal any apparent change in the surface morphology of thin silicon nanowires. Due to the precision that can be achieved from FESEM images when measuring a diameter, HRTEM

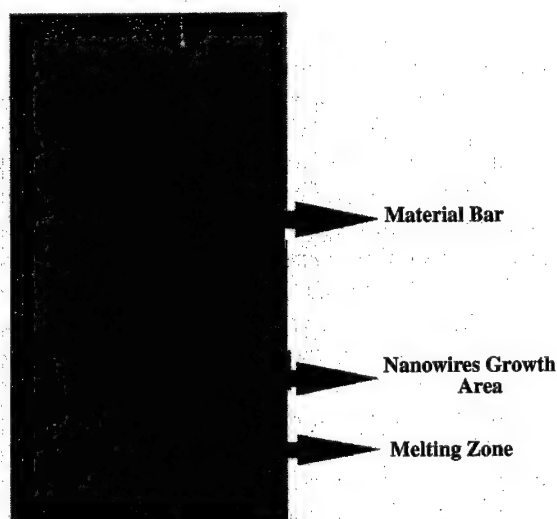


Fig. 1. The growth area of silicon nanowires on a silicon raw material bar.

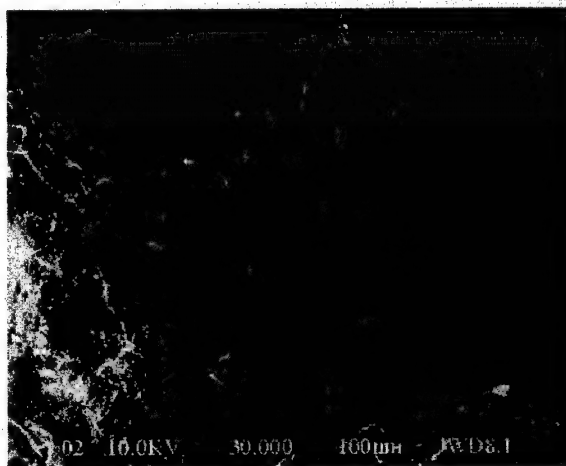


Fig. 2. FESEM images of silicon nanowires with a growth time of 10 min.

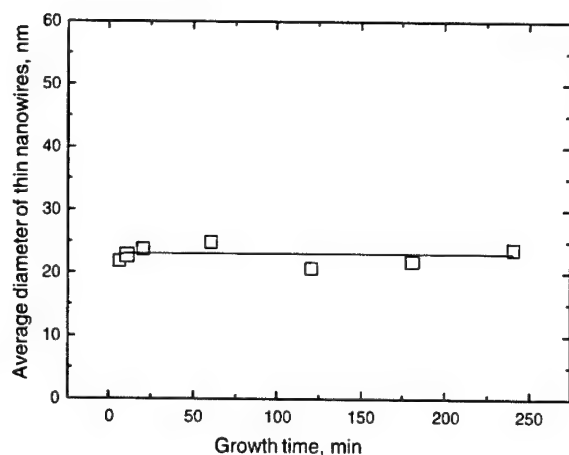


Fig. 3. Growth-time dependence of the diameter of thin silicon nanowires from FESEM observation results.

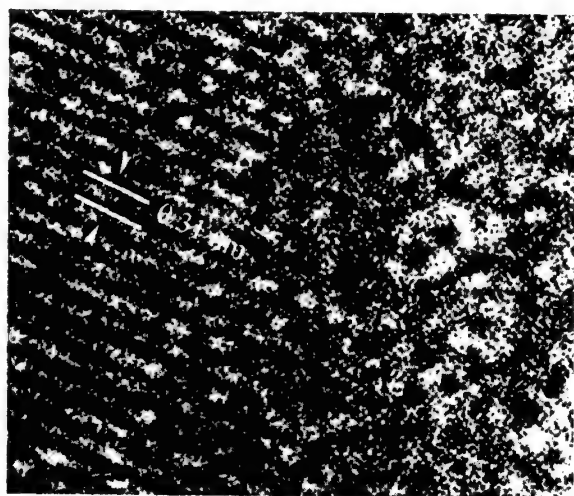


Fig. 4. HRTEM image of a body of thin silicon nanowires.

analyses on these thin nanowires are also used to confirm the results in Fig. 3. Moreover, a double-layer structure was observed, and the ratio between the SiO_2 amorphous layer and the thickness of the Si crystalline core was found to be around 2:1, as shown in Fig. 4.

According to traditional VLS theory, if the metallic impurities mediate the growth of nanowires, the metallic impurities should be detected in the tip of nanowires. But the energy-dispersed spectroscopy analysis of nanowires shows that no

any excess metallic elements are found on the tip of nanowires. Therefore, in the present work, we think that the growth of these thin nanowires may be explained on the basis of an oxide-assisted growth mechanism. The vapor of SiO_x was transferred by argon gas from the FZ melting area to the surface of the silicon bar at a downstream region (it is 1.5–2 cm from the melting-zone center; the temperature was measured to be about 1233–1273 K). According to the oxide-assisted growth mechanism, the initial nucleation on the surface of the silicon bar appears to be a vapor–solid (VS) process. If the nucleation involved an intermediate liquid phase, then the diameter of the wire would vary with the ambient pressure and the growth temperature as in the metal-catalyzed VLS method [8–10]. The liquid droplet has a high adsorption rate for the Si-containing nanoclusters from the vapor. When the SiO_x droplet becomes supersaturated with Si and decomposes, the excessive Si precipitates out, resulting in one-dimensional growth of Si crystalline nanowires. The ambient pressure is assumed to define the size of the liquid drops at the top of nanoparticles during the nucleation process, which in turn controls the diameter of the nanowires. Because growth time is the only condition that varies, the important factor determining the diameter of nanowires is that the ambient pressure be kept stable and that the surface becomes saturated with a minimum of free energy. Therefore, any further expanding in the radial direction is impossible for these thin nanowires. The diameter of thin nanowires, consequently, should not vary; however, the quantity and length could be increased with an extended growth time. In short, no obvious variation in the average diameter of these thin nanowires could be found in Fig. 3, even though the fabrication time had been increased.

On the other hand, the TEM results in Fig. 5 for large nanowires show an interesting phenomenon when the fabrication time exceeds 120 min. That is, some small nanowires with diameters of 10–30 nm sub-grow on the surface of large nanowires with diameters of 200–400 nm. In addition, the selected-area electron diffraction (SAED) analysis of large nanowires indicates that they are almost

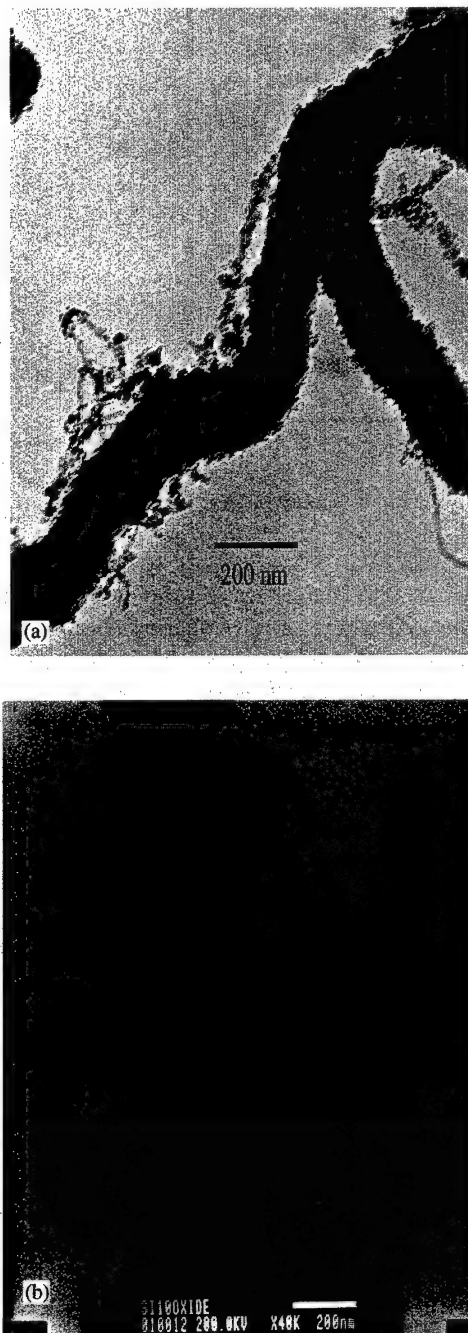


Fig. 5. TEM images of thin nanowires that were sub-grown on the surface of large silicon nanowires.

amorphous SiO_2 . Moreover, some of the thin nanowires sub-grown on the surface of the large nanowires still have a double-layer structure with a

crystalline silicon core and an amorphous SiO_2 outer shell.

As mentioned above, although there was no obvious variation in the diameter of thin nanowires, the occurrence of large nanowires with diameters of 200–400 nm was also observed. And additional time did not result in regularizing the growth-time dependence of the diameter of the large nanometers. The SAED measurements have shown that these large nanowires are amorphous SiO_2 . This result indicates that the vapor of SiO_x from the FZ melting area deposits on the surface of the silicon bar and that there is no decomposition. In other words, some large nanoclusters in the SiO_x vapor directly condense to form homogeneous amorphous nanoparticles of SiO or SiO_2 solid. In addition, the all-large nanoparticles on the surface of a silicon bar would not form a semi-liquid droplet. Furthermore, the ambient pressure cannot control the tip radius to cause regularity in the distribution of the diameter of the nanowires. This growth process produces only thick nanowires with large diameters. Therefore, large amorphous nanowires are produced by directly depositing SiO_x along one dimension, which is actually a VS growth process. These large nanowires are formed with higher surface-defect density and the defect sites on the amorphous wires could be non-stoichiometric oxide, oxygen vacancies or precipitations. With increasing growth time, the defect sites on the surface of large amorphous nanowires develop and provide more opportunity for the nucleation of thin nanowires, while the smooth surface of other thin nanowires maintains a minimum of free energy. This kind of nucleation on the surface of large nanometers occurs as a result of the VL process in combination with the defect movement or accumulation. During this nucleation process, small nanoparticles or the small stretch-outs on the surface of large nanowires act as energetically favorable sites for absorbing the clusters from the vapor, since the highly curved fine tips become semi-liquid. As the clusters keep being absorbed into the tips from the vapor, the one-dimensional eventual growth of nanowires happens on the surface of the large nanowires. Several tips on a given large nanowire can be suitable for growth.

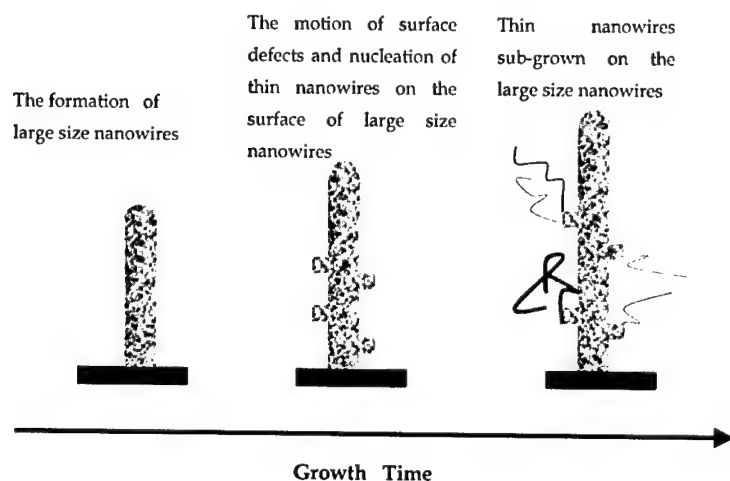


Fig. 6. A developed model for the process of thin nanowires sub-growing on the surface of large silicon nanowires.

Thus, several nanowires could grow on the same large nanowire to form a tree-like structure as shown in Fig. 5. Based on these considerations about the growth of large nanowires with increasing growth time, a tree-like growth model can be assumed in order to develop Lee's model for exploring the mechanism of nanowire growth. Fig. 6 illustrates the proposed growth model, which has been divided into three stages, i.e., (a) the formation of large nanowires; (b) the nucleation process from VS and surface defect development; and (c) the sub-growth of thin nanowires on the surface of large nanowires.

Further work is underway to investigate the oxide-concentration dependence of the diameter of Si nanowires.

4. Conclusions

Silicon Nanowires were fabricated by using the FZ melt-vapor method. The growth-time dependence of the size and morphology of silicon nanowires reflects the dynamic behavior of nanowire growth with an oxide-assisted growth mechanism. No obvious diameter variation of thin

nanowires (20–30 nm) was found with increasing the time. However, a new phenomenon in which thin nanowires sub-grew on the surface of large nanowires (200–400 nm) was observed after silicon nanowires had been grown for a long time, and a related model was proposed.

References

- [1] A.I. Klimovskaya, I.P. Ostrovski, A.S. Ostrovskaya, *Phys. Status Solidi A* 153 (1996) 465.
- [2] J. Westwater, D.P. Gosain, S. Tomiya, S. Usui, *J. Vac. Sci. Technol. B* 15 (1997) 554.
- [3] T. Ono, H. Saitoh, M. Esashi, *Appl. Phys. Lett.* 70 (1997) 1852.
- [4] Y.F. Zhang, Y.H. Tang, N. Wang, C.S. Lee, S.T. Lee, *Appl. Phys. Lett.* 72 (1998) 1835.
- [5] S.T. Lee, Y.F. Zhang, N. Wang, Y.H. Tang, I. Bello, C.S. Lee, Y.W. Chung, *J. Mater. Res.* 14 (1999) 4503.
- [6] Z.W. Pan, Z.R. Dai, L. Xu, S.T. Lee, Z.L. Wang, *J. Phys. Chem. B* 105 (2001) 2507.
- [7] Quanli Hu, Guoqing Li, Hiroshi Suzuki, Hiroshi ARAKI, Tetsuji Noda, *Jpn. J. Appl. Phys.* 41 (2002) L7.
- [8] Y.F. Zhang, Y.H. Tang, N. Wang, C.S. Lee, I. Bello, S.T. Lee, *J. Crystal Growth* 197 (1999) 136.
- [9] R.S. Wagner, W.C. Ellis, *Appl. Phys. Lett.* 4 (1964) 89.
- [10] E.I. Givargizov, *J. Crystal Growth* 32 (1975) 20.



ELSEVIER

Available online at www.sciencedirect.com

SCIENCE @ DIRECT®

Journal of Crystal Growth 246 (2002) 69–72

JOURNAL OF
**CRYSTAL
GROWTH**

www.elsevier.com/locate/jcrysgr

Structural characterization of epitaxial lateral overgrown GaN on patterned GaN/GaAs(001) substrates

X.M. Shen*, Y. Fu, G. Feng, B.S. Zhang, Z.H. Feng, Y.T. Wang, H. Yang

State Key Laboratory on Integrated Optoelectronics, Institute of Semiconductors, Chinese Academy of Sciences, P.O. Box 912, Beijing 100083, People's Republic of China

Received 16 August 2002; accepted 23 August 2002

Communicated by M. Schieber

Abstract

Epitaxial lateral overgrown (ELO) cubic GaN (c-GaN) on SiO₂ patterned GaN/GaAs(001) substrates by metalorganic vapor phase epitaxy was investigated using transmission electron microscopy and X-ray diffraction (XRD) measurements. The density of stacking faults (SFs) in ELO c-GaN was $\sim 6 \times 10^8 \text{ cm}^{-2}$, while that in underlying GaN template was $\sim 5 \times 10^9 \text{ cm}^{-2}$. XRD measurements showed that the full-width at half-maximum of c-GaN (002) rocking curve decreased from 33 to 17.8 arcmin, indicating the improved crystalline quality of ELO c-GaN. The mechanism of SF reduction in ELO c-GaN was also discussed.

© 2002 Elsevier Science B.V. All rights reserved.

PACS: 81.10.-h; 68.55.Jk; 81.15.Gh; 61.72.Nn

Keywords: A1. Transmission electron microscopy; A1. X-ray diffraction; A3. Epitaxial lateral overgrowth; A3. Metalorganic vapor phase epitaxy; B1. Cubic gallium nitride

1. Introduction

The III–V nitrides are attractive for high brightness short wavelength light emitting diodes (LEDs) and laser diodes (LDs) [1]. However, the use of highly lattice-mismatched substrates such as sapphire (0001) and GaAs (001) for the growth of these semiconductors has inevitably led to high densities of extended defects, which are dominantly threading dislocations (TDs) in hexagonal GaN (h-GaN) and stacking faults (SFs) in cubic GaN (c-GaN) epilayers. These defects are detri-

mental, especially for GaN-based LDs, which are usually achieved when the defect density is reduced to a low level. For this reason epitaxial lateral overgrowth (ELO) was introduced in the growth of GaN by hydride vapor phase epitaxy (HVPE) [2] and metalorganic vapor phase epitaxy (MOVPE) [3,4].

Recently, the ELO of GaN on patterned sapphire and 6H-SiC substrates has been reported to reduce TD density by several orders of magnitude. More importantly, a GaN-based LD with a lifetime longer than 10^4 h was also realized successfully by using this technique [5]. However, all the investigations so far have been focused on h-GaN, and only limited studies on ELO of c-GaN

*Corresponding author.

E-mail address: xmshen@red.semi.ac.cn (X.M. Shen).

have been reported in the literature [6–8]. Fu et al. found that pure c-GaN could be obtained on SiO_2 patterned GaN/GaAs (001) substrates successfully using ELO technique under optimized growth conditions [6]. However, the microstructure of ELO c-GaN is little understood. In this paper, we report our recent work on structural characterization of ELO cubic GaN. From our plane-view TEM observations, the density of stacking faults in c-GaN was reduced by about one order of magnitude via ELO. In addition, XRD rocking curve measurements showed that the crystal quality of c-GaN was improved after selective area lateral overgrowth.

2. Experimental procedure

The ELO was carried out by low pressure (76 Torr) MOVPE. After $\sim 0.6 \mu\text{m}$ thick c-GaN epilayer was deposited on GaAs (001) substrate using conventional two-step MOVPE, $\sim 70 \text{ nm}$ SiO_2 thin film was deposited on the c-GaN as mask material by RF-sputtering. Standard photolithography and chemical wet etching were used to pattern the $\text{SiO}_2/\text{GaN}/\text{GaAs}(001)$ substrate. Windows were opened along both the $[110]$ and $[1\bar{1}0]$ crystallographic directions of the substrate with the window openings of $3 \mu\text{m}$ wide and each SiO_2 square mask area of $10 \mu\text{m} \times 10 \mu\text{m}$. Prior to ELO, the grid-like SiO_2 patterned substrate was cleaned using ethanol, acetone, trichloroethylene and DI water. TEGa and ammonia were used as Ga and N sources, respectively. H_2 was the carrier gas. The

temperature and time of the re-growth process were 850°C and 120 min, respectively.

The morphology of as-grown ELO c-GaN was investigated by a JEOL-JSM-6301F scanning electron microscope. Transmission electron microscopy (TEM) and X-ray diffraction (XRD) were used to study the structural quality of ELO GaN films. TEM samples were prepared for both the conventional two-step grown c-GaN epilayer and the ELO c-GaN epilayer. In order to observe the defect density near-surface region of c-GaN epilayer by plane-view TEM, the TEM samples were thinned from the substrate side using conventional procedures involving the sequence of mechanical grinding and Ar-ion milling. The TEM observations were carried out on a Hitachi H-800 transmission electron microscope operated at 200 kV. X-ray rocking curve measurement was used to characterize the crystal quality and investigate the crystallographic tilting of the ELO c-GaN layer which is frequently observed in ELO h-GaN using a Rigaku double crystal X-ray diffractometer with $\text{Cu K}_{\alpha 1}$ radiation.

3. Results and discussion

Fig. 1 shows the plane-view (a) and cross-sectional (b) SEM images of the ELO-GaN sample. In Fig. 1(a), the regrowth of GaN in the window area can be clearly seen, indicating the excellent selectivity of c-GaN growth with the SiO_2 amorphous mask. As can be seen in Fig. 1(b), we obtained reverse trapezoid GaN stripes bounded

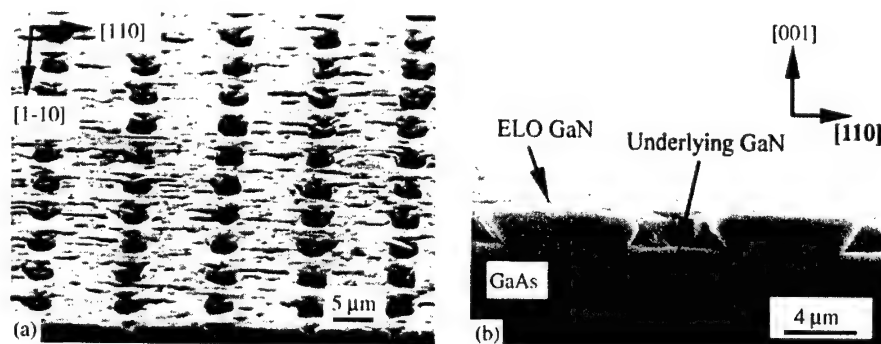


Fig. 1. SEM micrographs of ELO cubic GaN; (a) plane-view, (b) cross-sectional.

with (001) top and (111)B sidewalls when the windows were oriented along the $[1\bar{1}0]$ direction. Trapezoid shaped ELO-GaN stripes will be obtained when the windows were oriented along the $[110]$ direction (not shown here). That's why the $[1\bar{1}0]$ oriented stripes are wider than the $[110]$ ones (Fig. 1(a)). Therefore, the morphology of the ELO-GaN stripes depends strongly on the orientation of the window openings, which can be explained by the different growth rates of the GaN (111)A and (111)B planes [6]. For lateral overgrowth, the $[1\bar{1}0]$ -oriented windows are better than the $[110]$ -oriented ones, for the easier coalescence of the neighboring ELO-GaN stripes can be expected.

The stacking fault density in the near-surface region of the underlying GaN template is $\sim 5 \times 10^9 \text{ cm}^{-2}$, as estimated using plane-view TEM images such as shown in Fig. 2(a). Considering the overlapping of SFs in the GaN template, the actual density will be somewhat greater. As for ELO-GaN, the SF density near the top surface is estimated to be $\sim 6 \times 10^8 \text{ cm}^{-2}$, as shown in Fig. 2(b). The reduction of SF density in the ELO-GaN can be explained as follows: (1) the annihilation of the stacking faults probably occurred during the re-growth from the underlying GaN template and lateral overgrowth of c-GaN over the SiO_2 mask area; (2) each SiO_2 mask area will prevent propagation of a large portion of the stacking faults in the underlying GaN, therefore the SF density can be reduced greatly; (3) the stress relaxation probably helps to reduce the SF density in ELO c-GaN. Fig. 3 is the schematic diagram of the SF reduction mechanism during ELO process.

Obviously, the SF reduction mechanism in c-GaN ELO is very different from the TD reduction mechanism in h-GaN ELO, which is mainly due to the bending of TDs [9,10]. It can be concluded safely that the SF density will be reduced further by optimizing the ELO parameters, such as the thickness of the SiO_2 mask, the fill factor, the growth temperature, and the V/III ratio, etc. Further research to optimize these parameters is under way.

We have performed XRD rocking curve measurements for the ELO-GaN sample with the ω axis parallel to $[110]$ or $[1\bar{1}0]$ direction. Fig. 4 is the c-GaN (002) rocking curves of the conventional GaN template (square) and the ELO-GaN (triangle). It is worth noting that the full-width at half-maximum (FWHM) of the (002) rocking curve of the ELO-GaN is 17.8 arcmin, which is much smaller than that of the underlying GaN template, 33 arcmin, indicating the improved crystalline quality of ELO c-GaN. In addition, no crystallographic tilting, which is detrimental and can be frequently observed in the ELO of h-GaN [11,12], was found for our ELO c-GaN. It

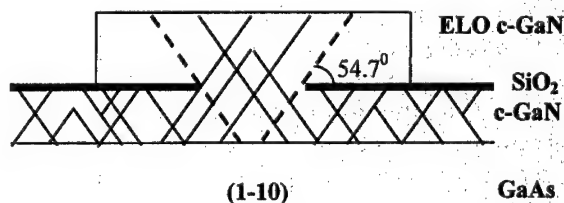


Fig. 3. Schematic diagram of reduction mechanism of SFs during ELO of cubic GaN.

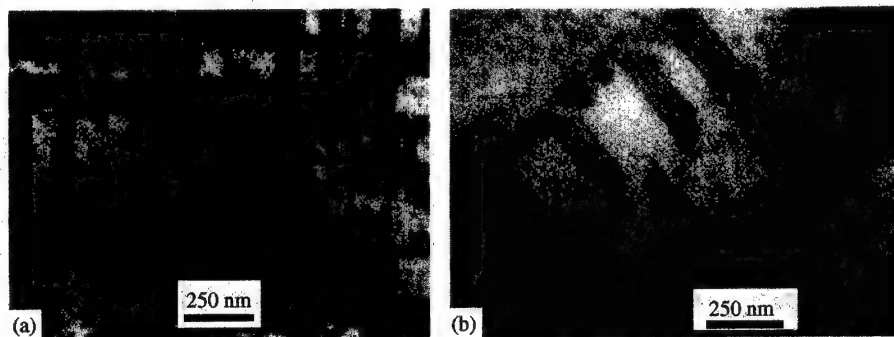


Fig. 2. Plane-view TEM images of cubic GaN; (a) underlying GaN, (b) ELO GaN.

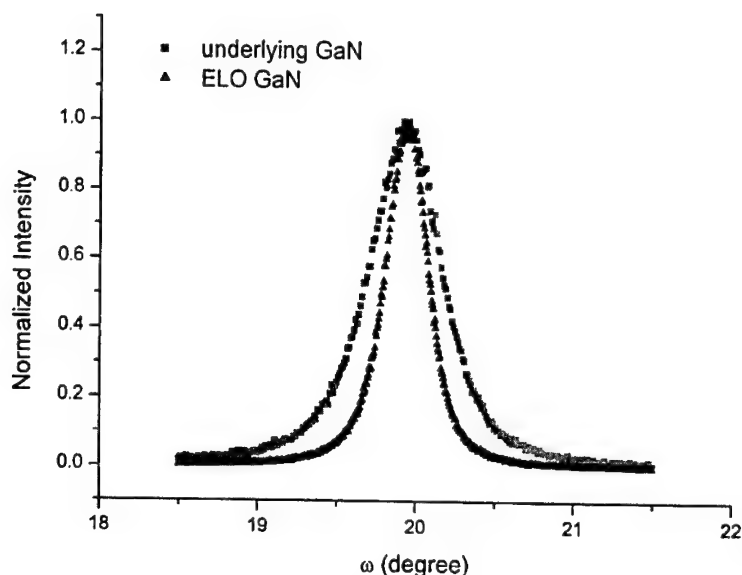


Fig. 4. XRD rocking curves of underlying and ELO cubic GaN.

means the present c-GaN ELO can be a promising technique to grow device quality c-GaN on GaAs(001) substrates.

4. Conclusions

The structural quality of the epitaxial lateral overgrown c-GaN on grid-like SiO₂ patterned GaN template was characterized by TEM and XRD. The density of stacking faults in c-GaN was reduced by about one order of magnitude via ELO. The FWHM of c-GaN (002) rocking curve decreased from 33 to 17.8 arcmin, indicating the improved crystalline quality of ELO c-GaN. No crystallographic tilting was found for the ELO c-GaN.

Acknowledgements

The authors acknowledge financial support from the Chinese National Natural Science Foundation (No. 69825107) and the NSFC-RGC Joint Program (Nos. NSFC5001161953 and N.HKU028/00).

References

- [1] S. Nakamura, S.F. Chichibu, *Introduction to Nitride Semiconductor Blue Lasers and Light Emitting Diodes*, Taylor & Francis, New York, 2000.
- [2] A. Usui, H. Sunakawa, A. Sakai, A.A. Yamaguchi, *Jpn. J. Appl. Phys. Part 2* 36 (1997) L899.
- [3] O. Nam, M.D. Bremser, T.S. Zheleva, R.F. Davis, *Appl. Phys. Lett.* 71 (1997) 2638.
- [4] H. Marchand, X.H. Wu, J.P. Ibbetson, P.T. Fini, P. Kozodoy, S. Keller, J.S. Speck, S.P. Denbaars, U.K. Mishra, *Appl. Phys. Lett.* 73 (1998) 747.
- [5] S. Nakamura, M. Senoh, S. Nagahama, et al., *Appl. Phys. Lett.* 72 (1998) 211.
- [6] Y. Fu, H. Yang, D.G. Zhao, et al., *J. Crystal Growth* 225 (2001) 45.
- [7] J. Wu, M. Kudo, A. Nagayama, et al., *Phys. Stat. Sol. A* 176 (1999) 557.
- [8] J. Suda, T. Kurobe, S. Nakamura, et al., *Jpn. J. Appl. Phys.* 39 (2000) L1081.
- [9] K. Horibuchi, N. Kuwano, K. Oki, et al., *Phys. Stat. Sol. A* 180 (2000) 171.
- [10] P. Vennéguès, B. Beaumont, V. Bousquet, M. Vaille, P. Gibart, *J. Appl. Phys.* 87 (2000) 4175.
- [11] G. Feng, X.H. Zheng, Y. Fu, J.J. Zhu, X.M. Shen, B.S. Zhang, D.G. Zhao, Y.T. Wang, H. Yang, J.W. Liang, *J. Crystal Growth* 240 (2002) 368.
- [12] M.H. Kim, Y. Choi, J. Yi, M. Yang, J. Jeon, S. Khym, S. Leem, *Appl. Phys. Lett.* 79 (2001) 1619.



ELSEVIER

Available online at www.sciencedirect.com

SCIENCE @ DIRECT®

Journal of Crystal Growth 246 (2002) 73–77

JOURNAL OF CRYSTAL GROWTH

www.elsevier.com/locate/jcrysgro

Temperature dependence of stresses in GaN/AlN/6H-SiC(0001) structures: correlation between AlN buffer thickness and intrinsic stresses in GaN

J. Keckes^{a,*}, G. Koblmue^b, R. Averb^b

^a *Erich Schmid Institute for Material Science, Austrian Academy of Sciences and Institute of Metal Physics, University of Leoben, Jahnstrasse 12, A-8700 Leoben, Austria*

^b *Infineon Technologies AG, D-81739 München, Germany*

Received 28 June 2002; accepted 10 September 2002

Communicated by K.W. Benz

Abstract

X-ray diffraction is used to characterize residual stresses in GaN/AlN/6H-SiC(0001) structures grown by molecular beam epitaxy. The measurements in the temperature range of 25–600°C document a change of stresses in GaN and AlN layers, as interpreted by the specific mismatch of thermal expansion coefficients. Primarily, the influence of AlN buffer thickness on the stress state of GaN is evaluated. With the increase of AlN buffer thickness from 20 to 200 nm the room-temperature stress in GaN thin films changes from 0.015 to –0.833 GPa. Likewise, the effect of stress on the energy band gap is further shown by photoluminescence measurements, indicating a shift of the near band gap emission in the GaN layers with varying stress. The results thus suggest a possibility for stress engineering in GaN thin films on 6H-SiC(0001) substrates.

© 2002 Elsevier Science B.V. All rights reserved.

PACS: 61.10.–i; 68.55.–a; 81.15.Jj; 81.05.Ea

Keywords: A1. Stresses; A1. X-ray diffraction; A3. Molecular beam epitaxy; B1. Gallium nitride

1. Introduction

The mechanical and optical properties of GaN thin films grown heteroepitaxially on foreign substrates depend decisively on the amount of residual strain formed during the deposition process [1,2]. The strain can hamper the properties

of GaN-based devices or, alternatively, *intentionally* produced strain can modify the optical and electronic performance of the devices. The intentionally created strains can be produced by inserting a buffer layer with a specific thickness between GaN and substrate, as it was demonstrated in the case of GaN/AlN/Al₂O₃(0001) structures [3].

Besides GaN growth on sapphire, GaN thin films have also been successfully grown on 6H-SiC substrates by various deposition techniques. Both

*Corresponding author. Tel.: +43-3843-804-301; fax: +43-3843-804-116.

E-mail address: keckes@unileoben.ac.at (J. Keckes).

compressive and tensile in-plane stresses were detected using X-ray diffraction (XRD) [4–6], Raman and photoluminescence spectroscopy [5,7–9], and high resolution transmission electron microscopy [6] in GaN/6H–SiC(0001) systems. The amount of in-plane stress in GaN on 6H–SiC depends significantly on growth conditions and film thickness [4–9]. Though, in many studies AlN buffer layers have been applied to modify the stress behavior of GaN on 6H–SiC, there has been no systematic work analyzing the temperature-dependent stress behavior of GaN/AlN/6H–SiC heterostructures and an influence of AlN buffer thickness.

In this letter, the relationship between AlN buffer thickness and stress behavior in GaN/AlN/6H–SiC structures is studied using XRD *ex situ* in the temperature range of 25–600°C. The main goals are to compare the temperature development of stress in GaN thin films, evaluate the influence of the buffer thickness and, moreover, analyze the contribution of thermal and intrinsic stress to the total stress.

2. Experimental procedure

One GaN/6H–SiC and three GaN/AlN/6H–SiC structures were grown using molecular beam epitaxy. For all structures, the thickness of the GaN layer was 1 μm . In the case of the GaN/AlN/6H–SiC structures, three different AlN buffer thicknesses of 20, 100 and 200 nm were used. The deposition temperatures for the GaN and AlN layers were 740°C and 780°C, respectively. In order to achieve excellent film quality, it was necessary to grow GaN under Ga-rich conditions [10]. Therefore, Ga/N ratios varying from 2.5 to 6.3 were chosen, while AlN was grown near-stoichiometrically with 5% excess Al.

Monochromatized Cu- $K\alpha$ radiation was used for the diffraction experiments. Pole figures and $\theta/2\theta$ measurements were applied to characterize the structural properties of the layers using a Seifert PTS 3000 XRD goniometer equipped with a high-temperature texture attachment provided by Anton Paar GmbH. Moreover, photoluminescence measurements of the GaN films were

performed at –196°C using a He–Cd laser ($\lambda = 325 \text{ nm}$) as excitation source.

3. Results and discussion

To verify the crystallographic quality of the thin films and to characterize the orientations of GaN, AlN and 6H–SiC in the goniometer coordinate system, pole figures were measured. In the case of the GaN/AlN/6H–SiC structure with a 200 nm AlN thick buffer layer, it was possible to determine the crystallographic orientation and strains also in the AlN sublayer.

In order to evaluate volume-averaged strains in four GaN heteroepitaxial layers and in the 200 nm thick AlN buffer layer, lattice spacings were determined by $\theta/2\theta$ measurements at different temperatures. For each layer, the measurements were performed by scanning GaN 00.6, 10.6, 20.5 and 21.3 or AlN 00.6, 10.5, 20.4 and 21.2 reflections (and their crystallographic equivalents) in a temperature cycle starting at room temperature (25°C), heating up to 600°C and then cooling down back to room temperature with 50°C steps. At each measurement temperature, the structures were analyzed for approximately 10 min. The results were reproducible and no hysteresis was observed for all four GaN layers as well as for the 200 nm AlN buffer layer.

The results of lattice spacing measurements were used to calculate stresses in the layers using the approach described in our previous reports [11,12]. Since the measurements indicated the presence of a biaxial stress state in the thin films (with $\sigma_{33} = 0$), only volume-averaged in-plane stress $\langle \sigma_{11} \rangle$ was evaluated with the assumptions $\langle \sigma_{11} \rangle = \langle \sigma_{22} \rangle$ and $\langle \sigma_{21} \rangle = 0$.

The temperature-dependent (T) in-plane stresses $\langle \sigma_{11}^T \rangle$ were refined from the diffraction data using temperature-dependent single crystal compliances S_{ijkl}^T of hexagonal GaN and AlN using ratios for unstressed lattice parameters $(c_0/a_0)^T$ of GaN and AlN adopted from Refs. [13,14].

The values of room temperature (RT) in-plane stresses $\langle \sigma_{11}^{\text{RT}} \rangle$ in GaN thin films are presented in Fig. 1. The results indicate a clear dependence of $\langle \sigma_{11}^{\text{RT}} \rangle$ in GaN on the AlN buffer thickness—with

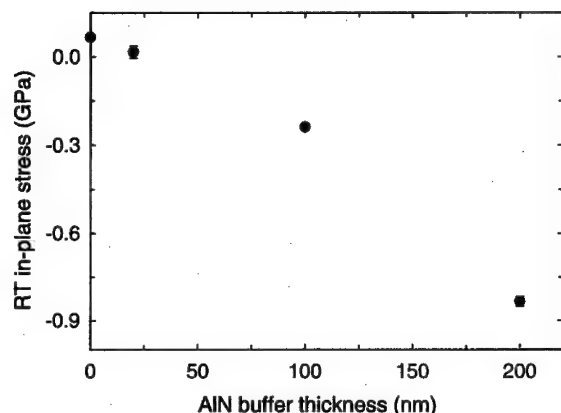


Fig. 1. Volume-averaged room-temperature (RT) stress values in GaN/6H-SiC and in GaN/AlN/6H-SiC structures with different thickness of AlN buffer layer. With the increase of AlN buffer thickness, the compressive stress contribution in GaN increases.

the increase of buffer thickness, compressive in-plane stress in GaN increases as well. In the GaN/6H-SiC structure (without AlN buffer layer), a tensile stress of 66 MPa was observed, while in the GaN/AlN/6H-SiC structure with a 200 nm AlN buffer layer a compressive stress of –833 MPa was found. These data suggest a possibility for stress engineering in GaN thin films on 6H-SiC—by selecting a certain AlN buffer thickness, it should be possible to prepare GaN with a desired in-plane stress, or even eliminate the total stress.

The room-temperature stress values in Fig. 1 represent a superposition of growth (intrinsic) and thermal (extrinsic) stress contributions resulting from the film growth procedure and the cooling down to room temperature, respectively. The elevated-temperature XRD measurements were used to evaluate the magnitude of thermal stresses and estimate intrinsic stresses in the layers. In Fig. 2, the temperature dependance of stresses in the four GaN layers as well as in the 200 nm AlN buffer layer are presented. Though, the values of $\langle \sigma_{11}^{RT} \rangle$ differ significantly (Fig. 1), the slopes of $\langle \sigma_{11}^T \rangle$ versus temperature ($\partial \langle \sigma_{11}^T \rangle / \partial T$) exhibit very similar behavior—the temperature increase causes an increase of the compressive stress contribution in all layers (Fig. 2). In the case of all three GaN films grown on AlN, the slopes

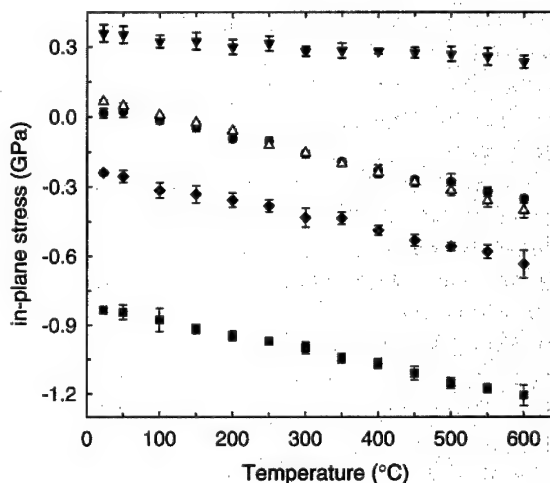


Fig. 2. Temperature dependencies of in-plane stresses: (Δ) GaN layer of a GaN/6H-SiC structure, GaN layers of GaN/AlN/6H-SiC structures with AlN buffer thicknesses of 20 nm (●), 100 nm (◆), and 200 nm (■), and 200 nm thick AlN buffer layer (▼). The results document that the AlN buffer thickness influences significantly the intrinsic (and finally also the total) stresses in GaN layers. The slopes of stress dependencies for GaN layers are –8.9, –6.72, –6.55, –6.6 GPa/°C for structures with 0, 20, 100 and 200 nm thick AlN buffer, respectively.

$\partial \langle \sigma_{11}^T \rangle / \partial T$ are identical within experimental error, while for the GaN thin film grown directly on 6H-SiC, the tensile in-plane stress decreases more rapidly with the temperature. For the 200 nm AlN buffer layer, the slope $\partial \langle \sigma_{11}^T \rangle / \partial T$ is the smallest and the total change of stress in the whole temperature range is only about 125 MPa.

The temperature behavior of stress $\langle \sigma_{11}^T \rangle$ in Fig. 2 can be interpreted by the differences between the in-plane thermal expansion coefficients (TECs) α_a of GaN, AlN and 6H-SiC. Generally, the α_a values predetermine the amount of thermal strain/stress accumulated in the epitaxial layers during the cool down procedure after the deposition process and thus the absolute change of total strain $\Delta \epsilon_{\text{total}}^T$ equals the change in thermal strain $\Delta \epsilon_{\text{thermal}}^T$, which can be expressed by [12]

$$\Delta \epsilon_{\text{total}}^T = \Delta \epsilon_{\text{thermal}}^T = \frac{\int_{RT}^T (\alpha_a^{\text{(substrate)}} - \alpha_a^{\text{(layer)}}) dT}{1 + \int_{RT}^T \alpha_a^{\text{(substrate)}} dT}. \quad (1)$$

The TECs published in the literature are in the order $\alpha_a^{\text{GaN}} > \alpha_a^{\text{AlN}} \cong \alpha_a^{\text{SiC}}$ (with the magnitudes

5.59, 4.15 and $4.2 \cdot 10^{-6} \text{ K}^{-1}$, respectively) [7]. The relatively small decrease of *volume-averaged* stress in the 200 nm AlN buffer layer with the temperature increase (Fig. 2) documents that the thermal strain results from the interaction of AlN with the substrate, while the influence of the GaN layer is negligible and $\alpha_a^{\text{AlN}} > \alpha_a^{\text{SiC}}$ applies. The larger slopes of $\langle \sigma_{11}^T \rangle$ versus temperature ($\partial \langle \sigma_{11}^T \rangle / \partial T$) for GaN thin films grown on 6H-SiC or AlN/6H-SiC (Fig. 2) indicate the larger difference between the TECs of GaN and substrate. Interestingly, the slope $\partial \langle \sigma_{11}^T \rangle / \partial T$ for GaN on 6H-SiC differs slightly from that of GaN on AlN/6H-SiC, which could be interpreted by the influence of the buffer layer on the microstructure of GaN grown there on. Atomic force microscopy images ($1 \times 1 \mu\text{m}^2$ scans) revealed a strongly increased surface roughness of 20 nm for GaN/6H-SiC compared to only 0.3 nm for GaN/AlN/6H-SiC, respectively.

The results in Fig. 2 moreover indicate that the reason for the specific dependance of room-temperature stresses $\langle \sigma_{11}^{\text{RT}} \rangle$ in GaN (Fig. 1) are probably different intrinsic stresses formed in the GaN layers during the growth process. Linear extrapolation of the temperature-dependent stresses $\langle \sigma_{11}^T \rangle$ (Fig. 2) to the growth temperature of GaN (740°C) yields stress values of -0.52 , -0.45 , -0.73 , -1.3 GPa in the GaN layers grown on 6H-SiC with AlN buffer thicknesses of 0, 20, 100 and 200 nm, respectively. When supposing a reversible behavior of thermal stresses in the GaN layers, the extrapolated values can be considered as the magnitudes of intrinsic stresses present in the GaN layers before cooling down after growth. It can therefore be concluded that the compressive intrinsic stress in the GaN layers on 6H-SiC increases with AlN buffer thickness, while cooling after growth modifies the magnitudes of stress according to the TECs mismatch (Eq. (1)). In other words, the thermal stress contribution is independent of the buffer thickness, while the AlN buffer layers of specific thickness influence significantly the intrinsic stress, i.e. the relaxation mechanisms during growth of the GaN layer.

Since there is a strong effect of stress on the energy band gap, the influence of the residual in-plane stress on the shift of the near band gap emission in the GaN layers was identified by

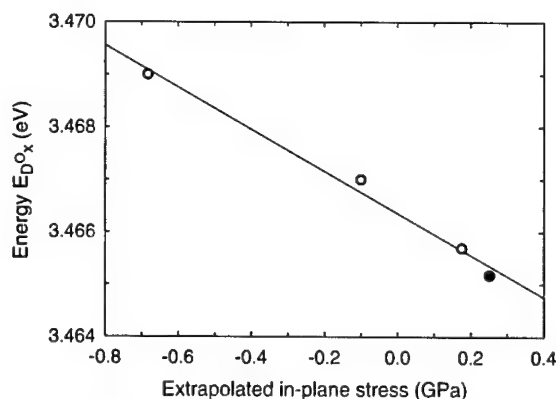


Fig. 3. Bound exciton energy (E_{D^0X}) versus extrapolated in-plane stress at -196°C of GaN layers evaluated from one GaN/6H-SiC (●) and three GaN/AlN/6H-SiC (○) heterostructures.

photoluminescence measurements. By extrapolating the stresses $\langle \sigma_{11}^T \rangle$ from Fig. 2 to -196°C values of 0.25 to -0.7 GPa were obtained. Fig. 3 shows a linear relationship between in-plane stress and near band gap emission, i.e. the energy E_{D^0X} of the exciton bound to a neutral donor. With increasing AlN buffer thickness from 0 to 200 nm, which according to Figs. 1 and 2 is equivalent to a decrease of tensile in-plane stress by 0.848 GPa, a luminescence shift of 3.7 meV to higher energies is observed in this range. This linear relationship can be expressed by

$$E_{D^0X} = 3.4663 \text{ eV} - 0.004 \frac{\text{eV}}{\text{GPa}} \quad (2)$$

and further allows to determine the near band gap emission for completely relaxed GaN. Thus fully relaxed GaN, i.e. in-plane stress equals 0, would imply a bound exciton energy of 3.4663 eV at -196°C , which compares favorably to reported values of 3.462 and 3.465 eV in Refs. [5,15], respectively.

4. Conclusions

Stresses in GaN/6H-SiC(0001) and in GaN/AlN/6H-SiC(0001) structures are characterized in the temperature range of 25 – 600°C using XRD. The results document that the thickness of AlN buffer layers influences significantly the intrinsic

and finally also the room-temperature (total) stress in GaN thin films. Stress in AlN on SiC are tensile and changes only with the temperature since $\alpha_a^{\text{AlN}} \cong \alpha_a^{\text{SiC}}$. While GaN directly grown on SiC is under tensile stress at room temperature, both increasing AlN buffer thickness and measurement temperature result in an increase of the compressive in-plane stress component in GaN.

References

- [1] S.C. Jain, M. Willander, J. Narayan, R. Van Overstraeten, *J. Appl. Phys.* 87 (2000) 965.
- [2] E.V. Etzkom, D.R. Clarke, *J. Appl. Phys.* 89 (2001) 1025.
- [3] W. Rieger, T. Metzger, H. Angerer, R. Dimitrov, O. Ambacher, M. Stutzmann, *Appl. Phys. Lett.* 68 (1996) 970.
- [4] W. Li, W.X. Ni, *Appl. Phys. Lett.* 68 (1996) 2705.
- [5] W.G. Perry, T. Zheleva, M.D. Bremser, D.F. Davis, W. Shan, J.J. Song, *J. Electron. Mater.* 26 (1997) 224.
- [6] P. Waltereit, O. Brandt, A. Trampert, M. Ramsteiner, M. Reiche, M. Qi, K.H. Ploog, *Appl. Phys. Lett.* 74 (1999) 3660.
- [7] T.W. Weeks, M.D. Bremser, K.S. Ailey, E. Carlson, W.G. Perry, R.F. Davis, *Appl. Phys. Lett.* 67 (1995) 401.
- [8] V.Y. Davydov, N.S. Averkiev, I.N. Goncharuk, D.K. Nelson, I.P. Nikitina, A.S. Polkovnikov, A.N. Smirnov, M.A. Jacobson, O.K. Semchinova, *J. Appl. Phys.* 82 (1997) 5097.
- [9] N.V. Edwards, M.D. Bremser, R.F. Davis, A.D. Batchelor, S.D. Yoo, C.F. Karan, D.E. Aspnes, *Appl. Phys. Lett.* 73 (1998) 2808.
- [10] H. Riechert, R. Averbek, A. Graber, M. Schiele, U. Strauß, H. Tews, *Mater. Res. Soc. Symp. Proc.* 449 (1997) 149.
- [11] J. Keckes, J.W. Gerlach, B. Rauschenbach, *J. Crystal Growth* 219 (2000) 1.
- [12] J. Keckes, J.W. Gerlach, R. Averbek, H. Riechert, S. Bader, B. Hahn, H.-J. Lugauer, A. Lell, V. Härle, A. Wenzel, B. Rauschenbach, *Appl. Phys. Lett.* 79 (2001) 4307.
- [13] R.R. Reeber, K. Wang, *MRS Internet J. Nitride Semicond. Res.* 6 (2001) 3.
- [14] K. Wang, R.R. Reeber, *Mater. Res. Soc. Symp. Proc.* 482 (1998) 863.
- [15] K. Pakula, A. Wyszomolek, K.P. Korona, J.M. Baranowski, R. Stepniewski, I. Grzegory, M. Bockowski, J. Jun, S. Krukowski, M. Wroblewski, S. Porowski, *Solid State Commun.* 97 (1996) 919.



ELSEVIER

Available online at www.sciencedirect.com

SCIENCE @ DIRECT®

Journal of Crystal Growth 246 (2002) 78–84

JOURNAL OF
**CRYSTAL
GROWTH**

www.elsevier.com/locate/jcrysgro

Crystal structure and ferroelectricity of nanocrystalline barium titanate thin films

Moo-Chin Wang^{a,*}, Fu-Yuan Hsiao^b, Chi-Shiung Hsi^c, Nan-Chung Wu^b

^a *Department of Mechanical Engineering, National Kaohsiung University of Applied Sciences, 415 Chien-Kung Road, Kaohsiung 80782, Taiwan*

^b *Department of Materials Science and Engineering, National Chen Kung University, 1 Ta-Hsueh Road, Tainan, 70101, Taiwan*

^c *Department of Materials Engineering, I-Show University, 1 Hsueh-Cheng Road, Section 1, Ta-Hsu, Kaohsiung, Taiwan*

Received 20 July 2002; accepted 26 July 2002

Communicated by M. Schieber

Abstract

The nanocrystalline thin films of barium titanate (BaTiO_3) have been deposited on the Pt/Ti/SiO₂/Si substrates by RF magnetron sputtering at 500°C. The XRD result shows only single perovskite structure phase of BaTiO_3 and the intensity of reflection decreases with decreasing film thickness. The film deposited at 500°C has a thickness of 45.0 nm and is composed of granular crystallites of about 30.0 nm in size. The crystallite size decreases with decreasing film thickness. The structure changes from tetragonal to pseudocubic. The remnant polarization (P_r) and coercive field (E_c) of the 45.0 nm thick BaTiO_3 films are $5 \mu\text{C}/\text{cm}^2$ and 1.5 kV/cm, respectively, exhibiting ferroelectricity, being one-eighth and 10 times of the bulk values, respectively.

© 2002 Elsevier Science B.V. All rights reserved.

Keywords: A1. Crystal structure; A3. Polycrystalline deposition; B2. Ferroelectric materials

1. Introduction

Apart from the obvious advantages such as smaller size, lighter weight, and easier integration, ferroelectric thin films offer additional benefits including (1) lower operating voltage, (2) higher speed, and (3) unique sub-microlevel structures. Equally important, however, is the fact that many materials, which are not difficult to fabricate in dense form as a bulk material, are relatively easy to produce as thin films [1]. Ferroelectric films can

display a wide range of dielectric, pyroelectric, piezoelectric, and electro-optical properties [2,3]. The potential utilization of these properties in a new generation of devices has driven intensive studies on the synthesis, characterization, and determination of processing–microstructure–property relationships of ferroelectric thin films in the past several years [3]. For example, the high dielectric permittivities of perovskite-type materials can be advantageously used in ferroelectric non-volatile memory (FeRAM) and dynamic random access memories (DRAMs) [4].

The perovskite-type oxides have emerged as one of the most important classes of oxides both

*Corresponding author. Fax: +886-62502734.

E-mail address: dragon@cc.kuas.edu.tw (M.-C. Wang).

technologically and scientifically since the discovery of high- T_c superconductivity in layered perovskite oxides [5,6]. Among many perovskites, barium titanate (BaTiO_3) is the earliest known perovskite-type ferroelectric and has many applications in electronics [7,8] and electro-optical devices [9,10]. Of concern in the preparation of thin films of BaTiO_3 is the development of elements with high dielectric constant. Moreover, BaTiO_3 thin films of highly perfect crystallinity are also required for fabricating optical devices and integrated microelectronic devices. The ability to achieve these objectives may also have advantages in fabricating artificial multilayer materials [11].

Most of the BaTiO_3 thin films have been fabricated by chemical vapor deposition [12,13], sputtering [14–16], vacuum evaporation [17,18] and laser ablation methods [19,20]. These as-grown films are usually amorphous, or polycrystalline and do not show ferroelectricity. High annealing temperatures ($> 600^\circ\text{C}$) in an oxygen atmosphere are required to exhibit ferroelectricity [17].

In the present paper, the crystal structure and ferroelectricity properties of nanocrystalline ferroelectric BaTiO_3 thin films deposited on the Pt/Ti/ SiO_2 /Si substrates at 500°C by RF magnetron sputtering have been investigated using X-ray diffraction (XRD), scanning electron microscopy (SEM), scanning transmission electron microscopy (STEM), and electron diffraction (ED).

2. Experimental procedure

2.1. Sample preparation

The BaTiO_3 ceramic targets were prepared as follows. Commercial BaTiO_3 (purity 99.0%, supplied by Strem Chem. Co., USA) were weighted and ball milled with acetone and alumina balls for 24 h. The mixture was dried by an IR lamp and subsequently ground and sieved. The powders, through an 80-mesh sieve, were then mixed with 1.0 wt% poly-vinyl acetate (PVA) binder and pressed at 180 MPa to form a disk, 5.08 cm in diameter. Sintering of the samples was conducted with a heating rate of $4^\circ\text{C}/\text{min}$ after the binders

were burned out at 600°C for 30 min. The samples were then heated at a heating rate of $1.0^\circ\text{C}/\text{min}$ to 1300°C , held at 1300°C for 5 h and finally cooled to room temperature at a rate of $3^\circ\text{C}/\text{min}$.

The n -Si (100) wafer was cleaned by a standard process. The substrate size was of $10.0\text{ mm} \times 10.0\text{ mm} \times 0.50\text{ mm}$. A high-quality silicon oxide layer was grown by thermal oxidation to obtain a 600.0 nm thick film. The capacitor structure comprised Pt top and bottom electrodes with an 8.0 nm Ti film layer deposited by RF magnetron sputtering with a Ti target. The 200.0 nm thick Pt bottom electrode was sputter deposited at 400°C . Both metals were sputtered in an Ar atmosphere at a working pressure of 1.0×10^{-2} Torr with an applied power of 150 W. Lastly, the substrate was annealed in N_2 atmosphere at 400°C for 30 min in order to increase the adhesion between layers.

The BaTiO_3 thin films were also deposited on the Pt films by RF magnetron sputtering. The overall deposition conditions for the preparation of the nanocrystalline BaTiO_3 thin films were listed in Table 1. The Pt top electrodes with a thickness of 50.0 nm and diameters of 150.0, 250.0 and 350.0 nm were patterned by a shadow mask process.

2.2. Films characterization

The thickness of the BaTiO_3 thin films was determined using a SEM (Model XL-40 FEG SEM, Philips, the Netherlands) and a Tencor Alpha-Step 500 profilometer. The BaTiO_3 film thickness ranged from 45.0 to 450.0 nm.

The phase identification of the BaTiO_3 thin films with various thickness was examined using X-ray diffraction with a $\text{Cu K}\alpha$ radiation and an Ni filter, operated at 30 kV, 20 mA and scanning rate of $0.25^\circ/\text{min}$ (Model Rad IIA, Rigaku Co., Tokyo, Japan).

The morphology of the surface and cross section of the BaTiO_3 thin films was examined by SEM (Model XL-40 FEG SEM). The foils for STEM (Model JEOL 3013, JEOL Ltd., Tokyo, Japan) were prepared via a conventional technique: the sample was sliced to a thickness of about $30\text{ }\mu\text{m}$ mechanically and ion beam-thinned to electron transparency. Electron diffraction (ED)

Table 1

RF magnetron sputtering conditions for prepared nanocrystal BaTiO₃ thin films

Target diameter (cm)	5.08
Target–substrate distance (cm)	4.0
Background pressure (10 ^{−5} Torr)	2
Working pressure (10 ^{−2} Torr)	1
Sputtering gas	O ₂ + Ar
O ₂ /(O ₂ + Ar)	2/(2 + 8)
RF power (W)	100
Substrate temperature (°C)	500

examinations were also made on carefully thinned foils of the BaTiO₃ thin films, operated at an accelerating voltage of 200 kV.

A polarization–electric field (P–E) hysteresis loop was examined using a modified Sawyer–Tower circuit with a 5 kHz sine wave at 25°C. A mica capacitor of 1 nF was used to detect the stored charge amount.

3. Results and discussion

3.1. Crystal structure of the BaTiO₃ thin films

The XRD patterns of the sintered BaTiO₃ target and 450.0 nm thick BaTiO₃ films deposited on various substrates are shown in Fig. 1. It indicates that the crystallinity of the BaTiO₃ thin films deposited on the Pt-coated Si substrate is better than the Pt-uncoated Si substrate. This result can be caused by the lattice misfits between BaTiO₃ ($a = 0.3994$ nm)/Pt ($a = 0.3923$ nm) and BaTiO₃/SiO₂ ($a = 0.5431$ nm). Since the crystallinity of Pt is better than SiO₂ it upgrades the nucleation and growth of the BaTiO₃ thin films on Pt surface.

Fig. 1 also shows that the crystal structure of the BaTiO₃ target is tetragonal and the perovskite structure of the BaTiO₃ thin films is cubic. Arlt et al. [21] have pointed out that for very dense BaTiO₃ ceramics, at grain size less than 1 μ m, the tetragonal distortion of the BaTiO₃ unit cell decreases at RT to $(c/a - 1) < 1\%$. Moreover, a change from the tetragonal to the pseudocubic structure gradually takes place. In general, the XRD line broadening is a result of the combined effect of crystallite size, nonuniform strain and

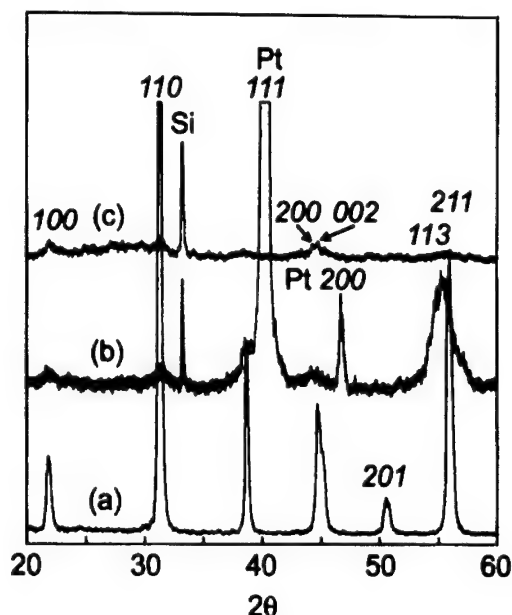


Fig. 1. XRD patterns of the BaTiO₃ sintered ceramic target and 450.0 nm thick BaTiO₃ films deposited on various substrates: (a) BaTiO₃ target, (b) Pt-coated Si substrate and (c) Pt-uncoated Si substrate.

instrumental broadening [22]. Keijser et al. [23] also have pointed out that for every small crystallite, the latter two contributions may be neglected. In the present study, an additional contribution to the XRD line broadening can be expected as a result of shift in lattice constant due to the fact that the BaTiO₃ thin film is composed of crystallites of different sizes.

Furthermore, the full-width at half-maximum (FWHM) of the (110) reflection of the BaTiO₃ films becomes larger than the target. An increase in FWHM is mainly caused by a decrease in grain size, which is calculated from the FWHM and agrees with the crystallite size determined by the STEM image.

Fig. 2 shows the XRD patterns of the BaTiO₃ thin films with various thicknesses deposited on the Pt-coated Si substrates at 500°C. It is found that the intensity of the reflections decreases with decreasing film thickness. This phenomenon is due to the fact that the film is thinner than the signal made with XRD radiation at lower levels, leading to the weak reflection intensity. Kwak et al. [12]

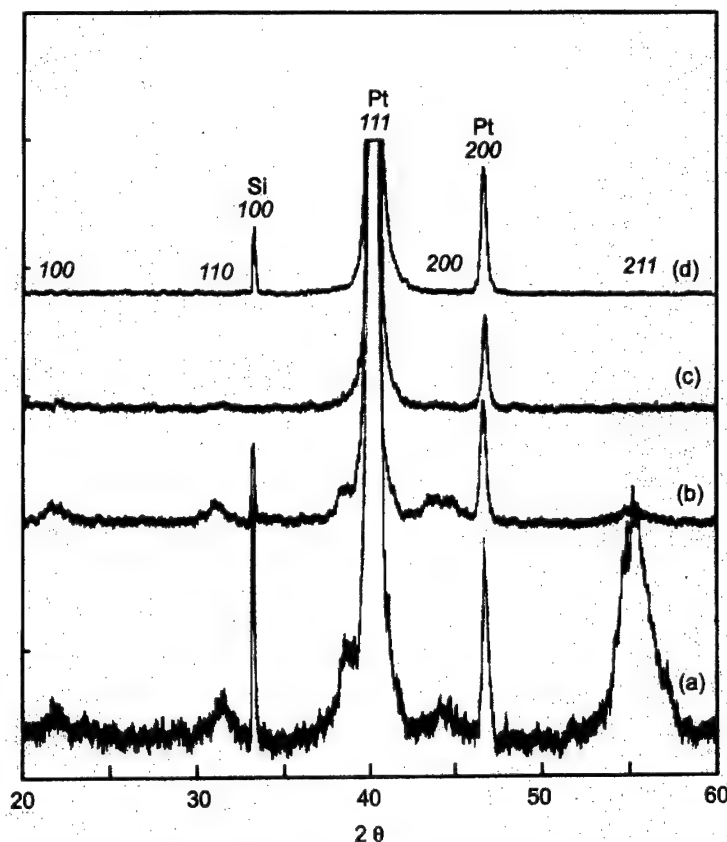


Fig. 2. XRD patterns of various BaTiO_3 films deposited on Pt-coated Si substrates: (a) 450.0 nm, (b) 150.0 nm, (c) 90.0 nm, and (d) 45.0 nm.

also have pointed out that the radial thickness variation depends strongly on the growth parameters, such as deposition time, substrate temperature, working pressure and total flow rate. In the present study, the latter three parameters are fixed. Hence, the variation simply depends on the deposition time. Fig. 2(d) shows an amorphous result, but according to the SEM (Fig. 3(b)), STEM (Fig. 5(a)), and ED pattern (Fig. 5(b)), the 45.0 nm thick crystalline BaTiO_3 films are observed.

3.2. Morphology of the BaTiO_3 thin films

The SEM micrographs of the surface of the BaTiO_3 thin films with various thicknesses are shown in Fig. 3. It indicates that for the film

thickness of 450.0 nm (Fig. 3(a)), the surface is relatively smooth, with grooved grain boundaries. At the film thickness of 45.0 nm (Fig. 3(b)), the surface shows some residual pits. This result can be caused by the following two possible routes. One is the energetic particle bombardment on the growing film that leads to the ejection of previously deposited atoms. Another one is that during nucleation and growth on the substrate the formation of islands grow large enough to touch and coalescence. During the coalescence stage, the islands are inter-connected with remnant channels. After a continuous growth, the channel may shrink to the size of pits, and finally the continuous films are formed [24]. After the atoms have lost their kinetic energies, these pits successively shrink and create a smooth and continuous film.

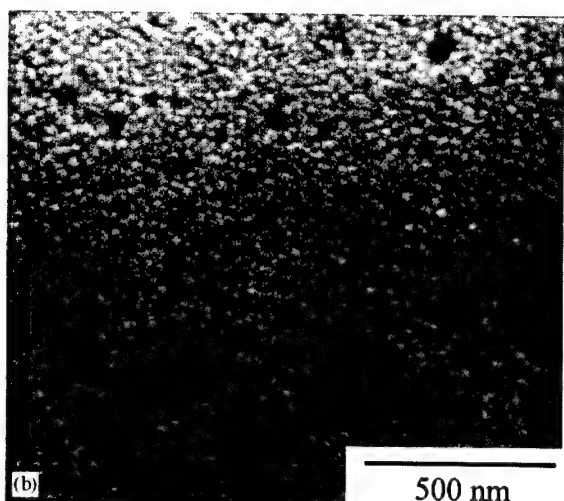
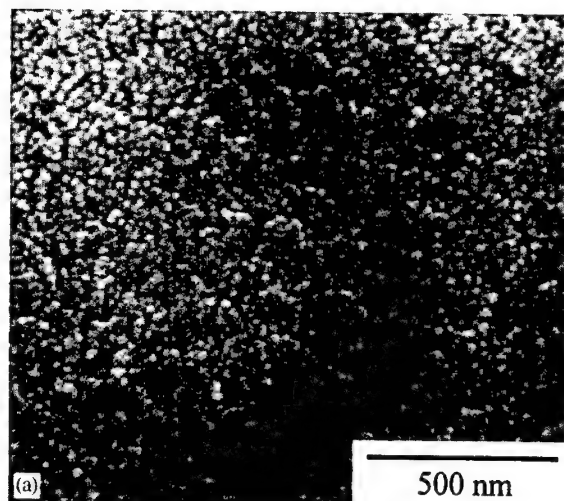


Fig. 3. SEM micrographs of various BaTiO_3 thin films: (a) 450.0 nm and (b) 45.0 nm.

Fig. 3 also indicates that the crystallite size of the BaTiO_3 thin films increases with increasing film thickness. This result is caused by increasing the deposition time and the BaTiO_3 film thickness. In the present study, all BaTiO_3 thin films have been prepared under the same condition except the variation of the deposition time. Hence, increased deposition time creates an effect similar to heat treatment at 500°C and leads to increased BaTiO_3 crystallite size.

The cross sectional SEM micrograph of the 450.0 nm thick BaTiO_3 films is shown in Fig. 4. It is found that the film appears smooth and dense

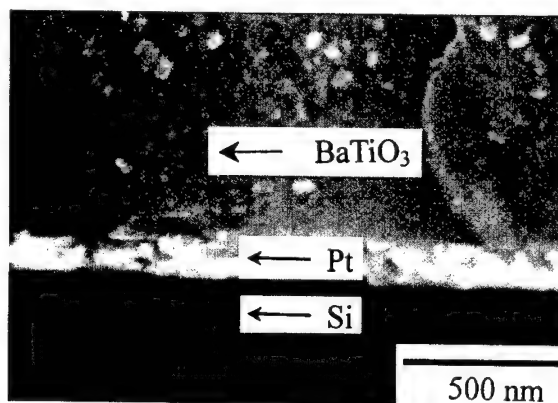


Fig. 4. Cross sectional SEM micrograph of the 450.0 nm thick BaTiO_3 film.

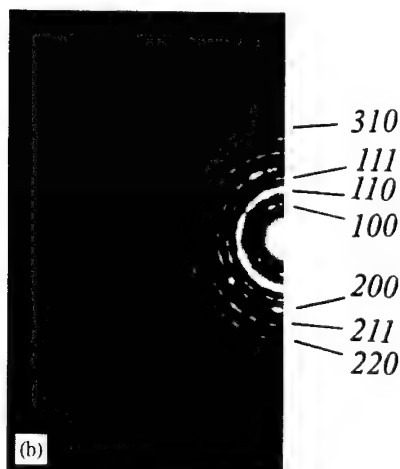
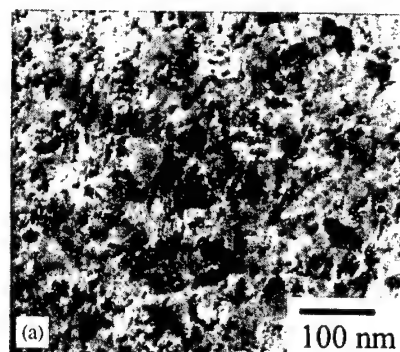


Fig. 5. STEM micrographs of the BF image and ED pattern of the 45.0 nm thick BaTiO_3 films: (a) BF image shows the granular crystallite with a size about 30.0 nm for 45.0 nm thick films, (b) ED pattern of the black granular crystallite in Fig. 5(a).

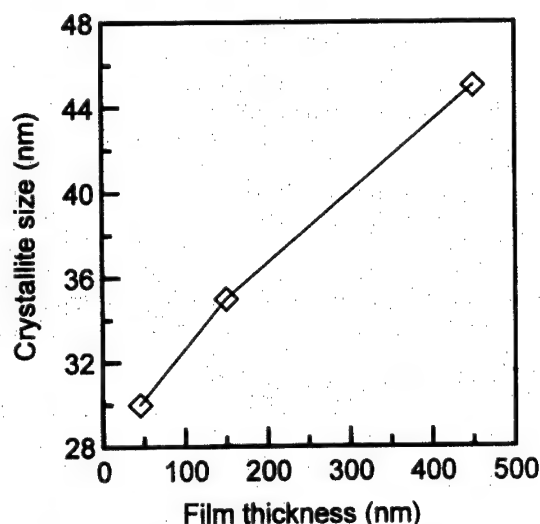


Fig. 6. Thickness vs. nanocrystallite size of the BaTiO₃ thin films deposited at 500°C.

without microcracks. The interlayer adhesion seems very good.

Fig. 5 shows the STEM bright field (BF) micrographs and electron diffraction pattern of the 45.0 nm thick BaTiO₃ films. The BaTiO₃ thin films reveal granular crystallite (Fig. 5(a)), and the crystallite sizes are about 30.0 nm. Figs. 5(b) is the corresponding ED pattern of the black granular crystallite shown in Fig. 5(a), indicating the cubic structure of BaTiO₃.

The thickness dependence of the crystallite size of the BaTiO₃ thin films deposited at 500°C is shown in Fig. 6. It indicates that the relationship between crystallite size and thickness is in a linear mode. This result reveals that at a substrate temperature = 500°C and RF power = 100 W, the nanocrystallite size of the BaTiO₃ thin films still increases with increasing thickness, i.e. deposition time.

3.3. Ferroelectricity of the nanocrystalline BaTiO₃ thin films

The polarization vs. electric field (P–E) hysteresis loop of the BaTiO₃ capacitors is obtained by applying triangular voltage at a frequency of 10 kHz. Figs. 7(a) and (b) are the hysteresis loops of the 150.0 and 450.0 nm thick BaTiO₃ thin films,

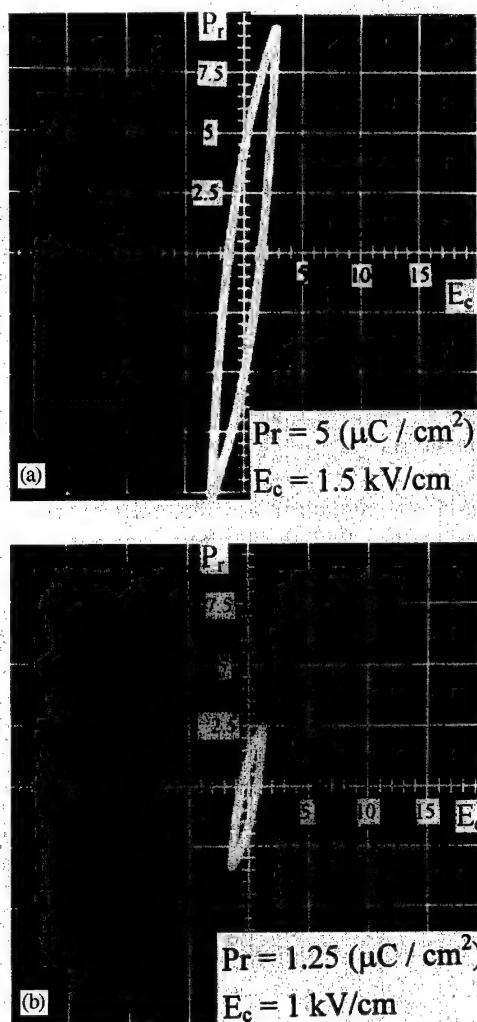


Fig. 7. Polarization vs. electric field (P–E) hysteresis loop of the BaTiO₃ capacitors: (a) film thickness 150.0 nm and (b) film thickness 450.0 nm.

respectively. While the nanocrystalline BaTiO₃ thin films exhibit ferroelectricity, the shape of the hysteresis loops of both films is slim. However, the 450.0 nm thick films exhibit larger remnant polarization ($P_r = 5 \mu\text{C}/\text{cm}^2$) and coercive field ($E_c = 1.5 \text{ kV}/\text{cm}$) than the 150.0 nm thick one ($P_r = 1.25 \mu\text{C}/\text{cm}^2$ and $E_c = 1 \text{ kV}/\text{cm}$), being one-eighth and ten times of the bulk values [25].

Figs. 1 and 5 show that the crystal structure of the nanocrystallines BaTiO₃ thin films is cubic, and the cubic structure of BaTiO₃ must have the

paraelectric phase. In the present study, no paraelectric–ferroelectric transition can be seen [26]. According to the result of Fig. 7, the BaTiO₃ thin films exhibit ferroelectricity. This result indicates that the crystal structure of the nanocrystalline BaTiO₃ thin films is not normal cubic BaTiO₃ but pseudocubic. It is concluded that the structure change of the BaTiO₃ thin films from tetragonal to pseudocubic due to the deposition at 500°C is substantially due to the formation of granular crystallites with size as less than 45.0 nm.

4. Conclusions

The crystal structure and ferroelectricity of the nanocrystalline BaTiO₃ thin films deposited by RF magnetron sputtering have been investigated. The XRD result shows only single perovskite structure in the BaTiO₃ thin films. The 45.0 nm thick film deposited at 500°C is composed of granular crystallites with a size of about 30.0 nm. The nanocrystallite size of the BaTiO₃ thin films increases with increasing thickness. The crystal structure changes from tetragonal to pseudocubic due to the deposition of nanocrystalline BaTiO₃. The 450.0 nm thick films exhibit larger remnant polarization ($P_r = 5 \mu\text{C}/\text{cm}^2$) and coercive field ($E_c = 1.5 \text{ kV}/\text{cm}$) than the 150.0 nm thick one ($P_r = 1.25 \mu\text{C}/\text{cm}^2$ and $E_c = 1 \text{ kV}/\text{cm}$), being one-eighth and ten times of the bulk values.

Acknowledgements

This work was supported by National Science Council, Taiwan, the Republic of China under Contract No. NSC89-2216-E-151-011, which is gratefully acknowledged. Help in experimental works and suggestion from Prof. M.P. Hung, Prof. M.H. Hon, Ms. L.J. Wang and Mr. J.M. Chen are deeply appreciated.

References

- [1] G.H. Haertling, *J. Vac. Sci. Technol.* 9 (1991) 414.
- [2] L.M. Sheppard, *Ceram. Bull.* 71 (1992) 85.
- [3] O. Auciello, A.I. Kingon, S.B. Krupanidhi, *MRS Bull.* 20 (1996) 25.
- [4] M. Suzuki, *J. Ceram. Soc. Jpn. Int. Ed.* 103 (1995) 1088.
- [5] M.A. Beno, L. Soderholm, D.W. Capone II, D.G. Hinks, J.D. Jorgensen, J.D. Grace, I.K. Schuller, C.U. Segre, K. Zhang, *Appl. Phys. Lett.* 51 (1987) 57.
- [6] I.K. Schuller, J.D. Jorgensen, *MRS Bull.* 14 (1989) 27.
- [7] P.J. Harrop, D.S. Campbell, *Thin Solid Films* 2 (1968) 273.
- [8] F.T. Wooten, *Proc. IEEE* 55 (1967) 564.
- [9] N.F. Borelli, M.M. Layton, *IEEE Trans. Electron Devices* ED-16 (1969) 511.
- [10] A.B. Kaufman, *IEEE Trans. Electron Devices* ED-16 (1969) 569.
- [11] K. Iijima, T. Terashima, K. Yamamoto, K. Hirata, Y. Bando, *Appl. Phys. Lett.* 56 (1990) 527.
- [12] B.S. Kwak, K. Zhang, E.P. Boyd, A. Erbil, B.J. Wilkens, *J. Appl. Phys.* 69 (1991) 767.
- [13] H. Nakazawa, H. Yamane, T. Hirai, *Jpn. J. Appl. Phys.* 1 (30) (1991) 2200.
- [14] B.A. Baumet, L.H. Chang, A.T. Matsuda, T.L. Tsai, C.J. Tracy, R.B. Gregoy, P.L. Fejes, N.G. Cave, W. Chen, D.J. Taylor, T. Otsuki, E. Fujii, S. Hayashi, K. Suu, *J. Appl. Phys.* 82 (1997) 2558.
- [15] K. Fujimoto, Y. Kobayashi, K. Kubota, *Thin Solid Films* 169 (1989) 249.
- [16] V.S. Oharmadhikari, W.W. Grannemann, *J. Vac. Sci. Technol. A* 1 (1983) 483.
- [17] Y. Iijima, T. Terashima, K. Yamamoto, K. Hirata, Y. Bando, *Appl. Phys. Lett.* 56 (1990) 527.
- [18] J.R. Slack, J.C. Burfoot, *Thin Solid Films* 6 (1970) 233.
- [19] D. Roy, S.B. Krupanidhi, *Appl. Phys. Lett.* 61 (1992) 2057.
- [20] M.G. Norton, C.B. Carter, *J. Mater. Res.* 5 (1990) 2762.
- [21] G. Arlt, D. Hennings, G. de With, *J. Appl. Phys.* 58 (1985) 1619.
- [22] B.D. Cullity, *Elements of X-ray Diffraction*, Addison-Wesley, Reading, MA, 1978, pp. 284–292.
- [23] M. de Keijser, G.J.M. Dormans, P.J. van Veldhoven, D.M. de Leeuw, *Appl. Phys. Lett.* 59 (1991) 3556.
- [24] B. Chapman, *Glow Discharge Process*, Wiley, New York, 1980, pp. 201–203.
- [25] W.G. Mertz, *Phys. Rev.* 81 (1951) 1064.
- [26] M.C. Wang, F.Y. Hsiao, C.S. Hsi, N.C. Wu, *Jpn. J. Appl. Phys.* (in press).

Preparation of high-quality anthracene crystals using double run selective self-seeding vertical Bridgman technique (DRSSVBT)

A. Arulchakkaravarthi^a, C.K. Lakshmanaperumal^a, P. Santharaghavan^b,
K. Sivaji^c, Rakesh Kumar^d, S. Muralithar^d, P. Ramasamy^{a,*}

^a Crystal Growth Centre, Anna University, Chennai-25, India

^b National Tsing Hua University, Tsing Chu, Taiwan

^c Materials Science Centre, Department of Nuclear Physics, University of Madras, Chennai-25, India

^d Nuclear Science Centre, New Delhi-110 067, India

Received 20 April 2002; accepted 26 July 2002

Communicated by M. Schieber

Abstract

Anthracene crystals were grown by double run selective self-seeding vertical Bridgman technique. The crystal is subjected to FTIR spectral studies, etching studies and double crystal X-ray rocking studies. The crystals grown were tested for their performance as scintillators by a timing resolution setup using ²²Na 511 keV gamma source.

© 2002 Elsevier Science B.V. All rights reserved.

Keywords: A1. Defects; A1. X-ray diffraction; A2. Bridgman technique; A2. Growth from melt; B1. Aromatic compounds; B1. Organic materials; B2. Scintillator materials; B3. Scintillators

1. Introduction

The very early part of material research on organic crystals starts with aromatic hydrocarbons, which have been, though not extensively, used for scintillation counting. The growth of organic crystals starts with synthesis and purification of the starting material. Detailed account on the preparation of aromatic hydrocarbon starting materials, in particular anthracene, has been detailed by many authors [1–3]. The purity

evaluation of the purified materials using different purification methods has also been reported [1]. Such high purification is essential for the preparation of high-quality crystals [4]. Many methods are used in the crystal preparation, such as (i) solution growth, (ii) sublimation technique, (iii) Czochralski technique, and (iv) Bridgman technique. The limitations for the use of solution growth and the yield of small crystals in sublimation technique, undercooled melt technique and Kyropoulos technique have been already reported [5]. The X-ray rocking and X-ray topographic studies of Cz-grown organic monoclinic crystals invariably reveal closely aligned sub-crystals [6]. All the

*Corresponding author. Fax: +91-44-2352774.

E-mail address: pramasamy@annauniv.edu (P. Ramasamy).

above-said difficulties identified by many authors had made us prefer Bridgman growth technique for the growth of anthracene crystals. Apart from the transparency of crystals, there exists structural imperfection and it can be identified using easy, versatile etching technique or by the X-ray topographic technique for organic crystals. But the scintillating crystals can be tested by studying the lifetime of the scintillation output in the particle detection characteristics. Here in this report we had adopted the double run selective self-seeding technique (DRSSVBT) for the growth of anthracene crystals. The grown crystals were characterized by using double crystal X-ray rocking and FTIR studies. Timing resolution studies were done using anthracene crystals and the high quality of the DRSSVBT-grown anthracene crystal is being substantiated.

2. Experimental procedure

2.1. Setup

Several sophisticated setups used for the growth of organic molecular crystals were reported by many authors. Here the authors used a two-zone heating cylindrical oven 65-cm long with a high resistive super kanthal wire. The glass-heating oven is enclosed co-axially by two glass cylinders to prevent heat fluctuation due to ambient temperature variation. The starting material is scintillation grade SRL-make anthracene of 99% purity. The substance was purified by recrystallizing in distilled dimethyl sulphoxide and dimethyl formamide for several times. Finally, the substance was zone refined for several times. The final substance was analyzed using fluorescence and it exhibits good blue fluorescence.

2.2. Double run selective self-seeding vertical Bridgman technique (DRSSVBT)

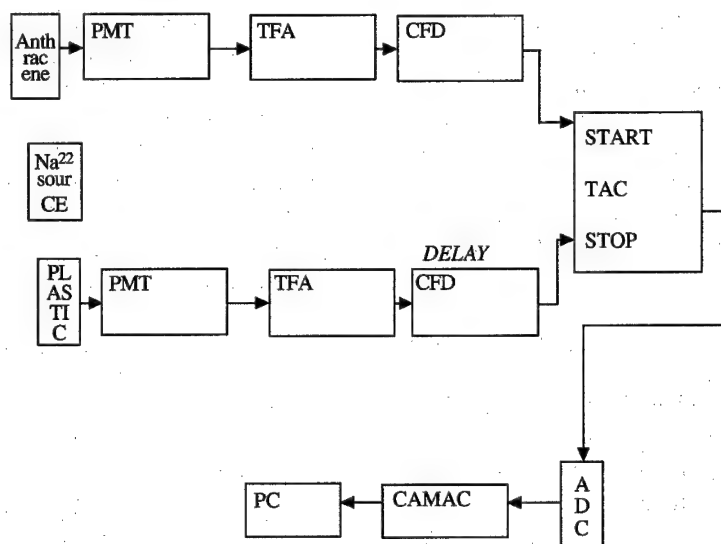
The selective seeding ampoules with different cone angles [10,12] were used for the growth. The cone angle from 15° to 17° suits best for the growth of the anthracene crystal. The entire ampoule was designed in conical shape; this

completely avoids cracks due to the strain exerted by the ampoule contraction. The substance was melted in the upper zone by keeping the temperature of the upper zone of the furnace at 230°C. The gradient is set such that the growth starts from the top of the second zone i.e., 31–33 cm from the top of the furnace and the growth is continued by translating the ampoule downwards. After observing complete growth, the upper zone of the furnace was kept as 190°C, the ampoule was translated upwards to the upper zone and then the temperature of lower zone was kept at 80°C at the middle of the second zone, i.e. 46 cm. Then the ampoule was translated at 0.5 mm/h after leaving for annealing until the ampoule crossed the middle of the second zone. Now the temperature was lowered with steps of 1°C/h up to room temperature. Thus translation was done two times before the final cooling, thus employing “double run” in the selective self-seeding vertical Bridgman technique abbreviated (DRSSVBT).

2.3. Characterization

IR spectra was recorded by using KBr pelleting technique. Etching studies were done by using Leitz Weitzler Optical Microscope. The cleaved crystals were etched using freshly prepared etchant nitric acid, glacial acetic acid, and water for 2 min. The crystals cleaved from the middle of the grown ingot were subjected to X-ray rocking analysis for (002) reflections by using a Rigaku X-ray diffractometer.

The grown crystals were cut and polished using the inner diameter cutter and fine alumina polish. The timing resolution setup was performed by the crystal grown by DRSSVBT by using the setup as shown in Fig. 1. The two anti-collinear 511 keV gamma ray emitting source was used and the two gamma rays produced scintillation light pulse in the scintillators. The start pulse was produced by anthracene crystal and the stop pulse was produced by plastic. The pulses were processed by a timing filter amplifier (TFA) and constant fraction discriminator (CFD) and fed to stop and start the time to amplitude converter (TAC). Detailed account on the time resolution setup was reported by the authors [10].



PMT - Photo Multiplier tube
 TFA - Timing Filter Amplifier
 CFD - Constant Fraction Discriminator
 TAC - Time to Amplitude Converter
 ADC - Analog to Digital Converter
 CAMAC - Computer Automated Measurement And Control

Fig. 1. Timing resolution setup.

3. Results and discussions

The double run Bridgman technique has been adopted for the successful growth of anthracene crystals. The crack-free crystals of more than 12-cm length were produced. The selected cone type ampoule has resulted in crack-free anthracene crystals (Fig. 2) with considerable reduction of striations near the ampoule wall regions.

The crystal shows less etch pits with negligible low angle grain boundaries. FTIR spectral studies were performed using the KBr pelleting technique. The middle of the IR spectrum (Fig. 3) of anthracene provides a characteristic peak due to C–H stretch at 3047 cm^{-1} which is very sharp. The sharpness of the peak illustrates that the hydrogen atoms in the anthracene ring are not exerting any bonding interaction with molecules. The skeletal vibrations of the ring could be assigned to peaks 1615 , 1500 and 1445 cm^{-1} . The presence of four adjacent hydrogen atoms is evidenced by the peak at 719 cm^{-1} . The powder X-ray diffraction studies were done and lattice parameters were calculated.

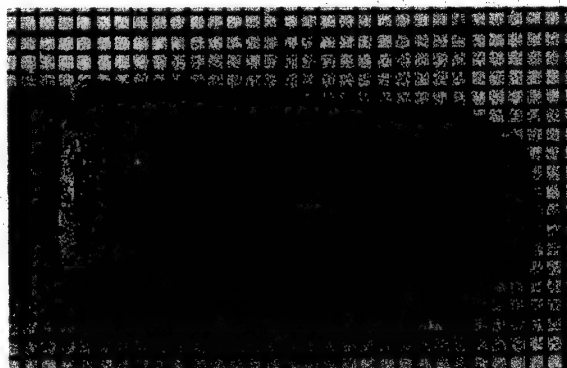


Fig. 2. Photograph of the DRSSVBT-grown anthracene crystal.

The X-ray rocking studies has been done by using a Rigaku X-ray diffractometer with $\text{CuK}\alpha$ radiation. The conventional method and DRSSVBT-grown crystal were cleaved and reflections have been recorded for the (002) plane. The FWHM of the rocking curve recorded using conventional method grown crystal was 46.3 arcsec (Fig. 4). The DRSSVBT-grown crystal shows FWHM of

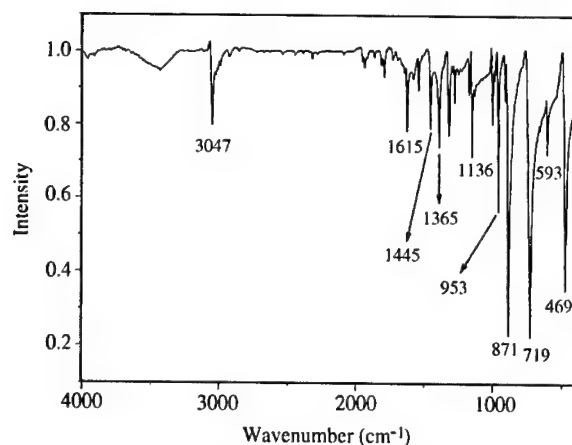


Fig. 3. IR spectrum of anthracene.

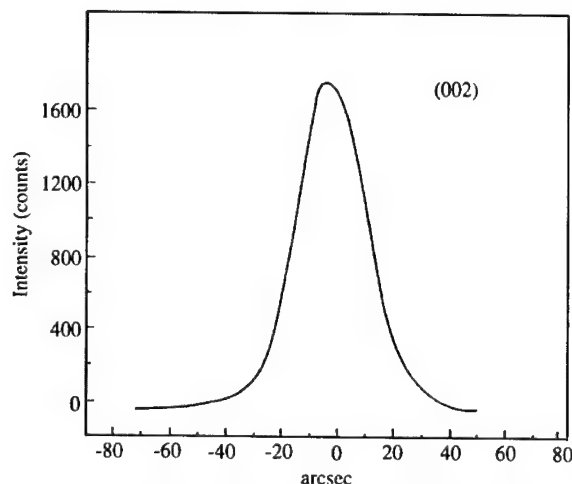


Fig. 4. X-ray rocking curve for the conventional method grown crystal.

29.03 arcsec (Fig. 5). In addition to the main peak, there was a satellite peak in the lower delta theta side with an intensity of $\frac{1}{4}$ of the main peak. The centroid separation between the main peak and satellite peak is about 16 arcsec. This separation may be attributed to the least low angle grain boundaries, which are separated by means of a few arcsec [7]. By Gaussian fitting, it also shows a similar FWHM of about 27 arcsec. This may be due to reduced small-angle grain boundaries and due to the reduced dislocation, planar and stacking fault defects. The migration of these disloca-

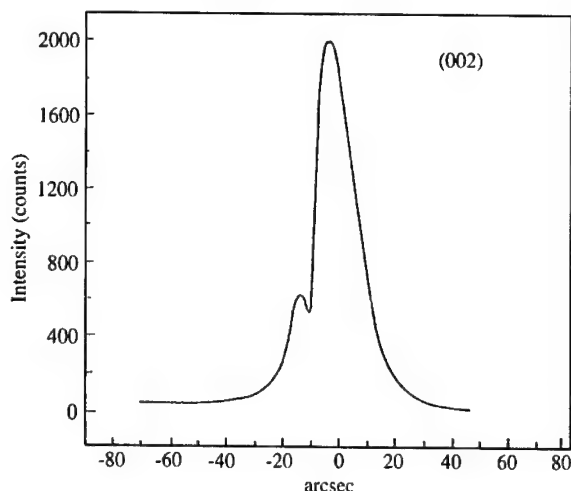


Fig. 5. X-ray rocking curve for the DRSSVBT-grown crystal.

tions is possible during annealing [7] and in DRSSVBT, the second run annealing and slow cooling reduces thermal stresses. The defect characterization done by Uedono et al. [8] has revealed the production of thermal equilibrium defects from 450 to 350 K. This temperature region lies in the cooling region of the grown crystal.

The defect concentration is given by

$$C(T) = \exp(S_F/k_B) \exp(-E_F/k_B), \quad (1)$$

where S_F , E_F , and k_B are the formation entropy, formation energy of the defect and Boltzmann constant, respectively. These defects are thermal equilibrium defects and are of size 0.2 nm^3 which is equivalent to the divalent defect sizes in metals and semiconductors. These defects are due to the thermal agitation of the molecules at high temperatures. Thermal fluctuation is an enhancing factor of such defects. Apart from growth, post-annealing is a must for several hours and then slow translation from 450 to 350 K reduces most of such defects.

It is evident from previous reports that trans-stilbene normally has better timing characteristics than anthracene [9]. However, anthracene crystals grown by DRSSVBT yield a time resolution of 1.3 ns (Fig. 6) which is better than the best time resolution of 2.1 ns of SSVBT-grown trans-stilbene crystal [10]. The calibration was done by

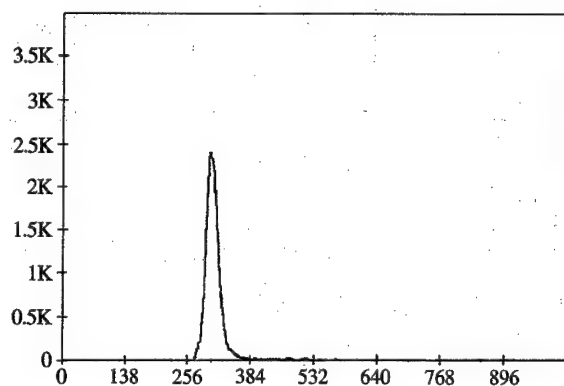


Fig. 6. Timing resolution for ^{22}Na 511 gamma ray.

introducing 20 ns delay for the grown crystal. The time per channel calibration yields 1.468 ns/channel. Timing characteristics are attributed to the intrinsic property of the crystal [11]. The starting part of the curve denotes the anthracene crystal's scintillation light output. The decay time [12] was calculated by taking the starting part of the crystal and was found to be 1.6 ns. The major defects in anthracene crystals slowly cooled from the melt are dislocation free [13]. But the annealing of the whole crystal leads to cracks and heating and cooling takes a long period. High thermal sensitivity and minor thermal shock leading to deep penetrating cracks and high thermal strain make the total crystal annealing very difficult. So part by part annealing leads to crack-free crystals with minimum defects. So the reduction of the thermal defects was created during the cooling of the crystal after growth in the second run of DRSSVBT. Thus, the establishment of the DRSSVBT technique has considerably reduced the thermal defects.

4. Conclusion

DRSSVBT has been proposed and it was established for the growth of anthracene. The quality of the grown crystal was established by time resolution studies. The chemical stability of

the grown crystal was also substantiated by using FTIR and XRD studies. The lattice parameter evaluated by powder diffraction studies was in good agreement with the JCPDS values. The etching studies exhibit rarefied etch pits and there are no low-angle grain boundaries. Quality assessment of crystals grown by DRSSVBT was made using the double crystal X-ray diffractometry and timing resolution studies. The rocking curve of conventional method grown crystals exhibits an FWHM of 46.3 arcsec. For the DRSSVBT-grown crystals, X-ray rocking curve exhibits an FWHM of 29 arcsec. An additional low intense peak in the rocking curve indicates the low defects due to effective control of thermal defects in the DRSSVBT-grown crystal.

References

- [1] B.J. McArdle, J.N. Sherwood, *Chemistry and Industry*, 15th April 1985, p. 268.
- [2] N. Karl, in: H.C. Freyhardt (Ed.), *Crystals: Growth, Properties, Applications*, Vol. 2, Springer, Berlin, 1980, p. 1.
- [3] R.C. Sangster, J.W. Irvine, *J. Chem. Phys.* 24 (1956) 670.
- [4] B.J. McArdle, J.N. Sherwood, *The growing of organic crystals*, in: P.M. Dryburgh, B. Cockyne, K. Barraclough (Eds.), *Advanced Crystal Growth*, Prentice-Hall, Englewood Cliffs, NJ, 1986.
- [5] J.N.S. Herwood, S.J. Thomson, *J. Sci. Instrum.* 37 (1960) 242.
- [6] J. Bleay, R.M. Hooper, R.S. Narang, J.N. Sherwood, *J. Crystal Growth* 43 (1978) 589.
- [7] J.D. Wright, *Molecular Crystals*, Cambridge University Press, UK, Second Edition, 1995.
- [8] A. Uedono, M. Tachibana, M. Shimizu, M. Satoh, K. Kojima, *Jpn. J. Appl. Phys.* 35 (1996) 3623.
- [9] J.B. Birks, *The Theory and Practice of Scintillation Counting*, Pergamon, London, 1964.
- [10] A. Arulchakkaravarthi, P. Jayavel, P. Santhanaraghavan, P. Ramasamy, *J. Crystal Growth* 234 (2002) 159.
- [11] Kai Siegbahn, *Alpha-, Beta- and Gamma-Ray Spectroscopy*, Elsevier North-Holland Publications, Amsterdam, 1965.
- [12] A. Arulchakkaravarthi, P. Santhanaraghavan, R. Kumar, S. Muralithar, P. Ramasamy, *Materials Research Innovations*, in print.
- [13] N. Ide, I. Okada, K. Kojima, *J. Phys.: Condensed Matter* 2 (1990) 5489.



ELSEVIER

Available online at www.sciencedirect.com

SCIENCE @ DIRECT®

Journal of Crystal Growth 246 (2002) 90–98

JOURNAL OF
**CRYSTAL
GROWTH**

www.elsevier.com/locate/jcrysgro

Relationships between DTA and DIL characteristics of nano-sized alumina powders during θ - to α -phase transformation

Fu Su Yen*, Jiun Long Chang, Pei Ching Yu

Department of Resources Engineering, National Cheng Kung University, 1 University Rd, Tainan 70101, Taiwan, ROC

Received 4 January 2002; accepted 26 August 2002

Communicated by C.D. Brandle

Abstract

The dynamic characteristics observed on differential thermal analysis (DTA) and dilatometric (DIL) profiles during θ - to α -phase transformation of nano-sized Al_2O_3 powders were examined using three sets of powder compacts of different θ -sizes and forming pressures. It is found that the time needed for performing the transformation of one θ -crystallite of critical size to one α -nucleus (d_{c0} - to $d_{c\alpha}$ - Al_2O_3) at a heating rate of $10^\circ\text{C}/\text{min}$ is around 1.5 min. The formation reaction does not depend on the θ -crystallite size of the powder system nor does it on the bulk density of the compact. The action of forming primary crystallites, d_p - Al_2O_3 from α -nuclei is brought about in a simple manner if the number of $d_{c\alpha}$ -nuclei is sufficient to form a d_p -crystallite. And if the θ -crystallites reach the critical size of phase transformation, d_{c0} at first deflection point on DIL profiles (T_d) simultaneously, d_p - Al_2O_3 crystallites would have climax of formation at the temperature close to T_p of the exotherm on DTA. In this case, a quasi-homogeneous nucleation-growth mechanism could be obtained. The preliminary estimated temperature of the exothermic peak can be lower than 1015°C . And the temperature interval of exothermic peak can be small than 30°C . The ultimate relationship between DTA/DIL profiles of θ -powder compacts is formulated.

© 2002 Elsevier Science B.V. All rights reserved.

PACS: 61.43.Gt; 64.70.Kb; 65.70.+y

Keywords: A1. Growth models; A1. Phase equilibria; B1. Nano-materials; B1. Oxides

1. Introduction

Techniques of differential thermal analysis (DTA) and dilatometric (DIL) measurements have been extensively employed to investigate the thermal behavior of various materials. For phase transformation of alumina powders, it is especially

important that in determining the transformation temperature DTA techniques are always employed [1–6]. The recent study on examining α - Al_2O_3 crystallite growth during θ - to α -phase transformation of nano-sized alumina powders using DIL measurements [7] is a new attempt that extends the technique to examine phenomena other than thermal shrinkage. Along with investigations on critical and primary crystallite size phenomena during the phase transformation, inferences derived from DIL measurements lead to the

*Corresponding author. Tel.: +886-6-235-5603; fax: +886-6-238-0421.

E-mail address: yfs42041@mail.ncku.edu.tw (F.S. Yen).

conclusion that the primary crystallite of α -Al₂O₃ (d_p -Al₂O₃) [4–7] is a mono-crystallite particle. However, there are no reports of studies related to the thermal behavior between DTA and DIL observations for nano-sized alumina powder systems.

θ - to α -Al₂O₃ phase transformation is considered to be achieved by a nucleation and growth process [4–10]. During the thermal treatment, the θ -Al₂O₃ crystallite grows, exceeding the critical size ($d_{c\theta}$) needed for the formation of α -Al₂O₃ nucleus ($d_{c\alpha}$), and the nucleation of α -Al₂O₃ nuclei takes place [4–6,11,12]. Moreover, the formation of the α -Al₂O₃ nucleus occurs from one θ -Al₂O₃ crystallite to one α -Al₂O₃ nucleus. Continuous heating leads to the growth of α -crystallites to the primary size (d_p) [4–6], and the phase transformation is accomplished. Previous studies [4–6,8–11] have reported that the transformation starts at temperatures around 1000–1150°C (using a heating rate of 10°C/min), or lower [13]. The θ -particles were mono-crystallites with a size determined to be approximately 22 nm (critical size of phase transformation, $d_{c\theta} = \sim 22$ nm, XRD-Scherrer formula [14] on $(20\bar{2})_0$) [1,7,12,13] at the nucleation stage. The primary crystallite size of phase transformation, d_p -Al₂O₃ was in the range of 45–50 nm ($d_p = 40$ –45 nm [15], XRD-Scherrer formula on $(012)_\alpha$), which was formed by the coalescence of the $d_{c\alpha}$ -Al₂O₃ nuclei instead of growth by grain boundary migration [4–6]. At the end of the transformation, the secondary recrystallization of α -Al₂O₃ starts. The α -crystallite coarsens and agglomeration occurs [5,6]. The transmission electronic microscopic examination also revealed [10] that the fast growing α -colonies intermingle with pores surrounded by a θ -matrix. The α -colonies consist of vermicular-shaped particles (or finger growth [11]) separated by large elongated pores. The cross-sectional diameter of the α -Al₂O₃ crystallites ranges from 75 to 100 nm, and they are single-crystalline.

Typical DTA profiles of nano-sized alumina powders during θ - to α -phase transformation are described previously [4–6]. It is an exothermic reaction that is mainly related to the formation of α -nuclei and possibly slightly influenced by the growth to primary crystallites of the α -nuclei [5,6].

The exothermic profile is characterized by temperatures T_n , the lowest temperature at which the initiation of θ - to α -Al₂O₃ phase transformation can be detected by DTA instruments, T_b , the temperature at which the blooming of the large amounts of θ - to α -Al₂O₃ phase transformation starts, T_p , peak temperature for α -Al₂O₃ nucleus formation, and T_e , offset temperature. The profile can be divided into two, lower ($T_n - T_b$) and higher ($T_b - T_p - T_e$) temperature components. The former can extend for a wider temperature range, forming a broad and flat plateau, depending on the existence of heavy agglomerated θ -Al₂O₃ particles in the powder system [15]. The latter is sharp and strong. Powder systems with θ -crystallite of larger sizes and closer to each other will initiate the phase transformation at lower temperatures on DTA profiles [6,15].

Descriptions of typical DIL measurement profiles of Al₂O₃ powder compacts during phase transformation were reported elsewhere [7,16]. The shrinkage behavior with respect to rate of heating is generally opposite to that of common green compacts [7,17]: For θ -Al₂O₃ powder compacts, as the heating rate decreases, the magnitude of shrinkage decreases, instead of increasing as generally experienced by other powder compacts. This is because more amounts and earlier presence of d_p -Al₂O₃ crystallite in the transformation system eventually results in the expansion of the compact system [7]. The densification behavior of alumina compacts was investigated using shrinkage characteristics of the compacts during θ - to α -Al₂O₃ phase transformation [15]. Recent studies on examining the growth characteristics of α -Al₂O₃ crystallite during θ - to α -Al₂O₃ phase transformation employed the DIL profile characteristics as the basis for judging the primary crystallite, d_p -Al₂O₃ as a mono-crystallite particle. Further, the characteristic temperatures observed on the corresponding DTA profiles are also found on the DIL profiles. In general, the compact undergoes three steps of DIL reactions [7]: (1) Fast shrinking step: at the beginning, a fast rate of shrinking that results from a fast growth of a great number of θ -crystallites to the size of $d_{c\theta}$ is observed. The first sign of starting the phase transformation or the nucleation of α -Al₂O₃, T_n

takes place in this step. (2) Slowdown shrinkage step: then it comes to the first point of deflection (here designed as T_d , also refer to Fig. 1d), at which large amount of d_{c0} - Al_2O_3 occurs. The temperature T_d was close to that of T_b on DTA profiles. (3) Stagnant step: the second deflection point (T_{pd}) appears (Fig. 1d). The rate of shrinkage becomes sluggish, because the d_{cx} - Al_2O_3 crystallites keep on occurring and the system now is occupied by the presence of increasing amounts of d_p - Al_2O_3 crystallites. The larger d_p -crystallite shows plate-like shape, resulting in an expansion of the compacts. The temperature T_{pd} was close to T_p temperature on DTA profiles. The shrinkage remains sluggish till point T_c (on DTA profiles) appeared. Then the shrinking of the compact rejuvenated.

In this study, detailed relationships between DTA and DIL measurements experienced by nano-sized alumina powders during θ - to α -phase transformation are examined. Basically, the DTA reveals the formation rate of d_{cx} - Al_2O_3 crystallite during thermal treatments while the DIL measurement discloses the growth rate of crystallites d_{c0} -, d_{cx} -, and d_p - Al_2O_3 during the phase transformation. Thus, it is very much possible to formulate the dynamic phenomena between the crystallites of various sizes. Prior to this study, no reports existed that revealed the time durations needed for the phase transformation. The focus of this paper is to investigate the time duration (temperature difference) needed for the transformation of d_{c0} - to d_{cx} - Al_2O_3 crystallites and for the growth from d_{cx} - to d_p - Al_2O_3 . Three de-agglomerated nano-sized θ - Al_2O_3 powder systems [15] that were pressed into compact with three different uniaxial pressures were investigated. The residual stress resulting from compact fabrication was evaluated by a previous study and found to be negligible [15]. No further examinations were made in this study.

2. Experimental procedures

2.1. Sample preparation

Three θ - Al_2O_3 powders with crystallite sizes of 11.3, 17.7, and 21.8 nm (XRD-Scherrer formula)

designated as samples *S*, *M*, and *L*, respectively, prepared by calcination of boehmite (Remet Chemical Corp. USA) were used as the starting materials. The first yield pressure was derived from uniaxial compaction behavior of the powders measured using a universal testing machine (Micro-computer universal testing machine, Type 8510). Green compacts (1.0 cm in diameter and 0.13–0.17 cm in thickness) of the θ - Al_2O_3 powders were then fabricated using pressures of 245, 500 and 755 MPa, designated as 2, 5, and 7, representing three different pressure conditions. The sample numbers were then labeled as S2, S5, and S7, etc. A total number of 27 compact samples were prepared. All data listed in Tables 1 and 2 are mean values of three samples. The basic physical properties of the starting materials and the prepared compacts are listed in Table 1 [15].

2.2. Characterization

DIL measurements (DIL, Thermische Analyse DIL 420 C) and Differential thermal analysis (DTA, Netzsch STA 409C) up to temperature 1450°C were obtained for these θ - Al_2O_3 compacts by a heating rate of 10°C/min. Measurements for the characteristic temperatures on DTA profiles were derived using commonly used amplified initial temperature [18] that is the intersection of two tangent lines drawing from the profiles. The first and second deflection points of DIL profiles were obtained directly from first differential curves provided by the instrument.

Calculations for relative densities of the powder compacts were obtained using the expression

$$\text{relative density (\%)} = \frac{\text{sample weight (g)}}{\text{sample volume (mL}^3\text{)} \rho_0} \times 100. \quad (1)$$

Here ρ_0 is the specific gravity of θ - Al_2O_3 . The sample volume was obtained by direct measurement using a micrometer.

Table 1
Physical properties of the starting materials

Sample No.	Calcination (°C/h)	Yield pressure ^a (MPa)	Crystalline phase	θ -Al ₂ O ₃ size ^b (nm)		Relative density (%)		
				XRD	BET	Pressure (MPa)		
						245	500	755
S	900/2	190.264	θ (δ)	11.3 (–)	16.2	41.6	49.4	52.9
M	990/2	147.931	θ	17.7	19.2	41.1	48.1	51.9
L	1050/6	156.568	θ (α)	21.8 (51.1)	30.5	43.0	47.9	52.0

^aFirst yield pressure.

^bXRD-Scherrer formula, BET-N₂.

Table 2
Relationships among characteristic temperatures on DTA/DIL profiles (unit: °C)

Sample	S			M			L		
Pressure	2	5	7	2	5	7	2	5	7
Density (%) ^a	41.6	49.4	52.9	41.1	48.1	51.9	43.0	47.9	52.0
T_p	1217	1199	1185	1218	1193	1182	1220	1203	1186
T_{pd}	1204	1189	1175	1213	1193	1182	1220	1203	1186
$T_p - T_{pd}$	13	10	10	5	0	0	0	0	0
T_b	1192	1176	1169	1174	1174	1163	1186	1169	1156
T_d	1197	1182	1170	1203	1182	1168	1205	1188	1170
$T_b - T_d$	–5	–6	–1	–9	–8	–5	–19	–19	–16
$T_p - T_b$	25	23	16	24	19	19	34	34	30
$T_p - T_d$	20	17	15	15	11	14	15	15	14

^aDensity (%) = $\frac{\text{sample weight}}{\text{volume of sample} \times \rho_0} \times 100$.

3. Results and discussion

3.1. DTA and DIL profiles

Figs. 1 and 2 illustrate typical DIL and DTA profiles of the three sets of θ -Al₂O₃ powder compacts prepared in this study. The heating rate was 10°C/min. The two important characteristic temperatures, T_d and T_{pd} on the DIL profile may correspond to the two temperatures, T_b and T_p , respectively, on the DTA profile (also refer to Fig. 1d). However, neither the temperatures of T_d and T_b nor that of T_{pd} and T_p must be identical. Variations of the four temperatures, T_d , T_b , T_{pd} , and T_p are summarized and listed in Table 2.

The characteristic temperatures of both DTA and DIL varied with the θ -crystallite size and the density (relative density) of the compacts. Firstly,

higher densities would result in lower peak (T_p) temperatures. A 10% increase in relative density would reduce $\sim 35^\circ\text{C}$ of T_p , from 1220°C to 1185°C (Table 2). Meanwhile, the temperature T_n which is the lowest temperature at which the initiation of θ - to α -Al₂O₃ phase transformation can be detected by DTA instruments was obscured, because the inter-crystallite distance of the θ -crystallites was highly homogenized by deagglomeration using pressure treatments. And the growth of θ -crystallites to the size d_{c0} in the powder system now became concentrated, occurring at temperature T_d (DIL) [7,15]. Initiating the action of θ -crystallite growth needed a fast shrinkage of the compact. Correspondingly, when most of θ -crystallites in the compact system reached the size of d_{c0} , the shrinkage rate lowered, which resulted in the occurrence of the first

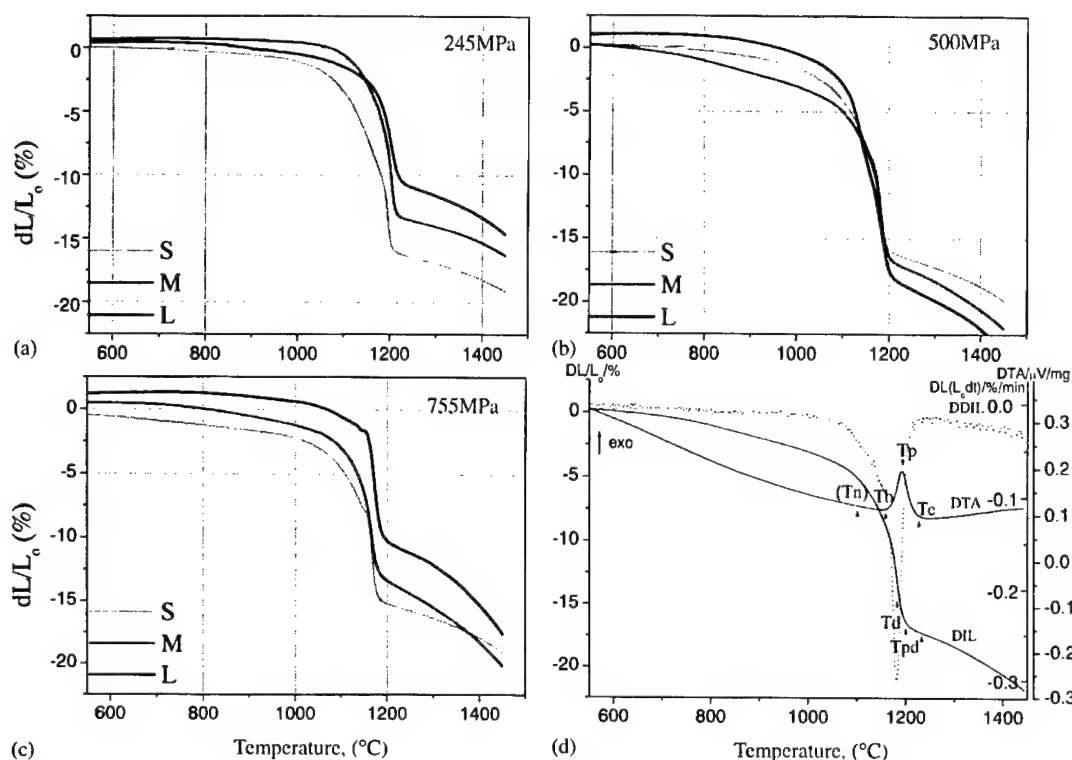


Fig. 1. Typical DIL profile variations of green compacts with varying θ -sizes and forming pressures. The heating rate was $10^\circ\text{C}/\text{min}$. Three θ -powders with mean sizes of 11.3 (S), 17.7 (M), and 21.8 (L) nm and three forming pressures, 245, 500, and 755 MPa were adopted in the examination. Characteristic temperatures on DIL with relation to that on DTA profiles are shown in Fig. 1d.

deflection point, T_d . Thus, it is noted that the T_d must represent the temperature at which the formation of abundant $d_{cx}\text{-Al}_2\text{O}_3$ nuclei of phase transformation is ready to start. Comparing the temperatures of T_d with that of T_b on DTA, or the temperature from which the formation of abundant $d_{cx}\text{-Al}_2\text{O}_3$ nuclei starts, it was found that the temperature T_d (on DIL) of compacts fabricated with finer θ -sized powders and pressed into higher densities would approach the temperature T_b (on DTA). However, in general, powder systems with coarser θ -crystallites that reach d_{c0} size easily would show temperatures T_b lower than that of T_d , indicating that substantial amounts of coarser θ -crystallites in the systems would reach the d_{c0} size faster and transform to $d_{cx}\text{-Al}_2\text{O}_3$ nuclei before the rest but the main part of the θ -crystallites of the systems reach the d_{c0} size. Thus, for systems of coarser θ -crystallites, it is difficult to

obtain a simultaneous growth for the individual θ -crystallites. And, on DTA measurements, the temperature ranges of these exothermic peaks are wider ($T_p - T_b$ in Table 2). Compared to coarser θ -crystallite systems, finer θ -systems shows narrower temperature ranges for the exothermic reaction. Also, an increase in relative density narrowed the peak width. And the T_b appeared at temperatures close to T_d , especially for compacts with higher density, indicating that the formation of $d_{cx}\text{-Al}_2\text{O}_3$ nuclei would mostly start after the θ -crystallites in the compacts reached the size of d_{c0} .

The temperature range T_b to T_p is the period when abundant $d_{cx}\text{-Al}_2\text{O}_3$ occurs. Meanwhile large amounts of $d_p\text{-Al}_2\text{O}_3$ are formed, because the mean α -crystallite size of the powder system remains at the same value of ~ 45 nm ($=d_p$) [4–7]. It should be noted that the climax of $d_{cx}\text{-Al}_2\text{O}_3$ formation appears at temperature T_p . It is

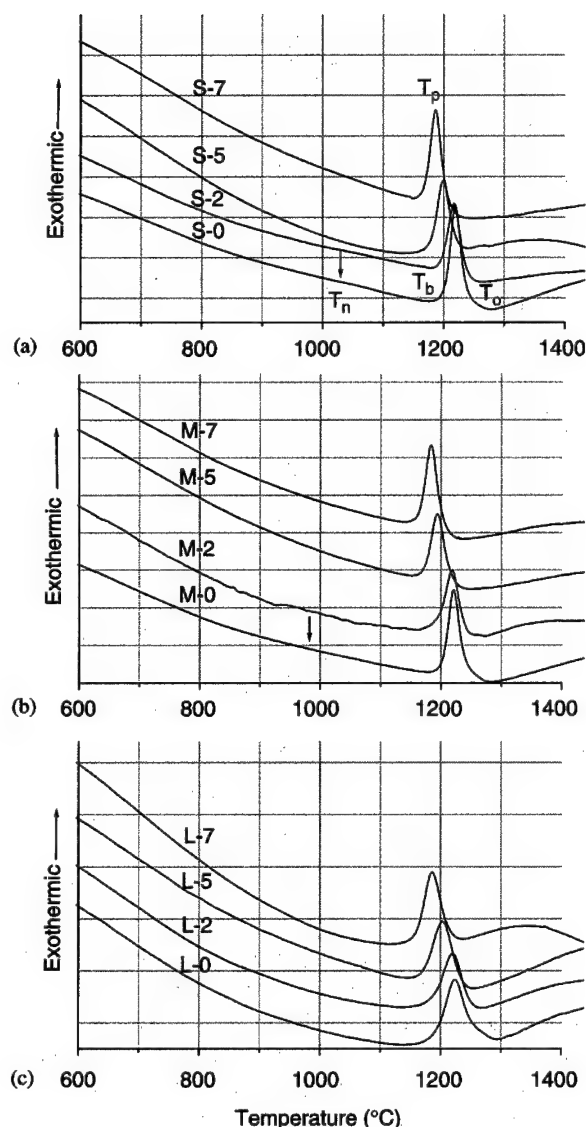


Fig. 2. Typical DTA profile variations of green compacts with varying θ -sizes (S, M, and L) and forming pressures showing reduction in peak temperature as relative density increases. The heating rate was $10^\circ\text{C}/\text{min}$. Compacts used in the measurement were identical with that used in Fig. 1. Forming pressure 2, 5, and 7 denote 245, 500, and 755 MPa, respectively.

possible that most of $d_p\text{-Al}_2\text{O}_3$ occurs at temperature around T_p , because the temperature of second deflection point, T_{pd} observed on DIL profiles, which results from the expansion of the powder system occurs close to T_p . This is observed when

the compact was formed by coarser θ -crystallites (Table 2). It is noted that the T_{pd} of compacts formed by finer θ -crystallites appeared at temperatures lower than T_p , indicating that the formation of $d_p\text{-Al}_2\text{O}_3$ crystallites would start before the formation climax for $d_{cx}\text{-Al}_2\text{O}_3$ [4–6]. It should be noted that, since compacts with lower density means higher porosity of the compact that permits a presence of relatively higher amounts of $d_p\text{-Al}_2\text{O}_3$ crystallites in the compact without resulting in expansion. Thus, compacts that fabricated by finer θ -crystallites and pressed with higher pressure eventually move the T_{pd} to lower temperatures. And the minimum amount of d_p -crystallites needed for inducing expansion of the samples is also smaller.

3.2. T_d vs. T_b and T_p

The appearance of first deflection point T_d reflected that substantial amounts of $d_{c\theta}\text{-Al}_2\text{O}_3$ crystallites were accumulated so that the shrinking momentum induced by θ -crystallite growth was highly diminished. Exceeding this point, θ - to α -phase transformation of the powder system followed, and large amounts of $d_{cx}\text{-Al}_2\text{O}_3$ (α -nuclei) occurred. Thus, when temperature T_d appears, it must imply that the required conditions for phase transformation of θ - to $\alpha\text{-Al}_2\text{O}_3$ (α -nuclei) have been mostly set up. Subsequently, if the transformation is accomplished in a narrow temperature range, the temperature of T_d must not be higher than that of T_b on DTA profiles, the temperature at which large amounts of α -phase formation is ready to start. And the real temperature of large amounts of α -phase formation that results from the $d_{c\theta}\text{-Al}_2\text{O}_3$ crystallites accumulated at T_d (on DIL) is T_p (on DTA).

3.2.1. Transformation of $d_{c\theta}$ - to $d_{cx}\text{-Al}_2\text{O}_3$ started at temperatures lower than T_d

A detailed examination of the temperatures T_d and T_b (Table 2) would reveal that visible amounts of $d_{cx}\text{-Al}_2\text{O}_3$ formation occurred at temperatures lower than T_d . This was especially obvious when the θ -crystallites became coarser. The temperature difference was $>15^\circ\text{C}$. However, the situation

could vary as the size of θ -crystallite varied from coarse to fine. In powder systems with finer θ -sizes, there can be fractions of the crystallites highly agglomerated that may not get eliminated even when high-pressure treatments are used. θ -crystallites in the agglomeration would coarsen to the size of d_{c0} at a faster rate due to the shorter distance in mass transportation, resulting in the earlier formation of d_{cx} - Al_2O_3 (α -nucleus). It is clear that the elimination in agglomeration state of the finer θ -crystallites, for example, using a higher forming pressure, would assist the overlapping of points T_d and T_b . For powder systems with coarser θ -sizes, the overlapping of T_d and T_b can be difficult since part of the crystallites could have reached the size of d_{c0} easily, resulting in the earlier formation of d_{cx} - Al_2O_3 . This means that, for coarser θ -powder systems, it is more difficult to obtain simultaneous phase transformation. The solution might be to prepare coarse θ -powders with identical crystallite as well as particle size. This seems impossible thus if a narrow temperature range of exothermic reaction or a simultaneous phase transformation is required, θ -powders with as small crystallite size as possible are preferred.

3.2.2. Duration required for transformation of one d_{c0} -crystallite to one d_{cx} -crystallite

Comparing the temperatures T_p and T_d , it is clear that there is a constant difference of $\sim 15^\circ\text{C}$ between the two. This is important to the dynamic study, because the difference discloses the temperature difference or time needed for performing d_{c0} - to d_{cx} - Al_2O_3 formation at a heating rate of $10^\circ\text{C}/\text{min}$. It is clear that the formation reaction is dependent on neither the θ -crystallite size of the powder system nor the bulk density of the compact.

3.2.3. Temperature limit of T_d

Increasing the relative density of compact would lower the T_d temperature. However, it is possible that there is a limit for T_d of the θ -powder system. At the moment, it is insufficient data to carry out the limit for T_d in this study. However, if it must be done, the temperature limit could be lower than 1000°C (Fig. 3a).

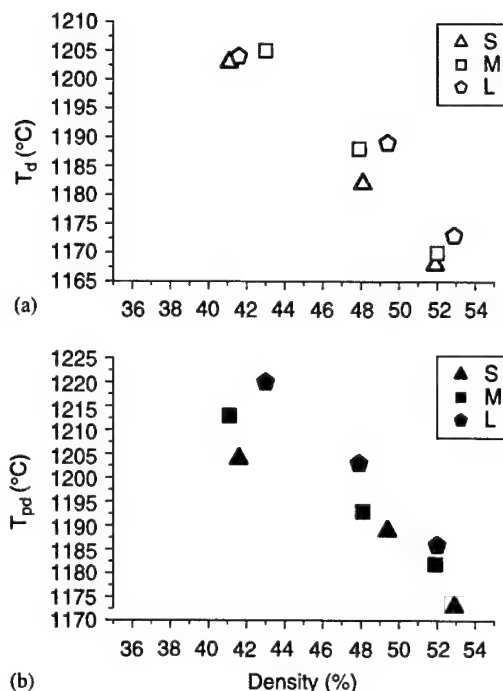


Fig. 3. Temperature reductions of first (T_d) (a) and second (T_{pd}) (b) deflection points on DIL profiles with the increase in relative density of compacts prepared with θ -powders of different sizes.

3.3. T_{pd} vs. T_b and T_p

During θ - to α -phase transformation, the shape of α - Al_2O_3 crystallites evolves from short-rod to flaky during the growth process [5,7]. Once the presence of d_p - Al_2O_3 particles accumulating to an extent that is sufficient to bring a thermal expansion, instead of shrinking to the compact, then the T_{pd} point will occur on DIL profiles [7]. As shown in Table 2, the temperature T_{pd} can be similar to T_p for the coarser θ -size compacts. For compacts with finer θ -crystallite sizes, temperature T_{pd} was lower than T_p [5]. Meanwhile, compacts with similar density (Table 2) would shrink more during thermal treatments if they were formed by finer θ -size powders (θ -crystallite grew to size d_{c0}), it denotes that only a smaller amount of d_p -crystallite formation was required for the compact with higher shrinkage to induce the thermal expansion. However, if samples with varying densities are compared, it would be clear that the

higher the density the lower would be the T_{pd} temperature obtained, indicating that a higher bulk density favors the formation of d_{ca} - Al_2O_3 nucleus and subsequent formation of d_p - Al_2O_3 at lower temperatures. Moreover, if higher pressures were employed, the temperature T_{pd} would come close to T_p for the finer θ -sized powder compacts (Table 2, refer to *S* samples). Thus, it is certain that the action of forming d_p - Al_2O_3 from d_{ca} 's may parallel to the occurrence of d_{ca} - Al_2O_3 nuclei if the number of d_{ca} - Al_2O_3 nuclei is sufficient to form a d_p -crystallite at the temperature range (of ~ 1000 – 1100°C). Thus, the primary crystallite would occur ahead of the starting of abundant amounts of d_{ca} -nucleus formation. Also it is difficult to find d_{ca} -nuclei in the phase transformation system, especially for highly dense compact systems in which θ -crystallites are de-agglomerated. And if the θ -crystallites reach the size d_{c0} at first deflection point on DIL profiles (T_d) simultaneously, d_p - Al_2O_3 crystallites would reach climax of formation at the temperature coinciding with that of exothermic reaction, T_p . Further, because the d_{c0} - Al_2O_3 would transform to d_{ca} - Al_2O_3 nuclei by the following 15°C (using $10^\circ\text{C}/\text{min}$ heating rate) that reached the climax at temperature T_p , the d_p - Al_2O_3 crystallites would reach climax of formation at or slightly after T_p , resulting in the overlap of T_p and T_{pd} . And this is why for samples of θ -powder compacts, especially for those pre-treated with higher pressures [14], it would be difficult to find T_n point on DTA profile.

3.4. Ultimate DTA/DIL profiles

An inference that may be drawn is that the ultimate DTA/DIL profiles of de-agglomerated θ -powder compacts with as small θ -sizes as possible and it is necessary to pressed them into 100% relative density with respect to θ - Al_2O_3 , because it will provide the most basic information of thermal reaction during θ - to α -phase transformation of nano-sized alumina powders. Fig. 3 shows the trends of temperature reductions of the two deflection points, T_d (Fig. 3a) and T_{pd} (Fig. 3b) on DIL profiles for the various compacts prepared by three θ -powders. Clearly, the two temperatures lowered as the relative density increased. Subse-

quently, it is also clear that the T_p temperature on DTA profiles would decrease as the relative density increases. And temperatures T_{pd} would overlap or be after T_p . A preliminary estimation for temperature T_d at a relative density of 100% could be lower than 1000°C . The T_p temperature estimated in a previous study is 1000 – 1050°C [15]. Taking the temperature difference of 15°C for the $T_d - T_p$, then the peak temperature of the exotherm will be lower than 1015°C that is comparable to the temperature previously reported. It should be noted that, in this case, T_b , the beginning of abundant amounts of d_{ca} - Al_2O_3 formation can approach T_p , because the formation of d_{ca} - Al_2O_3 presumably starts simultaneously.

Fig. 4 displays the ultimate DTA/DIL profiles during θ - to α -phase transformation of θ -powder compacts. It should be noted that the compact is pressed into 100% relative density using well-de-agglomerated θ -powders with particle sizes as small as possible. The temperatures of T_d and T_p are around 1000°C and 1015°C , respectively. A duration of <3 min or $<30^\circ\text{C}$ of temperature interval can be achieved for exothermic reaction of phase transformation. It should be noted that the temperature interval (or time interval) dose not release information about the interval needed for

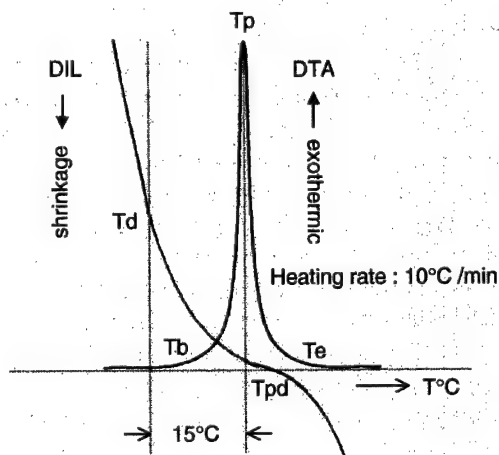


Fig. 4. Schematic representation of the relationships between ultimate DTA and DIL profiles during θ - to α -phase transformation of nano-sized Al_2O_3 powders. Assume that the compact is prepared using θ - Al_2O_3 crystallites of sizes as small as possible and pressed into 100% relative density.

θ - to α -phase transformation but the interval for formation of $d_{c\alpha}$ - Al_2O_3 nuclei of the powder system. And clearly, compacts formed using coarser or agglomerated θ -powders will show a wider duration of exothermic reaction, because part of the θ -crystallites will reach d_{c0} - Al_2O_3 at temperatures before or after 1000°C eventually.

4. Conclusions

This study examined the dynamic characteristics observed on DIL and DTA profiles during θ - to α -phase transformation of three sets of nano-sized Al_2O_3 powder compacts. Comparing temperatures of the exothermic peak, T_p and the first deflection, T_d on DTA and DIL profiles, respectively, it is clear that the time needed for performing one θ -crystallite of critical size transforming to one α -nucleus (d_{c0} - to $d_{c\alpha}$ - Al_2O_3) at a heating rate of 10°C/min is around 1.5 min. The formation reaction does not depend on the θ -crystallite size of the powder system nor does it on the bulk density of the compact.

The action of forming primary crystallites, d_p - Al_2O_3 from α -nuclei is brought about in a simple manner if the number of $d_{c\alpha}$ -nuclei is sufficient to form a d_p -crystallite. And if the θ -crystallites reach the critical size of phase transformation, d_{c0} at first deflection point on DIL profiles (T_d) simultaneously, d_p - Al_2O_3 crystallites would have climax of formation at the temperature close to T_p of the exotherm on DTA. In this case, a quasi-homogeneous nucleation-growth mechanism is obtained. Dealing with the powder system, the preliminary estimated lowest temperature of the exothermic peak can be lower than 1015°C. And since the exotherm reflects mainly the formation of α -nuclei, the duration for the exothermic peak of phase transformation can be <3 min, or temperature interval <30°C, if a heating rate of 10°C/min is employed.

Acknowledgements

The authors wish to express their grateful acknowledgement to professor H.Y. Hsiang of National Cheng Kung University for the valuable discussions. This study was financially supported by the National Science Foundation of ROC under Contract No. 89-2216-E006-092.

References

- [1] L. Pach, R. Roy, S. Komarneni, *J. Mater. Res.* 5 (1990) 278.
- [2] D.S. Tsai, C.C. Hsieh, *J. Am. Ceram. Soc.* 74 (4) (1991) 830.
- [3] R.A. Shelleman, G.L. Messing, *J. Am. Ceram. Soc.* 71 (5) (1988) 317.
- [4] H.L. Wen, Y.Y. Chen, F.S. Yen, C.Y. Huang, *Nano-Struct. Mater.* 11 (1999) 89.
- [5] H.L. Wen, F.S. Yen, *J. Crystal Growth* 208 (2000) 696.
- [6] P.L. Chang, F.S. Yen, K.C. Cheng, H.L. Wen, *Nano-Letters* 1 (5) (2001) 253.
- [7] F.S. Yen, H.L. Wen, Y.C. Hsu, *J. Crystal Growth* 233/4 (2001) 761.
- [8] F.W. Dynys, W. Halloran, *J. Am. Ceram. Soc.* 65 (9) (1982) 442.
- [9] X. Yang, A.C. Pierre, D.R. Uhlmann, *J. Non-Crystalline Solids* 100 (1988) 371.
- [10] W. Dynys, J.W. Halloran, in: L.L. Hench, D.R. Ulrich (Eds.), *Ultrastructure Processing of Ceramics, Glasses and Composites*, Wiley, New York, 1984, p. 84.
- [11] P.A. Badkar, J.E. Bailey, *J. Mater. Sci.* 11 (1976) 1794.
- [12] C. Chou, T.G. Nieh, *Thin Solid Films* 221 (1992) 89.
- [13] H.J. Youn, J.W. Jang, I.T. Kim, K.S. Hong, *J. Colloid Interface Sci.* 211 (1999) 110.
- [14] B.D. Cullity, *Elements of X-ray Diffraction*, 2nd Edition, Addison-Wesley, London, 1978.
- [15] F.S. Yen, M.Y. Wang, J.L. Chang, *J. Crystal Growth* 236 (2002) 197.
- [16] C. Legros, C. Carry, P. Bowen, H. Hofmann, *J. Eur. Ceram. Soc.* 19 (1999) 1967.
- [17] H.K.J. Opfermann, J. Blumm, W.D. Emmerich, *Thermochim. Acta* 318 (1998) 213.
- [18] W. Smykalla-Kloss, *Differential Thermal Analysis, Application and Results in Mineralogy*, Springer, Berlin, 1974.



ELSEVIER

Available online at www.sciencedirect.com

SCIENCE @ DIRECT®

JOURNAL OF
CRYSTAL
GROWTH

Journal of Crystal Growth 246 (2002) 99–107

www.elsevier.com/locate/jcrysgr

Characteristics and crystal structure of the $\text{Ba}(\text{Zr}_x\text{Ti}_{1-x})\text{O}_3$ thin films deposited by RF magnetron sputtering

Moo-Chin Wang^{a,*}, Chung-Yi Chen^b, Chi-Shiung Hsi^c, Nan-Chung Wu^b

^a Department of Mechanical Engineering, National Kaohsiung University of Applied Sciences, 415 Chien-Kung Road, Kaohsiung 80782, Taiwan

^b Department of Materials Science and Engineering, National Cheng Kung University, 1 Ta-Hsueh Road, Tainan 70101, Taiwan

^c Department of Materials Engineering, I-Shou University, 1 Hsueh-Cheng Road, Section 1, Ta-Hsu, Kaohsiung, Taiwan

Received 8 August 2002; accepted 18 August 2002

Communicated by M. Schieber

Abstract

$\text{Ba}(\text{Zr}_x\text{Ti}_{1-x})\text{O}_3$ ($\text{BZ}_x\text{T}_{1-x}$ for short) thin films deposited by RF magnetron sputtering on Pt/Ti/SiO₂/Si substrates were studied. X-ray diffraction, scanning electron microscopy, energy dispersive spectrometry and profilometry were utilized to study the deposition characteristics and crystal structure of the $\text{BZ}_x\text{T}_{1-x}$ thin film. The $\text{BZ}_x\text{T}_{1-x}$ thin film sputtered at RF power = 130 W has a maximum deposition rate. The deposition rate of the $\text{BZ}_x\text{T}_{1-x}$ thin films decreases with increasing working pressure and $\text{O}_2/(\text{O}_2 + \text{Ar})$ ratio. The effects of the $\text{O}_2/(\text{O}_2 + \text{Ar})$ ratio, RF power and working pressure on the Zr/(Zr + Ti) ratio of the $\text{BZ}_x\text{T}_{1-x}$ thin films are not very significant. When sputtered at substrate temperature = 300°C and RF power = 100 W, the $\text{BZ}_x\text{T}_{1-x}$ thin films are amorphous and transforms to the crystalline $\text{BaZr}_x\text{Ti}_{1-x}\text{O}_3$ phase with a (1 0 0) preferred orientation when the RF power increases from 100 to 160 W. The surface of the $\text{BZ}_x\text{T}_{1-x}$ thin films is relatively smooth and dense and has columnar structure.

© 2002 Elsevier Science B.V. All rights reserved.

Keywords: A1. Crystal structure; A3. Polycrystalline deposition; B1. Perovskites; B2. Ferroelectric materials

1. Introduction

Ferroelectric thin films with the perovskite-type (ABO_3) structure have emerged as one of the most important classes of oxides both technologically and scientifically because the discovery of high- T_c superconductivity in layered perovskite oxides [1–3] has attracted much attention for memory applications [4]. A 1 G bit dynamic random access memory (DRAM), which contain 10^9 cells sur-

rounded by peripheral devices, will handle command and voltage levels [5]. All DRAM chips manufactured to date use capacitors containing electrodes made of doped silicon or polysilicon and dielectric films of silicon dioxides and/or silicon nitride. Incorporating a new dielectric, performance and reliability are firmly established [5].

Recently, many kinds of high dielectric constant thin film ferroelectric materials such as BaTiO_3 , SrTiO_3 , $(\text{Ba}_{1-x}\text{Sr}_x)\text{TiO}_3$, $\text{Pb}(\text{Zr,Ti})\text{O}_3$ and $\text{Pb}_{1-x}\text{La}_x(\text{Zr}_{1-y}\text{Ti}_y)_{1-x/4}\text{O}_3$ have been of great interest for an application to cell capacitors of DRAM which require a very high density of stored

*Corresponding author. Fax: +886-62502734.

E-mail address: dragon@cc.kuas.edu.tw (M.-C. Wang).

charge [6–10]. Among these materials, BaTiO₃ film is the most promising capacitor material in future DRAM applications because of the low-leakage current at operating voltage as well as high dielectric constant [11,12]. In the past several years, many studies have been carried out focusing on the deposition techniques and electrical properties of the (Ba_{1-x}Sr_x)TiO₃ (BST) films [7,11,13–15].

In conventional ceramics, zirconia has been shown by Brager [16] and Kulscar [17] to increase the orthorhombic–tetragonal transition temperature in BaTiO₃, while slightly lowering the tetragonal–cubic transition. Verbitskaia et al. [18] have reported that the BaZrO₃ addition to BaTiO₃ has an effect similar to ZrO₂ in that it decreases the axial ratio (*c/a*) of the tetragonal phase, in agreement also with the result by Kell and Hellicar [19]. On the other hand, Armstrong et al. [20] have also pointed out the effects of a small addition of ZrO₂ on the microstructure, dielectric properties and, in particular, the grain boundary structure of BaTiO₃.

Pb(Zr,Ti)O₃ thin films possessing a broad range of chemical composition and ferroelectric properties are applied as pyroelectric, piezoelectric and electro-optic devices [21,22]. Pb(Zr,Ti)O₃ films with a Zr/Ti ratio of 50/50 and of a thickness ranging from 170 to 210 nm, deposited on Pt coated Si substrates by the multi-ion-beam reactive sputtering system at room temperature and at a deposition rate about 1.8 nm/min, have been reported by Krupanidhi et al. [23]. Hu and Krupanidhi [9] have also pointed out that the degree of (100) orientation, remanant polarization, coercive field and dielectric constant of the ferroelectric Pb(Zr,Ti)O₃ thin films are strongly dependent on the ion-beam flux and oxygen ion bombardment energy. Barium lead zirconate titanate [(Ba,Pb)(Zr,Ti)O₃] thin films have been successfully fabricated from a stoichiometric target by RF magnetron sputtering and the dielectric properties of these films have been investigated by Torii et al. [24]. However, studies on deposition characteristics of the Ba(Zr_xTi_{1-x})O₃ thin films prepared by RF magnetron sputtering have not been elaborated.

In the present study, the characteristics and crystal structure of the Ba(Zr_xTi_{1-x})O₃ thin films

deposited on the Pt/Ti/SiO₂/Si substrates by RF magnetron sputtering have been investigated using X-ray diffraction (XRD), scanning electron microscopy (SEM), energy dispersive spectrometry (EDS) and profilometry. The purpose of this study is to investigate the relationships among RF power, working pressure, O₂/(O₂ + Ar) ratio and substrate temperature.

2. Experimental procedure

2.1. Sample preparation

The Ba(Zr_xTi_{1-x})O₃ ceramic targets with various *x* values were prepared. The chemical composition of each target is as listed in Table 1. Commercial BaZrO₃ (purity 99.9%, Johnson Matthey, Inc., West Chester, PA, USA) and BaTiO₃ (purity 99.9%, supplied by Noah Tech. Co., San Antonio, TX, USA) were weighed and ball-milled with acetone and alumina balls for 10 h. The mixture was dried by an infrared lamp and subsequently ground and sieved. The powders through an 80-mesh sieve were then mixed with 1.0 wt% of polyvinyl acetate (PVA) binder and pressed at 180 MPa to form a disk 5.0 cm in diameter. Sintering of the samples was conducted at a heating rate of 4.5°C/min after the binders were burned out at 600 for 30 min. The samples were then heated at a heating rate of 1.5°C/min to 1100°C, held at this temperature for 2 h and finally cooled to room temperature at a rate of 3°C/min.

The *n*-Si(100) wafer was cleaned by a standard process. The substrate size was of 10.0 × 10.0 × 0.5 mm³. A high quality silicon oxide layer was grown by thermal oxidation to obtain a 200.0 nm thick film. The capacitor structure comprised

Table 1
Chemical composition of stoichiometric ceramic targets for the Ba(Zr_xTi_{1-x})O₃ (BZ_xTI_{1-x}) thin films

Starting material	Sample notation and composition (mol%)		
	BZ _{0.1} TI _{0.9}	BZ _{0.2} TI _{0.8}	BZ _{0.3} TI _{0.7}
BaZrO ₃	10	20	30
BaTiO ₃	90	80	70

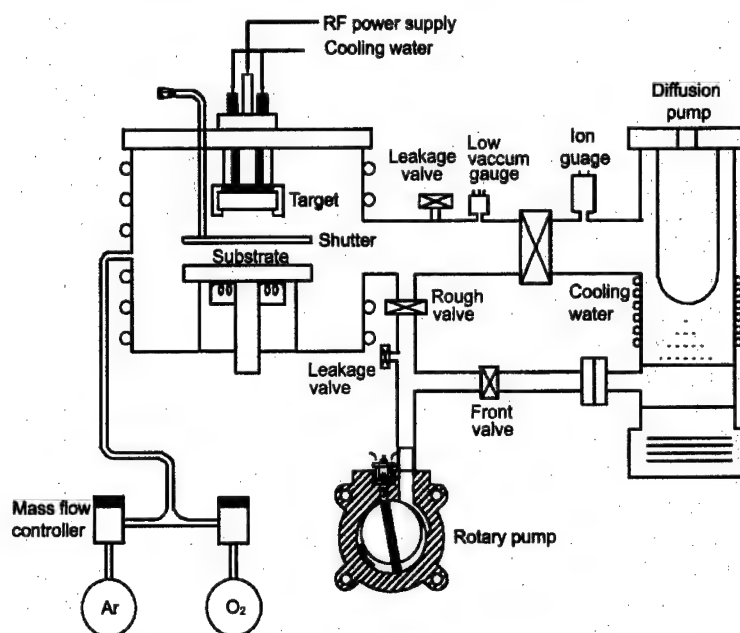


Fig. 1. Schematic diagram of the sputtering apparatus for the preparation of the BZ_xTi_{1-x} thin films.

platinum (Pt) top and bottom electrodes with a 5.0 nm Ti film layer deposited by RF magnetron sputtering with a Ti target. The 500.0 nm thick Pt bottom electrode was sputter deposited at 400°C. Both metals were sputtered in an Ar atmosphere at a working pressure of 1.0×10^{-2} Torr with an applied RF power of 150 W.

The $Ba(Zr_xTi_{1-x})O_3$ (BZ_xTi_{1-x}) thin films with various x values were also deposited on the Pt films by RF magnetron sputtering. The sputtering apparatus is shown schematically in Fig. 1. The overall deposition parameters for the preparation of the BZ_xTi_{1-x} thin films are listed in Table 2. The Pt top electrodes with a thickness of 50.0 nm and diameters of 150.0, 250.0 and 350.0 nm were patterned by a shadow mask process.

2.2. Films characterization

The thickness of the BZ_xTi_{1-x} thin films with various x values was determined by an automatic ellipsometer (Rudolph Research Co.) using an He-Ne laser (wavelength 6328 Å) as a detecting probe as well as a Tentor Alpha-Step 200 profilometer. The BZ_xTi_{1-x} thin films had the composition range

Table 2
Rf magnetron sputtering parameters for the preparation of the $Ba(Zr_xTi_{1-x})O_3$ thin films

Target diameter (cm)	5.0
Target-substrate distance	3.6
Background pressure (10^{-5} Torr)	2
Working pressure (10^{-3} Torr)	5–15
Sputtering gas	Ar or (Ar + O ₂) mixture
RF power (W)	100–160
Substrate temperature (°C)	300–500
Deposition time (min)	60
Film thickness (nm)	500.0

of x varying from 0.1 to 0.3 and the thickness remained around 500.0 nm.

The phase identification of the BZ_xTi_{1-x} thin films samples was examined using XRD with Cu K_α radiation and a Ni filter, operated at 30 kV, 20 mA and a scanning rate of 0.25°/min (Model Rad II A, Rigaku Co., Tokyo, Japan).

The morphology of the cross section and the fracture surface of the BZ_xTi_{1-x} thin films were examined by SEM (Model S-4200, Hitachi Ltd., Tokyo, Japan). The chemical composition was

analyzed with EDS (Model Noran Vantage, USA) employing an internal standard method.

3. Results and discussion

3.1. Effect of sputtering parameters on the deposition rate of the BZ_xT_{1-x} thin film

When the working pressure = 5×10^{-3} Torr, $O_2/(O_2 + Ar)$ ratio = $1/(1+9)$ and substrate temperature = 500°C , the effects of the RF power and Zr content on the deposition rate of the BZ_xT_{1-x} thin films are shown in Fig. 2. It indicates that the deposition rate has the same trend for the three kinds of the BZ_xT_{1-x} thin films. The deposition rate increases with RF power increasing from 100 to 130 W. This phenomenon is caused by the high energy electrons in the plasma, hence increasing the efficiency of gas ionization. On the other hand, the voltage of a plasma sheath decreases with increasing RF power and enhances the sputtering of a target [25]. Hence the higher deposition rate is obtained when the RF power increases.

From Fig. 2, it is also found that the deposition rate of the BZ_xT_{1-x} thin film decreases when the

RF power increases from 130 to 160 W. This phenomenon can be caused by the gas density reduction effect in magnetrons [26,27] and/or resputtering [28]. Hoffman [26] has postulated that the reduction in gas density is a function of magnetron current and an effective deposition rate depends on the relatively energetic species to deposition thickness. Thus, at high discharge currents, when the gas density is lower, the deposition film is subject to higher bombardment rates than at low discharge currents. Rosnagel [27] have reported that the reduction in the local gas density in front of a magnetron cathode is a result of gas heating by the energetic, sputtered atoms emitted from the cathode surface is heated as the sputtered atoms are thermalized or the energy is to kT , where k is the Boltzmann constant [29]. This result leads to decreases in the partial pressure of oxygen and argon near the target, causing the decreased deposition rate.

On the other hand, Kester and Messier [28] have also pointed out that the bombardment of a growing thin film by negative ions can lead to a thickness change in the film through the process of resputtering. The macro effect of resputtering includes a slowing of the film growth rate and, in some cases, a complete suppression of the film growth as well as an etching of the substrate material. Sputtering power is seen to have an important influence on the resputtering but belongs to a class of parameters which affects both deposition and etching in the same way [28].

For RF power = 130 W, $O_2/(O_2 + Ar)$ ratio = $1/(1+9)$ and substrate temperature = 500°C , the relationships among deposition rate, working pressure and Zr content are shown in Fig. 3. It indicates that the deposition rate of each thin film decreases with increasing working pressure. This result is caused by the increased working pressure, which leads to the decreased mean free path of the sputtered particles. Tahar et al. [29] have pointed out that during sputtering, the atoms or molecules of a target are subject to collisions with ambient gas atoms and other sputtered atoms resulting in a partial loss of energy and direction during their transit to the substrate. Hence, the motion of both sputtered atoms and ions is thus impeded by the working pressure. The probability of the sputtered

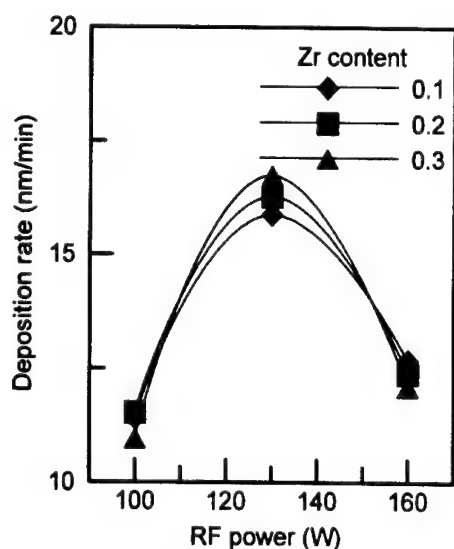


Fig. 2. Effect of RF power and Zr content on the deposition rate of the BZ_xT_{1-x} thin films when deposited at working pressure = 5×10^{-3} Torr, $O_2/(O_2 + Ar)$ ratio = $1/(1+9)$ and substrate temperature = 500°C .

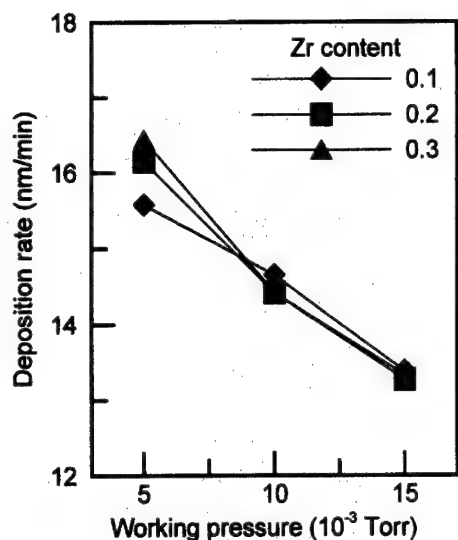


Fig. 3. Relationships among deposition rate, working pressure and Zr content for the deposition at RF power=130 W, $O_2/(O_2 + Ar)$ ratio=1/(1+9) and substrate temperature=500°C.

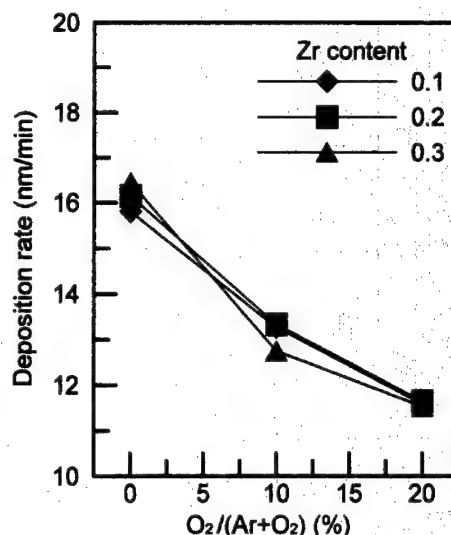


Fig. 4. Effect of the $O_2/(O_2 + Ar)$ ratio and Zr content on the deposition rate of the BZ_xTi_{1-x} thin films when deposited at RF power=130 W, working pressure= 5×10^{-3} Torr and substrate temperature=500°C.

atoms collided with other particles in the plasma decreases when working pressure decreases and the increased mean free path of the sputtered atoms makes those have a sufficient energy to attain to the substrate, resulting in the nucleation and growth of the film [30].

In the sputtering process, pure O_2 and a mixture of O_2 and Ar or N_2 are usually used as a sputtering gas. The use of inert gas ions avoids chemical reaction at the target and substrate. The effects of the $O_2/(O_2 + Ar)$ ratio and Zr content on the deposition rate of the BZ_xTi_{1-x} thin films are shown in Fig. 4 for RF power=130 W, working pressure= 5×10^{-3} Torr and substrate temperature=500°C. It is found that the deposition rate decreases with increasing $O_2/(O_2 + Ar)$ ratio.

Sugiyama et al. [31] have pointed out that the target position effect increases with increasing O_2 partial pressure which reduces the energy of the particles to attain the substrate and their mobility, making it more difficult for the sputtering particles to bombard the substrate and causing the deposition rate to decrease with increasing O_2 partial pressure. On the other hand, at a given RF power the thermalization region shifts toward the target by increasing the O_2 partial pressure [29]. This

result leads to the oxidation of the target [32,33] and possible resputtering of the film [34].

3.2. Effect of sputtering parameters on the chemical composition of the BZ_xTi_{1-x} thin films

Fig. 5 shows the effect of the $O_2/(O_2 + Ar)$ ratio and Zr content on the oxygen atom concentration of the BZ_xTi_{1-x} thin films deposited at RF power=130 W, working pressure= 5×10^{-3} Torr and substrate temperature=500°C. It indicates that the oxygen atom content in the BZ_xTi_{1-x} thin films increases with increasing $O_2/(O_2 + Ar)$ ratio. The effect of the $O_2/(O_2 + Ar)$ ratio on the oxygen atom content of the BZ_xTi_{1-x} thin films is not significant.

The effect of the RF power and Zr content on the $Zr/(Zr + Ti)$ ratio in the BZ_xTi_{1-x} thin films is shown in Fig. 6 for the deposition at work pressure= 5×10^{-3} Torr, $O_2/(O_2 + Ar)$ ratio=1/(1+9) and substrate temperature=500°C. It is found that the $Zr/(Zr + Ti)$ ratio in the BZ_xTi_{1-x} thin films is slightly greater than in the target material. This result is caused by both a higher sputtering yield and a greater sticking coefficient of Zr than Ti.

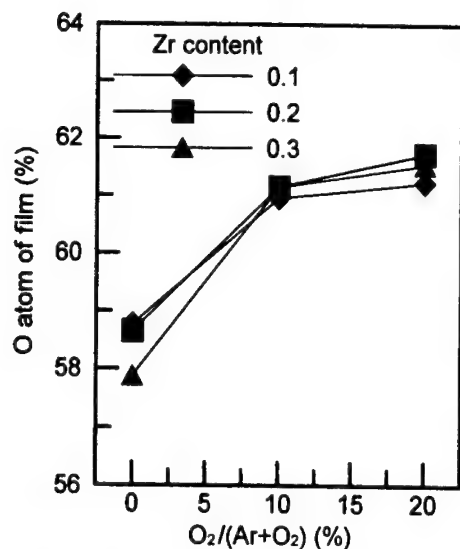


Fig. 5. Effect of the O₂/(O₂ + Ar) ratio and Zr content on the oxygen atom concentration of the BZ_xTi_{1-x} thin films when deposited at RF power = 130 W, working pressure = 5×10^{-3} Torr and substrate temperature = 500°C.

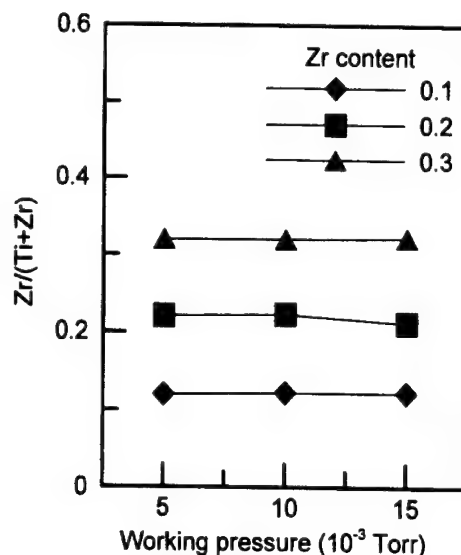


Fig. 7. Relationships among Zr/(Zr + Ti) ratio, working pressure and Zr content for the BZ_xTi_{1-x} thin films when deposited at RF power = 130 W, O₂/(O₂ + Ar) ratio = 1/(1 + 9) and substrate temperature = 500°C.

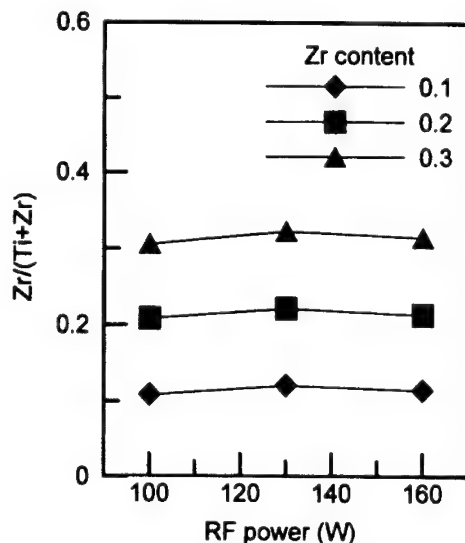


Fig. 6. Effect of the RF power and Zr content on the Zr/(Zr + Ti) ratio of the BZ_xTi_{1-x} thin films when deposited at working pressure = 5×10^{-3} Torr, O₂/(O₂ + Ar) ratio = 1/(1 + 9), substrate temperature = 500°C.

Fig. 7 shows the relationships among the Zr/(Zr + Ti) ratio, working pressure and Zr content when the BZ_xTi_{1-x} thin films are deposited at RF power = 130 W, O₂/(O₂ + Ar) ratio = 1/(1 + 9) and

substrate temperature = 500°C. It also indicates that the Zr/(Zr + Ti) ratio in the BZ_xTi_{1-x} thin films is yet slightly greater than in the target material, i.e. the Zr/(Zr + Ti) ratio in the BZ_xTi_{1-x} thin films is slightly greater than the expected value. Figs. 5 and 6 also show that the effect of the RF power and working pressure on the Zr/(Zr + Ti) ratio of the BZ_xTi_{1-x} thin films is not substantial.

3.3. Effect of sputtering parameters on the crystallographic structure of the BZ_xTi_{1-x} thin film

When working pressure = 5×10^{-3} Torr, O₂/(O₂ + Ar) ratio = 1/(1 + 9) and substrate temperature = 300°C, the XRD patterns of the BZ_xTi_{1-x} thin films sputtered at various RF powers are as shown in Fig. 8. It indicates that the BZ_xTi_{1-x} thin films sputtered at RF power = 100 W are amorphous. This phenomenon is due to the fact that the low kinetic energy of the sputter-ejected species is not sufficient for the arrangement and crystallization of the films when sputtered at a low-substrate temperature and RF power. The crystallinity increases with increasing RF power

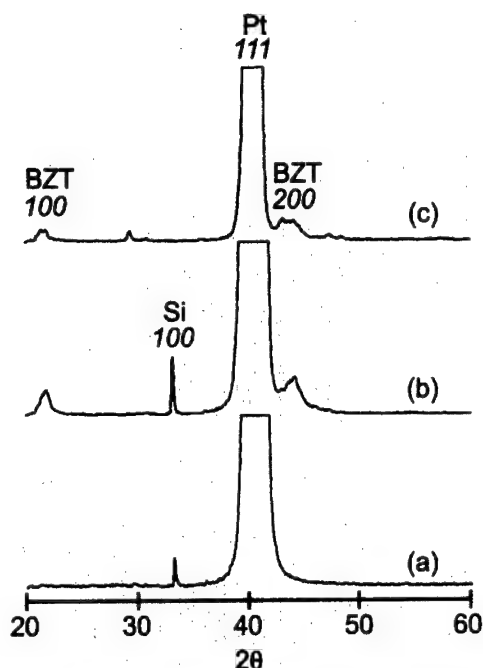


Fig. 8. XRD patterns of the BZ_xTi_{1-x} thin films deposited at various RF powers for working pressure = 5×10^{-3} Torr, $O_2/(O_2 + Ar)$ ratio = 1/(1+9) and substrate temperature = 300°C.

(Fig. 8(b) and (c)). This result is caused by the increased kinetic energy of the sputter-ejected species, leading to the enhanced arrangement and crystallization of atoms on the substrate. In Fig. 8(b) and (c), only the ($h00$) reflection of the $BaZr_xTi_{1-x}O_3$ phase is observed, which indicates that the thin film consists of the single $BaZr_xTi_{1-x}O_3$ phase epitaxially grown on the substrate. On the other hand, from Fig. 8(b) and (c), it is also found that the crystallinity gradually decreases. This result is caused by resputtering when the BZ_xTi_{1-x} thin films are deposited at an RF power = 160 W. This result corresponds to Fig. 2.

When the sputtered parameters are the same as above, the XRD patterns of the BZ_xTi_{1-x} thin films deposited at substrate temperature = 400°C and 500°C are shown in Figs. 9 and 10, respectively. From Figs. 8–10, it is seen that the amorphous BZ_xTi_{1-x} thin film transforms to the crystalline phase when the RF power increases from 100 to 160 W. Figs. 8–10 also show that the BZ_xTi_{1-x} thin films have the (100) preferred

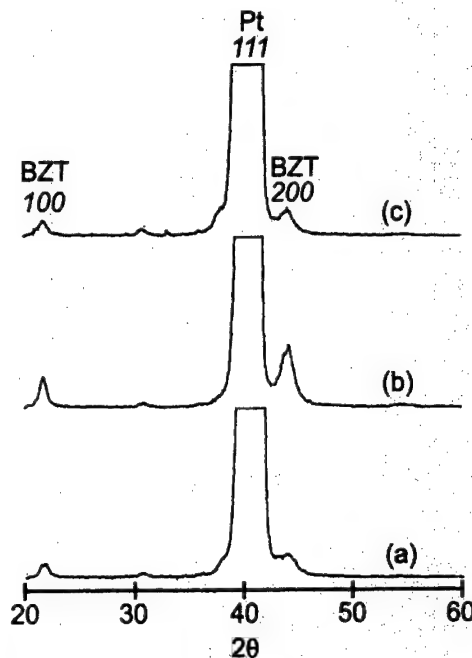


Fig. 9. XRD patterns of the BZ_xTi_{1-x} thin films deposited at various RF powers for working pressure = 5×10^{-3} Torr, $O_2/(O_2 + Ar)$ ratio = 1/(1+9), and substrate temperature = 400°C.

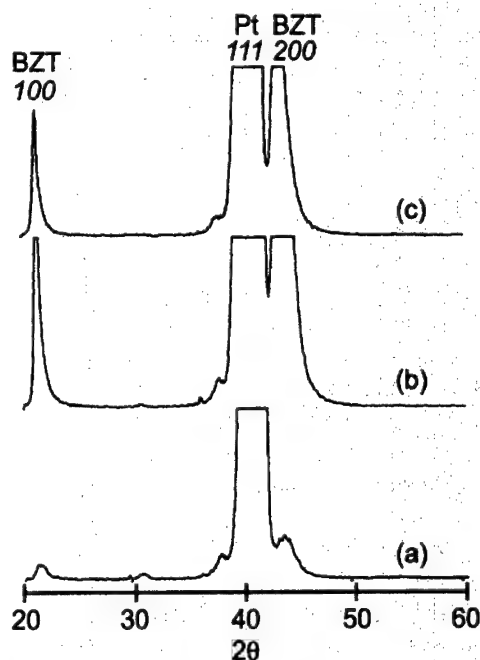


Fig. 10. XRD patterns of the BZ_xTi_{1-x} thin films deposited at various RF powers for working pressure = 5×10^{-3} Torr, $O_2/(O_2 + Ar)$ ratio = 1/(1+9) and substrate temperature = 500°C.

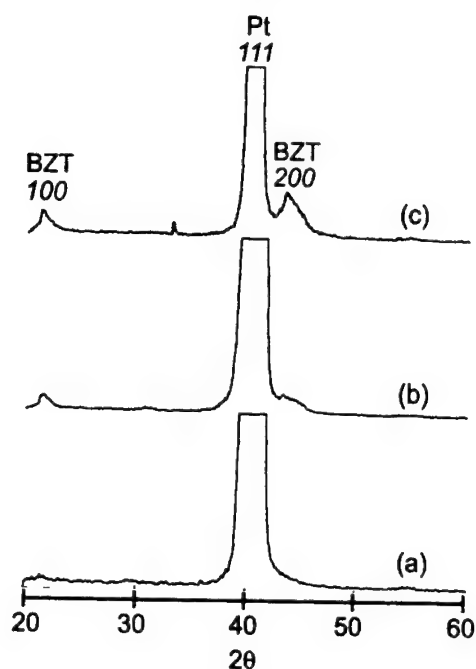


Fig. 11. XRD patterns of the BZ_xTi_{1-x} thin films deposited at various $O_2/(O_2 + Ar)$ ratio, for RF power = 130 W, working pressure = 5.0×10^{-3} Torr, substrate temperature = 300°C.

orientation and the (220) reflection is not masked by the Pt (111) reflection.

The XRD patterns of the BZ_xTi_{1-x} thin films sputtered at various $O_2/(O_2 + Ar)$ ratios are shown in Fig. 11 for RF power = 130 W, working pressure = 5.0×10^{-3} Torr and substrate temperature = 300°C. It is found that the sputtering gas does not contain O_2 and the BZ_xTi_{1-x} thin film is amorphous. The crystallinity of the BZ_xTi_{1-x} thin films increases with increasing $O_2/(O_2 + Ar)$ ratio. During deposition, the oxygen partial pressure plays a crucial role in the growth [29]. Buchanan et al. [35] also have pointed out that the addition of oxygen enhances the crystallization of the thin films regardless of the substrate temperature.

3.4. Microstructure of the BZ_xTi_{1-x} thin films

The SEM micrographs of the BZ_xTi_{1-x} thin films are shown in Fig. 12 when deposited at RF power = 130 W, working pressure = 5×10^{-3} Torr, $O_2/(O_2 + Ar)$ ratio = 1/(1 + 9) and substrate temperature = 500°C. Fig. 12(a) shows the surface

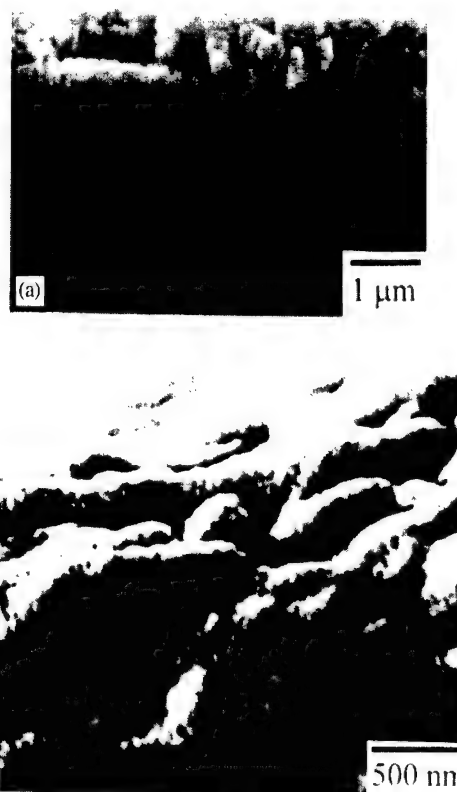


Fig. 12. SEM micrographs of the BZ_xTi_{1-x} thin films when deposited at RF power = 130 W, $O_2/(O_2 + Ar)$ ratio = 1/(1 + 9) and substrate temperature = 500°C: (a) surface morphology, and (b) fracture morphology.

morphology of the BZ_xTi_{1-x} thin films. The surface of the BZ_xTi_{1-x} thin films is relatively smooth and dense. The film exhibits obviously columnar grains. Fig. 12(b) shows the fracture morphology of the interior of the BZ_xTi_{1-x} thin films, also showing the columnar grain structure.

4. Conclusions

The $Ba(Zr_xTi_{1-x})O_3$ (BZ_xTi_{1-x}) thin films deposited by the RF magnetron sputtering on Pt/Ti/SiO₂/Si substrates have been characterized with respect to their deposition parameters. The BZ_xTi_{1-x} thin film sputtered at an RF

power = 130 W has a maximum deposition rate at working pressure = 5×10^{-3} Torr, $O_2/(O_2 + Ar)$ ratio = 1/(1 + 9) and substrate temperature = 500°C. The deposition rate of the BZ_xT_{1-x} thin films decreases with increasing the working pressure and $O_2/(O_2 + Ar)$ ratio. The ratio of the Zr/(Zr + Ti) in the BZ_xT_{1-x} thin films is slightly greater than in the target material. When sputtered at a substrate temperature = 300°C and an RF power = 100 W, the BZ_xT_{1-x} thin films are amorphous and they transform from amorphous to crystalline when the RF power increases from 100 to 160 W. The (200) reflection of the BZ_xT_{1-x} thin films is not masked by the Pt (111) reflection. The surface of the BZ_xT_{1-x} thin films is relatively smooth and dense, consisting of columnar grains.

Acknowledgements

This work was supported by the National Science Council, Taiwan, the Republic of China, under Contract No. NSC89-2216-E-151-004 which is gratefully acknowledged. Help in experimental work and suggestions from Prof. M.P. Hung, Prof. M.H. Hon, Mr. S.Y. Yao and Mr. J.M. Chen are deeply appreciated.

References

- [1] M.A. Beno, L. Soderholm, D.W. Capone II, D.G. Hinks, J.D. Jorgensen, J.D. Grace, I.K. Schuller, C.U. Segre, K. Zhang, *Appl. Phys. Lett.* 51 (1987) 57.
- [2] I.K. Schuller, J.D. Jorgensen, *Mater. Res. Soc. Bull.* 14 (1989) 27.
- [3] B.S. Kwak, K. Zhang, E.P. Boyd, A. Erbil, B.J. Wilkens, *J. Appl. Phys.* 69 (1991) 767.
- [4] K. Torri, *Ferroelectrics* 152 (1994) 157.
- [5] D.E. Kotechi, *Integrated Ferroelectrics* 16 (1997) 1.
- [6] J.T. Evans, R. Womack, *IEEE J. Solid State Circuit SSC-23* (1988) 1171.
- [7] T. Horikawa, N. Mikami, T. Makita, J. Tanimura, M. Kataoka, K. Sato, M. Nunoshita, *Jpn. J. Appl. Phys.* 1 (32) (1993) 4126.
- [8] T.Y. Tseng, *Proceeding of 1996 International Electron Devices and Materials*, 2–5, National Tsing Hua University, Hsinchu, Taiwan, 1996, p. 89.
- [9] H. Hu, S.B. Krupanidhi, *Appl. Phys. Lett.* 61 (1992) 1246.
- [10] M.H. Yeh, K.S. Liu, I.N. Lin, *Thin Solid Films* 258 (1995) 82.
- [11] Y.P. Wang, T.Y. Tseng, *J. Appl. Phys.* 81 (1997) 6762.
- [12] J.H. Joo, Y.C. Jeon, J.M. Seon, K.Y. Oh, J.S. Roh, J.J. Kim, *Jpn. J. Appl. Phys.* 1 (36) (1997) 4382.
- [13] B.A. Baumert, L.H. Chang, A.T. Matsuda, T.L. Tsai, C.J. Tracy, R.B. Gregory, P.L. Fejes, N.G. Cave, W. Chen, D.J. Taylor, T. Otsuki, E. Fujii, S. Hayashi, K. Suu, *J. Appl. Phys.* 82 (1997) 2558.
- [14] Y. Fukuda, H. Haneda, I. Sakaguchi, K. Numata, K. Aoki, A. Nishimura, *Jpn. J. Appl. Phys.* 1 (36) (1997) L1514.
- [15] K. Abe, S. Komatsu, *J. Appl. Phys.* 77 (1995) 6461.
- [16] E.J. Brajer, US Patent No. 2708243, 1955.
- [17] F. Kulscar, US Patent No. 2735024, 1956.
- [18] T.N. Verbitskaia, G.S. Zhdanov, Iu.N. Vennertsev, S.P. Soloviev, *Sov. Phys.-Crytallogr.* 3 (1958) 235.
- [19] R.C. Kell, N.J. Hellicar, *Acustica* 6 (1956) 235.
- [20] T.R. Armstrong, L.E. Margens, A.K. Maurice, R.C. Buchanan, *J. Am. Ceram. Soc.* 72 (1989) 605.
- [21] G.H. Haertling, *Ferroelectrics* 75 (1987) 25.
- [22] L.M. Scheppard, *Ceram. Bull.* 71 (1992) 85.
- [23] S.B. Krupanidhi, H. Hu, V. Kumar, *J. Appl. Phys.* 71 (1992) 376.
- [24] K. Torii, T. Kaga, E. Takeda, *Jpn. J. Appl. Phys.* 1 (31) (1992) 2989.
- [25] B. Grycy, B. Gross, E. Miklossy, *Non-Equilibrium Processes in Plasma Technology*, Elsevier Science Publishers B.V., Amsterdam, 1969, p. 354.
- [26] D.W. Hoffman, *Thin Solid Films* 107 (1983) 353.
- [27] S.M. Rossnagel, *J. Vac. Sci. Technol. A* 6 (1988) 19.
- [28] D.J. Kester, R. Messier, *J. Mater. Res.* 8 (1993) 1928.
- [29] R.B.H. Tahar, T. Ban, Y. Ohya, Y. Takahashi, *J. Appl. Phys.* 83 (1998) 2631.
- [30] H.C. Lee, J.Y. Lee, *J. Mater. Electron.* 5 (1994) 221.
- [31] K. Sugiyama, K. Taniguchi, K. Kuwabara, *J. Mater. Sci. Lett.* 9 (1990) 489.
- [32] E. Leja, A. Kolodiez, T. Pisarkiewicz, T. Stapinski, *Thin Solid Films* 76 (1981) 283.
- [33] M. Buchanan, J.B. Webb, D.F. Williams, *Thin Solid Films* 80 (1981) 373.
- [34] M. Mehra, H. Rhodes, *Mater. Res. Soc. Symp. Proc.* 70 (1986) 569.
- [35] M. Buchanan, J.B. Webb, D.F. Williams, *Appl. Phys. Lett.* 37 (1980) 213.

Directional CdS nanowires fabricated by chemical bath deposition

Hui Zhang, Xiangyang Ma, Jin Xu, Junjie Niu, Jian Sha, Deren Yang*

State Key Lab of Silicon Materials, Zhejiang University, 310027 Hangzhou, People's Republic of China

Received 15 March 2002; accepted 14 September 2002

Communicated by L.F. Schneemeyer

Abstract

Directional CdS nanowires have been fabricated by using chemical bath deposition (CBD) and porous anodic aluminum oxide (AAO) template. X-ray diffraction and selected area electron diffraction show that the nanowires are hexagonal polycrystalline in nature. Transmission electron microscopy (TEM) reveals that the diameters of nanowires are about 60 nm. Furthermore, the high-resolution TEM illustrates the lattice images of {002}, {101} and {100} planes in the nanowires. The directional growth of nanowires is verified by scanning electron microscopy. It is believed that the ion-by-ion mechanism dictates the CBD of CdS nanowires within the pores of AAO template.

© 2002 Elsevier Science B.V. All rights reserved.

PACS: 81.05.Dz; 81.05.Ys

Keywords: B1. Nanomaterials; B2. Semiconducting II–VI materials

1. Introduction

One-dimensional nanostructural materials have attracted much attention over the years due to their fundamental importance and potential applications in the nanodevices [1–8]. It is well known that CdS is a typical wide band gap II–VI semiconductor having a band gap 2.42 eV at room temperature. It has many commercial or potential applications in light-emitting diodes, solar cells, or other photoelectric devices. Recently, CdS nanowires have been fabricated by the electrodeposition

and the chemical solution transport (CST) methods [9–16]. In this paper, we have synthesized hexagonal polycrystalline CdS nanowires using an alternative method, i.e. CBD on porous anodic aluminum oxide (AAO) template. The basic idea behind this method is, on one hand, to make use of the nanosized pores in AAO for the confinement of growth of nanowires across the diameter, on the other hand, to take advantage of the orderly pores in the AAO template for the directional growth of CdS nanowires along the length. Compared with electrodeposition and CST, CBD has the advantages of simplicity, high efficiency and low cost, moreover, CBD is a well proved process for the preparation of CdS films [17–23].

*Corresponding author. Tel.: +86-571-8795-1667; fax: +86-571-8795-2322.

E-mail address: mseyang@ dial.zju.edu.cn (D. Yang).

2. Experiment

A pure Al plate (99.99%) was annealed at 500°C for 2 h in vacuum to form texture, then degreased in acetone. Subsequently, it was anodized at 16°C in oxalic acid solution at a constant voltage of 42 V for 3 h. As a result an anodic oxide layer was formed. The top part of this layer was disorderly, which was removed in a mixture of phosphoric acid and chromic acid. After this removal, the textured Al plate was anodized again for 10 h under the conditions identical to those for the first anodizing step. Then the backside Al layer of the specimen was removed in a saturated CuCl_2 solution. The bottom part of the membrane was removed by exposure to phosphoric acid at 30°C for 90 min, finally, the anodized aluminum oxide (AAO) in porous structure was formed and dried at 30°C. Because the diameters of pores (channels) of AAO lie in several tens of nanometers range.

CdS nanowires were deposited into the AAO template by reacting 0.02 M CdCl_2 , 0.05 M $(\text{NH}_2)_2\text{CS}$ and 0.05 M NH_4Cl in an aqueous solution using $\text{NH}_3 \cdot \text{H}_2\text{O}$ as a complexing agent. The pH of the solution was adjusted to 11 using $\text{NH}_3 \cdot \text{H}_2\text{O}$ and the bath temperature was 80°C. The chemical deposition lasted for 20 min, then the sample was achieved and washed with deionized water. After drying in a 60°C oven, the sample was annealed at 300°C for 1 h under N_2 atmosphere.

The phase of CdS nanowires incorporated into the AAO templates was characterized by powder X-ray diffraction (XRD), with Cu $\text{K}\alpha$ radiation. Transmission electron microscopy (TEM) with energy dispersive X-ray (EDAX) was applied to determine the morphology and composition. To obtain the specimen for TEM observation, AAO template was dissolved in 1 M NaOH at 60°C for 1 h with ultrasonic vibration, thus the CdS nanowires were dispersed uniformly in the solution. Then, a small drop of the solution was dipped on a Cu grid covered with carbon film. The directional growth of CdS nanowires was checked by scanning electron microscope (SEM).

3. Results and discussion

Fig. 1 shows the XRD spectrum for the CdS nanowires incorporated into the AAO template. As marked in the figure, the spectrum consists of two sets of peaks. According to the standard JCPDS cards, one set corresponds to the hexagonal structure with a nominal composition of CdS, and the other to $\gamma\text{-Al}_2\text{O}_3$.

Fig. 2 shows the typical TEM image of the CdS nanowires. It can be seen that this nanowire has a relatively straight morphology and a diameter of about 60 nm, which corresponds to the diameter of the pores within the template used. The lower left

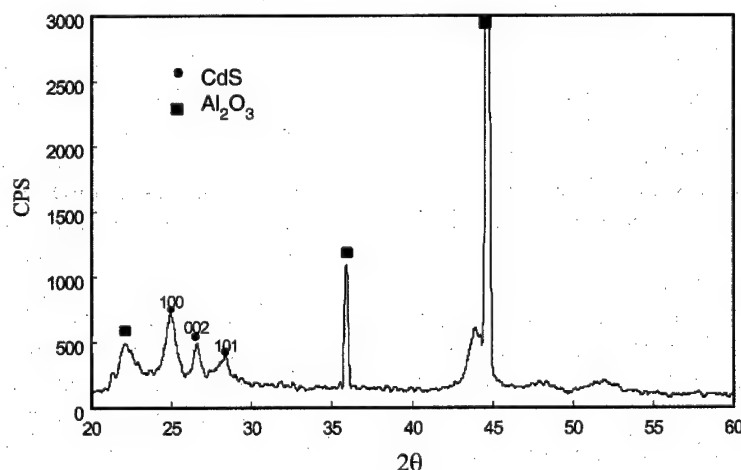


Fig. 1. XRD pattern of the CdS nanowires incorporated into AAO template.

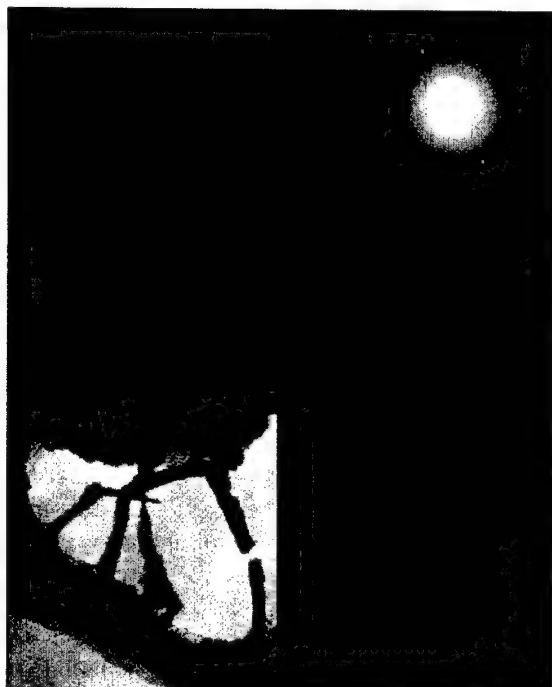


Fig. 2. TEM image of a typical CdS nanowire. The upper right inset is the corresponding SAED pattern; the lower left inset is an image of multi-CdS nanowires.

inset in Fig. 2 is an image of the multi CdS nanowires with diameter nearly the same as the single CdS nanowire. The upper right inset in Fig. 2 gives a selected area electron diffraction (SAED) pattern. In this pattern, the first and second diffraction spots correspond to the $\{002\}$ and $\{004\}$ planes with an interplanar spacing of about 3.34 and 1.62 Å, respectively, while the first and second diffraction circles correspond to the $\{110\}$ and $\{203\}$ planes with an interplanar spacing of about 2.13 and 1.33 Å, respectively. The above result indicates that the CdS nanowires are hexagonal polycrystalline in nature.

The EDAX spectrum of the CdS nanowire is shown in Fig. 3. The very strong peaks for Cd and S are found in the spectrum. Quantitative analysis shows that the CdS nanowires are deficient in S in terms of composition, probably due to the volatility of S. The O peak may be originated from the oxidation of CdS nanowires exposed to the air. The C and Cu peaks come from the copper grid used to support the CdS nanowires.

Fig. 4 shows the high-resolution transmission electron microscopy (HRTEM) images of the middle and fringe parts in a single CdS nanowire.

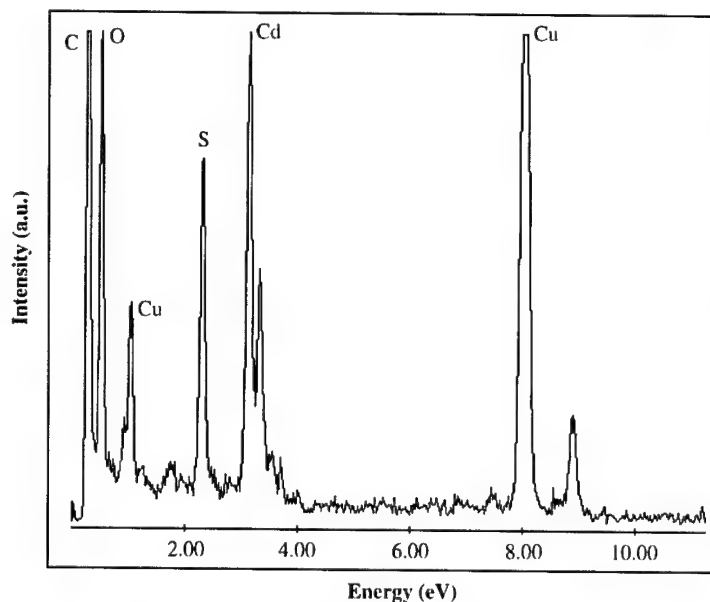


Fig. 3. The EDAX spectrum of a single CdS nanowire.

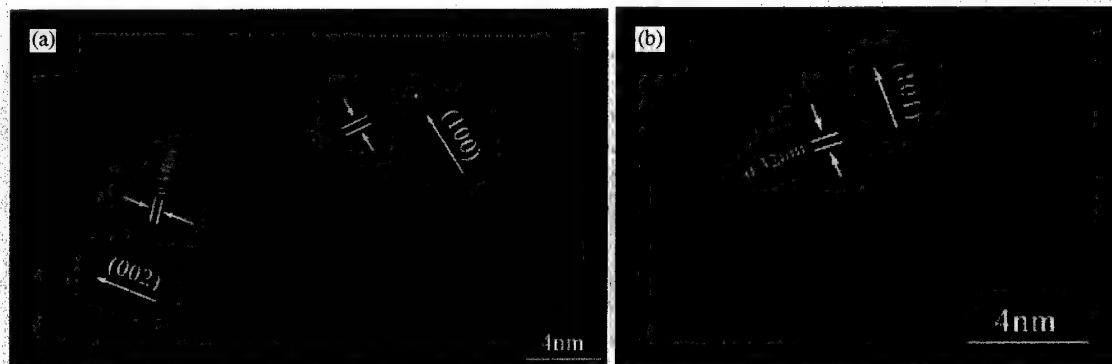


Fig. 4. HRTEM images of a single CdS nanowire at different positions: (a) middle and (b) fringe.

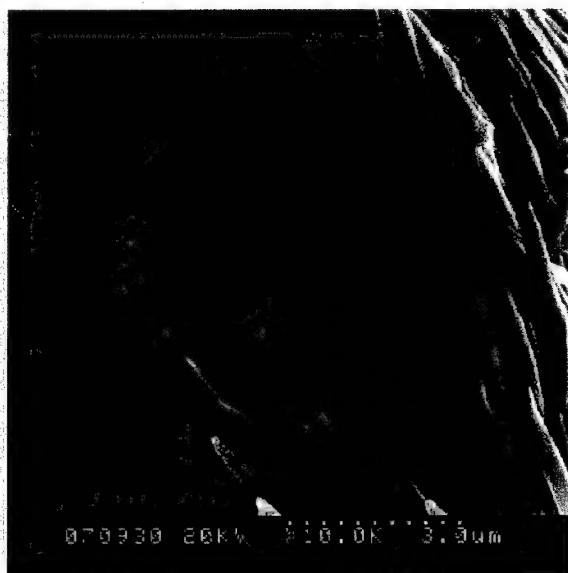


Fig. 5. Directional growth of CdS nanowires revealed by cross-sectional SEM.

Fig. 4(a) reveals that in the middle of the nanowire, the main lattice planes are $\{002\}$ and $\{100\}$ with spacings of about 0.34 and 0.36 nm, respectively. Fig. 4(b) shows that in the fringe of the nanowire, the main crystal plane is $\{101\}$ with a lattice spacing of about 0.32 nm. Therefore, the CdS nanowires have been again proved to be polycrystalline in nature with the major planes of $\{002\}$, $\{100\}$ and $\{101\}$, which is in accordance with the XRD pattern shown in Fig. 1.

Fig. 5 shows the SEM image of the cross-section of the sample. The directional growth of CdS nanowires was found, because of the confined growth of the nanowires in the orderly pores of an AAO template.

For the CdS thin films growth, two mechanisms have been put forward [24,25]. One is cluster-by-cluster mechanism described as following: in the ammonia-thiourea system, S^{2-} ions are released by the alkaline hydrolysis of thiourea and Cd^{2+} ions are released by dissociation of the corresponding ammonia complexes. As soon as the product of the free S^{2-} and Cd^{2+} ion concentrations exceeds the solubility product of CdS, the precipitation of CdS takes place. The other is ion-by-ion mechanism which consists of the following three steps: (1) the reversible adsorption on the substrate surface of dihydroxo-diamino cadmium, (2) the adsorption of thiourea by the formation of a metastable complex, (3) the formation of CdS and the site regeneration by the metastable complex decomposition. For the formation of CdS nanowires, it is believed to be dictated by ion-by-ion mechanism, because the CdS clusters formed in the solution via cluster-by-cluster mechanism are difficult to enter into the pores of AAO template.

4. Conclusions

In summary, we have synthesized the hexagonal polycrystalline CdS nanowires into the AAO templates using chemical bath deposition, which

is much simpler than other methods such as electrodeposition and CST. SEM indicates that CdS nanowires grow directionally due to the confinement of AAO pores. The diameters of the CdS nanowires are about 60 nm derived from the TEM. HRTEM images clearly show the lattice image of {002}, {101} and {100} planes of the nanowires. It is expected that the diameter of CdS nanowires can be further minimized by reducing the diameter of the pores in the AAO template. Furthermore, CBD method is also believed to be appropriate for the growth of other semiconductor nanowires.

Acknowledgements

The authors would like to appreciate the financial supports of 863 project No. (2001AA513023) and Zhejiang Provincial Natural Science Fund (No. 601092).

References

- [1] S. Iijima, *Nature* 354 (1991) 56.
- [2] H. Dai, E.W. Wang, Y.Z. Lu, S. Fan, C.M. Lieber, *Nature* 375 (1995) 769.
- [3] W. Han, S. Fan, Q. Li, Y. Hu, *Science* 277 (1997) 1287.
- [4] J.R. Heath, F.K. Le Goues, *Chem. Phys. Lett.* 208 (1993) 263.
- [5] Z.F. Ren, Z.P. Huang, J.W. Xu, J.H. Wang, P. Bush, M.P. Siegal, P.N. Provencio, *Science* 282 (1998) 1105.
- [6] M.S. Fuhrer, J. Nygard, L. Shih, M. Forero, Young-Gui Yoon, M.S.C. Mazzoni, Hyoung Joon Choi, *Science* 288 (2000) 494.
- [7] J. Kong, N.R. Franklin, C. Zhou, M.G. Chapline, S. Peng, K. Cho, H. Dai, *Science* 287 (2000) 622.
- [8] J. Hone, B. Batlogg, Z. Benes, A.T. Johnson, J.E. Fischer, *Science* 289 (2000) 1730.
- [9] D. Routkevitch, T. Bigioni, M. Moskovits, J. Ming Xu, *J. Phys. Chem.* 100 (1996) 14037.
- [10] J. Zhang, X. Yang, D. Wang, S. Li, Yi Xie, Younan Xia, Yitai Qian, *Adv. Mater.* 12 (2000) 1348.
- [11] D. Xu, Y. Xu, D. Chen, G. Guo, L. Gui, Y. Tang, *Adv. Mater.* 12 (2000) 520.
- [12] D. Routkevitch, T.L. Haslett, L. Ryan, T. Bigioni, C. Douketis, M. Moskovits, *Chem. Phys.* 210 (1996) 343.
- [13] D. Xu, Y. Xu, D. Chen, G. Guo, L. Gui, Y. Tang, *Chem. Phys. Lett.* 325 (2000) 340.
- [14] Y. Li, J. Wan, Z. Gu, *Mater. Sci. Eng. A* 286 (2000) 106.
- [15] J. Suh, J. Lee, *Chem. Phys. Lett.* 281 (1997) 384.
- [16] J.H. Zhan, X.G. Yang, S.D. Li, D.W. Wang, Y. Xie, Y.T. Qian, *J. Crystal Growth* 220 (2000) 231.
- [17] G. Sasikala, P. Thilakan, C. Subramanian, *Sol. Energy Mater. Sol. Cells* 62 (2000) 275.
- [18] J.G. Vazquez-Luna, R.B. Lopez Flores, M. Rubin-Falfan, L. Del, C. Gomez-Pavon, *J. Crystal Growth* 187 (1998) 380.
- [19] I.O. Oladeji, L. Chow, J.R. Liu, W.K. Chu, A.N.P. Bustamante, C. Fredricksen, A.F. Schulte, *Thin Solid Films* 359 (2000) 154.
- [20] A. Zehe, J.G. Vazquez Luna, *Sol. Energy Mater. Sol. Cells* 68 (2000) 217.
- [21] J. Herreo, M.T. Gutierrez, C. Guillen, J.M. Dona, M.A. Martinez, A.M. Chaparro, R. Bayon, *Thin Solid Films* 361–362 (2000) 28.
- [22] Y. Nosaka, K. Yamaguchi, H. Miyama, H. Hayashi, *Chem. Lett.* 87 (1988) 605.
- [23] M.A. Martinez, C. Guillen, J. Herrero, *Appl. Surf. Sci.* 140 (1999) 182.
- [24] J.M. Dona, J. Herrero, *J. Electrochem. Soc.* 144 (1997) 4081.
- [25] R. Ortega-Borges, D. Lincol, *J. Electrochem. Soc.* 140 (1993) 3464.

Thermal stability and interfacial reaction of TiB_x films deposited on (1 0 0)Si by dual-electron-beam evaporation

Young-Ki Lee*

Division of Information and Communication Engineering, Science and Engineering Research Institute (SERI), Uiduk University, Kyungju 780-713, South Korea

Received 15 August 2002; accepted 20 August 2002
Communicated by M. Schieber

Abstract

The thermal stability of non-stoichiometric TiB_x films with various boron-to-titanium ratios and the interfacial reaction in $\text{TiB}_x/(100)\text{Si}$ systems have been studied. $\text{TiB}_x/(100)\text{Si}$ samples were prepared by a dual-electron-beam evaporation process, and then annealed at various temperatures. These samples were characterized with X-ray photoelectron spectroscopy, X-ray diffraction, transmission electron microscopy, scanning electron microscopy, sheet resistance and stress measurement. For boron-rich TiB_x films with a ratio of $\text{B/Ti} \geq 2.0$, an apparent structural change is not observed even after annealing at 1000°C for 1 h. For titanium-rich films with a ratio of $\text{B/Ti} < 2.0$, however, there are two competitive solid phase reactions at Si– TiB_x interface as a result of annealing: the formation of a titanium silicide layer at the interface and the formation of a stoichiometric TiB_2 layer at the surface, indicating the silicide process. The sheet resistance and the internal stress for $\text{TiB}_x/(100)\text{Si}$ systems are changed by the solid phase reaction at Si– TiB_x interface.

© 2002 Elsevier Science B.V. All rights reserved.

PACS: 68.35.-p; 68.55.-a; 68.60.Pv; 81.05.je; 81.40.Ef

Keywords: A1. Characterization; A1. Morphological stability; B1. Borates; B1. Titanium compounds

1. Introduction

Metallization schemes have been investigated to provide reliable Ohmic contacts in semiconductor technology. Transition-metal nitrides and borides have been proposed as contact materials and/or passive diffusion barriers in integral circuits metallization [1–9]. Among borides, titanium

boride (TiB_x) is a very interesting material for VLSI applications in metallization schemes because of the high thermal stability and low bulk resistivity [5–9]. The thermal expansion coefficient of bulk TiB_2 is $4.6 \times 10^{-6} \text{ K}^{-1}$ which is close to Si ($2.5 \times 10^{-6} \text{ K}^{-1}$). It may thus be possible to deposit TiB_x films on the single crystal silicon with very low stress. Furthermore, TiB_x films that varied from titanium-rich to boron-rich have been shown to be useful in many applications for microelectronic devices. For example, boron-rich

*Tel.: +82-54-760-1631; fax: +82-54-760-1504.

E-mail address: yklee@mail.uiduk.ac.kr (Y.-K. Lee).

TiB_x ($x > 2.0$) films are considered for application as a boron diffusion source into p-type Si substrate. Titanium-rich TiB_x ($x < 2.0$) films, on the other hand, are expected to form the $\text{TiB}_2/\text{TiSi}_2/\text{Si}$ contact by a simple post-annealing process, as shown in the Ti-rich TiN_x ($x < 1.0$)/Si system, which favors the formation of a low contact resistance and good adhesion to the Si substrate. This type of silicide fabrication allows the formation of a silicide in a desired location without the need for an additional lithographic step.

The purpose of this research is to evaluate the thermal stability of non-stoichiometric TiB_x films with various boron-to-titanium ratios and the interfacial reaction in $\text{TiB}_x/(100)\text{Si}$ systems as a result of vacuum annealing for its potential application in silicon-based microelectronic devices. Non-stoichiometric TiB_x films were deposited by a dual-electron-beam evaporation process, which allows the composition to be varied from titanium-rich to boron-rich [10]. The characteristics of as-deposited and annealed $\text{TiB}_x/(100)\text{Si}$ samples were then investigated by means of X-ray photoelectron spectroscopy (XPS), X-ray diffraction (XRD), transmission electron microscopy (TEM), scanning electron microscopy (SEM), sheet resistance and internal stress measurement.

2. Experimental procedure

P-type silicon wafers, $\langle 100 \rangle$ oriented with a resistivity of $8\text{--}11\ \Omega\text{cm}$, were cut into $25 \times 25\text{ mm}^2$ pieces and used as substrate materials throughout this work. The wafers were cleaned with organic solvents, rinsed in distilled water, then immersed in a buffered HF acid solution (5% HF in H_2O) for at least 30 s in order to remove a thin native oxide layer on the surface, and finally rinsed in distilled water prior to deposition.

TiB_x films were grown by co-evaporation process of titanium (99.9%, 5 mm diameter rod shape) and boron (99.9%, lump shape) from separate sources, heated with dual-electron-beam guns in a chamber which was first pumped down to less than 4×10^{-7} Torr. The substrate temperature was kept constant at 500°C in all experiments.

In order to reduce the amount of gaseous impurities that incorporated in source materials, Ti and B sources were pre-evaporated for about 60 s before deposition. The boron-to-titanium ratio of the TiB_x film was obtained by adjusting the power applied to the two independent constituents. The typical evaporation rate for titanium was kept constant at 0.63 nm/s at 600 W throughout this work, while the boron evaporation rate was varied from 0 to 0.93 nm/s by adjusting the power in the range of $0\text{--}800\text{ W}$. The deposition rate was monitored with a quartz resonator plate. The total thickness of the TiB_x film was measured by a surface profilometry (Dektak) on steps after deposition. The composition of the TiB_x film was determined by electron probe microanalysis (EPMA) and X-ray photoelectron spectroscopy (XPS) analysis. In order to investigate the thermal stability of non-stoichiometric TiB_x films ($0 \leq \text{B}/\text{Ti} \leq 2.5$) and the interfacial reaction in $\text{TiB}_x/(100)\text{Si}$ systems, samples prepared at various deposition conditions were annealed for 1 h in the temperature range of $300\text{--}1000^\circ\text{C}$. During vacuum annealing the base pressure of the annealing system was maintained at 5×10^{-7} Torr.

TEM (JEM-2000FX, JEM-200), selected area diffraction (SAD) and XRD were used to characterize the crystalline structure of the thin films. TEM samples were prepared by ultrasonic cutting to 3 mm diameter and thinning from the silicon side with mechanical polishing and chemical etching ($\text{HF}:\text{HNO}_3 = 1:1$). The internal stress of the thin films was calculated by measuring the radius of curvature of the Si substrate using an X-ray Lang camera with a proportional counter. This technique is identical in principle with the optical Newton ring technique that has been described in detail by Angilello et al. [11]. The sheet resistance was measured at room temperature by a conventional four-point probe method equipped with Cu probes.

3. Results and discussion

The SAD patterns for as-deposited samples with various boron-to-titanium ratios are shown in Fig. 1. For a ratio of $\text{B}/\text{Ti} = 0.59$, only single phase

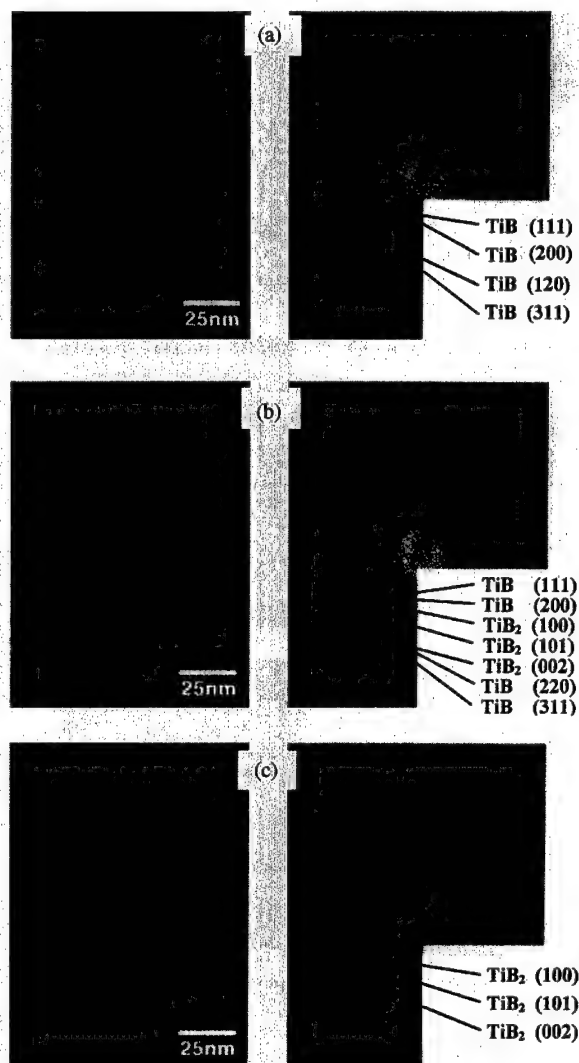


Fig. 1. Selected area diffraction patterns and bright field TEM images for as-deposited $\text{TiB}_x/(100)\text{Si}$ samples as a function of boron-to-titanium ratio: (a) $\text{B/Ti} = 0.59$, (b) $\text{B/Ti} = 1.24$, and (c) $\text{B/Ti} = 2.38$.

TiB with the cubic structure of the ZnS(B3) type is observed. As the boron concentration increases, however, the TiB_2 phase with the hexagonal structure of $\text{AlB}_2(\text{C32})$ type evolves gradually. Samples with a ratio of $\text{B/Ti} \geq 2.0$ exhibit only single phase TiB_2 , indicating the existence of excess boron atoms in these films. These results are in good agreement with those obtained by XRD [10]. As known from the bright field TEM images in

Fig. 1, also, as-deposited TiB_x films deposited at 500°C are uniform and very fine polycrystalline structure. This was additionally confirmed by atomic force microscopy and XRD. By employing the XRD peak width (FWHM), the crystallite size was estimated to be approximately 19 nm for $\text{B/Ti} = 0.59$ and 10 nm for $\text{B/Ti} = 2.38$. This suggests that the grain growth of titanium was impeded by the presence of boron during deposition. As a result of the strong directionality of the covalent boron–boron bonds in boride materials [12], boride films show a pronounced tendency to form extremely fine-grained to amorphous structures if low-temperature PVD processes are used [13]. Ti-B and Ti-B-N materials are generally interpreted as being nano-crystalline [14].

Fig. 2 shows XRD patterns for $\text{TiB}_x(\text{B/Ti} = 0.59)/(100)\text{Si}$ samples annealed for 1 h at various temperatures. After annealing at 500°C for 1 h or longer, there is no evidence of a silicide or other compounds at the Si-TiB_x interface. On

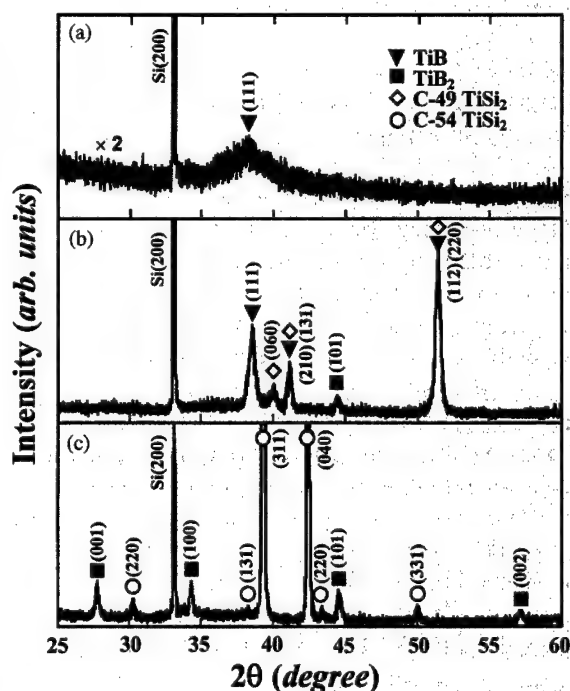


Fig. 2. X-ray diffraction patterns for the $\text{TiB}_x(\text{B/Ti} = 0.59)/(100)\text{Si}$ samples as a function of annealing temperature: (a) as-deposited, (b) 600°C for 1 h, and (c) 900°C for 1 h.

annealing at 600°C for 1 h, however, the Ti atom in TiB_x films with $\text{B/Ti} < 1.0$ migrate into the Si substrate by diffusion in the opposite direction, thereby the C49-TiSi_2 forms during annealing by the silicide process and at the same time the single TiB phase transforms to TiB_2 phase, as shown in Fig. 2(b). It is considered that there are two competitive solid phase reactions at Si– TiB_x interface as a result of annealing: the formation of the C49-TiSi_2 phase at Si– TiB_x interface and the formation of stoichiometric TiB_2 phase at a part of TiB_x layer, indicating the silicide (self-aligned silicide) process. At temperatures above 800°C, the metastable C49-TiSi_2 is transformed to stable C54-TiSi_2 and the coexistence of TiB and TiB_2 is observed. However, the TiB phase is completely transformed to the TiB_2 phase by annealing at 900°C (Fig. 2(c)). For annealed $\text{TiB}_x/(100)\text{Si}$ samples with $1 \leq \text{B/Ti} < 2.0$, the thermal stability of non-stoichiometric TiB_x films and the solid phase reaction are also similar to those for annealed samples with $\text{B/Ti} < 1.0$. For the samples with boron-rich composition ($\text{B/Ti} \geq 2.0$), on the other hand, an apparent structural change is not observed.

Fig. 3 shows SAD patterns and bright field TEM images for $\text{TiB}_x/(100)\text{Si}$ samples with various boron-to-titanium ratios annealed at 1000°C for 1 h. As shown from SAD patterns in Fig. 3(a) and (b), in addition to the sharp diffraction rings from stoichiometric TiB_2 phase, many diffraction spots derived from C54-TiSi_2 phase are observed. However, the sample with B-rich composition ($\text{B/Ti} \geq 2.0$) in Fig. 3(c) shows only single phase TiB_2 , which has uniform and very fine polycrystalline structure. These results are in agreement with the results observed by XRD. As shown in bright field TEM images taken from the region corresponding to the SAD pattern of Fig. 3, also, the grain size of C54-TiSi_2 is much larger than that of TiB_2 . The TiB_2 layer (light area) in TEM image exists uniformly. However, the grains of C54-TiSi_2 (dark area) agglomerate and grow extensively. It is consequently clear that Ti atoms in the sub-stoichiometric TiB_x ($\text{B/Ti} < 2.0$) start to react with Si to form a titanium silicide at Si– TiB_x interfaces, whereas B atoms in the over-stoichiometric TiB_x ($\text{B/Ti} > 2.0$) diffuse into the

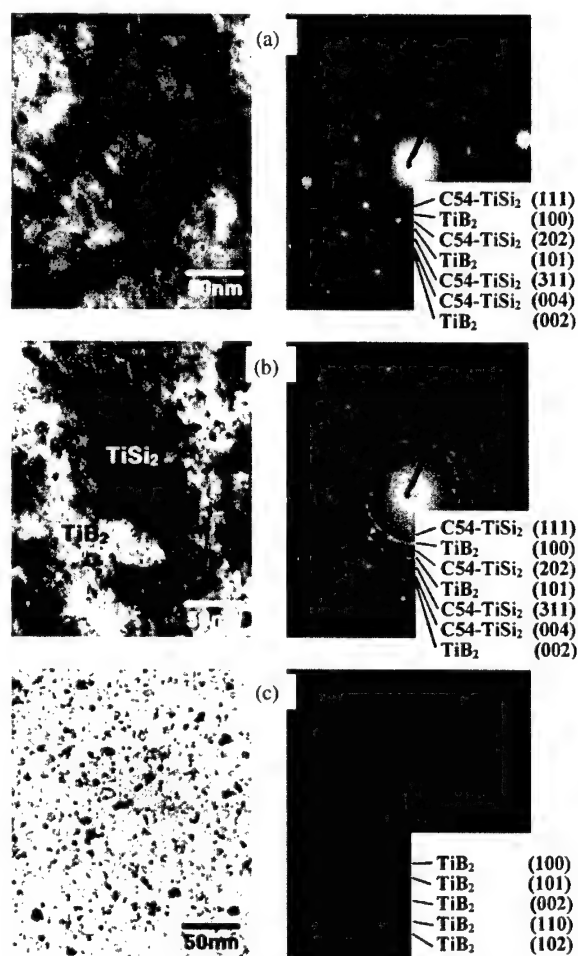


Fig. 3. Selected area diffraction patterns and bright field TEM images for annealed $\text{TiB}_x/(100)\text{Si}$ samples as a function of boron-to-titanium ratio: (a) $\text{B/Ti} = 0.59$, (b) $\text{B/Ti} = 1.24$, and (c) $\text{B/Ti} = 2.38$. All anneals were carried out at 1000°C for 1 h.

substrate in order to form the stoichiometric TiB_2 phase.

In order to confirm the interfacial reaction for $\text{TiB}_x/(100)\text{Si}$ systems, some annealed samples were analyzed by XPS concentration depth profiles. Vacuum annealing creates a wide diffused region, indicating that a solid phase reaction has occurred at the interface. Fig. 4(a) shows the depth profile for the $\text{TiB}_x(\text{B/Ti} = 1.24)/(100)\text{Si}$ sample annealed at 1000°C for 1 h. The boride film with a ratio of $\text{B/Ti} = 1.24$ is transformed from the non-stoichiometric to the stoichiometric composition

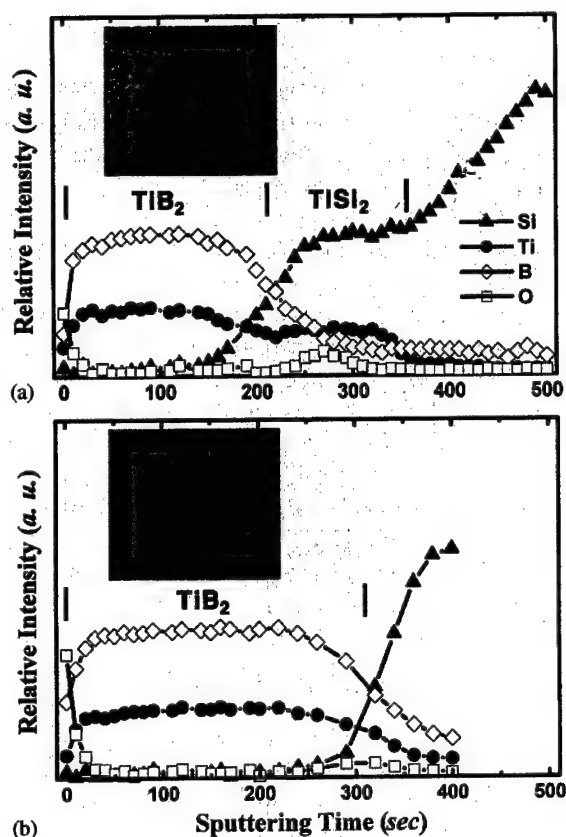


Fig. 4. XPS depth profiles for annealed TiB_x ($B/Ti=1.24$)/ $(100)Si$ samples as a function of boron-to-titanium ratio: (a) $B/Ti=1.24$, and (b) $B/Ti=2.38$. All anneals were carried out at $1000^\circ C$ for 1 h.

($B/Ti=2.0$). Also, there is a significant variation in the titanium signal, indicating that excess titanium is consumed during the formation of a silicide at the interface. The composition of a silicide as derived from the XPS profile is close to $Ti/Si=2.0$, showing $C54-TiSi_2$ phase in accordance with XRD and SAD results (Figs. 2 and 3(b)). As shown in SEM image (Fig. 4(a)), also, a rough surface morphology appears on the surface of TiB_x ($B/Ti=1.24$)/ $(100)Si$ sample annealed at $1000^\circ C$ for 1 h due to the remarkable inter-diffusion behavior at the $Si-TiB_x$ interface. This indicates that excess titanium atom in the sub-stoichiometric TiB_x film reacts with the underlying Si substrate resulting in the formation of a titanium silicide layer. As shown in Fig. 4(b), however, the boron and

titanium distributions for the sample with B-rich composition ($B/Ti \geq 2.0$) are fairly uniform from the film surface to the interface, and the boron-to-titanium ratio is close to the stoichiometric composition ($B/Ti=2.0$). This suggests that excess boron atom in the over-stoichiometric TiB_x ($B/Ti > 2.0$) film diffuses into the substrate as a result of the decomposition of B-rich TiB_x film by annealing. Ryan et al. have also reported that excess boron atom in boron-rich TiB_x ($x > 2.0$) film appears to be the source of the boron for inter-diffusion in p-type Si and the boron surface concentration increases with increasing the boron-to-titanium ratio of the boride film [15]. As shown in SEM image, also, the annealed TiB_x ($B/Ti=2.38$) film has a very smooth surface, since an apparent structural change is not observed even after annealing at $1000^\circ C$ for 1 h.

Fig. 5 shows the variation of the $(101)TiB_2$ peak for annealed TiB_x ($B/Ti=2.38$)/ $(100)Si$ samples as a function of annealing temperature. Note that 44.53° refers to the diffraction angle of $(101)TiB_2$ peak obtained from JCPDS card (08-0121). In as-deposited sample, the $(101)TiB_2$ peak is observed at low diffraction angle, indicating the existence of excess boron atoms in this film. The $(101)TiB_2$ peak shifts toward 44.53° gradually

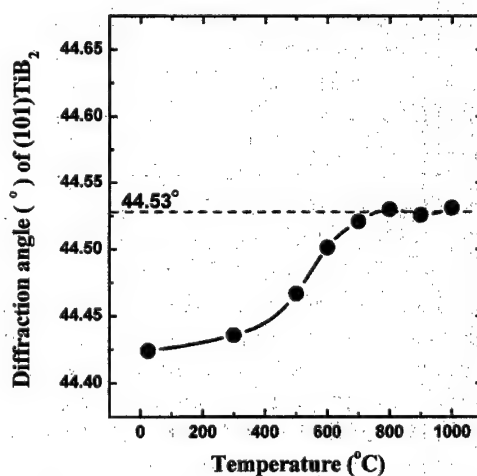


Fig. 5. Diffraction angle of $(101)TiB_2$ peak for annealed TiB_x ($B/Ti=2.38$)/ $(100)Si$ samples as a function of annealing temperature. Note that 44.53° refer to the diffraction angle of $(101)TiB_2$ peak obtained from JCPDS card (08-0121).

until it is annealed at 600°C for 1 h. At temperatures above 700°C, however, the peak does not change significantly as a result of the transformation from non-stoichiometric TiB_x to stoichiometric TiB_2 phase. This makes the boron-rich titanium boride ($\text{B/Ti} > 2.0$) films act as a boron source, doping the underlying silicon substrate during heat treatment.

The sheet resistance as a function of annealing temperature is shown in Fig. 6. All as-deposited samples exhibit a sheet resistance of between 14 and 23 Ω/\square . The resistivity, ρ ($= R \times t_f$, R : sheet resistance, t_f : film thickness), increases linearly with increasing the boron-to-titanium ratio of the film. A similar result has been reported for TiB_x films deposited by reactive sputtering in a mixture of argon and 6% diborane [16]. Therefore, it is considered that the resistivity for as-deposited TiB_x films directly correlates with the nominal B/Ti ratio of the film. On annealing, however, the sheet resistance changes as shown in Fig. 6. For the pure Ti film, the sheet resistance increases gradually with temperature until 500°C. The increase in sheet resistance at these low temperatures is most likely caused by impurity effects produced as a result of Si diffusion into the pure Ti

film. At 600°C, however, the sheet resistance decreases steeply due to the formation of a Ti silicide at the interface, as shown in Fig. 2(b). At temperature above 700°C, the sheet resistance is mostly dominated by the formation of the C54- TiSi_2 phase. For all annealed TiB_x samples, the sheet resistance behaves identically up to 500°C. However, TiB_x samples annealed above 600°C can be divided into two groups, depending on the sheet resistance. The sheet resistance in the first group ($\text{B/Ti} < 2.0$) decreases abruptly as a result of the formation of stoichiometric TiB_2 phase on the surface as well as the formation of a Ti silicide at the interface. On the other hand, the sheet resistance in the second group ($\text{B/Ti} \geq 2.0$) decreases gradually due to the transformation from non-stoichiometric TiB_x to stoichiometric TiB_2 phase. It is suggested that the sheet resistance variation for annealed TiB_x samples results from the thermal stability of non-stoichiometric TiB_x films and the interfacial reaction in $\text{TiB}_x/(100)\text{Si}$ systems.

Fig. 7 shows the $\text{TiSi}_2/\text{TiB}_2$ ratio and the sheet resistance of annealed $\text{TiB}_x/(100)\text{Si}$ samples as a function of the nominal B/Ti ratio. All anneals were carried out at 1000°C for 1 h. As shown in Fig. 7, the sheet resistance attains its maximum value in TiB_x films with $\text{B/Ti} \geq 2.0$ that exhibits only single phase TiB_2 , and decreased linearly with

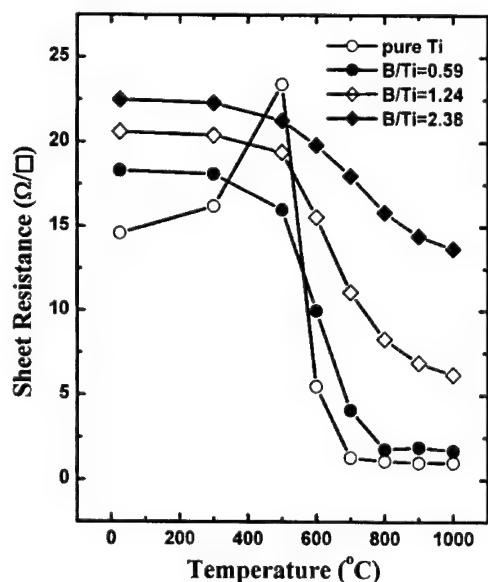


Fig. 6. Sheet resistance for $\text{TiB}_x/(100)\text{Si}$ samples as a function of annealing temperature. All anneals were for 1 h in vacuum.

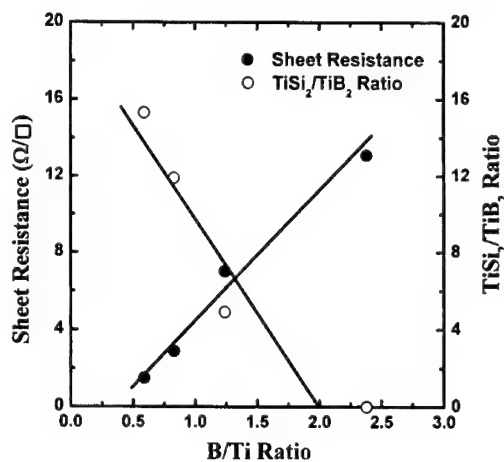


Fig. 7. $\text{TiSi}_2/\text{TiB}_2$ intensity ratio and sheet resistance for annealed $\text{TiB}_x/(100)\text{Si}$ samples as a function of boron-to-titanium ratio. All anneals were carried out at 1000°C for 1 h.

increasing $\text{TiSi}_2/\text{TiB}_2$ ratio. The sheet resistance for TiB_x samples with $\text{B}/\text{Ti} < 2.0$ is due mostly to the formation of a Ti silicide at the interface, although there may possibly be some contribution from factors such as film thickness, grain size, etc.

Fig. 8 shows the internal film stress for annealed TiB_x/Si samples as a function of annealing temperature, where T and C refer to tensile and compressive, respectively. The as-deposited Ti film has a very low tensile stress, which does not change significantly up to 400°C . At 500°C , the tensile stress for the Ti film changes to a compressive stress due to the inter-diffusion of Si atoms into the Ti layer indicating the atomic peening effect [17]. Above this annealing temperature, the film exhibits a tensile stress. The tensile stress increases with increasing annealing temperature up to 900°C . It is suggested that this is due to the formation of a Ti silicide that has about 23% smaller volume than Ti. Moreover, all as-deposited TiB_x films have a tensile stress. The tensile stress increases gradually as the nominal B/Ti ratio increases. The stress exhibits the maximum value in the range of compositions ($1.0 < \text{B}/\text{Ti} < 2.0$) consisting of two Ti–B compound phases, e.g. TiB and TiB_2 . For films with a ratio of $\text{B}/\text{Ti} \geq 2.0$ that exhibit a single TiB_2 phase, the tensile stress decreases gradually owing to the atomic peening

effect inducing a compressive stress [10,17]. However, the stress for all TiB_x films is changed by annealing at 600°C or higher temperature, although the stress does not change significantly up to 500°C . For the annealed TiB_x sample with $\text{B}/\text{Ti} = 0.59$, the tensile stress is somewhat higher than that for pure Ti sample due to the existence of a TiB_2 layer with a tensile stress, although overall the variation of the internal film stress is very similar to that for pure Ti sample, as shown in Fig. 8. Also, the stress behaviors for annealed $\text{TiB}_x/(100)\text{Si}$ samples with $1 \leq \text{B}/\text{Ti} < 2.0$ are similar to those for samples with $0 < \text{B}/\text{Ti} < 1.0$. On the other hand, the stresses for the samples with $\text{B}/\text{Ti} > 2.0$ decreases gradually as a result of the grain growth of TiB_2 phase as well as the inter-diffusion of excess boron atoms into the Si substrate. The stress variation for Ti/Si and TiB_x/Si systems is explained well by the solid phase reaction at Si– TiB_x interface.

4. Conclusions

In this study, the thermal stability of non-stoichiometric TiB_x films ($0 \leq \text{B}/\text{Ti} \leq 2.5$) and the interfacial reaction in the $\text{TiB}_x/(100)\text{Si}$ systems have been studied. For boron-rich TiB_x/Si samples with a ratio of $\text{B}/\text{Ti} \geq 2.0$, an apparent structural change is not observed on annealing. For titanium-rich samples with $\text{B}/\text{Ti} < 2.0$, however, there are two competitive solid phase reactions at Si– TiB_x interface: the formation of a titanium silicide layer at the interface and the formation of stoichiometric TiB_2 layer at the surface, indicating the silicide (self-aligned silicide) process. For all annealed TiB_x/Si samples, the sheet resistance behaves identically up to 500°C . However, TiB_x samples annealed above 600°C can be divided into two groups, depending on the sheet resistance. The sheet resistance in the first group ($\text{B}/\text{Ti} < 2.0$) decreases abruptly as a result of the formation of stoichiometric TiB_2 phase on the surface as well as the formation of a Ti silicide at the interface. On the other hand, the sheet resistance in the second group ($\text{B}/\text{Ti} \geq 2.0$) decreases gradually due to the transformation from non-stoichiometric TiB_x to stoichiometric TiB_2 . The internal stresses for

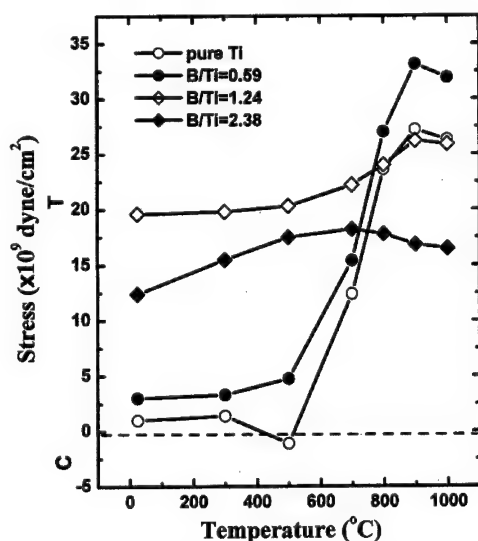


Fig. 8. Residual stress for $\text{TiB}_x/(100)\text{Si}$ samples as a function of annealing temperature. All anneals were for 1 h in vacuum.

all as-deposited Ti/Si and TiB_x/Si systems have a tensile stress. The stresses for annealed samples changes with the B/Ti ratio: the tensile stress for samples with $\text{B/Ti} < 2.0$ increases owing to the formation of a Ti silicide at the interface, whereas those for samples with $\text{B/Ti} \geq 2.0$ decreases due mostly to the grain growth of the TiB_2 phase as well as the decomposition of B-rich TiB_x film. The internal stress variation for Ti/Si and $\text{TiB}_x/(100)\text{Si}$ systems is explained well by the solid phase reaction at Si– TiB_x interface.

References

- [1] M. Wittmer, B. Studer, H. Melchior, *J. Appl. Phys.* 52 (1981) 5772.
- [2] M. Wittmer, *Appl. Phys. Lett.* 36 (1980) 456.
- [3] H.V. Seefeld, N.W. Cheung, M. Mäenpää, M.A. Nicolet, *IEEE Trans. Electron. Dev.* 27 (1980) 873.
- [4] M. Wittmer, *Appl. Phys. Lett.* 37 (1980) 540.
- [5] C. Feldman, F.G. Satkiewicz, N.A. Blum, *J. Less-Common Met.* 82 (1981) 183.
- [6] J.R. Shappirio, J.J. Finnegan, R.A. Lux, D.C. Fox, *Thin Solid Films* 119 (1984) 23.
- [7] J.R. Shappirio, J.J. Finnegan, R.A. Lux, J. Kwiatkowski, H. Kattelus, M.-A. Nicolet, *J. Vac. Sci. Technol. A* 3 (1985) 2255.
- [8] M.A. Nicolet, *Thin Solid Films* 52 (1978) 415.
- [9] H. Hollence, *J. Vac. Sci. Technol.* 6 (1986) 2661.
- [10] Y.K. Lee, *J. Crystal Growth* 226 (2001) 521.
- [11] J. Angilello, F. d'Heurle, S. Pettersson, A. Segmüller, *J. Vac. Sci. Technol.* 17 (1980) 471.
- [12] J. Etourncau, P. Hagenmüller, *Philos. Mag.* 52 (3) (1985) 589.
- [13] J.E. Greene, in: D.T.J. Hurle (Ed.), *Handbook of Crystal Growth*, Vol. 1, Elsevier, Amsterdam, 1993, p. 640.
- [14] W. Gissler, *Surf. Coat. Technol.* 68/69 (1994) 556.
- [15] J.G. Ryan, S. Roberts, G.J. Slusser, E.D. Adams, *Thin Solid Films* 153 (1987) 329.
- [16] H.-O. Böhm, S. Berg, M. Ostling, C.S. Petersson, V. Deline, F.M. d'Heurle, *J. Vac. Sci. Technol. B* 3 (1985) 997.
- [17] A. Pan, J.E. Greene, *Thin Solid Films* 78 (1981) 25.



ELSEVIER

Available online at www.sciencedirect.com

SCIENCE @ DIRECT®

Journal of Crystal Growth 246 (2002) 121–126

JOURNAL OF CRYSTAL GROWTH

www.elsevier.com/locate/jcrysgr

Growth and characterization of $\text{Pb}_{1-x}(\text{Mg}_{1-y}\text{Sr}_y)_x\text{S}$ thin films prepared by hot-wall epitaxy

S. Abe*, K. Masumoto

The Research Institute for Electric and Magnetic Materials, 2-1-1 Yagiyama-minami, Sendai 982-0807, Japan

Received 12 August 2002; accepted 22 August 2002

Communicated by M. Schieber

Abstract

We have investigated new quaternary solid solution semiconductor $\text{Pb}_{1-x}(\text{Mg}_{1-y}\text{Sr}_y)_x\text{S}$ ($x < 0.1$) thin films which have been fabricated on a BaF_2 (111) substrate by using hot-wall epitaxy. It has been found that the energy band gap can be controlled desirably under keeping the lattice constant and monitoring the growth conditions. The properties of the optical absorption edge observed are suggestive of a direct energy band gap structure. The Hall mobility for the films changes monotonically from 4423 to 337 cm^2/Vs at 77 K with increasing x . The full-width at half-maximum of the films lattice-matched to PbS increases from 133 to 208 arcsec in proportion to x under the lattice misfit of 4.3% between the film and the BaF_2 .

© 2002 Elsevier Science B.V. All rights reserved.

PACS: 68.55.-a; 68.55.Jk; 61.10.-i; 78.40.-q

Keywords: A3. Hot wall epitaxy; B1. Sulfides; B2. Semiconducting lead compounds; B2. Semiconducting quaternary alloys; B3. Laser diodes

1. Introduction

The lead chalcogenide solid solution semiconductors are thought to be applied to the mid-infrared laser operating at around 3 μm . Such a laser is mainly considered for use in an advanced measurement system for the detection of hydrocarbon pollutants in the air [1]. To date, interband lasers made of lead-salts [2,3] and III–V compounds [4–6] or intersubband quantum cascade lasers [7] have been developed for practical uses in

the wavelength region. In addition to these conventional edge emitting lasers, optically pumped vertical-cavity surface-emitting lasers have also been developed by using lead-salts [8]. A continuous wave (cw) operation at RT, however, has not been realized yet.

The major advantage of the lead-salts for the present purpose is that the rate of nonradiative Auger recombination is about two orders of magnitude smaller than in III–V and II–VI compounds which have energy band gaps comparable with those of the lead-salts [9,10]. In order to raise the operating temperature, it is important to choose an appropriate material for a cladding

*Corresponding author. Fax: +81-22-245-8031.

E-mail address: abe@denjiken.ne.jp (S. Abe).

layer in a heterostructure laser. As such, for a proper cladding layer, we previously proposed a new quaternary solid solution semiconductor $\text{Pb}_{1-x}(\text{Mg}_{1-y}\text{Sr}_y)_x\text{S}$, and found on the bulk material that the compound was one of the candidates for cladding layer in the interband laser [11]. However, the quaternary thin film has not been fabricated yet. In the present study, we have investigated the fabrication of the quaternary $\text{Pb}_{1-x}(\text{Mg}_{1-y}\text{Sr}_y)_x\text{S}$ ($x < 0.1$) thin films using the hot-wall epitaxy method, and examined the growth conditions and the structural and semi-conducting properties.

2. Experimental procedure

A $\text{Pb}_{1-x}(\text{Mg}_{1-y}\text{Sr}_y)_x\text{S}$ thin film was grown on a cleaved BaF_2 (111) substrate by means of a hot-wall epitaxy (Fig. 1). The apparatus used consists of four electric furnaces, which are for substrate, wall, source and reservoir, as shown in the figure, and can be controlled independently in temperature. PbS, Mg (4N pure) and Sr (2N pure) coated with liquid paraffin, since the surface of Sr was easily oxidized in the air, are used as the source

materials and S (6N pure) is used as the reservoir material. It should be noted that vapor pressures of solid Mg and Sr [12] are much larger than that of PbS [13] and increase in proportion to temperature. Thus, the source materials of PbS, Sr and Mg are located at the wall area and the source area, being separated from each other by using the quartz liner in the growth tube as shown in the figure. The reservoir-temperature is precisely controlled around room temperature by circulating water in the water jacket. The PbS compound used was synthesized from the elements with 6N purity in the present study.

Thermal etching of the substrate was performed at a substrate-temperature of 773 K for 30 min before the growth of the $\text{Pb}_{1-x}(\text{Mg}_{1-y}\text{Sr}_y)_x\text{S}$ thin films, while Mg was preheated at a source-temperature of 793 K for 30 min to stabilize the vaporizing Mg-flux through the growth run.

The lattice constants and the growth orientation of the films were determined by high-resolution X-ray diffraction with a four crystal monochromator (RIGAKU SLX-2000). The electrical properties were measured by the van der Pauw method. The thickness of the films was measured by a surface texture analysis system (ULVAC:DEK-TAK 3030ST). The spectral transmittance at room temperature of the films was observed by a Fourier-transform infrared spectroscopy (FT-IR, JASCO: FT/IR-350).

3. Results and discussions

Fig. 2 shows the lattice constant and the energy band gap measured at room temperature for the $\text{Pb}_{1-x}(\text{Mg}_{1-y}\text{Sr}_y)_x\text{S}$ thin films, as a function of the source-temperature (T_{sou}). The substrate-temperature (T_{sub}), wall-temperature (T_{w}) and reservoir-temperature (T_{r}) were kept constant at 648, 823, and 393 K, respectively. Here, the lattice constants were obtained from the (444) peak on the X-ray diffraction pattern observed in the epitaxial films grown in the $\langle 111 \rangle$ direction. It is seen that the energy band gap increases with T_{sou} , while the lattice constant is nearly constant at around 0.5933 through 0.5936 nm with T_{sou} . Thus, it would be possible to fabricate the laser diodes

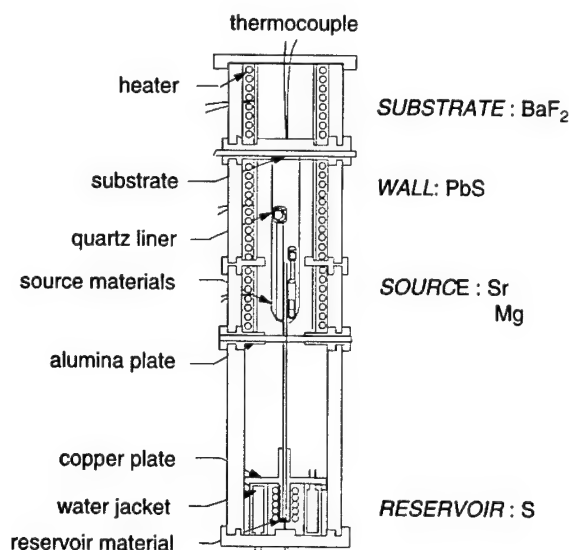


Fig. 1. Schematic representation of the hot-wall epitaxy apparatus used for the fabrication of $\text{Pb}_{1-x}(\text{Mg}_{1-y}\text{Sr}_y)_x\text{S}$ thin films.

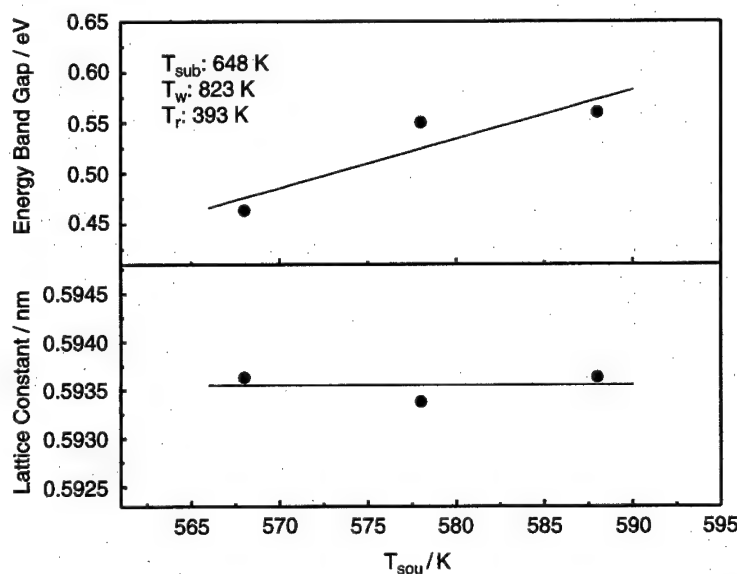


Fig. 2. Lattice constant and energy band gap of $\text{Pb}_{1-x}(\text{Mg}_{1-y}\text{Sr}_y)_x\text{S}$ thin films as a function of source-temperature (T_{sou}).

with lattice-matched double-hetero structure such as $\text{Pb}_{1-x}(\text{Mg}_{1-y}\text{Sr}_y)_x\text{S}/\text{PbS}/\text{Pb}_{1-x}(\text{Mg}_{1-y}\text{Sr}_y)_x\text{S}$ employing the hot-wall epitaxy with the two growth tubes, where the difference in the energy band gap between the $\text{Pb}_{1-x}(\text{Mg}_{1-y}\text{Sr}_y)_x\text{S}$ cladding layer and a PbS active layer can be controlled desirably. Although the refractive index of the $\text{Pb}_{1-x}(\text{Mg}_{1-y}\text{Sr}_y)_x\text{S}$ thin films was not measured in this study, the cladding layer might be expected to confine an emitted light within the active layer according to the empirical rule, that a larger energy band gap brings a smaller refractive index [14].

Fig. 3 shows the typical absorption edges at room temperature for the $\text{Pb}_{1-x}(\text{Mg}_{1-y}\text{Sr}_y)_x\text{S}$ thin films lattice-matched to PbS within an accuracy of $\pm 2 \times 10^{-4}$ nm. Previously we found that the relation between the energy band gap E_g and the composition x of the $\text{Pb}_{1-x}(\text{Mg}_{1-y}\text{Sr}_y)_x\text{S}$ on the bulk followed the expression $E_g = 0.41 + 1.79x + 4.97x^2$ [11], under keeping the composition y of 0.65. The composition x of the thin films was thus estimated using this relation and by substituting the energy band gaps obtained from the measurement by FT-IR for the films. The square of the absorbance include a contribution from reflection losses at the air-semiconductor

interface, but an approximate correction with the use of measured values for the real part of the index at wavelengths greater than the edge does not significantly alter the extrapolated absorption edges [15]. As can be seen in the figure, the absorption edges shift with respect to x . This shift in the optical absorption edge suggests that the $\text{Pb}_{1-x}(\text{Mg}_{1-y}\text{Sr}_y)_x\text{S}$ system has the direct energy band gap structure within the composition range below $x = 0.1$, although MgS which is one of the components in the system has the indirect energy band gap structure [16]. So the energy band gap shown in Fig. 2 was determined by the linear extrapolation to zero of the absorbance squared. Moreover, in addition to the use of these films as the cladding layer for mid-infrared region, the $\text{Pb}_{1-x}(\text{Mg}_{1-y}\text{Sr}_y)_x\text{S}$ system with the direct energy band gap structure also provides the utilization as an active layer emitting the light in the near infrared region.

Fig. 4 shows the Hall mobility at 77 K of the $\text{Pb}_{1-x}(\text{Mg}_{1-y}\text{Sr}_y)_x\text{S}$ thin films as a function of x . The films were fabricated so as to be lattice-matched to PbS by regulating the growth conditions. The growth of these epitaxial films was performed under an excess of sulfur vapor pressure larger than that needed for the

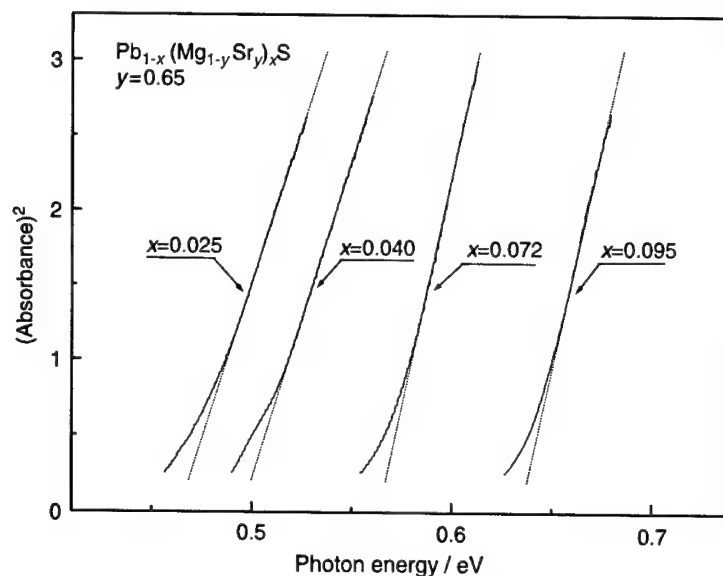


Fig. 3. Typical absorption edges at room temperature of $\text{Pb}_{1-x}(\text{Mg}_{1-y}\text{Sr}_y)_x\text{S}$ thin films lattice-matched to PbS within an accuracy of $\pm 2 \times 10^{-4}$ nm.

stoichiometric composition, for which the reservoir-temperature was regulated. These growth conditions led the films to p-type conductivity with mirror-like appearance. In the figure, the Hall mobility of the $\text{Pb}_{1-x}(\text{Mg}_{1-y}\text{Sr}_y)_x\text{S}$ thin films is seen to decrease monotonically from 4423 to $337 \text{ cm}^2 \text{ V}^{-1} \text{ s}^{-1}$ with increasing x . Besides, it was found that the Hall mobility decreased with an increase of temperature (T), exhibiting T^n dependence. The index number n evaluated in the temperature range between 100 K and room temperature is shown as a function of x in the inset of Fig. 4. The index number reflects the scattering factor in the Hall mobility. As seen in Fig. 4, the number n of the $\text{Pb}_{1-x}(\text{Mg}_{1-y}\text{Sr}_y)_x\text{S}$ thin film increases from -2.2 to -0.8 with increasing x . It is known that when a Hall mobility of an alloy is limited by a disorder scattering, the index number n is -0.5 [17]. It is deduced from the result that the Hall mobility of the $\text{Pb}_{1-x}(\text{Mg}_{1-y}\text{Sr}_y)_x\text{S}$ thin films below $x = 0.1$ would not be subject to the disorder scattering. Hence other reasons which are surmised to be a polar-optical phonon and an impurity, would be considered as the scattering factor.

As the quality of laser diode depends considerably on crystallinity of the layers, the crystal

properties of the $\text{Pb}_{1-x}(\text{Mg}_{1-y}\text{Sr}_y)_x\text{S}$ thin films were investigated. Fig. 5 shows the full-width at half-maximum (FWHM) of X-ray rocking curve at (444) Bragg reflection for the $\text{Pb}_{1-x}(\text{Mg}_{1-y}\text{Sr}_y)_x\text{S}$ thin films, as a function of x . Because the X-ray diffraction patterns indicate that the films consist of a single phase crystal, it is considered that the quaternary solid solution would be formed in the present films. It was found that the addition of MgS or SrS to PbS caused the change of the lattice constant and resulted in an isolattice constant line for the $\text{Pb}_{1-x}(\text{Mg}_{1-y}\text{Sr}_y)_x\text{S}$ system lattice-matched to PbS at $y = 0.65$ for any x value [12]. In Fig. 5, the FWHM of the $\text{Pb}_{1-x}\text{Mg}_x\text{S}$ thin films increases rapidly in proportion to x , which seems to be due to a large difference in ionic radius between Pb and Mg in the system. On the other hand, the values of FWHM in the films lattice-matched to PbS drop markedly, and they varied only from 133 to 208 arcsec. Namely, the crystallinity of the $\text{Pb}_{1-x}(\text{Mg}_{1-y}\text{Sr}_y)_x\text{S}$ thin films seems to be improved with respect to the Sr concentration in the $\text{Pb}_{1-x}(\text{Mg}_{1-y}\text{Sr}_y)_x\text{S}$ system. This improvement might be due to the close ionic radius of Sr to that of Pb in the system. It is further considered that the preparation of the film by employing a

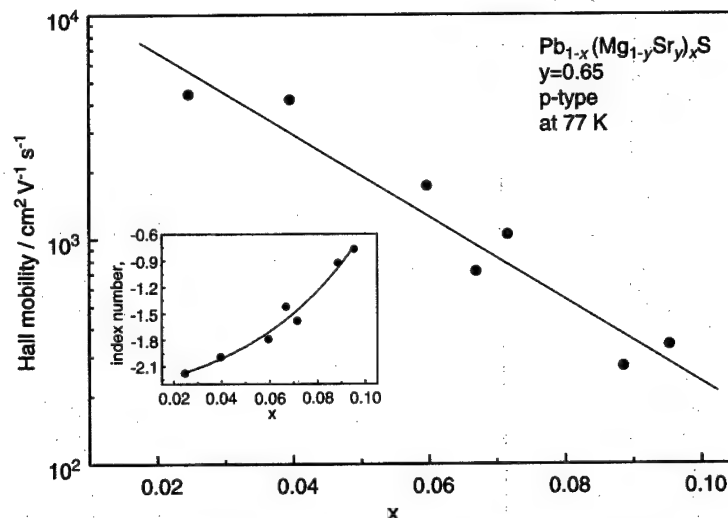


Fig. 4. Hall mobility at 77 K of Pb_{1-x}(Mg_{1-y}Sr_y)_xS thin films lattice-matched to PbS as a function of x . The inset shows the index number derived from the temperature dependence of Hall mobility as a function of x .

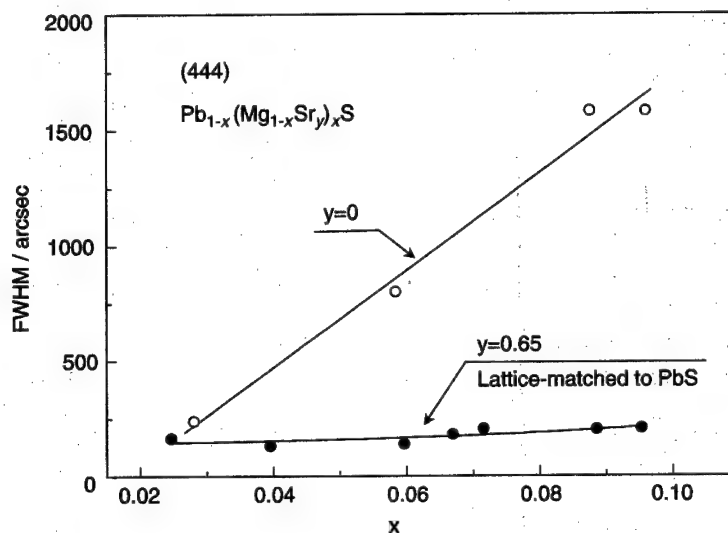


Fig. 5. FWHM of X-ray rocking curve at (444) for Pb_{1-x}(Mg_{1-y}Sr_y)_xS thin films as a function of x .

PbS substrate would result in the improvement in the FWHM of the thin films, since the lattice misfit of 4.3% exists between the film lattice-matched to PbS and the BaF₂ substrate.

Table 1 shows the typical properties of the Pb_{1-x}(Mg_{1-y}Sr_y)_xS thin films prepared in the present study. The carrier concentration of

the Pb_{1-x}(Mg_{1-y}Sr_y)_xS thin films tends to decrease slightly from 10^{17} to 10^{16} cm⁻³ with increasing x , suggesting that the vacancies in the cation sublattices in the Pb_{1-x}(Mg_{1-y}Sr_y)_xS system decreases in proportion to x . Here again the growth condition led the films to p-type conductivity. Concerning a surface morphology of these films

Table 1

Typical properties of $\text{Pb}_{1-x}(\text{Mg}_{1-y}\text{Sr}_y)_x\text{S}$ thin films prepared in this study

Type of conductivity	x	Energy band gap (eV)	Lattice constant (nm)	Carrier concentration (cm^{-3}) (77 K)	Hall mobility ($\text{cm}^2 \text{V}^{-1} \text{s}^{-1}$) (77 K)	FWHM ω (arcsec)
p	0.02 ₅	0.46	0.5936	3.9×10^{17}	4423	165
p	0.04 ₀	0.50	0.5937	1.4×10^{17}	4178	133
p	0.06 ₀	0.54	0.5937	2.1×10^{17}	1721	140
p	0.07 ₂	0.57	0.5936	2.1×10^{17}	1045	205
p	0.09 ₅	0.63	0.5934	8.0×10^{16}	337	208

changed from a rough appearance to a mirror-like one with respect to the reservoir-temperature, the films of n-type conductivity with mirror-like appearance was not obtained in this study. Therefore, the doping technique is required especially for n-type conductivity to obtain a mirror-like surface under excess of sulfur.

As the conclusion of the present study, it could be pointed out that a heterostructure laser operating at higher temperature than that reported so far is expected to be fabricated by using the new quaternary solid solution semiconductor $\text{Pb}_{1-x}(\text{Mg}_{1-y}\text{Sr}_y)_x\text{S}$.

References

- [1] K. Masumoto, N. Koguchi, S. Takahashi, T. Kiyosawa, I. Nakatani, Sci. Rep. Natl Res. Inst. Metals 6 (1985) 101.
- [2] N. Koguchi, T. Kiyosawa, S. Takahashi, J. Crystal Growth 81 (1987) 400.
- [3] A. Ishida, N. Sakurai, K. Aikawa, H. Fujiyasu, Solid-State Electron 37 (1994) 1141.
- [4] H.K. Choi, G.W. Turner, M.J. Manfrs, M.K. Connors, Appl. Phys. Lett. 68 (1996) 2936.
- [5] W.W. Bewley, H. Lee, I. Vurgaftman, R.J. Menna, C.L. Felix, R.U. Martinelli, D.W. Stokes, D.Z. Garbuzov, J.R. Meyer, M. Maiorov, J.C. Connolly, A.R. Sugg, G.H. Olsen, Appl. Phys. Lett. 76 (2000) 256.
- [6] R.Q. Yang, J.L. Bradshaw, J.D. Bruno, T. Pham, D.E. Wortman, R.L. Tpbber, Appl. Phys. Lett. 81 (2002) 397.
- [7] J. Faist, F. Capasso, D.L. Sivco, A.L. Hutchinson, S.N.G. Chu, A.Y. Cho, Appl. Phys. Lett. 72 (1998) 680.
- [8] W. Heiss, T. Schwarzl, G. Springholz, K. Biermann, K. Reimann, Appl. Phys. Lett. 78 (2001) 862.
- [9] C. Findley, C.R. Pidgeon, B.N. Murdin, A.F.G. van der Meer, A.F.G. Langerak, C.M. Ciesla, J. Oswald, G. Springholz, G. Bauer, Phys. Rev. B 58 (1998) 12908.
- [10] R. Klann, T. Hofer, R. Buhleier, T. Elsaesser, J.W. Tamm, J. Appl. Phys. 77 (1995) 277.
- [11] S. Abe, K. Masomoto, J. Crystal Growth 220 (2000) 126.
- [12] A.N. Nesmetanov, Vapor Pressure of the Chemical Elements, Elsevier, Amsterdam, 1963.
- [13] K.C. Mills, Thermodynamic Data for Inorganic Sulphides, Selenides and Tellurides, Butterworths, London, 1974.
- [14] T.S. Moss, Optical Properties of Semiconductors, Butterworths, London, 1959, p. 48.
- [15] H. Holloway, G. Jesion, Phys. Rev. B 26 (1982) 5617.
- [16] R. Pandey, J.E. Jaffe, B. Kunz, Phys. Rev. B 43 (1991) 9228.
- [17] L. Makowski, M. Glicksman, J. Phys. Chem. Solids 34 (1973) 487.



ELSEVIER

Available online at www.sciencedirect.com

SCIENCE @ DIRECT®

Journal of Crystal Growth 246 (2002) 127–132

JOURNAL OF CRYSTAL GROWTH

www.elsevier.com/locate/jcrysgro

Investigation of interfacial microstructures of MBE-grown $\text{NdF}_3/\text{Si}(111)$ heterostructures

N.T. Cho^a, J.M. Ko^{b,*}, K.B. Shim^a, T. Fukuda^b

^a Department of Ceramic Engineering, Hanyang University, Seoul 133-791, South Korea

^b Institute of Multidisciplinary Research for Advanced Materials, Tohoku University, Sendai 980-8577, Japan

Received 18 August 2002; accepted 23 August 2002

Communicated by M. Schieber

Abstract

NdF_3 layers were grown on $\text{Si}(111)$ substrates at 400°C, 550°C and 700°C by molecular beam epitaxy. Their images scanned by atomic force microscope showed that the NdF_3 layers on $\text{Si}(111)$ substrates grew as islands with spiral step patterns. As function of growth temperature, their interfacial characteristics such as orientational alignment, defects, and crystallinity were investigated by transmission electron microscope (TEM) combined with selected area electron diffractometer. In particular, the relationship between interfacial microstructure and crystalline quality of overall NdF_3 layers were explained by comparing the result of TEM observation with full-width at half-maximum values for X-ray rocking curves of both $(11\bar{2}0)$ in-plane and (0002) out-of-plane diffractions of NdF_3 layers.

© 2002 Elsevier Science B.V. All rights reserved.

PACS: 61.10.Kw; 61.72.-y; 68.55.-a; 87.64.Ee

Keywords: A1. Defects; A1. High-resolution X-ray diffraction; A1. Transmission electron microscopy; A3. Molecular beam epitaxy; B1. Fluorides

1. Introduction

Semiconductor/insulator/semiconductor heterostructures using fluorides as the insulating materials have been studied for applications such as high-speed integrated circuits (ICs) and optoelectronic ICs. For last several decades, alkaline-earth difluoride layers grown on various semiconductor substrates have been extensively studied as the insulating materials [1–6]. However, heterostruc-

tures involving rare-earth trifluoride layers seem to be more attractive owing to their high potential in applications such as lasers emitting at short wavelength by up-conversion [7–9] and monolithic wave-guides [10].

We have grown rare-earth trifluoride layers on $\text{Si}(111)$ substrates by molecular beam epitaxy (MBE) and investigated their surface characteristics such as surface morphology, growth mechanism, layer crystallinity, and epitaxial relationship [11–13]. In this article, we report on the interfacial microstructures of $\text{NdF}_3/\text{Si}(111)$ heterostructures MBE-grown at different temperatures, which were investigated by transmission electron microscope

*Corresponding author. Tel.: +81-22-217-5167; fax: +81-22-217-5102.

E-mail address: jm-ko@tagen.tohoku.ac.jp (J.M. Ko).

(TEM) equipped with selected area electron diffractometer (SAD). Also, we present the effect of the interfacial defect structures on the layer crystalline quality, which was estimated by full-width at half-maximum (FWHM) values for X-ray rocking curves from high-resolution X-ray diffraction (XRD) measurement.

2. Experimental procedure

Si (111) substrates with $30 \times 30 \text{ mm}^2$ area and 0.5 mm thick, were cleaned chemically by the modified method of Ishizaka and Shiraki [14] and were inserted into the ultrahigh vacuum chamber (Eiko EL 10A MBE system) with the base pressure $\sim 5.0 \times 10^{-10}$ Torr. To remove thin oxide contamination layers, Si substrate was heated at 950°C for 30 min. 4N-grade NdF_3 powder was charged into boron nitride crucibles of conventional effusion cell and evaporated onto the Si (111) substrates at three different temperatures of 400°C , 550°C and 700°C .

The surface morphology of the resulting layers was investigated by atomic force microscope (AFM) in air, using a Digital Instruments Nanoscope IIIa. The interfacial microstructure of NdF_3/Si (111) heterostructures was observed by TEM (Jeol 2000EX). The orientational alignment of grains at the interfacial region was investigated by SAD. The cross-section specimens were prepared by the following process: two surfaces of the grown layers were fastened to each other by epoxy and cut perpendicularly to the surface, and then are polished to $40 \mu\text{m}$, dimpled and epoxied with 3 mm Mo-grid before ion milling in 3 kV. The layer crystallinity was studied by XRD using a high-resolution diffractometer (ATX-G, Rigaku Corp.). Particularly, FWHM values for X-ray rocking curves were obtained by out-of-plane ($2\theta - \omega$ scan) and in-plane ($2\theta_\chi - \Phi$ scan) diffraction measurements.

3. Results and discussion

For NdF_3 layers grown on Si (111) substrates at 400°C , 550°C and 700°C , the surface morpho-

logical features have been observed by AFM and reported in our previous paper [12]. It was characterized by a noteworthy feature that all layers were composed of hexagonal-shaped islands or hillocks with spiral step patterns. Each island or hillock was associated with one or several screw dislocations. This forms mostly double-armed spiral patterns, i.e. two single-step spirals with the same turn directions, that project oppositely from the dislocation core and show an alternating tendency to polygonize according to one of the two equilateral triangles of opposite orientation.

The cross sections of the NdF_3/Si (111) interfaces grown at each temperature were observed by TEM-SAD for the investigation of growth mechanism in initial growth stage and defect origin of the layers. For the NdF_3/Si (111) heterostructure grown at 400°C , the TEM image showed that the NdF_3 layer was composed of upper and lower regions of two different contrasts marked as A and B, respectively, in Fig. 1a. We assume that A-region was of good alignment in epitaxial growth, whereas B-region was a polycrystalline phase. The SAD patterns of Fig. 2b confirmed that crystallites of both A- and B-regions aligned preferentially along $[0002]$ direction with orientational relationship of $[0002]_{\text{NdF}_3} \parallel [111]_{\text{Si}}$ for epitaxial growth direction, i.e. perpendicular to the interface. A-region may be considered as a monocrystalline phase that was grown well orderly following this orientational relationship. However, the $[0002]$ direction of most grains at the B-region was tilted down or up from $[111]$ direction of Si (111) substrate to be consequently a polycrystalline phase. The tilting angle was estimated to be around 3° by SAD pattern. Such tilted grains began to form at the interfacial region of NdF_3 layer and Si (111) substrate, probably due to the considerable strain from lattice mismatch of the layer and substrate at the initial growth stage. As another possible reason, we note some volume of clusters at the interface, which was circled by dot line in Fig. 2a. The clusters can be probably attributed to the abnormal growth following nucleation in a relatively low temperature of 400°C . The clusters can also be explained by contamination that has not been eliminated perfectly during substrate cleaning

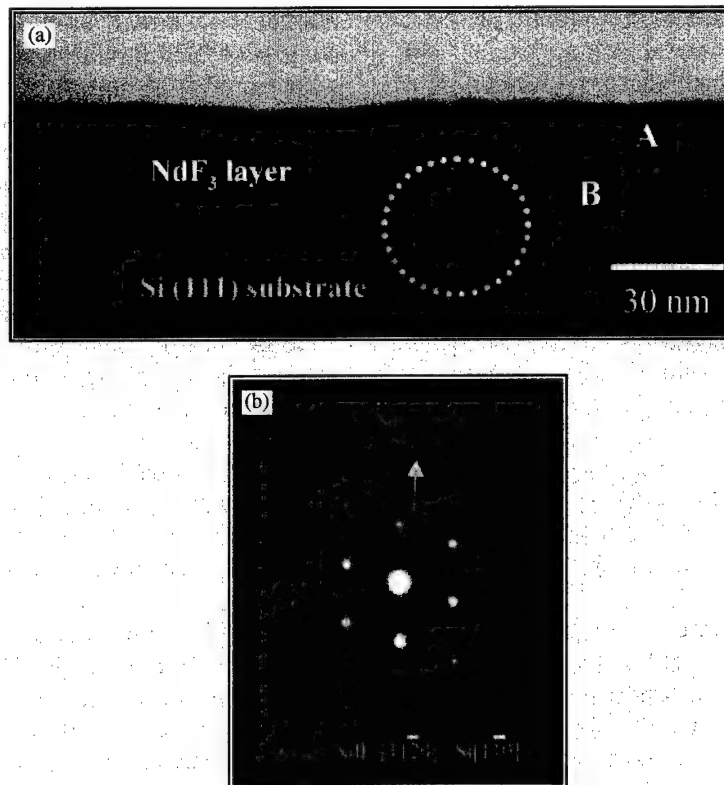


Fig. 1. (a) A cross-sectional TEM micrograph of NdF_3/Si (111) layer (layer thickness ~ 30 nm) grown at 400°C and (b) selected area electron diffraction pattern taken for Si $[1\bar{1}0]$ and NdF_3 $[11\bar{2}0]$ direction.

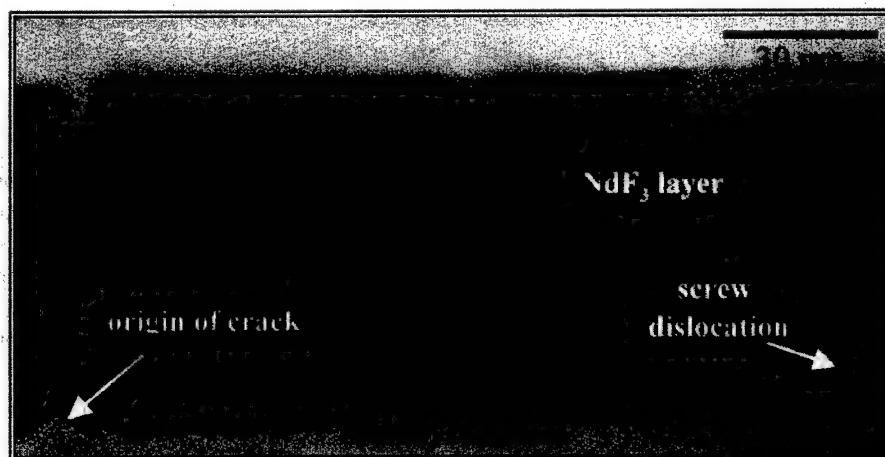


Fig. 2. A cross-sectional TEM micrograph of NdF_3/Si (111) layer (layer thickness ~ 60 nm) grown at 550°C .

process. The undesirable formation of such clusters induced additional stress around the interfacial region, and enhanced the formation of the tilted polycrystalline grains at B-region. As the thickness of the overall NdF_3 layer increased, A-region became dominant and B-region was embedded by A-region at last.

The NdF_3 layer grown at 550°C contained no secondary phase (Fig. 2). The micrograph of NdF_3/Si (111) interface shows that the NdF_3 layer of uniform thickness ($\sim 60\text{ nm}$) includes defects such as stacking faults, screw dislocations and microcracks. These defects started to propagate from the NdF_3/Si (111) interface. In the interface region, abnormally grown clusters of 3–4 nm size were observed and it was confirmed by minute examination of lattice image that the crystallographic orientation of the layer near the interface is strongly influenced by the abnormally grown clusters. Defects contained in the layer were attributed to the induced stress near the interface, which was developed by the orientational mismatch of NdF_3 (0002) plane. As the thickness of the layer increased, the (0002) planes of the NdF_3 layer were aligned parallel with each other, relaxing the induced stress by making screw dislocations or stacking faults. Also, the induced stress around the clusters provides origin of microcrack by the difference of thermal expansion coefficient during the cooling process. It was reported that the thermal coefficient of the lattice mismatch between NdF_3 layers and Si (111) substrates along the $[1\ 1\ \bar{2}\ 0]_{\text{NdF}_3} \parallel [1\ 1\ \bar{2}]_{\text{Si}}$ direction, was estimated to be 6.04% at room temperature [12].

The TEM micrograph in Fig. 3a, shows the interfacial structure of NdF_3 layers grown at 700°C . The NdF_3 layer of uniform thickness ($\sim 40\text{ nm}$) was observed. The diffraction pattern achieved from that region confirmed that the NdF_3 layer was grown on Si (111) substrate with the epitaxial relationship of $\text{NdF}_3(0002) \langle 1\ 1\ \bar{2}\ 0 \rangle \parallel \text{Si}(111) \langle 1\ \bar{1}\ 0 \rangle$ and the crystallinity of the NdF_3 layer grown at 700°C were improved compared to those of the layers grown at 400°C and 550°C . Intermediate phase of 3–5 nm thickness was observed in the NdF_3/Si (111) interface and this phase was thought to be expanded NdF_3 layer, which was formed by the induced stress

developed by lattice mismatch, or Nd–Si–F-based compound which was synthesized by relatively high temperature during initial growing process. The NdF_3 layers showed a trend that the density of defects in the NdF_3 layer decreased with the thickness of intermediate phase increasing. Therefore, the intermediate phase is thought to compensate the induced stress developed by the lattice mismatch during the growing process or the difference of thermal expansion coefficients during the cooling process.

For the investigation of crystallinity, XRD analysis for out-of-planes and in-planes of NdF_3 layers was done and a noteworthy feature was observed in in-plane rocking curve of NdF_3 layer grown at 700°C . As shown in Fig. 4, two separated peaks were observed from the NdF_3 (3 3 $\bar{6}$ 0) plane. The right peak shows small deviation depending on the grazing angle from 0.20° to 0.30° , whereas the left near 81.4° increased abruptly with the increase in grazing angle. This feature indicates that two lattice-plane groups with slightly different lattice parameters exist within the NdF_3 layer grown at 700°C and, in particular, the plane group close to the substrate was expanded. The expanded layer is considered to originate from the intermediate layer observed in the NdF_3/Si (111) interface (in Fig. 3a) or from the modification of crystal structure by itself due to induced stress.

The crystal structure of NdF_3 is reported to belong to tysonite-type structure. In case of tysonite, the structure has not been reported obviously because of the high mobility of F^- ions at room temperature. Apparently, NdF_3 can crystallize in at least two different modifications (space groups Pc_1 and $\text{P6}_3/\text{mmc}$), the first corresponding to ordering and a lower symmetry of the anionic array ($Z = 6$) and the second in which the anionic array is less ordered and has a higher symmetry ($Z = 2$). Moreover, it was reported that F^- ions in tysonite structure can transport with ease in perpendicular c -axis [15]. Therefore, the result of in-plane X-ray rocking curves can be explained by modification or expansion of tysonite structure by the transition of F^- ions into typical crystallographic site by the induced tensile stress during cooling process. Due to the difference of thermal expansion coefficient, tensile stress is

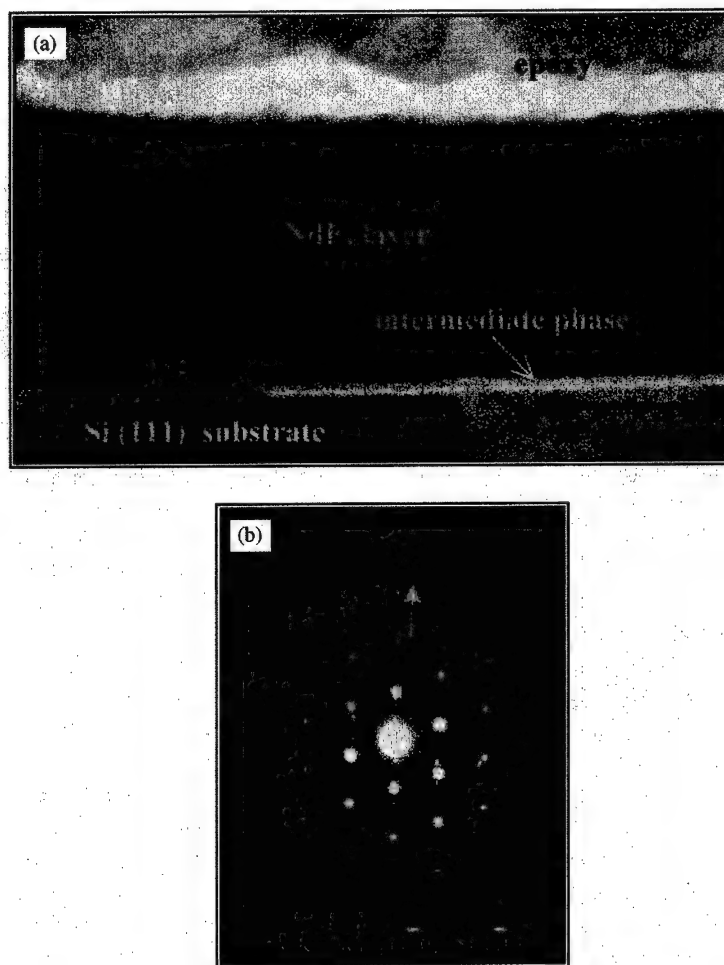


Fig. 3. (a) A cross-sectional TEM micrograph of $\text{NdF}_3/\text{Si}(111)$ layer (layer thickness ~ 40 nm) grown at 700°C and (b) selected area electron diffraction pattern taken for $\text{Si}[1\bar{1}0]$ and $\text{NdF}_3[11\bar{2}0]$ direction.

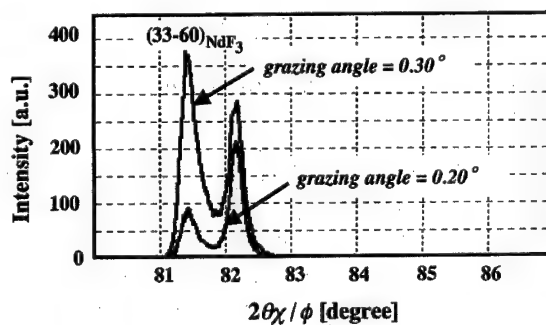


Fig. 4. X-ray rocking curves of $(33\bar{6}0)_{\text{NdF}_3}$ diffraction with different grazing angles of incident X-ray beams (0.20° and 0.30°).

loaded into the NdF_3 layer, more severely into the area close to substrate. Considering the intensity deviation of left-side peak and the volume effect of XRD, the phenomena observed in the in-plane X-ray rocking curve can be explained more reasonably by the modification or expansion of tysonite structure due to the transition of F^- ion sites than the expanded intermediate phase in the interface.

The crystallinity of grown layers at 400°C , 550°C and 700°C were measured by FWHM value of in-plane and out-of-plane as shown in Fig. 5. The FWHM value of 550°C had the highest value

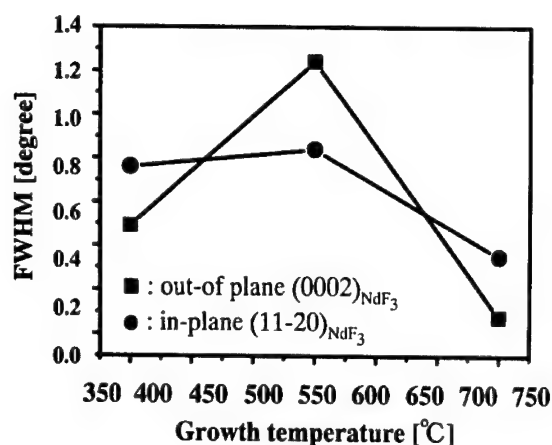


Fig. 5. Dependence of FWHM values of both out-of plane (0002)_{NdF₃} and in-plane (11-20)_{NdF₃} rocking curves on growth temperature (400°C, 550°C, and 700°C).

in both in-plane and out-of-plane, whereas lowest values were measured at 700°C. The NdF₃ layer grown at 700°C showed improved crystallinity compared with that of layers grown at 400°C and 500°C. These results are well agreed with the cross-sectional view of the NdF₃/Si (111) depending on the growth temperature. The decrease of crystallinity of the NdF₃ layer grown at 550°C is attributed to the induced stress developed by abnormally grown clusters in initial growth stage. On the contrary, the increase of that of 700°C is probably attributed to Nd–Si–F-based intermediate phase or expanded NdF₃ layer formed in NdF₃/Si (111) interface and also attributed to modified tysonite structure influenced by F[−] ion transition into typical crystallographic site in the underside of NdF₃ layer.

4. Summary

NdF₃ layers were grown depending on the growth temperature. The surface morphology from AFM images showed that the NdF₃ layers were grown as islands associated with spiral growth mechanism. The crystallinity and the interfacial structure of NdF₃/Si (111) were investigated by XRD analysis for in-plane and out-of-plane and TEM-SAD. As results of XRD and

diffraction patterns by TEM analysis, NdF₃ layers were grown conformably on Si (111) substrate with the epitaxial relationship of NdF₃(0002) $\langle 11\bar{2}0 \rangle \parallel \text{Si}(111)\langle 1\bar{1}0 \rangle$. In the interface region, polycrystalline secondary phase, abnormally grown clusters and intermediate or expanded NdF₃ layers were observed. The secondary phase and abnormally grown clusters decreased the crystallinity, whereas the expanded or intermediate phase in the interface increased the crystallinity by compensating the induced stress that was developed by the lattice mismatch in initial growth stage. Also, separate two peaks were observed in in-plane X-ray rocking curve for (33 $\bar{6}$ 0) plane is attributed to the expansion of tysonite structure by F[−] ion migration. For the device applications, the intermediate phase and expansion of the structure are thought to be desirable for the improvement of crystallinity and stress relaxation mechanisms.

References

- [1] T. Asano, H. Ishiwara, J. Appl. Phys. 55 (1984) 3566.
- [2] S. Siskos, C. Fontaine, A. Munoz-Yague, Appl. Phys. Lett. 44 (1984) 1146.
- [3] K. Sugiyama, J. Appl. Phys. 56 (1984) 1733.
- [4] S. Sinharoy, R.A. Hoffman, J.H. Rieger, R.F.C. Farrow, A.J. Noreika, J. Vac. Sci. Technol. A 3 (1985) 842.
- [5] K. Tsutsui, H. Ishiwara, T. Asano, S. Furukawa, Appl. Phys. Lett. 46 (1985) 1131.
- [6] B. Schumann, G. Kühn, W. Gasch, G. Wagner, R. Flaggmeyer, O. Müller, W. Hauße, J. Crystal Growth 82 (1987) 405.
- [7] L.E. Bausa, R. Legros, A. Munoz-Yague, Appl. Phys. Lett. 59 (1991) 152.
- [8] C.C. Cho, W.M. Duncan, T.H. Lin, S.K. Fan, Appl. Phys. Lett. 61 (1992) 1757.
- [9] S. Uda, K. Adachi, K. Inaba, T. Yao, A. Kasuya, T. Fukuda, Jpn. J. Appl. Phys. 36 (Part 2) (1997) L41.
- [10] D.K. Fork, F. Armani-Leplingard, M. Lui, R.A. McFarlane, J. Lightwave Technol. 14 (1996) 611.
- [11] J.M. Ko, S.D. Drubin, T. Fukuda, K. Inaba, J. Vac. Sci. Technol. A 18 (3) (2000) 922.
- [12] J.M. Ko, K. Inaba, S.D. Durbin, T. Fukuda, J. Crystal Growth 212 (2000) 155.
- [13] J.M. Ko, K. Lebbou, C. Dujardin, C. Pedrini, S.D. Durbin, T. Fukuda, Opt. Mater. 19 (2002) 139.
- [14] A. Ishizaka, Y. Shiraki, J. Electrochem. Soc. 133 (1986) 666.
- [15] A. Rhandour, J.M. Reau, S.F. Matar, S.B. Tian, P. Hagenmuller, Mater. Res. Bull. 20 (1985) 1309.

CrN single-crystal growth using Cr–Ga–Na ternary melt

Masato Aoki^{a,*}, Hisanori Yamane^a, Masahiko Shimada^a, Takashi Kajiwara^b

^a*Institute of Multidisciplinary Research for Advanced Materials (IMRAM), Tohoku University, 2-1-1 Katahira, Aoba-ku, Sendai 980-8577, Japan*

^b*Department of Chemistry, Graduate School of Science, Tohoku University, Aramaki, Aoba-ku, Sendai 980-8577, Japan*

Received 11 September 2002; accepted 14 September 2002

Communicated by L.E. Schneemeyer

Abstract

Regular octahedral CrN single crystals with a maximum size of 75 μm were obtained by heating Cr–Ga–Na ternary melt at 850°C and 3 MPa of N_2 for 200 h. X-ray powder and single-crystal diffractometry revealed that the CrN single crystals had the cubic rock-salt structure with the lattice parameter $a = 4.1467(8)$ Å. The CrN single crystals exhibited antiferromagnetism below the Néel temperature of 290 K.

© 2002 Elsevier Science B.V. All rights reserved.

PACS: 61.10.Nz; 75.50.Ee; 81.10.Dn

Keywords: A1. Crystal morphology; A1. X-ray diffraction; A2. Growth from solutions; A2. Single-crystal growth; B1. Nitrides; B2. Magnetic materials

1. Introduction

CrN having the cubic rock-salt structure is a well-known hard coating material with excellent corrosion, oxidation, and wear resistance [1]. CrN powders have been synthesized by heating Cr metal at about 1000°C under N_2 or NH_3 atmosphere [2–5]. Recently, ammonolysis of Cr_2S_3 [6] and the benzene-thermal method [7] were applied to prepare CrN powders. Although films, coatings and powders of CrN were prepared in the previous

studies, there are no reports on growth of CrN bulk single crystals.

CrN shows antiferromagnetism with the Néel temperature of 273–286 K [4–6,8] unlike the superconducting rock-salt-type nitrides of TiN and VN. Thus, the magnetic structure also received much attention in the field of the basic science. The magnetic transition from paramagnetism to antiferromagnetism is accompanied by orthorhombic distortion of the cubic rock-salt structure at the Néel temperature.

In this study, we succeeded in preparing CrN single crystals by heating Cr–Ga–Na ternary melt at 800–850°C and 1–5 MPa of N_2 . The crystal structure was confirmed by X-ray diffraction of the single crystals and powdered samples. We also

*Corresponding author. Tel./fax: +81-22-217-5160.

E-mail addresses: aoki@iamp.tohoku.ac.jp (M. Aoki), yamane@tagen.tohoku.ac.jp (H. Yamane).

investigated the magnetic properties of the CrN single crystals.

2. Experimental procedure

Cr metal (Kojundo Chemical Laboratory, 99.9%), Ga metal (Rasa Industries, 99.99995%) and Na metal (Nippon Soda, 99.95%) were used as starting materials. In an Ar filled glove box ($O_2 < 1$ ppm, $H_2O < 1$ ppm), Cr (1 mmol), Ga (20 mmol) and Na (40 mmol) were weighed and charged into a BN crucible (Showa Denko, 99.5%, 16 mm inner diameter, 12 mm depth). After the crucible was put into a stainless-steel container, the container was connected to a N_2 gas feed line. The apparatus was similar to that used for GaN single-crystal growth using Na–Ga melt [9]. The sample was heated to a predetermined temperature in an Ar atmosphere. As soon as the sample had reached the set temperature, N_2 gas (Nippon Sanso, >99.9999%) was introduced into the container. Crystal growth experiments were carried out for 200 h at the temperatures of 800–850°C and N_2 pressures of 1–5 MPa. The total gas pressure in the stainless-steel container was kept at 5 MPa to reduce the loss of Na by evaporation. When the N_2 pressure was less than 5 MPa, Ar gas (Nippon Sanso, >99.9999%) was added to maintain the total gas pressure in the container at 5 MPa. After furnace cooling of the sample to room temperature, Na metal remaining in the crucible was removed by reaction with methanol and ethanol. Ga remaining as crystals of Na–Ga intermetallic compound ($Ga_{39}Na_{22}$) [10] was removed by dissolution in aqua regia. Comparative experiments using Cr–Ga (1 mmol:20 mmol) and Cr–Na (1 mmol:40 mmol) binary melts were also performed at 800°C and 5 MPa of N_2 for 200 h.

Products were characterized by X-ray powder diffractometry and energy dispersive X-ray spectroscopy (EDX). X-ray diffraction intensities for the powdered samples were collected using $CuK\alpha$ radiation with a diffractometer (Rigaku, RINT 2000). EDX spectrum was measured by an energy dispersive X-ray analyzer (NORAN, VOYAGER) installed in a scanning electron microscope (SEM: JEOL, JSM-6320F). The lattice parameter of CrN

was determined by the least squares method from X-ray powder diffraction data. X-ray powder diffraction data for the lattice parameter determination were collected on an imaging plate Guinier camera (HUBER, G670) using $CuK\alpha_1$ radiation ($\lambda = 1.54056 \text{ \AA}$). 2θ angles were corrected by using Si powder (Mitsuwa Chemicals, >99.999%) as an internal standard. Single-crystal X-ray diffraction intensities were measured by a diffractometer equipped with a two-dimensional CCD area detector (BRUKER, SMART1000). $MoK\alpha$ radiation ($\lambda = 0.71073 \text{ \AA}$) and the ω scan mode were used for the intensity measurements. Crystal structure parameters were refined by the program SHELXL-97 [11]. Magnetic susceptibility was measured with a SQUID magnetometer (QUANTUM DESIGN, MPMS₂) from 10 to 350 K under the magnetic field of 1000 G. Corrections were made for the diamagnetic susceptibility of the sample holder.

3. Results and discussion

3.1. CrN single-crystal growth

Fig. 1(a) shows an X-ray powder diffraction pattern of the products prepared at 800°C and 5 MPa of N_2 . Hexagonal wurtzite-type GaN and cubic rock-salt-type CrN were obtained at this experimental condition. The present temperature– N_2 pressure condition was deeply in the GaN formation region reported in the previous study in which the growth conditions of GaN single crystals using Na–Ga melt were investigated [12]. According to the published thermodynamical data [13], the standard free energy of formation of CrN is lower than that of GaN. Therefore, it was expected that the single phase of CrN could be obtained at higher temperatures and lower N_2 pressures than the above condition. At 850°C and 3 MPa of N_2 that was near the boundary condition of the GaN formation region, most of the products were CrN single crystals but a small amount of GaN formed. The single phase of CrN was synthesized at 850°C under a still lower N_2 pressure of 1 MPa. This condition was in the GaN decomposition region. X-ray powder diffraction

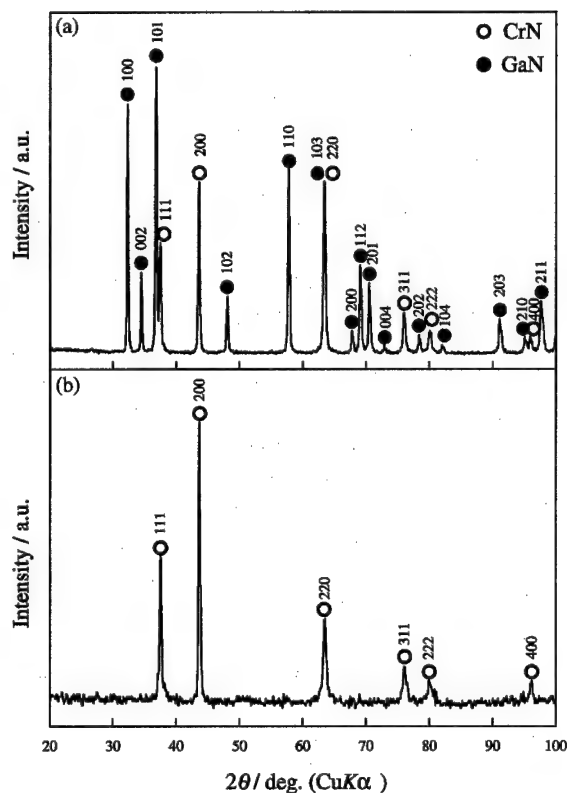


Fig. 1. X-ray powder diffraction patterns of products prepared by using the Cr–Ga–Na melt at 800°C under 5 MPa of N_2 (a) and at 850°C under 1 MPa of N_2 (b).

pattern of the sample is shown in Fig. 1(b). Fig. 2 shows an EDX spectrum of a CrN single crystal. Only Cr and N except a peak of background carbon were detected.

CrN single crystals synthesized at 850°C and 1 MPa of N_2 had the regular octahedral habit bounded by $\{111\}$ faces and a size of about 5 μm . Single crystals prepared at 850°C and 3 MPa of N_2 also had the regular octahedral shape and grew up to 75 μm . SEM images of the single crystals grown at this experimental condition are shown in Fig. 3. At 800°C and 5 MPa of N_2 , not only octahedral crystals with several tens of micrometers but also platelet crystals having about 200 μm were obtained. Regular triangular step edges were observed on the surfaces of platelet crystals. All the CrN single crystals obtained in this study were black.

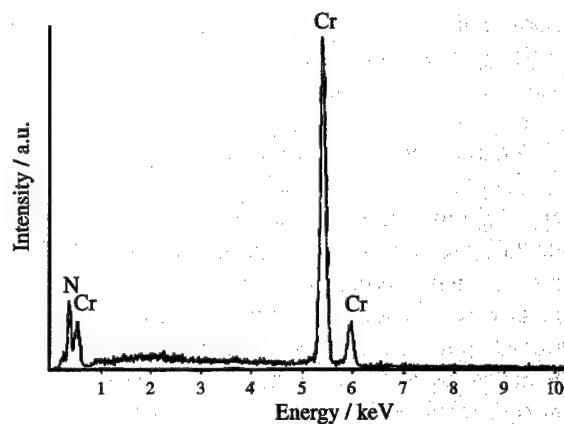


Fig. 2. EDX spectrum of a CrN single crystal prepared by using the Cr–Ga–Na melt.

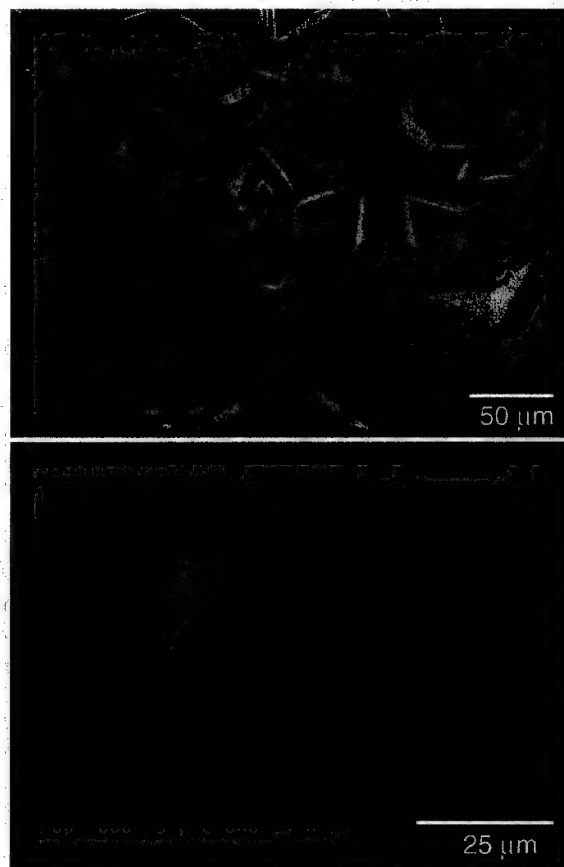


Fig. 3. SEM images of CrN single crystals synthesized at 850°C and 3 MPa of N_2 for 200 h using the Cr–Ga–Na melt.

To compare with the results of CrN single-crystal growth using the Cr–Ga–Na ternary melt, experiments using the Cr–Ga and Cr–Na binary melts were carried out at 800°C and 5 MPa of N₂ for 200 h. When the Cr–Ga melt was used, single crystals of CrGa₄ intermetallic compound [14] were deposited and no CrN crystals were obtained. Since Cr did not dissolve in molten Na and stayed in solid at the temperature of 800°C, CrN could not also be synthesized by using the Cr–Na melt. According to the Cr–Na binary phase diagram [15], the solubility of Cr in molten Na is almost zero.

From these results, CrN single crystals were obtained only by using Cr–Ga–Na ternary melt. The role of Ga is to dissolve Cr and the solubility of Cr in molten Ga at 800°C is about 10at% [16]. As discussed in the synthesis of GaN using the Na–Ga melt [17,18], Na would play the role of a catalyst to weaken the triple bond of N₂ molecule and to enhance the nitriding of Cr. CrN, a nitride of high melting-point metal, could be synthesized as single crystals at 800–850°C by using the Ga–Na metal flux which lowered the melting temperature of Cr metal with Ga and enhanced the nitriding of Cr with Na.

3.2. Crystal structure refinement

X-ray powder diffraction data revealed that the CrN single crystals prepared in this study had the cubic rock-salt structure at room temperature. The refined lattice parameter was $a = 4.1467(8)$ Å at 298 K. This value was in the range of 4.13–4.15 Å reported in the literatures [2,4–8].

The measurement conditions of the X-ray single-crystal diffraction experiment and the results of structure analysis are listed in Table 1. The R_1 factor and wR_2 factor for all data were 1.78% and 3.70%, respectively. Table 2 lists the calculated and observed structure factors. The thermal parameters ($U_{11} = U_{22} = U_{33}$) of Cr (atomic position, 0, 0, 0) and N (atomic position, 1/2, 0, 0) were 0.0031(13) and 0.002(2) Å², respectively.

3.3. Magnetic properties

Temperature dependences of molar susceptibility (χ_{mol}) and inverse molar susceptibility ($1/\chi_{\text{mol}}$)

Table 1

Crystal data and structure refinement for the CrN single crystal

Space group	$Fm\bar{3}m$
Z	4
Crystal size	$0.05 \times 0.05 \times 0.05$ mm ³
θ range for data collection	8.54–29.02°
Limiting indices	
h	–5–5
k	–5–4
l	–5–3
Reflection numbers	139
Refinement method	Full-matrix least squares on F^2
Data/restraints/parameters	12/0/4
S , goodness-of-fit on F^2	1.498
R indices (all data)	
R_1	0.0178
wR_2	0.0370
Extinction coefficient	0.0024(9)

Note: $R_1 = \sum ||F_o| - |F_c|| / \sum |F_o|$, $wR_2 = [\sum w(F_o^2 - F_c^2)^2 / \sum (wF_o^2)^2]^{1/2}$, $w = 1/[\sigma^2(F_o^2) + (0.0000P)^2 + 70.3985P]$, where F_o is the observed structure factor, F_c is the calculated structure factor, σ is the standard deviation of F_o^2 and $P = [\text{Max}(F_o^2, 0) + 2F_c^2]/3$. $S = [\sum w(F_o^2 - F_c^2)^2 / (n - p)]^{1/2}$, where n is the number of reflections and p is the total number of parameters refined.

Table 2

Calculated structure factors (F_c), observed structure factors (F_o) and standard deviations (σ) of F_o for the CrN single crystal

h	k	l	$10F_c$	$10F_o$	10σ
1	1	1	3289	3213	18
0	0	2	5003	5030	15
0	2	2	3950	3922	9
2	2	2	3327	3405	16
1	1	3	2337	2400	8
1	3	3	1838	1858	9
3	3	3	1546	1604	16
0	0	4	2917	2859	15
0	2	4	2627	2598	8
2	2	4	2413	2460	8
0	4	4	2119	2100	17
1	1	5	1546	1460	9

of the CrN single crystals prepared in this study are shown in Fig. 4. The Néel temperature (T_N) of the CrN single crystals was 290 K and the temperature width of the transformation from antiferromagnetism to paramagnetism was less than 3 K. The T_N temperature was slightly higher than the reported ones (273–286 K) [4–6,8]. It is

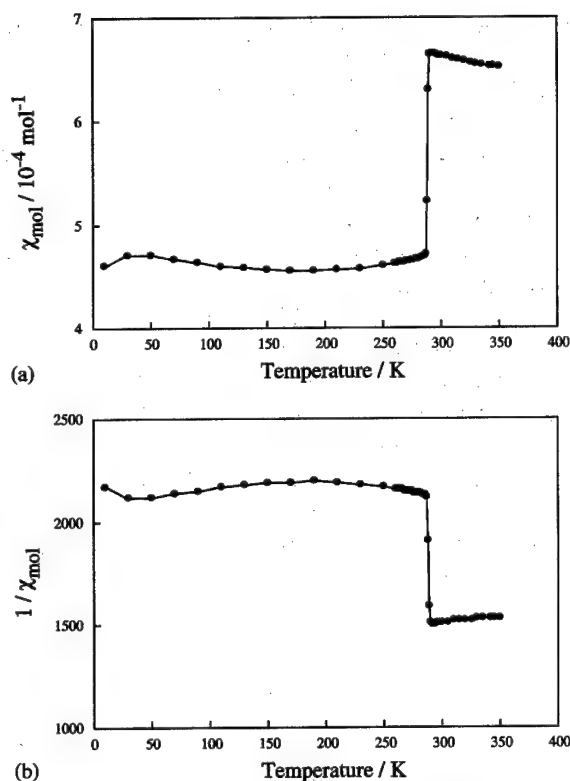


Fig. 4. Temperature dependences of molar susceptibility, χ_{mol} , (a) and inverse molar susceptibility, $1/\chi_{\text{mol}}$, (b) of the CrN single crystals.

known that the properties of CrN are very sensitive to non-stoichiometric composition. Browne et al. [5] investigated the effect of x in CrN_x on T_N and reported that nitrogen deficiency lowered T_N ; e.g., T_N of $\text{CrN}_{0.997}$ and $\text{CrN}_{0.980}$ were 286 and 276 K, respectively. They also pointed out that oxygen impurity in CrN broadened the transformation temperature width. Therefore, it was expected that the CrN single crystals prepared by using the Cr–Ga–Na melt were oxygen free and their chemical composition was close to stoichiometry.

Above T_N , the temperature dependence curve of $1/\chi_{\text{mol}}$ gave the Weiss constant (T_θ) of -2650 K, Curie constant (C) of 1.95 and magnetic moment (m) of $3.96\mu_B$ per Cr atom. The values of T_θ and m agreed with the values reported by Bloch et al. ($T_\theta = -2600$ K, $m = 4.09\mu_B$) [8]. The magnetic moment obtained in this study ($3.96\mu_B$) was

consistent with the theoretical value of $3.87\mu_B$ corresponding to a spin of $3/2$ for Cr^{3+} .

4. Conclusion

CrN single crystals were synthesized by heating the Cr–Ga–Na melt at 800 – 850°C and 1 – 5 MPa of N_2 . Regular octahedral single crystals of CrN with a maximum size of $75\mu\text{m}$ were obtained at 850°C and 3 MPa of N_2 for 200 h. The single crystals had the cubic rock-salt structure with the lattice parameter $a = 4.1467(8)\text{\AA}$ at 298 K. The CrN single crystals exhibited antiferromagnetism with the Néel temperature of 290 K.

Acknowledgements

We thank Professor T. Ito for his support and Y. Hayasaka for the EDX analysis. This work was supported in part by a grant from the Ministry of Education, Culture, Sports, Science and Technology.

References

- [1] B. Navinšek, P. Panjan, I. Milošev, *Surf. Coat. Technol.* 97 (1997) 182.
- [2] R. Blix, *Z. Phys. Chem. (B)* 3 (1929) 229.
- [3] Z.G. Pinsker, L.N. Abrosimova, *Sov. Phys. Crystallogr.* 3 (1958) 285.
- [4] L.M. Corliss, N. Elliott, J.M. Hastings, *Phys. Rev.* 117 (1960) 929.
- [5] J.D. Browne, P.R. Liddell, R. Street, T. Mills, *Phys. Status Solidi (A)* 1 (1970) 715.
- [6] P.S. Herle, M.S. Hegde, N.Y. Vasathacharya, S. Philip, *J. Solid State Chem.* 134 (1997) 120.
- [7] X.F. Qian, X.M. Zhang, C. Wang, K.B. Tang, Y. Xie, Y.T. Qian, *Mater. Res. Bull.* 34 (1999) 433.
- [8] D. Bloch, P. Mollard, J. Voiron, *C. R. Acad. Sci. Paris* 269 (1969) B-553.
- [9] M. Aoki, H. Yamane, M. Shimada, T. Sekiguchi, T. Hanada, T. Yao, S. Sarayama, F.J. DiSalvo, *J. Crystal Growth* 218 (2000) 7.
- [10] R.G. Ling, C. Belin, *Acta Crystallogr. B* 38 (1982) 1101.
- [11] G.M. Sheldrick, *SHELXL-97*, University of Göttingen, Germany, 1997.
- [12] M. Aoki, H. Yamane, M. Shimada, S. Sarayama, F.J. DiSalvo, *J. Ceram. Soc. Jpn.* 109 (2001) 858.

- [13] O. Knacke, O. Kubaschewski, K. Hesselmann (Eds.), *Thermochemical Properties of Inorganic Substances*, 2nd Edition, Springer, Berlin.
- [14] K. Schubert, T.R. Anantharaman, H.O.K. Ata, H.G. Meissner, M. Pötzschke, W. Rossteutscher, E. Stolz, *Naturwissenschaften* 47 (1960) 512.
- [15] M. Venkatraman, J.P. Neumann, in: T.B. Massalski, H. Okamoto, P.R. Subramanian, L. Kacprzak (Eds.), *Binary Alloy Phase Diagrams*, 2nd Edition, Vol. 2, ASM International, Columbus, Ohio.
- [16] J.D. Bornand, P. Feschotte, *J. Less-Common Met.* 29 (1972) 81.
- [17] H. Yamane, D. Kinno, M. Shimada, T. Sekiguchi, F.J. DiSalvo, *J. Mater. Sci.* 35 (2000) 801.
- [18] M. Aoki, H. Yamane, M. Shimada, S. Sarayama, F.J. DiSalvo, *Crystal Growth Des.* 1 (2001) 119.



ELSEVIER

Available online at www.sciencedirect.com

SCIENCE @ DIRECT®

JOURNAL OF
CRYSTAL
GROWTH

Journal of Crystal Growth 246 (2002) 139–149

www.elsevier.com/locate/jcrysgro

Surface imaging of a natural mineral surface using scanning-probe microscopy

D.G. Bokern¹, W.A.C. Ducker², K.A. Hunter, K.M. McGrath*

Department of Chemistry, University of Otago, P.O. Box 56, Dunedin, New Zealand

Received 5 August 2002; accepted 19 August 2002

Communicated by R. Kern

Abstract

The {001} surface of natural BaSO₄ was examined in air and aqueous solution using atomic force microscopy (AFM). On the atomic scale, the arrangement of ions on the {001} cleavage plane is the same (within experimental error) as in the bulk crystal. Fourier transform maps of the atomic scale AFM images yielded surface lattice parameters of $a = 5.54 \pm 0.04 \text{ \AA}$ and $b = 8.84 \pm 0.03 \text{ \AA}$, indicating that AFM images can be used to obtain crystallographic data of surfaces and to assign surface symmetry as compared with bulk structure. On the micrometre-scale we observed crystallographically orientated monosteps one unit cell (along the *c*-axis) in height and polysteps as well as etch figures with intrinsic 2₁ screw axis symmetry after dissolution in water on an overall heterogeneous {001} cleavage plane. In addition to etch pit formation, half-unit-cell-high steps following certain crystal directions ([210] and [010]) could be observed, emphasizing the structural control of the dissolution process. Prolonged exposure of a cleaved barite surface to ambient air led to significant surface rearrangement due to the formation and reprecipitation of surface-hydration species within an adsorbed layer of water. Atomistic models of the {001} cleavage plane, crystallographically oriented step edges along [210] and [010] and etch figure boundaries are reported. From these an understanding of the growth and dissolution processes of barite was derived in addition to an explanation of observed step retreat velocities based on surface charging and energetic arguments.

© 2002 Elsevier Science B.V. All rights reserved.

PACS: 68.35.Bs

Keywords: A1. Atomic force microscopy; A1. Surface structure; A2. Growth from solutions; B1. Barite; B1. Minerals

1. Introduction

X-ray crystallography is the classical method for examining the detailed structure of ionic crystals. An important shortcoming of this method is that it measures properties of the bulk crystal. In many situations the reactivity of crystalline solids is controlled by the nature of the crystal surface, which may through the presence of defects or

*Corresponding author. Tel.: +64-3-479-7932; fax: +64-3-479-7906.

E-mail address: kate@alkali.otago.ac.nz (K.M. McGrath).

¹Present address: SONY International (Europe) GmbH, Materials Science Laboratories, Advanced Technology Center Stuttgart, Stuttgart, Germany.

²Present address: Department of Chemistry, Virginia Institute of Technology, Blacksburg, VA 24061, USA.

Table 1
Structural properties of barite

Barite (BaSO ₄)	
Unit cell [8]	$a = 5.45 \text{ \AA}$, $b = 8.88 \text{ \AA}$, $c = 7.15 \text{ \AA}$ $Z = 4$; space group Pnma
Surface lattice parameters obtained from Fourier transform maps of 35 atomic scale AFM images ^a	$a = 5.30 \pm 0.04 \text{ \AA}$, $b = 8.84 \pm 0.03 \text{ \AA}$

^aThe systematic error in the calibration of the AFM piezo scanner is ca. 5%. The errors given in the table are those determined from averaging the 35 images. The data are precise to less than 1% and have an accuracy of approximately 5%.

reconstruction present quite different structural properties. The relatively recent technique of AFM offers the potential for examining surface crystal structure and reaction mechanisms. Here we report on the application of AFM to a study of the surface crystallographic properties of the natural mineral barite.

Barite is a simple ionic AB-type crystal of very low water-solubility ($K_{sp}(\text{BaSO}_4) = 1.05 \times 10^{-10} \text{ mol}^2 \text{ l}^{-2}$). It is also a naturally occurring mineral of considerable structural, morphological and geochemical importance. Barite commonly occurs in geological settings as well-formed crystals but also exists as fibrous, lamellar and earthy aggregates. Crystals of barite have a vitreous-to-resinous and occasionally pearly lustre, and are colourless or white when pure.

Barite is also a biologically synthesized skeletal material [1] and is important commercially because of its undesired occurrence in off-shore oil-recovery systems when sulphate-rich seawater comes in contact with sub-surface formation water containing relatively high barium ion concentrations. This results in highly insoluble barite scale which blocks production tubing [2]. It is used for gastrointestinal barium X-ray examinations, which utilizes its low solubility and the good X-ray absorption coefficient of barium. The free Ba^{2+} ion is fairly toxic.

Surface microtopographic studies, especially on minerals, are not very common and microtopographic imaging, with high sensitivity by AFM or scanning tunnelling microscopy has only recently gained wider acceptance in the field of mineral interfaces. Characterization of microtopography and atomic surface structure is essential for an understanding of interfacial processes that occur

at mineral surfaces. The focus of most current studies in this area is on the fundamental aspects of crystal growth and dissolution of simple structured minerals. Calcite has, in general, been the mineral of choice because of its geological importance and its suitability as a sample for AFM, due to low solubility and its ability to be easily cleaved. Recently, however, barite has also begun to gain attention [3–5]. Research has also considered the controlled nucleation and morphology of barium sulphate crystallites on highly ordered organic assemblies (e.g. surfactant films) as model systems to understand biomineralization [6–8].

Barium sulphate crystallizes in the orthorhombic Pnma space group with four formula units in each cell; Table 1 gives the dimensions for the bulk crystallographic phase structure [9]. Barite (001) is the face of lowest free energy [10], but cleavage along (210), (110) and (100) is also possible. Each of the different crystal faces (hkl) have different atomic or molecular structures and bonding properties, and hence different surface free energies, sorption properties and growth (or dissolution) rates.

In this study we were interested in determining the microtopography of the barite {001} surface and in revealing its atomic structure in relation to that of the bulk crystal.

2. Experimental details

Colourless (pure) and optically clear natural barite crystals (Geology Department, Otago University) were found to cleave along {001} using a razor blade mounted on a steel plate in a

'guillotine-like' fashion to reveal a macroscopic {001} cleavage plane. The same source of barite was used throughout the research. Once cleaved the sample was glued (Superfix™, cyanoacrylate ester) onto a magnetic stainless-steel sample puck and loaded onto the AFM scanner. A very thin crystal plate was required for two reasons: firstly, to approximate sample thicknesses used during calibration, and secondly, to aid in sealing the cell.

A commercially available AFM (NanoScope III, Digital Instruments), based on optical beam deflection together with a fluid- or air-cell and high aspect ratio Ultralever-tips (Park Scientific Instruments), was used in this work. 180 μm cantilevers with an integrated high aspect ratio single crystalline silicon conical tip (spring constant 0.26 N/m) were UV-irradiated (253.7 nm for 30 min) and installed into an air-cell or a glass (BK-7 glass) fluid-cell. A 15.2 μm (E) and a 1.25 μm (A) scanner were used. "Digital steps" in the images were avoided by reducing the z limit from 440 to 110 V. Data were taken in both variable deflection and constant deflection (force) modes at room temperature and only raw data are shown for deflection images. Height image raw data were flattened. Flattening is necessary for larger scans of relatively flat samples where the non-linearity of the piezo influences the appearance of the resulting image. Data are displayed in an arbitrarily chosen grey scale. Contrast in the images usually reflects the topography, lighter shading in grey scale representing higher surface features, darker shading representing lower features.

In order to reduce the repulsive contact force between tip and sample in water the instrument was operated at setpoints around the so-called "jump in" force [11]. This was achieved by successively approaching the tip towards the surface from a large tip-to-sample separation (zero interaction force) until the tip "jumped" into the usually strong long-range attractive force regime close to the total minimum of interaction (pre-contact mode) and then reducing the setpoint slightly. In a similar way, the desired scanning force could be selected by adjusting the setpoint while continuously obtaining a force curve and then switching into the scanning function. Integral gains up to 20 were used in obtaining height-mode

images and integral gains of less than 2 were used for deflection-mode images. To ensure reproducibility, experiments were repeated at different points on each sample and on different samples.

Force curves between the tip and sample were also measured using the Nanoscope III AFM and analysed as described previously [12].

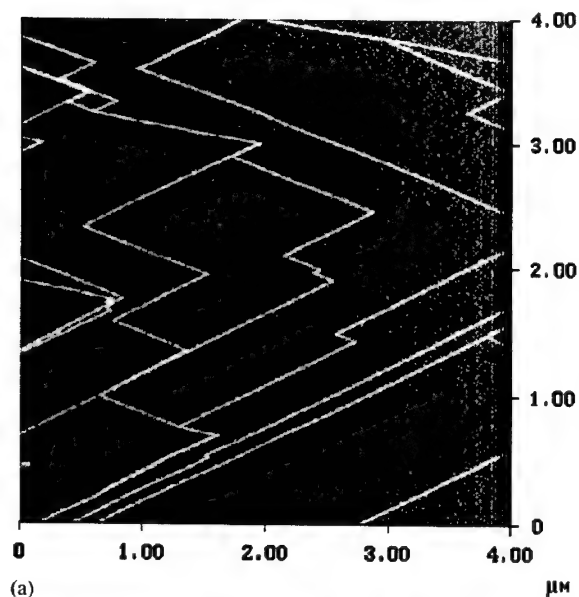
WebLabViewer Pro, from Molecular Simulations, Inc., was used to generate atomistic models of small blocks or layers from the 3D barite crystal structure, providing detailed visualization of the crystal's surface structure.

3. Results and discussion

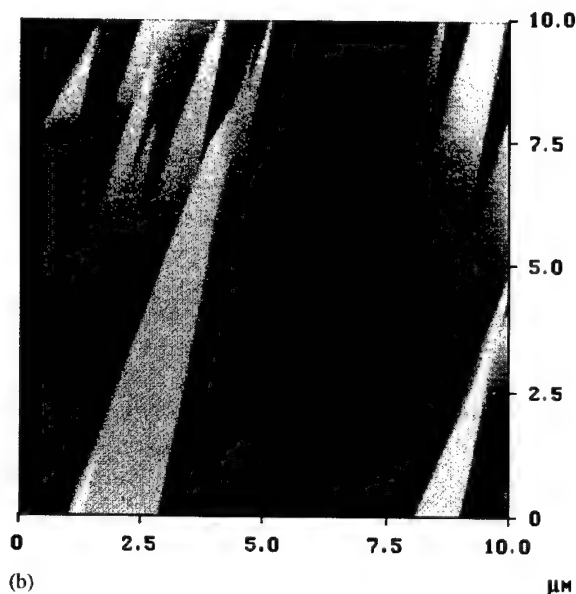
3.1. AFM imaging at the barite/water interface

Fig. 1(a) and (b) show the deflection and height images, respectively, of a typical micron-scale AFM image of a freshly cleaved BaSO_4 surface taken in air. The image shows atomically flat terraces separated by steps that are one unit cell high (c -axis, 7.15 Å). Image (b) is similar to that presented by Fenter et al. [13]. The step edges follow a rhombohedral {210} plane intersection, in difference with the {001} observation plane, and form two parallel sets at ca. 80°, which roughly represents the acute angle between {210} planes (78°). However, steps formed from both cleavage intersections are rare and often do not seem to follow any crystallographic outline as seen in Fig. 1(b), but rather indicate the direction of cleavage and fracture propagation, as described by Stipp et al. [14].

We also examined the surface morphology of BaSO_4 after exposure to ambient air. When viewed with a light microscope ($\times 600$), the surface was indistinguishable from a freshly cleaved surface, i.e. the crystal was transparent and the surface was reflective. In contrast, AFM imaging revealed that the barite samples were coated in a thick (4–8 nm), rough, soft surface layer (see Fig. 2). This surface layer could be easily displaced by scanning with an increased contact force, indicating that the new layer is loosely bound, and allowing us to measure the thickness. We postulate that this layer was formed by solubilization and reprecipitation of the



(a)



(b)

Fig. 1. (a) Large-scale AFM image of a freshly cleaved barite sample taken in air. The step height is one unit cell along the c -axis (7.15 \AA). The regular zigzag arrangement of these monosteps is crystallographically related to a rhombohedral intersection of a set of $\{210\}/\{\bar{2}10\}$ planes. (b) Height image in air of barite (001) showing surface monosteps due to direction of cleavage and fracture propagation rather than structural orientations as in (a).

surface atoms in the presence of atmospheric water and CO_2 . Further experiments using a controlled environment allowing intentional introduction of

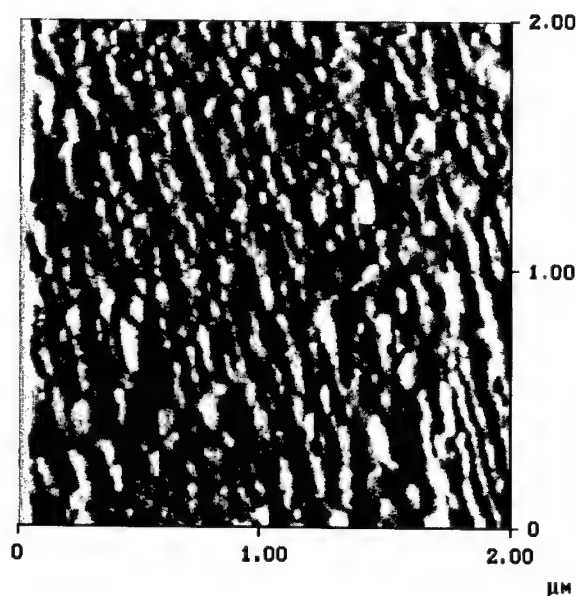


Fig. 2. AFM image of a barite surface left in ambient air for more than two days after cleavage. Surface rearrangement has taken place, possibly due to surface dissolution and reprecipitation of hydration species within a thin, invisible layer of water that is adsorbed from air humidity.

H_2O and/or CO_2 in a dry inert gas would allow for a greater understanding of this phenomenon.

The large morphological changes that occur on exposure to air suggest that surface studies of barite should only be performed on either freshly cleaved samples, or on samples that have been in a controlled environment. The surface is no longer crystalline after exposure to air. Similar observations have been published by Stipp and co-workers in a detailed AFM study [14] on surface rearrangement and surface-hydration species on calcite $\{10\bar{1}4\}$ cleavage faces in humidity- and CO_2 -controlled atmospheres. However, they found that the nature of reprecipitation depended on the original surface features on calcite, whereas we found that the entire surface was covered in an amorphous film.

Fig. 3 shows a higher magnification and higher resolution image of a freshly cleaved surface of barite. Periodic features are resolved, which have the same a , b lattice parameters as obtained from X-ray diffraction of the barite structure. However, in this picture we are only able to resolve the lattice

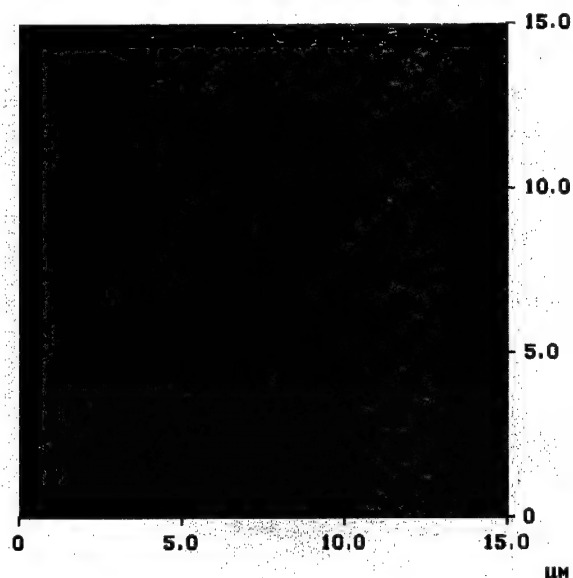


Fig. 3. AFM image taken in air on barite (001). Although, the surface unit cell correlates well with the a , b lattice constants of the X-ray structure, the fine structure is not reproduced owing to high interaction forces in air, multiple tip imaging and overlay of structures of the same periodicity.

of ions, and not individual defects, so this is not really 'atomic resolution'. The issue of atomic resolution in this system is the subject of an upcoming article.

Further support for the structural agreement between the surface unit cell (a , b) and the related XRD data can be obtained by taking Fourier transformation plots [15] of many larger-scale atomic images $40 \times 40 \text{ nm}^2$ scan size). This increases the signal-to-noise ratio and the summed images contain more data points, thereby producing more reliable integral values for a and b in comparison to a small scale (e.g. $5 \times 5 \text{ nm}^2$), with high-resolution, single image. The averaged values obtained via this process using measurements from 35 different experiments are given in Table 1. Fig. 4 shows a representative 2D FFT plot obtained from a 40 nm^2 AFM image of barite in water by applying a 2D fast Fourier transform (2D FFT) algorithm to the raw data. The data correspond well with the crystallographic bulk structure unit cell parameters, indicating that surface reconstruction is minimal.

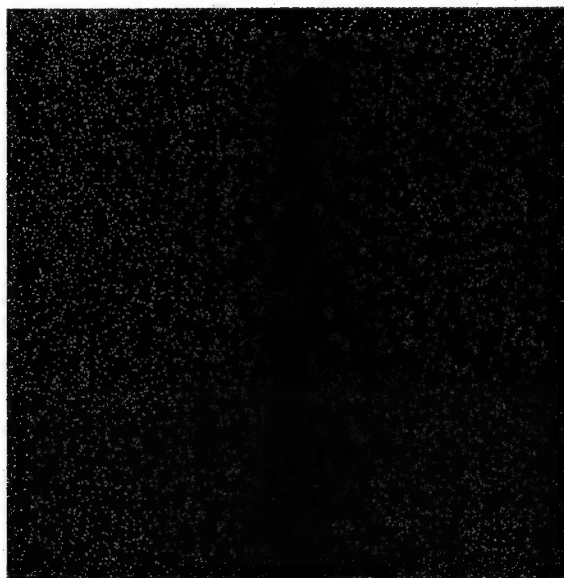


Fig. 4. A representative 2D FFT plot of a $40 \times 40 \text{ nm}^2$ AFM image of barite taken in water. The periodicities (peaks) correspond well with the crystal structure parameters. The extra peak at 0.47 nm probably results from the alternating orientation of sulphate surface ions within the original unit cell. However, there is no evidence for a pronounced reconstruction of the barite (001) surface. Higher orders of frequencies (periodicities) can also be seen.

In many 2D FFT plots of barite high-resolution images we observed additional peaks related to a periodicity of ca. 0.47 nm . In a study by Rachlin et al. [16] on Fourier analysis of AFM images of calcite it was noted that diffuse extra reflections on related low-energy electron diffraction (LEED) images might represent different orientations of CO_3^{2-} ions (i.e. surface reconstruction, since carbonate groups in the crystal structure of calcite have identical orientations with respect to the $\{10\bar{1}4\}$ cleavage face). Because of the inherent 2_1 screw symmetry of the barite structure the sulphate ions already have alternating orientations (as discussed below in Section 3.2; see Figs. 5 and 6). Hence, extra peaks might be expected even in the absence of any rearrangement of sulphate groups. However, the smaller periodicity in the direction of (10), the a -axis, remains somewhat unclear, as surface reconstruction normally leads to a larger surface unit cell. Application of a FFT to single high-resolution AFM images did not

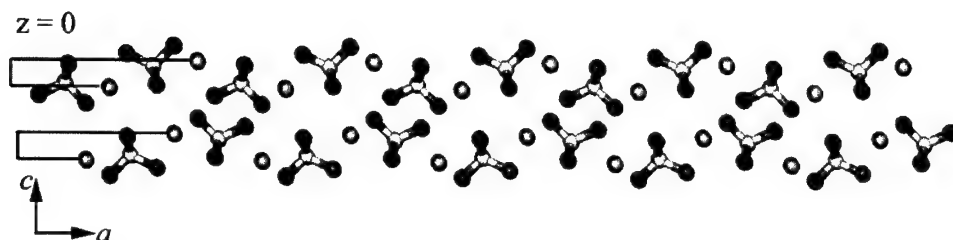


Fig. 5. The ac projection (i.e. view along $[010]$) of barite showing the upper and lower half of the unit cell and the four different height positions of the ions along the c -axis. The top layer of ions at $z = 0$ represents the actual (001) plane, shown in Fig. 6.

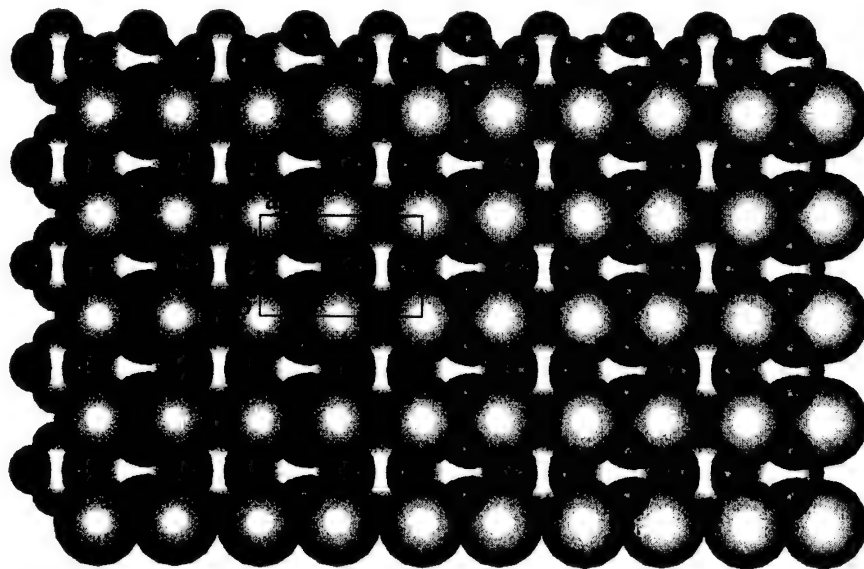


Fig. 6. The ab projection of the upper half layer of the barite structure shown in Fig. 5 onto (001) as a closed packed spheres model. The surface unit cell is indicated with $a = 8.88 \text{ \AA}$ and $b = 5.45 \text{ \AA}$. This figure can be compared with the AFM image shown in Fig. 3.

produce this additional peak, as would be anticipated for a surface reflecting the bulk symmetry.

The agreement, between XRD (bulk) and AFM (local) measurements, indicates that no significant surface reconstruction under formation of a different, usually larger surface lattice, occurs on the perfect $\{001\}$ cleavage plane in this system. Surface reconstructions have been reported for many metals and semiconductors under various conditions (mostly vacuum). Surface crystallographic studies by means of LEED on a wide range of materials including ionic, insulating substrates such as CaO (100), MgO (100) and ZnO ($10\bar{1}0$) or ($11\bar{2}0$) [17] have shown that at

the solid–vacuum interface most surfaces relax (i.e. a contraction of bond length) within a few percent of the bulk parameters. Usually, the lower the atomic packing and density of the surface, the larger the inward contraction. Since barite can be approximately assumed to consist of a closed packed arrangement of hard spheres, this possible relaxation is hindered. Another feature of surface relaxation involves the contraction of the interlayer distance between the first and the second layer of atoms at a surface. The height of a monostep measured in air is equivalent to the length of the unit cell along c , which reduces to a half-unit-cell-high step in water after dissolution.

In conclusion, there is no significant evidence for pronounced structural changes in the transition from the bulk to the surface for this mineral under the given environment (solid–air, solid–aqueous solution).

In addition to allowing imaging of barite's surface symmetry, AFM permits in situ monitoring of the dissolution of barite in water. Higgins et al. [5] have reported on the dissolution kinetics of the barium sulphate (001) surface using a 'hydrothermal' AFM operating in hot aqueous solutions up to 125°C. Despite the very low solubility of barite in water, we occasionally observed similar dissolution features after crystals were left in water under ambient conditions. The shape of these etch pits is shown in Fig. 7. Occasionally an etch pit only two $c/2$ layers deep can be seen, substantiating the 2_1 screw axis as the structure controlling symmetry element between the two layers of barite. Higgins et al. [5] measured various retreat rates of steps, comprising the walls of an etch pit (step velocity G , nm/s), pit

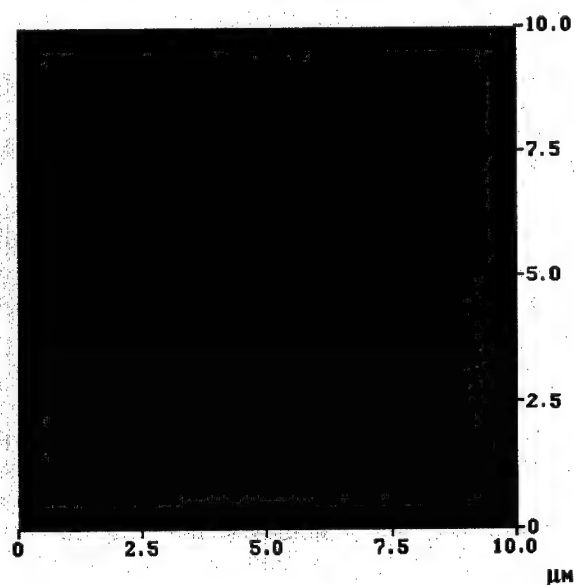


Fig. 7. AFM deflection image of a barite {001} cleavage face after several hours in water, during which the fluid cell of the instrument was flushed with water many times. Several crystallographically aligned dissolution etch pits are shown, which are bound by {210} and {010} faces, demonstrating a strong structural control of the dissolution process (see text).

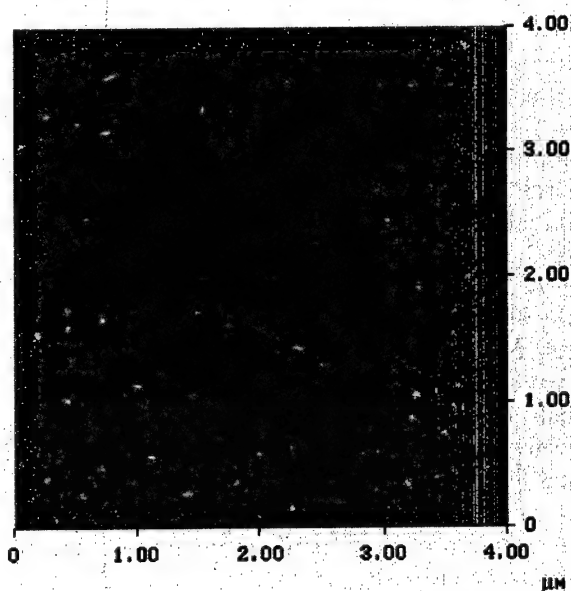


Fig. 8. AFM deflection image of $c/2$ surface steps receding during dissolution. Only every second step appears to be eroded, whereas the other steps keep a straight line.

nucleation rates, as well as the temperature dependence of step velocities in order to calculate the activation energies for different step directions. They concluded that a 2D birth-and-spread model most accurately describes the dissolution process. Interestingly, it was found that the step velocity is dependent on step height, although it is independent of step density (C , nm^{-1}), with a remarkable difference between single-layer ($c/2$, 3.5 Å thick) and double-layer (c , 7.1 Å thick) steps. The double-layer steps appear to recede faster. This differential step behaviour can be noticed in Fig. 8 where every second step appears to be highly kinked and eroded, presumably a double-layer step, whereas the other steps terminate as a straight line, indicating single-layer steps of greater stability.

3.2. Models of the barium sulphate {001} cleavage plane and step structures

Models of the barite unit cell and the (001) cleavage plane were generated using WebLab-Viewer Pro. These allowed us to view the atomic arrangement on terraces, at surface monosteps along different crystallographic directions, and at

etch figure boundaries. The input data for the models are based on the experimental cell parameters from a refinement of the X-ray structure (crystal symmetry, unit cell dimensions and atomic coordinates) [18]. The surfaces were generated by cleaving the bulk structure in such a way that initially there was no dipole moment perpendicular to the surface and therefore no surface charge.

A single unit cell of barite contains four units of the empirical formula, BaSO_4 , that are symmetry related through a 2_1 screw axis parallel to c . The unit cell can be divided into an upper and a lower half as indicated in Fig. 5 (the ac projection, i.e. viewed along the b -axis). Within each half of the unit cell the Ba^{2+} ions and the SO_4^{2-} ions occur at two different heights with respect to the c -axis. The distribution of Ba^{2+} ions parallel to (001) planes can be described by rows of Ba^{2+} ions along [010] directions (the b -axis) at two different levels within one half of the unit cell. Assuming the surface to be defined by Ba^{2+} rows at zero height ($z = 0$) it will also contain rows of SO_4^{2-} ions along the b -axis, which are at two heights but slightly shifted with respect to the Ba^{2+} . All sulphates are aligned such that an edge of the SO_4^{2-} tetrahedron is uppermost. The relative orientation of the two-edge oxygens is such that within each height level of the half-unit cell the sulphates have the same orientation (Fig. 5). The sulphate edges of the next level are rotated 90° and then shifted in their a , b -position (by a 2_1 screw axis) (Fig. 6).

This situation has important consequences, yielding two orientations for the actual atomic structure of the (001) cleavage plane, due to the assumption of a zero height ($z = 0$), for a surface layer of Ba^{2+} ions (Fig. 5). Acting as the reference layer, this requires an equal number of SO_4^{2-} ions with centre of mass slightly below the zero height plane. Removing pairs of Ba^{2+} and SO_4^{2-} creates a line or wall defect without charging up the crystal. This means that the dissolution or growth of the crystal can take place rapidly with the removal or addition of a single barium/sulphate ion normal to the (001) plane.

By rotating the model in Fig. 5 by 90° about the a -axis into the plane of the page, the ab projection onto (001) emerges, i.e. top view on the (001) surface as sensed by the AFM tip. In Fig. 6, this

projection is shown for better visualization of the top layer by using a closed packed CPK model.

The predominant structural step orientations on a freshly cleaved barite surface are along [210] or [120] directions or, after partial dissolution of the substrate layers, parallel to the b ([010]) axis. Steps parallel to the a -axis were not observed. Other cleavage steps, that do not follow any crystallographic direction, are likely to be due to the cleavage direction and fracture propagation as noted by Stipp et al. [14]. These steps are subsequently removed during the dissolution process receding in [010] or, faster, [210] directions. During exposure to water the formation of dissolution etch figures and some characteristic step erosions were observed (Figs. 7 and 8).

In air, the step heights were integral multiples of c . Immersing the sample in water usually led to steps of height $c/2$ that became deeper and more elongated along (001) with time. Experimentally, monosteps (or half-layer steps) exhibit a rather different dissolution behaviour, as can be seen in Fig. 8, where on a stepped {001} surface of barite in aqueous solution every second stepline appears to be eroded in a zigzag-like pattern (steps facing in a [210] direction), whereas the other half of the steps maintain a linear structure ([010] oriented steps). Theoretically, complementary information about structurally determined solution growth, the reverse phenomenon of the dissolution process, may be gained by using the 'inverse' etch pit shape as a replica for the morphology of a growing crystal. [4,19] A model for the {210} face is shown in Fig. 9, indicating a relatively open structure with barium and sulphate ions alternating over short distances with respect to both x , y and height (z) position. The ions could be easily removed by attacking water molecules without creating local barriers in terms of sterically or electrostatically unfavourable circumstances.

From the structural model shown in Fig. 10, for the [010] monolayer/half-unit-cell step, which appears to be the most stable step structure, it can be seen that this is the only configuration of the observed steps where barium ions as well as sulphate ions exist in close packed rows of either Ba^{2+} or SO_4^{2-} at two different heights. As shown in Fig. 5, in a barite monolayer there are two

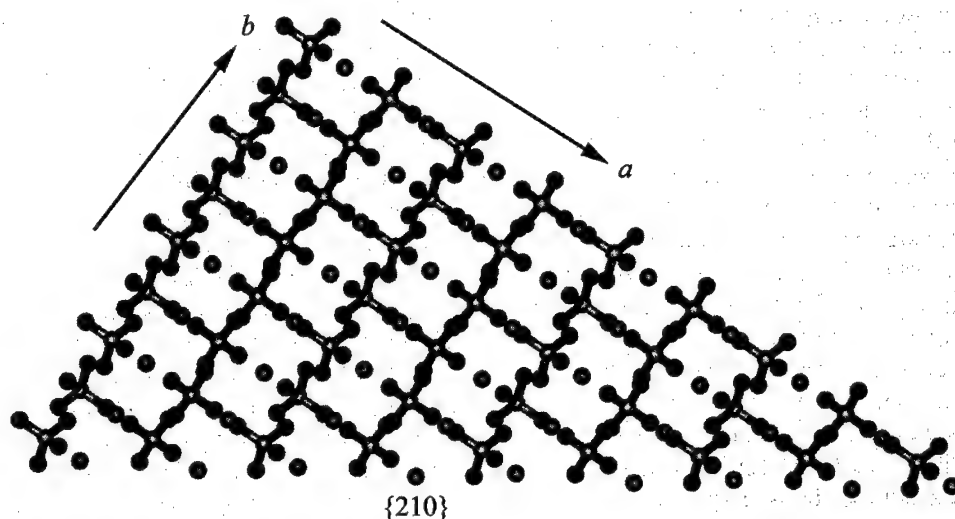


Fig. 9. Top view onto (001) showing the molecular structure of the top half layer of the fast receding $\{210\}$ face. The relatively open structure of alternating Ba^{2+} and SO_4^{2-} ions in lateral as well as in height position within the front row of step ions may explain the preferred dissolution in this direction.

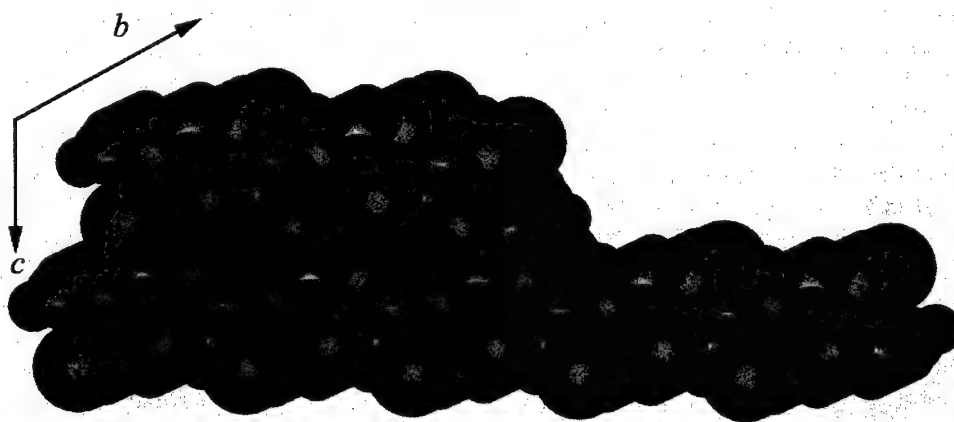


Fig. 10. Side view on a $c/2$ half-layer step along the b -axis ($[010]$ direction). Experimentally, this type of step recedes slower than steps oriented in $[210]$ direction. The model shows that barium and sulphate ions are alternating within the first two rows of a half layer, adding a sterical/electrostatic hindrance to the dissolution process. Water molecules would have to penetrate each stable row of Ba^{2+} or SO_4^{2-} at two different height positions, respectively, to remove a pair of Ba^{2+} or SO_4^{2-} during dissolution.

different heights for barium and two different heights for sulphate. Viewed along the a -axis, perpendicular to the b -axis, these rows are slightly shifted with respect to the position of the other sort of ion. In terms of the dissolution process, this means that to remove a pair of $\text{Ba}^{2+}/\text{SO}_4^{2-}$ ions, water molecules would have to penetrate each stable row, respectively. From a

structural argument, this situation is unfavourable for two reasons. First, due to an obvious steric hindrance, and second, because the other two possibilities for receding or dissolving steps along $[210]$ or (although not observed in water, it has been shown to be common in DTPA³) along $[100]$, the a -axis, are much more accessible.

For comparison, in the $[2\ 1\ 0]$ half-unit-cell step model, as shown in Fig. 9 the front face of ions alternates between Ba^{2+} and SO_4^{2-} irrespective of their relative height position, it is both a more open structure and, from an electrostatic point of view, a more easily balanced structure in the case of approaching water molecules. That is, contrary to the case of $[0\ 1\ 0]$ steps, it does not lead to a charge accumulation along that stepline, but rather to the most accessible face concerning the geometrical distribution of the ions as well as the distribution of charge density.

Etch pits, created during dissolution in water, are bounded by $\{0\ 1\ 0\}$ and $\{2\ 1\ 0\}$ or $\{1\ 2\ 0\}$ faces. The same arguments for the relationship between step structure and stability apply equally here. The atomistic model shown in Fig. 11 displays the geometric arrangement of an etch pit related to the crystal structure. As discussed earlier, steps along the b -axis ($\langle 0\ 1\ 0 \rangle$) terminate as rows of either barium or sulphate ions at the same height level regarding $(0\ 0\ 1)$, while the $\langle 2\ 1\ 0 \rangle$ steps have alternating barium and sulphate ions irrespective

of their relative heights with more space between them, which is an intrinsic property of any higher index face of closed packed structures. The triangular geometry of the etch pits implies that dissolution of barite occurs at a faster rate along $\langle 2\ 1\ 0 \rangle$ steps than along $\langle 0\ 1\ 0 \rangle$ steps. The differing retreat velocities then determine the aspect ratio of growing pits, which appears to be roughly constant in our experiments. Experimentally, this was also observed by Higgins et al. [5] who showed that single- and double-layer steps exhibit different step velocities themselves, independent of their crystallographic alignment. Indeed the velocity of a $[1\ 2\ 0]$ step was measured to be between two and three times faster than that of the corresponding $[0\ 1\ 0]$ steps, in accordance with our arguments based on surface charge and energy.

4. Conclusions

This study used AFM to characterize the barite surface structure at both the solid/air and the

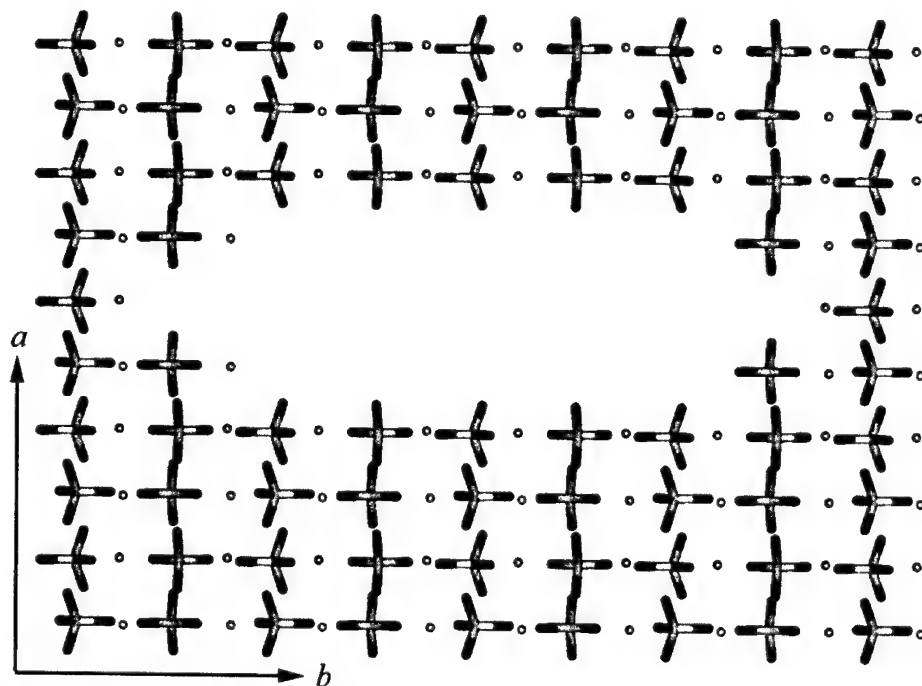


Fig. 11. The shape of an etch pit bound by $\{0\ 1\ 0\}$ and $\{2\ 1\ 0\}/\{\bar{2}\ 1\ 0\}$ or $\{1\ 2\ 0\}/\{\bar{1}\ 2\ 0\}$.

solid/solution interface. The results cover the barite microtopography and crystallographically determined control of cleavage and dissolution.

The low-solubility product of BaSO_4 (ca. $10^{-10} \text{ mol}^2 \text{ l}^{-2}$) in conjunction with its relatively large ionic radii make the (001) cleavage interesting for studying surface aspects in water with high resolution. Operating the AFM in water within a very low attractive force regime allowed stable imaging of the barite surface lattice and the relative position of the atoms within each unit cell. Lattice parameters (a, b) and ionic radii estimated from height images were in good agreement with the crystallographic bulk phase structure. No significant surface reconstruction was observed. A different kind of “reconstruction” may be interpreted as the reorientation of surface sulphate groups to minimize the overall free surface energy, seen as additional peaks on 2D FFT maps associated with the images.

Prolonged exposure of barite to ambient air led to significant surface rearrangement, probably due to the formation and reprecipitation of surface-hydration species within an adsorbed layer of water.

On the micrometer-scale of the barite {001} cleavage face we observed crystallographically orientated monosteps one unit cell (along the c -axis) in height and polysteps as well as etch figures showing the intrinsic 2_1 screw axis symmetry after dissolution in water on an overall heterogeneous {001} cleavage plane. In addition to etch pit formation, half-unit-cell-high steps following certain crystal directions ([210] and [010]) could be observed emphasizing the structural control of the dissolution process.

Atomistic models of the {001} cleavage plane, crystallographically oriented step edges along [210] and [010] and etch figure boundaries were used to provide further understanding of the structural features observed on the images. Ex-

perimentally measured step velocities could be reconciled with charging and energetic arguments based on these models.

Acknowledgements

DGB would like to thank the University of Otago for a post-graduate scholarship.

References

- [1] B.R. Heywood, S. Mann, *J. Am. Chem. Soc.* 114 (1992) 4681.
- [2] R. Eklund Jr., *Rocks Miner.* 40 (1965) 538.
- [3] A. Putnis, J.L. Junta-Rosso, M.F. Hochella Jr., *Geochim. Cosmochim. Acta* 59 (1995) 4623.
- [4] C.M. Pina, U. Becker, P. Risthaus, D. Bosbach, A. Putnis, *Nature* 395 (1998) 483.
- [5] S.R. Higgins, G. Jordan, C.M. Eggleston, K.G. Knauss, *Langmuir* 14 (1998) 4967.
- [6] R.J. Davey, S.N. Black, L.A. Bromley, D. Cottier, B. Dobbs, J.E. Rout, *Nature* 253 (1991) 549.
- [7] S. Mann, G.A. Ozin, *Nature* 382 (1996) 313.
- [8] A.L. Rohl, D.H. Gay, R.J. Davey, C.R.A. Catlow, *J. Am. Chem. Soc.* 118 (1996) 642.
- [9] A.A. Colville, K. Staudhammer, *Am. Mineral.* 52 (1967) 1877.
- [10] M. Miyake, et al., *Am. Mineral.* 63 (1978) 506.
- [11] F. Ohnesorge, G. Binnig, *Science* 260 (1993) 1451.
- [12] W.A. Ducker, T.J. Senden, R.M. Pashley, *Langmuir* 8 (1992) 1831.
- [13] P. Fenter, M.T. McBride, G. Srajer, N.C. Sturchio, D. Bosbach, *J. Phys. Chem. B* 105 (2001) 8112.
- [14] S.L.S. Stipp, W. Gutmannsbauer, T. Lehmann, *Am. Mineral.* 81 (1996) 1.
- [15] J.C. Russ, *The Image Processing Handbook*, CRC Press, Boca Raton, FL, 1992.
- [16] A.L. Rachlin, G.S. Henderson, M.C. Goh, *Am. Mineral.* 77 (1992) 904.
- [17] G.A. Somorjai, *Introduction to Surface Chemistry and Catalysis*, Wiley, New York, 1994.
- [18] P. Hartman, C.S. Strom, *J. Crystal Growth* 97 (1989) 502.
- [19] A.L. Ruoff, *Materials Science*, Prentice-Hall, Englewood Cliffs, NJ, 1973.



ELSEVIER

Available online at www.sciencedirect.com

SCIENCE @ DIRECT®

Journal of Crystal Growth 246 (2002) 150–154

JOURNAL OF **CRYSTAL
GROWTH**

www.elsevier.com/locate/jcrysgro

A new phase of cadmium titanate by hydrothermal method

Hao Wang^{a,*}, XiaoXue Zhang^a, AnPing Huang^a, HaiYan Xu^a, ManKang Zhu^a,
Bo Wang^a, Hui Yan^a, Masahiro Yoshimura^b

^a *The Key Laboratory of Advanced Functional Materials of China Education Ministry, Beijing Polytechnic University,
Beijing 100022, China*

^b *Materials and Research Laboratory, Tokyo Institute of Technology, Nagatsuta, Midori-ku, Yokohama 226-8503, Japan*

Received 19 August 2002; accepted 22 August 2002

Communicated by R. Kern

Abstract

A new phase of cadmium titanate was prepared by hydrothermal method under low temperature of 120°C. The electron diffraction investigation showed that the structure of the new phase is hexagonal with lattice parameters $a = b = 5.2099 \text{ \AA}$ and $c = 4.6811 \text{ \AA}$, which have been calibrated by its X-ray diffraction pattern. The X-ray photoelectron spectroscopy results suggested that the new phase can be described as CdTiO_3 . Furthermore, it was observed that the post-annealing at 700°C and 1050°C led to the transition of the new phase to the known ilmenite and then perovskite phase, respectively.

© 2002 Elsevier Science B.V. All rights reserved.

PACS: 81.20.Ka; 68.55.Nq

Keywords: A2. Hydrothermal crystal growth; B1. Cadmium compounds

1. Introduction

Cadmium titanate (CdTiO_3), belonging to the well known family of the titanium-based oxides, is gaining more and more attention due to its promising applications as a sensor material for the detection of NO_2 gas [1], optical fiber [2] and so forth. Furthermore, like the other titanium-based systems, it may have unexplored potential for applications in non-linear optics. As well known, CdTiO_3 crystallizes into a hexagonal ilmenite

structure below 1000°C, and into an orthorhombic distorted perovskite structure above 1050°C [3]. These two structures differ briefly in symmetry. The ilmenite structure has a threefold axis of rotational symmetry with $a = 5.2403 \text{ \AA}$ and $c = 14.838 \text{ \AA}$. In contrast, the perovskite structure is very asymmetric with $a = 5.348 \text{ \AA}$, $b = 7.615 \text{ \AA}$ and $c = 5.417 \text{ \AA}$ [4]. It is said that, previously, the perovskite phase of CdTiO_3 is ferroelectric and the ilmenite phase is not [5]. However, since Mattias and Remeika had found ferroelectric properties in LiNbO_3 which is a well-known monoaxial ferroelectric with an ilmenite-like structure, the problem of ferroelectric properties in the ilmenite

*Corresponding author.

E-mail address: haowang@bjpu.edu.cn (H. Wang).

phase remains to be clarified [6]. Therefore, CdTiO_3 represents an interesting system to investigate both the nature of the phase transition and the ferroelectric property [7].

As for the synthesis method, hydrothermal method has many advantages over other fabrication techniques, such as homogeneity, purity, and lowering down the reaction temperature considerably [8]. Furthermore, low temperature hydrothermal reactions have yielded a large number of metastable and novel inorganic materials which are difficult or impossible to be obtained by such method as conventional solid state recreation [9]. In this paper, we report a new phase of cadmium titanate synthesized at low temperature by hydrothermal method.

2. Experimental procedure

2.1. Synthesis

Analytically pure $\text{Cd}(\text{CH}_3\text{COO})_2$, $\text{Ti}(\text{C}_4\text{H}_9\text{O})_4$ and CH_3COOH in certain $\text{Cd}(\text{CH}_3\text{COO})_2/\text{Ti}(\text{C}_4\text{H}_9\text{O})_4$ molar ratios were dissolved in deionized water. The mixture was heated at 50°C and stirred constantly to achieve a light yellow transparent gel. The gel was then subjected to hydrothermal treatment in a 40 ml stainless steel autoclave lined with Teflon under autogenous pressure. The treatment was carried out using 0.5 M KOH as mineralizer at 120 – 240°C for 3 days. After treatment, the products were filtered, washed with distilled water, and dried at ambient temperature.

2.2. Characterization

The synthesized products were characterized by powder X-ray diffraction (XRD) on a Japan Rigaku D/Max-3C diffractometer using $\text{Cu K}\alpha$ radiation. Transmission electron microscopy (TEM) images were conducted using JEM-2000FX microscope. Electron diffraction patterns were taken at 160 kV with a selected area model. The composition and binding states of each component were studied by the X-ray photoelectron spectra (XPS) on a PHI-5300/ESCA system

with $\text{Mg K}\alpha$ radiation as the exciting source, where the binding energies were calibrated by referencing the C 1s peak to reduce the charge effect.

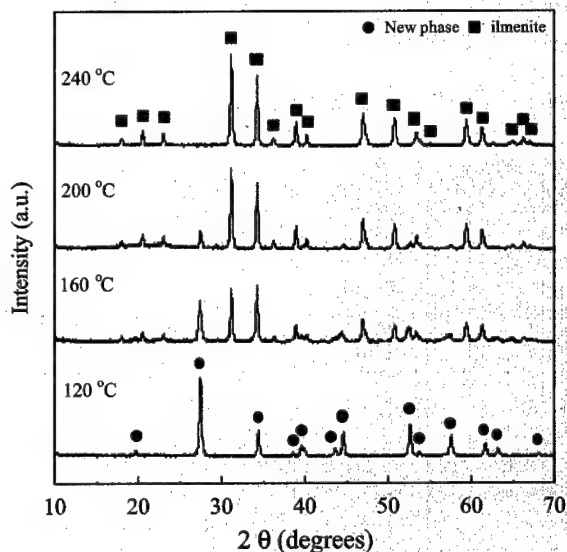


Fig. 1. XRD patterns of powders synthesized hydrothermally from 120°C to 240°C for 72 h.

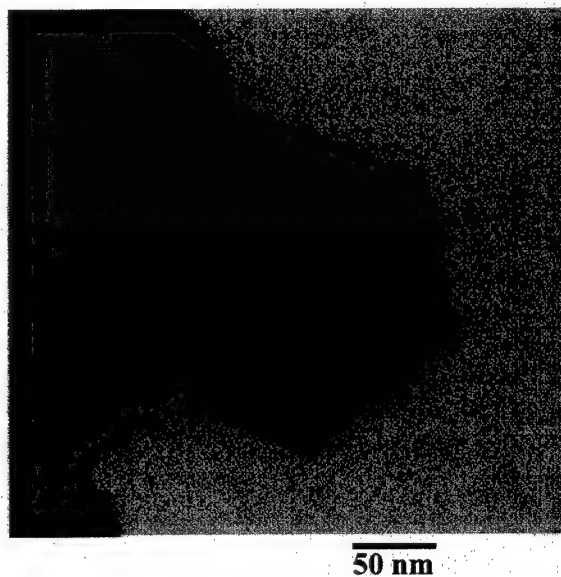


Fig. 2. TEM image of the powders hydrothermally synthesized at 120°C .

3. Results and discussion

The XRD patterns of products synthesized hydrothermally from 120°C to 240°C for 72 h are shown in Fig. 1. It is noted that there are two different kinds of diffraction patterns. At 240°C, all peaks can be indexed to the ilmenite phase, matching the JCPDS data (Card No: 29–277) perfectly. With the decrease of the temperature from 200°C to 160°C, the ilmenite phase plays a

less and less dominant role although it still takes the larger proportion. Till 120°C, it is worth noting that all diffraction peaks that we have known are not in agreement with such possible phases as CdTiO_3 , CdO , TiO_2 and Cd(OH)_2 . Even none of these patterns in the XRD database matches it well by XRD searching. From the above results we can see that, ilmenite CdTiO_3 could be obtained at 240°C. While at a relatively low temperature of 120°C, a possible new phase has been obtained which need further identification.

Fig. 2 shows the TEM image of the powders prepared at 120°C in which there is a hexagonal grain. Fig. 3(a) gives the electron diffraction pattern when the incident electron beam is perpendicular to the surface of this hexagonal grain. When the specimen was tilted with a small angle with the fixed co-plane edge-on, another diffraction pattern is achieved, which is shown in Fig. 3(b). According to these electron diffraction patterns, it is concluded that the new phase is a hexagonal structure and the lattice parameters could be calculated approximately. To confirm the information from the electron diffraction, we use XRD pattern of the new phase to validate the structure and modify the lattice parameters. The

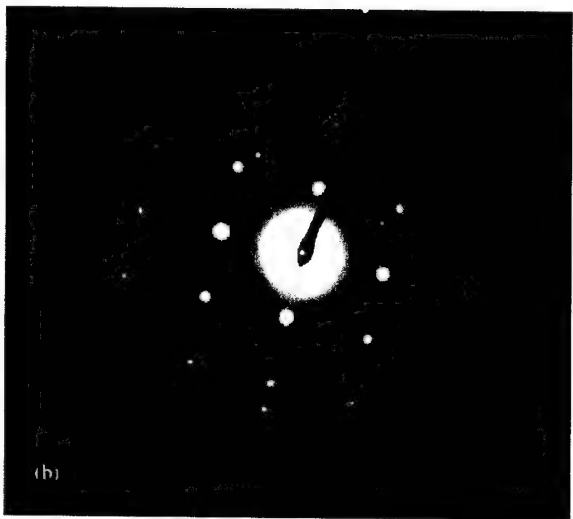
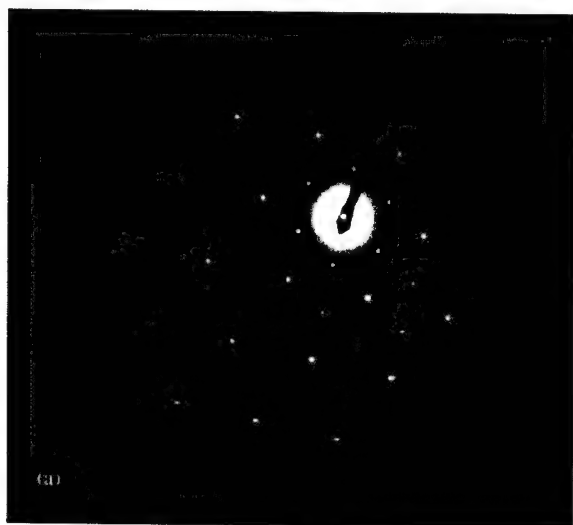


Fig. 3. Electron diffraction patterns corresponding to the grain in the above TEM image. The electron beam is (a) perpendicular to the surface of the grain, and (b) tilted with a small angle.

Table 1

Experimental and calculated interplanar spacings (d) based on a hexagonal cell with $a = b = 5.2099 \text{ \AA}$ and $c = 4.6811 \text{ \AA}$

hkl	$d_{\text{exp}} (\text{\AA})$	$d_{\text{cal}} (\text{\AA})$
100	4.5118	4.5119
101	3.2453	3.2485
110	2.6048	2.6049
002	2.3387	2.3405
111	2.2739	2.2762
200	2.2564	2.2560
102	2.0741	2.0776
201	2.0316	2.0323
112	1.7391	1.7410
210	1.7066	1.7053
211	1.6014	1.6023
300	1.5034	1.5040
103	1.4729	1.4727
212	1.3767	1.3783
113	1.3349	1.3386
220	1.3029	1.3024
203	1.2823	1.2833
302	1.2635	1.2653
311	1.2076	1.2089

experimental and calculated interplanar spacings d corresponding to the different plane indices are listed in Table 1. A satisfactory agreement was obtained between experiment and calculation. Consequently, a hexagonal unit cell with parameters $a = b = 5.2099 \text{ \AA}$ and $c = 4.6811 \text{ \AA}$ has been adopted.

XPS measurements have been performed to determine the composition of the new phase. Only Ti, Cd and O have been detected without any other contaminant species. The Cd 3d and Ti 2p

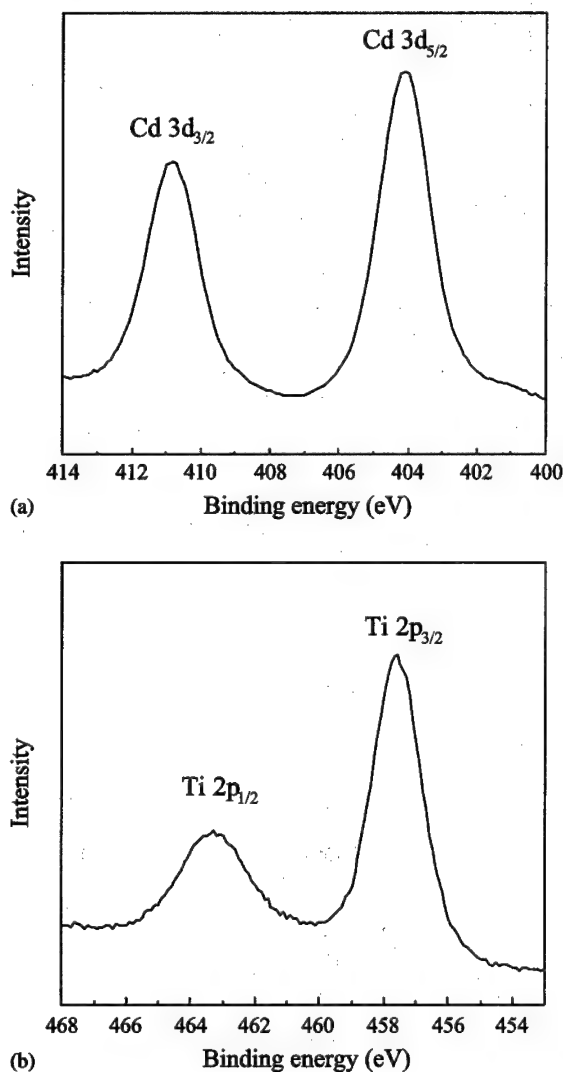


Fig. 4. Core level spectra of (a) Cd 3d, and (b) Ti 2p of the powders hydrothermally prepared at 120°C .

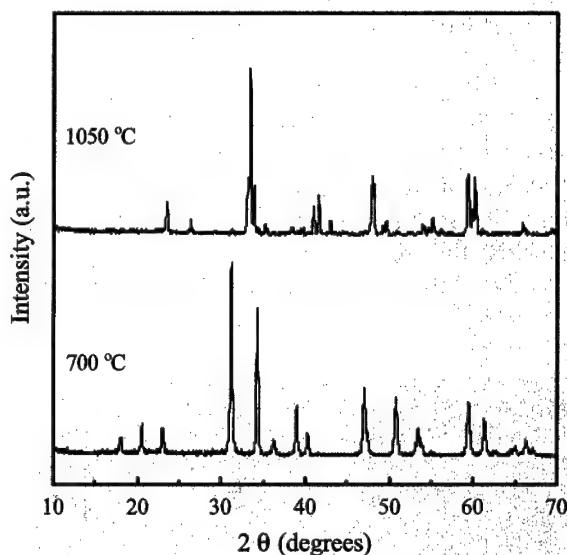


Fig. 5. XRD patterns of the new phase powders post-annealed at 700°C , and 1050°C .

core level spectra are shown in Fig. 4(a) and (b), respectively. The molar ratio of Ti and Cd is found to be 1:1. The binding energy corresponding to the Cd 3d and Ti 2p peaks is 404.1 eV and 457.7 eV , indicating that the valence of Cd and Ti is +2 and +4, respectively. With the result of the above composition analysis and valance determination, we could describe this new phase as CdTiO_3 .

To reveal the relationship between the new phase and the two known phases, the new phase products were annealed at 700°C and 1050°C for 5 h, respectively. The XRD patterns are given in Fig. 5. It is easy to see a full ilmenite phase has been obtained at 700°C . Meanwhile, a pure perovskite phase (JCPDS card No. 78–1015) has been obtained at 1050°C . It illustrates that the new phase transits to known ilmenite and perovskite phases upon annealing at high temperature. Further work on the detail information of the phase transition between the new phase and two known phases, and the properties of this new phase is under the way.

4. Conclusion

A new phase of cadmium titanate which is of hexagonal structure with the lattice parameters

of $a = 5.2099 \text{ \AA}$ and $c = 4.6811 \text{ \AA}$ was prepared under low temperature hydrothermal condition. The molar ratio of Cd and Ti is 1:1 and their valance is +2 and +4, leading to the description as CdTiO_3 . The new phase can transit into known ilmenite phase and perovskite phase with the post-annealing at 700°C and 1050°C , respectively.

References

- [1] T. Bein, K. Brown, G.C. Fye, C.J. Briler, J. Am. Ceram. Soc. 111 (1989) 7640.
- [2] H. Dislich, in: L.C. Klein (Ed.), Sol. Gel Technology for Thin Films, Fibers, Performs, Electronics and Speciality Shapes, Noyes Publications, Park Ridge, NJ, 1993, p. 50.
- [3] A. Montenero, M. Canali, G. Gnappi, D. Bersani, Appl. Organometal. Chem. 11 (1997) 137.
- [4] G.L. Catchen, S.J. Wukitch, D.M. Spaar, Phys. Rev. B 42 (1990) 1885.
- [5] Y.V. Kabirov, B.S. Kulbuzhev, M.F. Kupriyanov, J. Struct. Chem. 42 (2001) 815.
- [6] B.T. Mattias, J.R. Remeika, Phys. Rev. 76 (1949) 1886.
- [7] D. Bersani, P.P. Lottici, M. Canali, A. Montenero, G. Gnappi, J. Sol-Gel Sci. Technol. 8 (1997) 337.
- [8] M. Yoshimura, J. Mater. Res. 13 (1998) 796.
- [9] Y. Mao, G. Li, Y. Sun, S. Feng, J. Solid State Chem. 149 (2000) 314.

Growth, spectroscopic and thermal behavior of $\text{Cd}(\text{SCN})_2(\text{DMSO})_2$

X.Q. Wang^{a,*}, D. Xu^a, D.R. Yuan^a, M.K. Lu^a, X.F. Cheng^a, J. Huang^b,
G.W. Lu^c, S.Y. Guo^a, G.H. Zhang^a

^a State Key Laboratory of Crystal Materials, Institute of Crystal Materials, Shandong University, Jinan 250100, People's Republic of China

^b College of Environmental Science and Engineering, Institute of Modern Analysis, Shandong University, Jinan 250100, People's Republic of China

^c School of Chemical Engineering, Beijing University of Chemical Technology, 100029, People's Republic of China

Received 25 August 2002; accepted 27 August 2002

Communicated by M. Schieber

Abstract

Single crystals of the organometallic material, bis(dimethyl sulfoxide) cadmium thiocyanate (DSTC), $\text{Cd}(\text{SCN})_2(\text{DMSO})_2$, were grown from aqueous solution. The grown crystals were characterized by elemental analyses, X-ray powder diffraction, Raman, infrared and optical transmission spectroscopy and thermal analysis. The UV transparency cutoff of DSTC crystal is 263 nm. It exhibits good physicochemical stability up to 134°C, and the final residue of thermal decomposition is CdS.

© 2002 Elsevier Science B.V. All rights reserved.

PACS: 61.10; 81.10; 81.70; 82.80

Keywords: A1. Characterization; A1. Solvents; A1. X-ray powder diffraction; A2. Growth from solutions; A2. Single crystal growth; B1. Cadmium compounds

1. Introduction

The metal thiocyanates and their Lewis-base adducts are one of the interesting themes of structural chemistry [1]. All of them have chain structures in which respective side-by-side metal atoms are bridged by thiocyanate ions. Their

structural features bestow on them usefulness in nonlinear optics [2], chemical analysis [3], chemical, electrochemical metal sulfide thin film deposition [4] and the like.

Our previous work [5] has reported zinc cadmium thiocyanate, $\text{ZnCd}(\text{SCN})_4$ (ZCTC) crystal, an organometallic second-order nonlinear optical material which has a high nonlinearity, a wide transparency range, a high physicochemical stability, etc., and during the solvent selection for growth of ZCTC, the incorporation of DMSO

*Corresponding author. Tel.: +865318362822; fax: +865318565403.

E-mail address: xqwang@icm.sdu.edu.cn (X.Q. Wang).

solvent into the grown crystal led to the formation of another novel crystal: bis(dimethyl sulfoxide) cadmium thiocyanate (DSTC), $\text{Cd}(\text{SCN})_2(\text{DMSO})_2$. As a continuation of our research project on this metal thiocyanate system, we intended to grow and characterize the novel crystal. The crystal structure was reported previously [6]. It belongs to the triclinic crystallographic system, space group $P\bar{1}$, with cell parameters: $a = 5.9172(15) \text{ \AA}$, $b = 8.0811(12) \text{ \AA}$, $c = 8.1539(12) \text{ \AA}$, $\alpha = 114.533(5)^\circ$, $\beta = 100.912(11)^\circ$, $\gamma = 95.448(10)^\circ$, $V = 341.65(11) \text{ \AA}^3$, $Z = 1$, $D_c = 1.870 \text{ g/cm}^3$. In the present work, large single crystals of DSTC were grown from a mixed solvent of water–DMSO by means of temperature-lowering method. Some spectroscopic and thermal properties of DSTC were investigated by using elemental analyses, X-ray powder diffraction (XRPD), Raman and IR spectroscopy, thermogravimetric analysis (TGA) and differential scanning calorimetry (DSC) for the first time.

2. Experimental procedure

All the starting materials were of analytic reagent grade and used as purchased, and all the synthetic and growth processes were carried out in solutions. Elemental analyses were performed using the Perkin–Elmer 2400 instrument. The chemical composition of DSTC crystals was determined using the carbon, hydrogen, and nitrogen tests. The XRPD pattern of DSTC was registered with Rigaku D/Max- γ A diffractometer, operated at 40 KV and 50 mA, using Cu-target tube and a graphite monochromator. Fixed scatter and divergence slits of 1° and a 0.15 mm receiving slit were used. The intensity data were recorded by continuous scan in $2\theta/\theta$ mode from 10° to 60° with step size of 0.02° and scan speed of $4^\circ/\text{min}$.

The Raman spectra of DSTC crystal were measured on a LABRAM microscopic Raman spectrometer with a slit width of 100 nm, using a 100 mW Argon ion laser at 514.53 nm with a power density of $5 \text{ mW}/\mu\text{m}^2$ at the sample. Infrared (IR) spectra of DSTC together with dimethyl sulfoxide (DMSO) were recorded on a

Nicolet 20sx FTIR spectrometer at room temperature in the $4000\text{--}220 \text{ cm}^{-1}$ range.

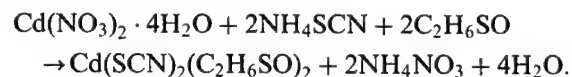
The optical transmission spectra of DSTC from the UV to NIR in the wavelength range from 190 to 3200 nm were recorded by using the Hitachi model U-3500 recording spectrophotometer. The light path direction was normal to the natural cleavage plane and thickness of the sample used was 3.24 mm.

TGA and DSC were carried out in the $20\text{--}650^\circ\text{C}$ temperature interval using the Perkin–Elmer model TGA-7 and the Mettler Toledo DSC822 $^\circ$ instruments, respectively, under nitrogen flux at a heating rate of $20^\circ\text{C}/\text{min}$. Samples were weighed in a platinum crucible with a microprocessor-driven temperature control unit and a TA data station was used.

3. Results and discussion

3.1. DSTC preparation and single crystal growth

Preparation of DSTC was accomplished according to the following reaction:



In the reaction, 15.2 g NH_4SCN , 30.9 g $\text{Cd}(\text{NO}_3)_2 \cdot 4\text{H}_2\text{O}$ and 20 ml DMSO were added in 60 ml water with stirring at the same time. After the pale red solution was left standing at room temperature for a while, white precipitated DSTC was separated and dried. To ensure the purity of the product, elemental analyses were performed. The results are summarized in Table 1

Table 1
Elemental analyses of DSTC ($\text{C}_6\text{H}_{12}\text{CdN}_2\text{O}_2 \text{ S}_4$) (molecular weight 384.82)

Element	Composition (%)	
	Theoretical	Measured
C	18.72	18.72
H	7.28	7.10
N	13.67	13.40

which demonstrate the validity of its chemical composition.

Single crystals can be easily grown by using of temperature-lowering method. Small transparent single crystals, free of macrodefects, obtained by



Fig. 1. As-grown typical single crystal of DSTC.

spontaneous nucleation from the saturated 3:1 (water:DMSO) solution of DSTC were selected as seed crystals. The typical growth procedure is as follows: an amount of 3:1 solution of DSTC with the pH value adjusted to 3.0 by adding HCl, is kept at 37.0°C ($\sim 2.0^\circ\text{C}$ above the saturation temperature) for at least 4 h. A seed crystal fixed by fusion to a thin platinum wire is introduced into the solution for half an hour at which time slight dissolution can be observed. The solution is then cooled to the initial growth temperature 35.0°C, and maintained at this temperature for at least 1 day. Subsequently, the crystal growth process is started. The rotation rate of the growing crystal is 30 rpm at the beginning of crystal growth, the temperature-lowering rate is $0.2^\circ\text{C}/\text{day}$. The temperature-lowering rate is gradually increased as the growth proceeds. In course of about 2 weeks, the temperature of this solution is lowered to about 30.0°C , and large single crystals of DSTC grow out. A typical single crystal shown in Fig. 1 was grown by this procedure.

If $\text{ZnCd}(\text{SCN})_4$ was dissolved in water/DMSO mixed solvents, DSTC can also be obtained

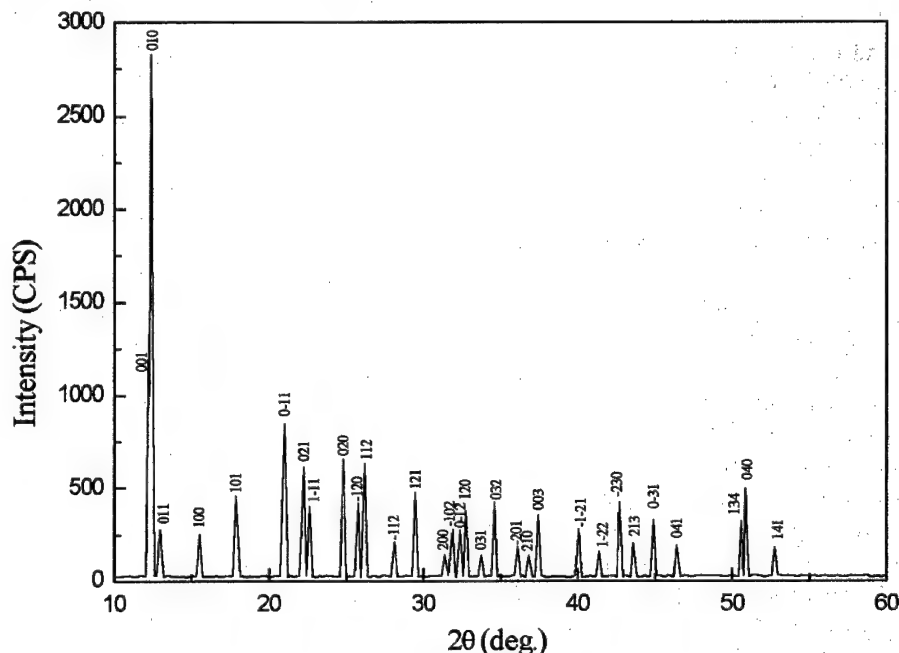
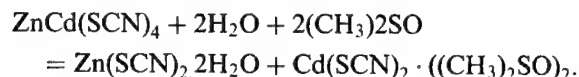


Fig. 2. XRPD pattern and diffraction indices of DSTC crystal.

because a new simple reaction occurred as follows:



According to the Hard Soft Acids and Bases concept [7–9], the harder metal ions show a pronounced affinity for coordination with harder ligands, while softer metal ions prefer coordination with softer ligands. Zn^{2+} and Cd^{2+} is harder and softer Lewis acid, while H_2O and $(\text{CH}_3)_2\text{SO}$ is harder and softer Lewis base, respectively. Therefore, Zn^{2+} and Cd^{2+} is coordinated with O atoms from H_2O and $(\text{CH}_3)_2\text{SO}$, respectively. Two compounds: DSTC ($\text{Cd}(\text{SCN})_2 \cdot ((\text{C} \cdot \text{H}_3)_2\text{SO})_2$) and $\text{Zn}(\text{SCN})_2 \cdot 2\text{H}_2\text{O}$ occur. The solubility of DSTC is much smaller than that of $\text{Zn}(\text{SCN})_2 \cdot 2\text{H}_2\text{O}$. Thus, $\text{Cd}(\text{SCN})_2 \cdot ((\text{CH}_3)_2\text{SO})_2$ precipitated and $\text{Zn}(\text{SCN})_2 \cdot 2\text{H}_2\text{O}$ remained in the solution.

3.2. X-ray powder diffraction (XRPD)

XRPD experiments showed that the synthesized material and the as-grown crystals contain a single phase of DSTC. The XRPD pattern and diffraction indices of the crystal are shown in Fig. 2. The triclinic unit-cell parameters calculated by TREOR program [10] according to the values of 2θ in the XRPD pattern are $a = 5.9155 \text{ \AA}$, $b = 8.1566 \text{ \AA}$, $c = 8.0734 \text{ \AA}$, $\alpha = 114.5491^\circ$, $\beta = 100.9912^\circ$, $\gamma = 95.4610^\circ$, $V = 341.13 \text{ \AA}^3$, respectively, which agree well with the results determined by R3m/E four-circle X-ray diffractometer [6].

3.3. Raman and IR spectra

The Raman spectra of DSTC crystal in the region $50\text{--}3000 \text{ cm}^{-1}$ are shown in Fig. 3. The observed bands along with their vibrational assignments are summarized in Table 2. Fig. 4 shows the IR transmission spectra of DSTC. The main IR spectral data of DSTC and DMSO are listed in Table 3. The absorption peaks assigned to SO stretching modes of DSTC appear at far lower frequencies compared with that of pure DMSO due to the coordination of O atoms with the Cd

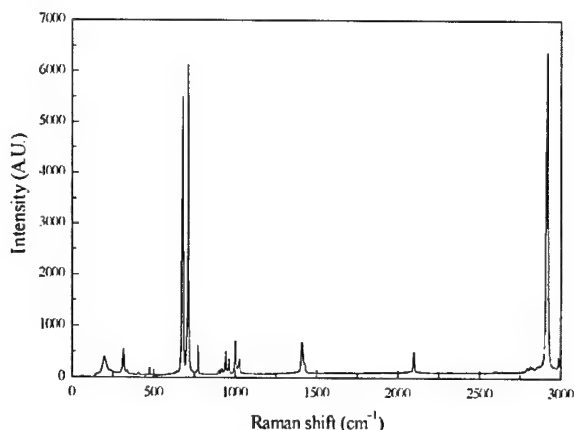


Fig. 3. Raman spectra of DSTC crystal in the region $50\text{--}3000 \text{ cm}^{-1}$.

Table 2

Observed Raman vibrational spectra data (cm^{-1}) and their assignments of DSTC crystal in the $50\text{--}3000 \text{ cm}^{-1}$ range

Raman spectra	Assignments
200.04	$\nu(\text{CdS})$
317.70, 338.30	$\nu(\text{CdN})$
410.02	$\nu(\text{CdO})$
455.81, 474.40	$\delta(\text{SCN})$
677.86	$\nu(\text{SCN})$
712.39, 772.88	$\nu(\text{CS})$
903.76, 918.18, 943.74, 962.85	$2\delta(\text{SCN})$
1002.54, 1027.83	$\nu(\text{SO})$
1412.76, 1429.26	$\delta(\text{CH}_3)$
2078.76, 2100.98	$\nu(\text{CN})$
2591.17	Lattice mode
2793.42, 2812.45, 2854.16	$\nu_1(\text{CH}_3)$
2910.65, 2916.89, 2988.97	$\nu_2(\text{CH}_3)$

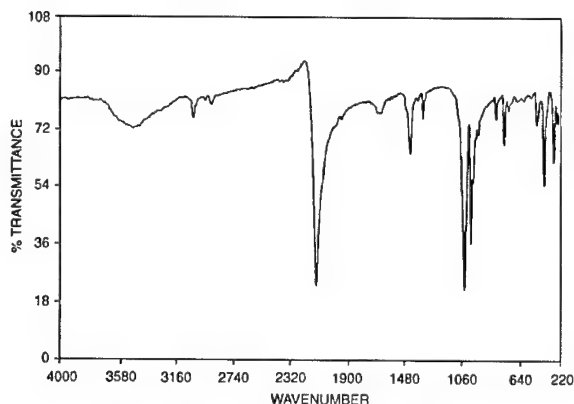


Fig. 4. IR transmission spectra of DSTC.

Table 3

Comparison of the main IR spectral data (cm^{-1}) of DSTC with DMSO in the $4000\text{--}220\text{ cm}^{-1}$ wavelength region

Assignment	DSTC	DMSO
ν_{CH}	3008.4, 2922.5, 2872.9	2999.2, 2913.2
ν_{CN}	2102.8	
δ_{CH}	1406.2	1436.7, 1406.1, 1314.3
ν_{SO}	1003.9	1050.4
$2\delta_{\text{SCN}}$	957.2, 942.7, 899.6	
ν_{CS}	770.7, 709.4	
δ_{SCN}	466.1, 412.0	
ν_{CdN}	341.8, 317.8	

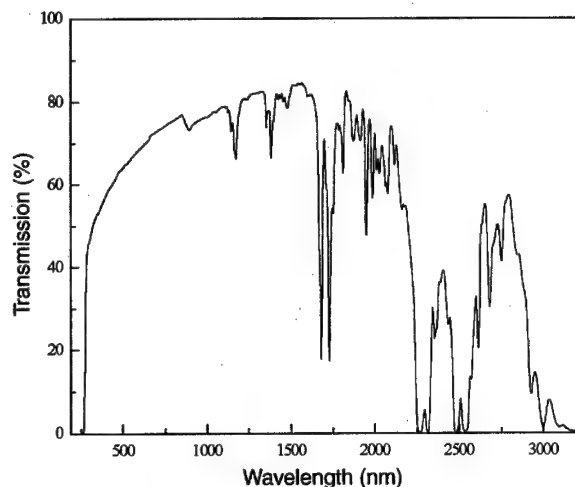


Fig. 5. Transmission spectra of DSTC crystal.

atoms, which cause weaker bonds between O and S in the coordinated DMSO molecules.

3.4. Optical transmission spectra

Since single crystals are mainly used in optical applications, the optical transmission range and the transparency cutoff are important. The transmission spectra of DSTC crystal is shown in Fig. 5. One can see that the transparent wave band lies in the range of $263\text{--}2260\text{ nm}$. The UV transparency cutoff of DSTC crystal occurs at 263 nm . There are two strong infrared absorption peaks at 1680 and 1929 nm , respectively, which are overtones of the CH stretching vibrations.

3.5. Thermal properties

At normal temperature and pressure, DSTC crystals possess good stability and do not show any hygroscopic and efflorescent effect for a long time. The analysis of the TGA (Fig. 6) and DSC (Fig. 7) curves shows that the thermal decomposition of DSTC begins at 134°C and proceeds in two steps. The first step is the decomposition of $\text{Cd}(\text{SCN})_2(\text{DMSO})_2$ to $\text{Cd}(\text{SCN})_2$, corresponding to one endothermic DSC peaks at 169°C . A small inflection point exhibiting a 41.1% weight loss at about 290°C in the TGA curve is in agreement with the theoretical value (40.6%) for two DMSO molecules. In the temperature range $290\text{--}610^\circ\text{C}$,

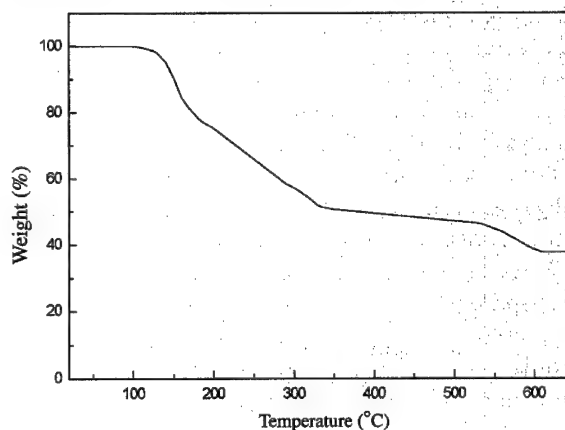


Fig. 6. TGA curve of DSTC crystal.

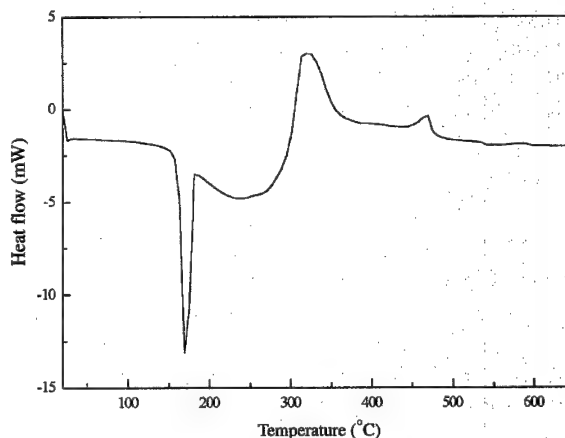
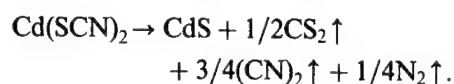
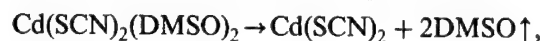


Fig. 7. DSC curve of DSTC crystal.

two exothermic peaks (at 320°C and 470°C, respectively) were observed. In this step, a half CS_2 , three-quarter $(\text{CN})_2$, and one-quarter N_2 molecules (calculated 21.2%) are lost which is in good agreement with the theoretical value (21.9%). The final residue is CdS .

The possible reactions of thermal decomposition (under nitrogen flux) can be expressed as



4. Conclusions

Single crystals of DSTC have been prepared and characterized by various ways. Slow temperature-lowering method is suitable for growing large high-quality DSTC single crystals. The elemental analysis, XPRD, Raman and IR spectroscopy studies have provided the basic structural and physical characteristics of the grown single crystals. Optical transmission studies show that the UV cutoff wavelength of DSTC is 263 nm and transparent wave band ranges 263–2260 nm. Although thermal analysis suggests that DSTC is stable up to 134°C, at normal temperature and pressure, however, the crystal possesses good stability and does not show any hygroscopic and efflorescent effect for a long time. The thermal decomposition process has been elucidated. This process involves two steps with the release of DMSO, the formation of cadmium thiocyanate, carbon bisulfide, dicyanogen, nitrogen gas, and the final product cadmium sulfide.

Acknowledgements

This work is supported by grants from the National Natural Science Foundation of China (69890230 and 60178029). The authors express thanks to Professor Y. Chen and Professor Y.Q. Zhou for the Raman spectra measurements, and Professor Z.H. Yang for the TGA and DSC measurements in the research project.

References

- [1] K. Nakamoto (Translated by D.R. Huang, R.Q. Wang), *Infrared and Raman spectra of inorganic and coordination compounds*, 3rd Edition, Wiley, Beijing, Chemical Industry Press, 1986 (in Chinese).
- [2] X.Q. Wang, W.T. Yu, D. Xu, M.K. Lu, D.R. Yuan, J.R. Liu, G.T. Lu, *Acta Cryst. C* 56 (2000) 1305.
- [3] B. Ptaszynski, E. Skiba, J. Krystek, *Thermochim. Acta* 319 (1998) 75.
- [4] T. Yoshida, K. Yamaguchi, T. Kazitani, T. Sugiura, H. Minoura, *J. Electroanal. Chem.* 473 (1999) 209.
- [5] X.Q. Wang, D. Xu, M.K. Lu, D.R. Yuan, G.H. Zhang, S.X. Xu, S.Y. Guo, X.N. Jiang, J.R. Liu, C.F. Song, Q. Ren, J. Huang, Y.P. Tian, *Mater. Res. Bull.* 36 (2001) 1287.
- [6] X.Q. Wang, W.T. Yu, D. Xu, D.R. Yuan, M.K. Lu, Y.P. Tian, F.Q. Meng, S.Y. Guo, M.H. Jiang, *Z. Kristallogr. NCS* 215 (2000) 91.
- [7] R.G. Pearson, *Science* 151 (1966) 172.
- [8] T. Yamaguchi, K. Yamamoto, H. Ohtaki, *Bull. Chem. Soc. Jpn.* 58 (1985) 3235.
- [9] K. Ozutsumi, T. Takamuku, S. Ishiguro, H. Ohraki, *Bull. Chem. Soc. Jpn.* 62 (1989) 1875.
- [10] P.E. Werner, L. Eriksson, M. Westdahl, *J. Appl. Cryst.* 18 (1985) 367.



ELSEVIER

Available online at www.sciencedirect.com

SCIENCE @ DIRECT®

JOURNAL OF CRYSTAL GROWTH

Journal of Crystal Growth 246 (2002) 161–168

www.elsevier.com/locate/jcrysgro

Sonochemical preparation of lead sulfide nanocrystals in an oil-in-water microemulsion

Hui Wang, Jian-Rong Zhang, Jun-Jie Zhu*

Key State Laboratory of Coordination Chemistry, Laboratory of Mesoscopic Materials Science, Department of Chemistry, Nanjing University, Nanjing 210093, People's Republic of China

Received 12 August 2002; accepted 22 August 2002

Communicated by M. Schieber

Abstract

Lead sulfide (PbS) nanocrystals have been successfully prepared in an oil-in-water microemulsion by a sonochemical method. The product is characterized by using techniques such as X-ray powder diffraction, transmission electron microscopy, X-ray photoelectron spectroscopy, and energy-dispersive X-ray analysis. The as-prepared PbS nanocrystals crystallize in a cubic structure and have an average crystal size of ca. 11 nm. The product is composed of uniform spherical nanoparticles with narrow size distribution and high purity. A probable mechanism for the formation of nanocrystalline PbS particles in a toluene-in-water microemulsion with the inducement of ultrasound irradiation is proposed.

© 2002 Elsevier Science B.V. All rights reserved.

PACS: 61.82.Rx; 61.82.Fk; 81.05.Ys

Keywords: A1. Nanostructures; A2. Growth from solutions; B1. Sulfides; B1. Nanomaterials; B2. Semiconducting materials

1. Introduction

Semiconductor nanocrystals have electronic properties intermediate between those of molecular entities and macrocrystalline solids and are at present the subject of intense research [1–4]. In the past decade, there has been much interest in the synthesis and physical characterizations of nanoscale sulfide semiconductive materials. Various new methods for the preparation of sulfide nanocrystals

have been reported in recent years such as employing ultraviolet irradiation [5], γ -ray irradiation [6,7], the solvothermal method [8–10], microwave assisted heating [11–13], chemical bath deposition [14], electrodeposition [15–17], the sonoelectrochemical method [18], and so on. It is worth mentioning that using microemulsions and ultrasound irradiation are two synthetic methods for nanosized sulfides that have been studied intensively and arousing more and more attention.

Microemulsions have been intensively used as spatially constrained microreactors for the controlled growth of inorganic materials [19–21]. In the case of a microemulsion, the reactions take

*Corresponding author. Tel.: +86-25-331-7761; fax: +86-25-3594976.

E-mail address: jjzhu@nju.edu.cn (J.-J. Zhu).

place in the core of the microemulsions and the hydrophilic head groups of the surfactant molecules. Surfactants provide several types of well-organized assemblies which provide specific sites, geometrical control and stabilization to particulate assemblies formed within the organized surfactant assemblies. Sulfide nanoparticles such as CdS, ZnS, CuS, PbS, have been successfully prepared by this method [22–25] and have been well characterized and studied.

Currently, ultrasound irradiation has become an important tool in chemistry. It provides an unusual mechanism for generating high-energy chemistry with extremely high local temperatures and pressures and an extraordinary heating and cooling rate. Sonochemistry drives principally from acoustic cavitation: the formation, growth, and implosive collapse of bubbles in liquids [26]. When solutions are exposed to strong ultrasound irradiation, bubbles are implosively collapsed by acoustic fields in the solution. High-temperature and high-pressure fields are produced at the centers of the bubbles. The implosive collapse of the bubbles generates a localized hotspot through adiabatic compression or shock wave formation within the gas phase of the collapsing bubbles. The conditions formed in these hotspots have been experimentally determined, with the transient temperature of ~ 5000 K, pressure of > 1800 atm and cooling rates in excess of 10^{10} K/s [27]. These extreme conditions formed during ultrasound irradiation have already been applied to prepare some nanophasic sulfides. For example, Suslick and his co-workers have sonicated a slurry of molybdenum hexacarbonyl and sulfur in an isodurene solution and obtained MoS_2 [28]. Gedanken's group synthesized ZnS coated on silica microspheres by sonicating a slurry of silica microspheres, thioacetamide and zinc acetate [29]. Similarly, as described in one of their earlier publications [30], ultrasonic irradiation of a slurry of silica microspheres, cadmium sulfate, and thiourea in an aqueous medium for 3 h would yield cadmium sulfide–silica composite. Gedanken and co-workers have also successfully established sonochemical methods for the fabrication of a variety of nanocrystalline metal sulfides such as HgS and PbS nanoparticles [31], $\text{Ag}_2\text{S}/\text{PVA}$ and

CuS/PVA nanocomposite [32], $\text{RuS}_{1.7}$ [33] and In_2S_3 [34] nanoparticles. The sonochemical formation of CdS nanoparticles in aqueous solutions [35,36] and in CS_2 –water–ethylenediamine system [37] have also been recently reported.

PbS is a typical narrow band gap semiconductor. It is one of the most attractive metal sulfides for a wide variety of applications, such as Pb^{2+} ion-selective sensors and IR detectors [31]. Various processes, including sintering precipitation, vacuum evaporation, and electrochemical deposition have been employed to produce PbS bulk material or PbS films [38–40]. In this paper, we report on a sonochemical method for the preparation of PbS nanocrystals in an oil-in-water microemulsion. Sulfur–toluene solution (STS) was chosen as the sulfur source. When STS was mixed with water in the presence of sodium lauryl sulfate (SLS) as the surfactant, a liquid–liquid heterogeneous system was formed. The cavitation behavior of ultrasound irradiation can lead to extraction, mixed phase reactions and emulsification in such a liquid–liquid heterogeneous system. Thus, an o/w microemulsion of toluene-in-water can be formed under ultrasound irradiation. This synthetic design was motivated by the known simple interaction between sulfur and ethylenediamine, but it provides special conditions for the formation and growth of the PbS nanocrystals in such a microemulsion system in the presence of high-intensity ultrasound irradiation.

2. Experimental section

All the reagents were of analytical purity, and were used without further purification. Lead acetate ($\text{Pb}(\text{Ac})_2 \cdot 2\text{H}_2\text{O}$) was purchased from Shanghai Chemical Reagent Factory (China). Ethylenediamine (en) and SLS were purchased from Nanjing Chemical Reagent Factory (China). Absolute ethanol and acetone were purchased from Beijing Chemical Reagent Factory (China). Distilled water was used throughout the experiments.

In a typical procedure, 5 ml STS was mixed with 95 ml aqueous solution containing 0.005 mol $\text{Pb}(\text{Ac})_2$, 0.4 g SLS and 5 ml ethylenediamine.

STS was prepared by stirring 1.0 g sulfur powders in 50 ml toluene at about 313 K till the sulfur powder was completely dissolved. Then the mixture was exposed to ultrasound irradiation under ambient air for 30 min. Ultrasound irradiation was accomplished with a high-intensity ultrasound probe (Xinzhi Co., China; JY92-2D; 0.6 cm-diameter; Ti-horn, 20 kHz, 60 W/cm²) immersed directly in the reaction solution. The sonication was conducted without cooling so that a temperature of about 333 K was reached at the end of the reaction. When the reaction finished, a black precipitate occurred. The precipitate was separated by centrifugation, washed with distilled water, absolute ethanol and acetone in sequence, and dried in air at room temperature for 8 h. The products are characterized by using techniques such as X-ray powder diffraction (XPRD), transmission electron microscopy (TEM), X-ray photoelectron spectroscopy (XPS), energy-dispersive X-ray analysis (EDAX).

The XPRD analysis was performed by Shimadzu XD-3A X-ray diffractometer at a scanning rate of 4°/min in the 2 θ range from 20° to 60°, with graphite monochromatized Cu K α radiation ($\lambda = 0.15418$ nm). TEM measurements were carried out by employing JEOL JEM-200CX TEM, using an accelerating voltage of 200 kV. The samples used for TEM observations were prepared by dispersing some products in ethanol followed by ultrasonic vibration for 30 min, then placing a drop of the dispersion onto a copper grid coated with a layer of amorphous carbon. The surface of the product was detected by X-ray photoelectron spectra recorded on ESCALAB MK II X-ray photoelectron spectrometer, using non-monochromatized Mg K α X-ray as the excitation source and choosing C1s (284.6 eV) as the reference line. EDAX measurements were performed on the PV9100 instrument.

3. Results and discussions

The XPRD pattern of the as-prepared PbS nanoparticles (Fig. 1) shows the presence of broad peaks corresponding to the cubic crystal structure. The positions and intensities of the peaks are in

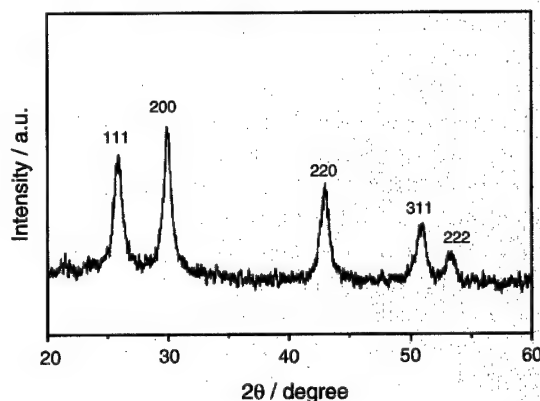


Fig. 1. XPRD pattern of the as-prepared PbS nanocrystals.

good agreement with the literature values for cubic phase PbS with a zinc blende structure.¹ The broadening of the peaks indicates that the crystal sizes are very small. The average size of the as-prepared PbS nanocrystals are estimated to 11 nm according to the Debye–Scherrer formula [41].

The dimensions and morphologies of the PbS nanocrystals are shown in the TEM image (Fig. 2a). It is apparent that the as-prepared PbS nanocrystals present uniform spherical morphologies and their sizes are in the range of 8–13 nm, which is in good accordance with the results calculated according to the XPRD pattern. The particle size distribution, measured directly from the TEM image is shown as histograms in Fig. 2b.

The product is also characterized by XPS and EDAX for the evaluation of their composition and purity. The wide scanning XPS spectrum of the as-prepared PbS nanocrystals is shown in Fig. 3. The C1s peaks should be corrected to 284.6 eV and all the other peaks should be corrected accordingly. The binding energies obtained from XPS analysis show good agreement with the literature [42]. No peaks of impurities such as Pb(0), Pb(IV) or N are observed in the spectrum, indicating the high purity of the product. Figs. 4a and b show the high-resolution XPS spectra of Pb(4f) and S(2p), respectively. Peak areas of Pb(4f) and S(2p) cores are measured and quantification of the peaks gives

¹ Joint Committee on Powder Diffraction Standards (JCPDS), File No 5-0592.

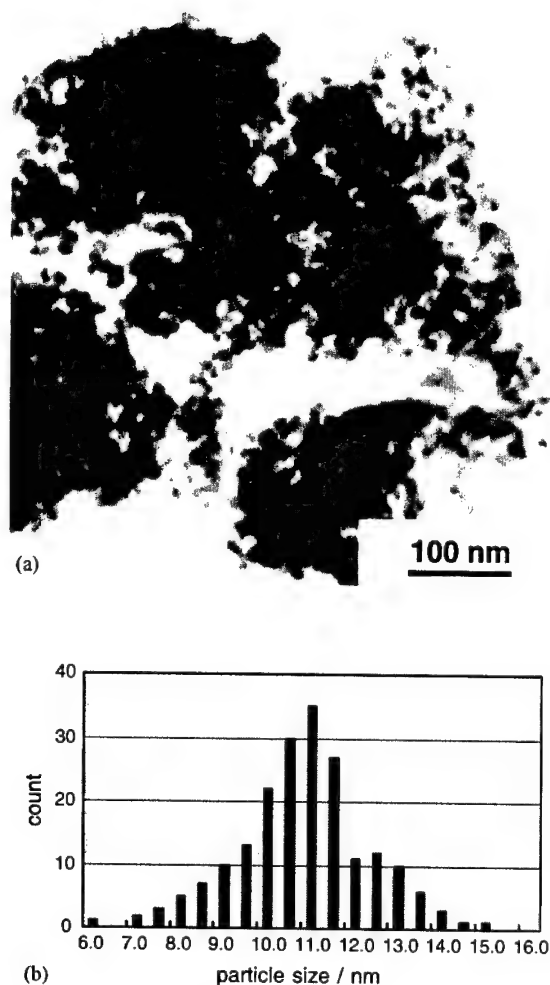
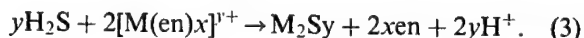
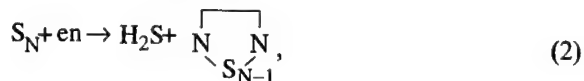
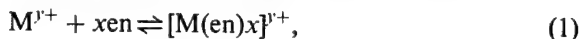


Fig. 2. (a) TEM image of the as-prepared PbS nanocrystals; and (b) particle size distribution picture obtained by direct measurements in the TEM image.

the ratio of Pb:S to be 1.19:1, which indicates that the surface of the sample is rich in Pb. XPS primarily monitors concentrations at the surface of the examined samples, which may not be representative of the sample as a whole. The deviation of atomic ratio of Pb:S to the expected 1:1 may be attributed to the excessive Pb^{2+} absorbed on the surface of PbS nanocrystals. The results of EDAX measurement reveal that the as-prepared PbS nanocrystals are of high purity and the average atomic ratio of Pb:S is 53.6:46.4, which also points out that the surface of the product is

rich in Pb. The results are consistent with the XPS results.

The formation of nanocrystalline lead sulfide is based on the known interaction between sulfur and ethylenediamine. Lelieui [43] and Parkin [44,45] have developed a room temperature liquid-amine route to metal chalcogenides based on the reactions of sulfur, selenium or tellurium with elemental metals in liquid ammonia in a pressure vessel. They pointed out that in sulfur-ammonia solutions, there were various sulfur imido anions (S_2N^- , S_3N^- , S_4N^-) as well as sulfur polyanions (S_6^{2-} , S_4^{2-}) and zero oxidation sulfur species (S_xNH_3^- , $x = 1-8$). Sulfur could also dissolve in organo-amine to produce colored N,N' -diamine-polysulfide solution and hydrosulfuric acid [46]. Ethylenediamine plays an important role in generating the active sulfur species, such as S^{2-} . Meanwhile, ethylenediamine as a strong bidentate ligand can co-ordinate with metal ions to give stable complexes in the form of chelate compounds $[\text{M}(\text{en})_x]^{y+}$. These chelate compounds would then react with the active sulfur species, leading to the formation of metal sulfides. The whole process can be described as below



The nature and morphology of the metal sulfides via such liquid-ammonia route greatly depend on the preparation conditions. When the reactions of a range of transition metals and main metals with sulfur-liquid ammonia solutions were carried out at room temperature in Teflon-in glass Younges-type pressure tubes, the as-prepared metal sulfides were mainly amorphous or poorly crystalline [45]. If such reactions were carried out under solvothermal conditions, nanocrystalline metal sulfides with different morphologies could be obtained [9,47]. Gedanken et al. [31] employed ultrasound irradiation to induce such liquid-ammonia reactions in ethylenediamine and managed to get nanocrystalline spherical HgS and rectangular PbS particles. In the present work, we

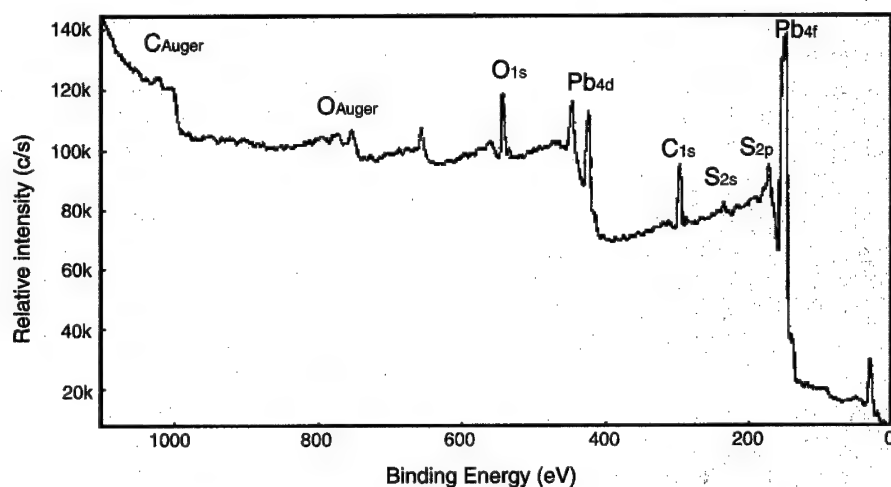


Fig. 3. The wide XPS spectrum of the as-prepared PbS nanocrystals.

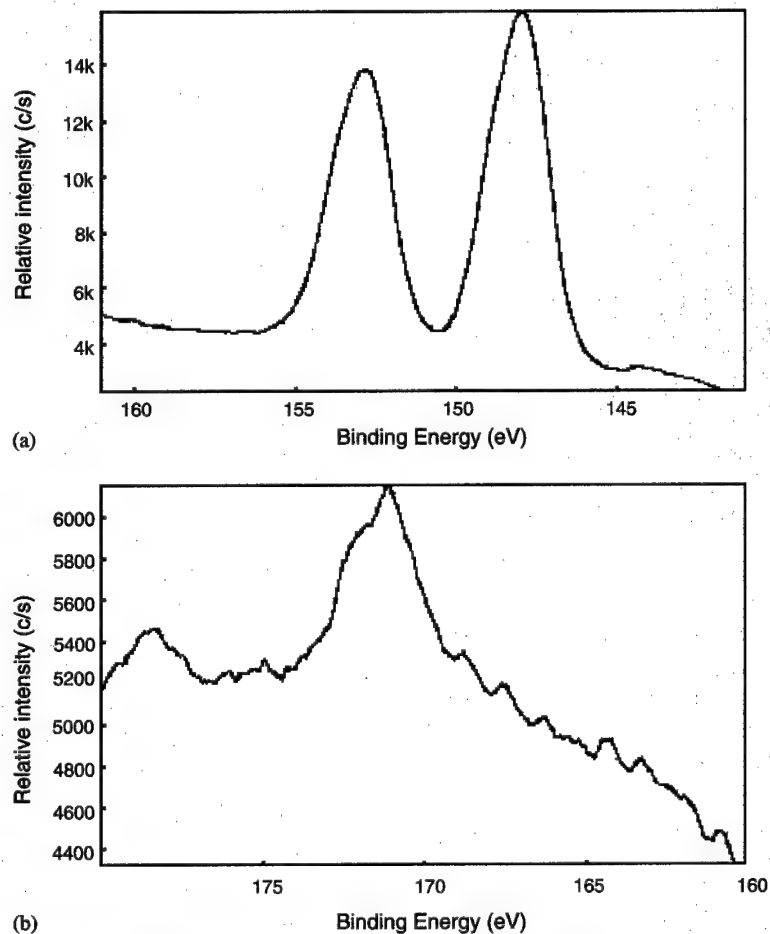


Fig. 4. High-resolution XPS spectra of the as-prepared PbS nanocrystals: (a) Pb (4f); and (b) S (2p).

design an ultrasound-induced microemulsion route to prepare lead sulfide nanocrystals based on the reactions described above. The schematic presentation of formation of lead sulfide nanocrystals is shown in Fig. 5.

In the toluene–water heterogeneous system, sulfur powder was dissolved in toluene, the oil phase, and $[\text{Pb}(\text{en})\text{x}]^{2+}$ and excessive ethylenediamine was in the water phase. No reaction took place at this stage. After SLS was added and the mixture was irradiated with high-intensity ultrasound for a period of time, toluene droplets were homogenized and sulfur began to react with ethylenediamine at the oil–water interface to give H_2S . SLS played a critical role in this process. It not only promoted the formation of the microemulsion as the oil droplet stabilizer, but also provided the sites for the reactions by bridging the oil–water interface. Then the released H_2S combined with $[\text{Pb}(\text{en})\text{x}]^{2+}$ to form PbS nuclei in the water phase. These freshly generated nuclei were unstable and have the tendency to grow into larger grains.

In the process of the formation of PbS nanocrystals, the ultrasound irradiation plays an important role. Sulfur can react with ethylenediamine at room temperature. However, it was found that in this system the reactions did not take place without the inducement of ultrasound irradiation, because sulfur and ethylenediamine existed in different phases, which restrained the reactions. Ultrasound waves that are intense enough to produce cavitation can drive chemical reactions such as oxidation, reduction, dissolution and

decomposition [27,48]. Other reactions driven by high-intensity ultrasound irradiation such as promotion of polymerization have also been reported to be induced by ultrasound. Ultrasound irradiation differs from traditional energy sources (such as heat, light or ionizing radiation) in duration, pressure and energy per molecule. It has been known that during the sonochemical process, three different regions [48] are formed: (a) the inner environment (gas phase) of the collapsing bubbles, where the elevated temperatures and pressures are produced; (b) the interfacial region between the cavitation bubbles and the bulk solution where the temperature is lower than in the gas-phase region but still high enough to induce a sonochemical reaction; (c) the bulk solution, which is at ambient temperature. Among the three regions mentioned above, it appears that the current sonochemical reactions occur within the interfacial region, yielding nanoparticles, because of the very high quenching rate experienced by the products. The critical temperature of ethylenediamine (591 K) is lower than that of water (647 K), so the velocity of the diffusion of ions and the interparticle collisions in ethylenediamine under ultrasound irradiation will be more rapidly due to its lower viscosity. When the bubbles collapse, the ethylenediamine in the water phase will be vaporized. These vaporized ethylenediamine molecules react with the sulfur dissolved in the toluene droplets via the connection of SLS which acts as the bridge over the oil–water interface, leading to the formation of the released H_2S . Moreover, ultrasound irradiation also affects the growth of the nanoparticles. Once the nuclei of

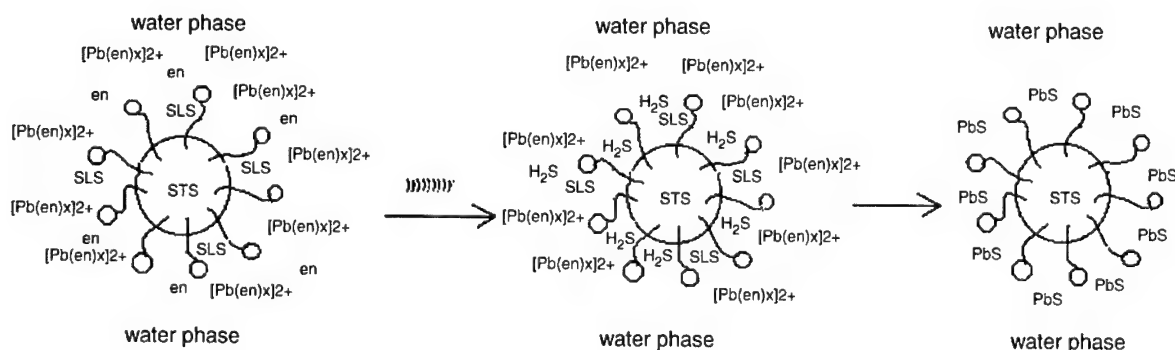


Fig. 5. The schematic presentation of sonochemical formation of PbS nanocrystals in o/w microemulsion.

PbS formed, they were unstable and have the a tendency to grow into larger grains. The increase of the grain size with sonication time can be explained by the effect of acoustic cavitation on PbS. The implosive collapse of a cavity on an extended solid surface in a liquid has been recognized to be different from the symmetrical implosion of cavities observed in homogeneous, pure liquids [49]. In the former case, asymmetric implosion results in the formation of high-speed microjets of liquids as well as shock waves that drive the solid particles to high velocities, which leads to interparticle collisions. The collisions between the PbS particles at high velocities result in increased local heating and condensation to form larger particles [50]. The increase in size of the PbS nanoparticles can also involve the crystal growth process. When the PbS nanoparticles formed, smaller particles had a large number of dangling bonds, defect sites, or traps [51]. During the reaction time, the surface states changed. Dangling bonds, defect sites or traps will decrease gradually, and the grains will grow. After a period of time under ultrasound irradiation, the surface states become stable, and the size of the grains cease to increase any more. In our experiments, 30 min was chosen as the sonication time. When the sonication time decreased to less than 20 min, the reactions was not completed. If the reaction time was prolonged to 1 h, the size and morphology of the products almost remained unchanged. Therefore, we may draw the conclusion that sonication for 30 min is suitable for both the nucleation and the growth of the PbS nanoparticles.

4. Conclusions

In summary, a novel sonochemical method for the preparation of PbS nanocrystals in oil-in-water microemulsions has been established. The products have uniform shape, narrow size distributions and high purity. The probable mechanism for the formation of nanocrystalline lead sulfide particles in a toluene–SLS–water microemulsion induced by ultrasound irradiation is proposed. We can foresee the extension of this method to the

preparation of other nanocrystalline metal sulfides.

Acknowledgements

This work is supported by the National Natural Science Foundation of China (Grant No. 50072006) and the Jiangsu Advanced Science and Technology Programme of China (Grant BG 2001039). The authors also thank Ms. Xiaoshu Wang and Ms. Xiaoning Zhao from Modern Analytic Center of Nanjing University for extending their facilities to us.

References

- [1] D. Dounghong, J. Ramsden, M. Gratzel, *J. Am. Chem. Soc.* 104 (1982) 29777.
- [2] Y. Wang, N. Herron, *J. Phys. Chem.* 95 (1991) 525.
- [3] A. Henglein, *Chem. Rev.* 89 (1989) 1861.
- [4] H. Weller, *Adv. Mater.* 5 (1993) 88.
- [5] C.Y. Wang, X. Mo, Y. Zhou, Y.R. Zhu, H.T. Liu, Z.Y. Chen, *J. Mater. Chem.* 10 (2000) 607.
- [6] X.C. Jiang, Y. Xie, J. Lu, L.Y. Zhu, W. He, Y.T. Qian, *Chem. Mater.* 13 (2001) 1213.
- [7] Y.D. Yin, X.L. Xu, *Chem. Commun.* (1998) 1641.
- [8] X.F. Qian, X.M. Zhang, C. Wang, Y. Xie, Y.T. Qian, *Inorg. Chem.* 38 (1999) 2621.
- [9] S.H. Yu, L. Shu, J. Yang, Z.H. Han, Y.T. Qian, Y.H. Zhang, *J. Mater. Res.* 14 (1999) 4157.
- [10] S.H. Yu, Y.S. Wu, J. Yang, Z.H. Han, Y. Xie, Y.T. Qian, X.M. Liu, *Chem. Mater.* 10 (1998) 2309.
- [11] H. Wang, J.R. Zhang, J.J. Zhu, *J. Crystal Growth* 233 (2001) 829.
- [12] J.J. Zhu, M.G. Zhou, J.Z. Xu, X.H. Liao, *Mater. Lett.* 47 (2001) 25.
- [13] A.V. Murugan, R.S. Sonawane, B.B. Kale, S.K. Apte, A.V. Kulkarni, *Mater. Chem. Phys.* 71 (2001) 98.
- [14] R.S. Mane, C.D. Lokhande, *Mater. Chem. Phys.* 65 (2000) 1 and references cited therein.
- [15] C.Y. Wang, Y. Zhou, Y.R. Zhu, H.J. Liu, Z.Y. Chen, *Mater. Res. Bull.* 35 (2000) 1463.
- [16] D. Routkevitch, T. Bigioni, M. Moskovits, J.M. Xu, *J. Phys. Chem.* 100 (1996) 14037.
- [17] D.S. Xu, D.P. Chen, Y.J. Xu, X.S. Shi, G.L. Guo, L.L. Gui, Y.Q. Tang, *Pure Appl. Chem.* 72 (2000) 127.
- [18] Y. Mastai, M. Homyonfer, A. Gedanken, *Adv. Mater.* 11 (1999) 1010.
- [19] M.P. Pileni, *J. Phys. Chem.* 97 (1993) 6961.
- [20] V. Pillai, P. Kumar, M.J. Hou, P. Ayyub, D.O. Shah, *Adv. Colloid Interface Sci.* 55 (1995) 241.

- [21] M.J. Schwuger, K. Stickdorn, R. Schomacker, *Chem. Rev.* 95 (1995) 849.
- [22] P. Liao, J.K. Tomas, *J. Colloid Interface Sci.* 117 (1987) 506.
- [23] R. Vogel, P. Hoyer, H. Weller, *J. Phys. Chem.* 98 (1994) 3183.
- [24] A.R. Kortan, R. Hull, R.L. Opila, M.G. Bawendi, M.L. Steingerwald, P.J. Carrol, L.E. Brus, *J. Am. Chem. Soc.* 112 (1990) 1327.
- [25] S.G. Dixit, A.R. Mahadeshwar, S.K. Haram, *Colloids Surf. A* 133 (1998) 69.
- [26] K.S. Suslick, *Ultrasound: Its Chemical, Physical and Biological Effects*, VCH, Weinheim, Germany, 1988.
- [27] K.S. Suslick, S.B. Choe, A.A. Cichowlas, M.W. Grinstaff, *Nature* 353 (1991) 414.
- [28] M.M. Mdleleni, T. Hyeon, K.S. Suslick, *J. Am. Chem. Soc.* 120 (1998) 6189.
- [29] N. Arul Dhas, A. Zaban, A. Gedanken, *Chem. Mater.* 11 (1999) 806.
- [30] N. Arul Dhas, A. Gedanken, *Appl. Phys. Lett.* 72 (1998) 2514.
- [31] J.J. Zhu, S.W. Liu, O. Palchik, Y. Koltypin, A. Gedanken, *J. Solid State Chem.* 153 (2000) 342.
- [32] R.V. Kumar, O. Palchik, Y. Koltypin, Y. Diamant, A. Gedanken, *Ultrasonics Sonochem.* 9 (2002) 65.
- [33] P. Jeevanandam, Y. Koltypin, Y. Gofer, Y. Diamant, A. Gedanken, *J. Mater. Chem.* 10 (2000) 2769.
- [34] S. Avivi, O. Palchik, V. Palchik, M.A. Slifkin, A.M. Weiss, A. Gedanken, *Chem. Mater.* 13 (2001) 2195.
- [35] G. Wang, G. Li, C. Liang, L. Zhang, *Chem. Lett.* (2001) 344.
- [36] J.Z. Sostaric, R.A. Caruso-Hobson, P. Mulvaney, F. Grieser, *J. Chem. Soc. Faraday Trans.* 93 (1997) 1791.
- [37] J.X. Huang, Y. Xie, B. Li, Y. Liu, J. Lu, Y.T. Qian, *J. Colloid Interface Sci.* 236 (2001) 382.
- [38] M. Sharon, K.S. Ramaiah, M. Kumar, M. Neumann-Spallart, C. Levy-Clement, *J. Electroanal. Chem.* 436 (1997) 49.
- [39] F.C. Meldrum, J. Flath, W. Knoll, *J. Mater. Chem.* 9 (1999) 711.
- [40] R. Thielsch, T. Bohmn, R. Reiche, D. Schlafer, H.D. Bauer, H. Botteher, *Nanostruct. Mater.* 10 (1998) 131.
- [41] H. Klug, L. Alexander, *X-ray Diffraction Procedures*, Wiley: New York, 1962.
- [42] C.D. Wagner, W.M. Riggs, L.E. Davis, J.F. Moulder, B.E. Muilenberg, *Handbook of X-ray Photoelectron Spectroscopy*, Perkin-Elmer, Physical Electronics Division, Eden Prairie, 1979.
- [43] P. Dubois, J.P. Lelieur, G. Lepoutre, *Inorg. Chem.* 28 (1989) 195.
- [44] G. Henshaw, I.P. Parkin, G.A. Shaw, *Chem. Commun.* (1996) 1095.
- [45] G. Henshaw, I.P. Parkin, G.A. Shaw, *J. Chem. Soc. Dalton Trans.* (1997) 231.
- [46] F.A. Cotton, G. Wilkinson, *Advanced Inorganic Chemistry*, 3rd Edition, Wiley, New York, 1972.
- [47] Q.Y. Lu, J.Q. Hu, K.B. Tang, Y.T. Qian, X.M. Liu, G.E. Zhou, *J. Solid State Chem.* 146 (1999) 484.
- [48] K.S. Suslick, D.A. Hammerton, R.E. Cline, *J. Am. Chem. Soc.* 108 (1986) 5641.
- [49] W. Lauterborn, A. Vogel, *Annu. Rev., Fluid Mech.* 16 (1984) 223.
- [50] S. Ramech, Y. Koltypin, A. Gedanken, *J. Mater. Res.* 12 (1997) 3271.
- [51] W. Chen, Z. Wang, Z. Lin, L. Lin, *J. Appl. Phys.* 82 (1997) 3111.



ELSEVIER

Available online at www.sciencedirect.com

SCIENCE @ DIRECT®

JOURNAL OF CRYSTAL GROWTH

Journal of Crystal Growth 246 (2002) 169–175

www.elsevier.com/locate/jcrysgro

Solvothermal preparation of Cu_2O crystalline particles

Shu-Jian Chen^a, Xue-Tai Chen^{a,*}, Ziling Xue^b, Li-Hong Li^a, Xiao-Zeng You^{a,*}

^a State Key Laboratory of Coordination Chemistry, Institute of Chemistry, Nanjing University, 22 Hankou Road, 210093 Nanjing, China

^b Department of Chemistry, University of Tennessee, Knoxville, TN 37996, USA

Received 30 August 2002; accepted 16 September 2002

Communicated by R. Kern

Abstract

A solvothermal process has been developed to prepare both the cubic single crystals and the spherical polycrystals of Cu_2O by the reduction of $\text{CuSO}_4 \cdot 5\text{H}_2\text{O}$ with D-glucose as a reductant in the presence of the different organic additives such as ethylene glycol, polyethylene glycol 200 (PEG-200), polyethylene glycol 400 (PEG-400), polyethylene glycol 10000 (PEG-10000), polyethylene glycol 20000 (PEG-20000) or polyvinyl pyrrolidone (PVP K-30). All the products were characterized using X-ray diffraction and transmission electron microscopy. The organic additives were found to play a key role in the formation of the Cu_2O crystals and lead to the different microstructures of the resultant Cu_2O . Two different mechanisms, diffusion mechanism and aggregation mechanism, were used to explain the formation of single crystals and polycrystals of Cu_2O , respectively. When PEG-10000, PEG-20000 or PVP K-30 was added into the reaction system, a diffusion mechanism contributes to the formation of the single crystals of Cu_2O , while aggregation mechanism prevails in the polycrystals of Cu_2O with EG, PEG-200 or PEG-400. The pH of the mixture was also found to be a key factor in deciding the final products.

© 2002 Elsevier Science B.V. All rights reserved.

PACS: 81.10.Aj; 73.61.Le; 81.10.Aj; 73.61.Ph; 81.10.-h

Keywords: A1. Characterization; A2. Crystallites; A2. Growth from solutions; B1. Oxides; B2. Semiconducting materials

1. Introduction

Cuprous oxide has attracted much current research interest since Cu_2O is an important metal-oxide p-type semiconductor [1–3] and has a direct band gap of 2.2 eV, which makes it a promising material for the conversion of solar energy into electrical or chemical energy [4,5].

Recently, Cu_2O was reported to act as a stable catalyst for water splitting under visible light irradiation (≤ 600 nm) although its exact role is unclear [6–8]. Cu_2O has been prepared by several different methods, such as electrodeposition [9–11], thermal relaxation [12], sonochemical method [13], vacuum evaporation [14] and liquid phase reduction of metal salts [15]. Dong et al. [16] have reported the preparation of Cu_2O by the reduction of $\text{CuSO}_4 \cdot 5\text{H}_2\text{O}$ with hydrazine as a reductant in the presence of glucose as a modifier, at room temperature. We report here a solvothermal route

*Corresponding author. Tel.: +86-25-3592309; fax: +86-25-3314502.

E-mail address: xtchen@netra.nju.edu.cn (X.-T. Chen).

to prepare Cu_2O by reduction of $\text{CuSO}_4 \cdot 5\text{H}_2\text{O}$ with D-glucose as a reductant in the presence of other organic additives as modifiers. Six different organic molecules EG, PEG-200, PEG-400, PEG-10000, PEG-20000 or PVP K-30, were used to control the reduction and growth process and gave various cuprous oxide crystalline particles of either single crystals or polycrystals. As claimed by Stupp and Braun [17], organic molecules, even in tiny quantity, could alter inorganic microstructures, offering a very powerful tool for the design of novel materials. The roles the organic molecules play in influencing crystallinity of Cu_2O crystals and the pH of the reaction mixture will be discussed.

2. Experimental procedure

Cu_2O crystals were prepared by the reaction of $\text{CuSO}_4 \cdot 5\text{H}_2\text{O}$, NaOH and D-glucose in the presence of different organic additives such as EG, PEG-200, PEG-400, PEG-10000, PEG-20000 or PVP K-30 under solvothermal condition (60°C) in an autoclave. The products were denoted as sample A–L, respectively. In a typical procedure, 20.0 ml of EG was mixed with 2.0 mmol of $\text{CuSO}_4 \cdot 5\text{H}_2\text{O}$ in 10.0 ml of distilled water with vigorous stirring in 50 ml of a flask, and then 8.0 mmol of NaOH in 5.0 ml of distilled water and 1.0 mmol of D-glucose were added into the solution. The total solution was then put into a Teflon-lined stainless steel autoclave of 50.0 ml of capacity. The autoclave was maintained at 60°C for 1 h without shaking or stirring and then was allowed to cool gradually to room temperature. A reddish precipitate was washed in an ultrasonic bath several times with distilled water and then with ethanol to remove the EG. The final product (sample A) was dried in a vacuum oven at 60°C for 3 h. The other samples (B–L) were prepared similarly as sample A and their reactants, reaction temperature and time are:

Sample B or H:

2.0 mmol of $\text{CuSO}_4 \cdot 5\text{H}_2\text{O}$ + 15.0 ml of water + 20.0 ml of PEG-200 + 9.0 mmol of NaOH + 1.0 mmol of D-glucose, 60°C , 1 h or 25 min, respectively.

Sample C or I:

2.0 mmol of $\text{CuSO}_4 \cdot 5\text{H}_2\text{O}$ + 15.0 ml of water + 20.0 ml of PEG-400 + 8.0 mmol of NaOH + 1.0 mmol of D-glucose, 60°C , 1 h or 25 min, respectively.

Sample D or J:

2.0 mmol of $\text{CuSO}_4 \cdot 5\text{H}_2\text{O}$ + 35.0 ml of water + 1.0 g of PEG-10000 + 10.0 mmol of NaOH + 1.0 mmol of D-glucose, 60°C , 1 h or 12 min, respectively.

Sample E or K:

2.0 mmol of $\text{CuSO}_4 \cdot 5\text{H}_2\text{O}$ + 35.0 ml of water + 1.0 g of PEG-20000 + 10.0 mmol of NaOH + 1.0 mmol of D-glucose, 60°C , 1 h or 12 min, respectively.

Sample F or L:

2.0 mmol of $\text{CuSO}_4 \cdot 5\text{H}_2\text{O}$ + 35.0 ml of water + 2.0 g of PVP K-30 + 8.0 mmol of NaOH + 1.0 mmol of D-glucose, 60°C , 1 h or 12 min, respectively.

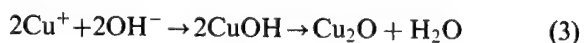
Sample G:

2.0 mmol of $\text{CuSO}_4 \cdot 5\text{H}_2\text{O}$ + 15.0 ml of water + 20.0 ml of EG + 8.0 mmol of NaOH + 1.0 mmol of D-glucose, 60°C , 1 h.

The products were characterized by X-ray diffraction [(XRD)XD-3A, Shimadzu Co.] with Cu K_α radiation ($\lambda = 1.5418 \text{ \AA}$) and transmission electron microscopy [(TEM)JEOL JEM-200CX]. The specimens for TEM were prepared by placing the solid products in absolute ethanol, immersing them in an ultrasonic bath for 15 min. A few drops of the suspension were placed onto a TEM grid. IR Spectra of samples were measured with a Bruker Vector22 IR spectrometer.

3. Results and discussion

In the overall reaction system, the Cu^{2+} ions are reduced first to Cu^+ by D-glucose [18]. The following reaction are believed to occur:



when the D-glucose powders were added into the Cu^{2+} salt system, the D-glucose powders were first contacted with organic additives, then D-glucose powders reached the pools, and the Cu^{2+} ions were reduced to Cu^+ by D-glucose. At the same time, if enough OH^- ions exist in the pools, the main reaction tendency of Eq. (3) becomes dominant. However, if quantity of OH^- ions were limited in the pools, the reaction of Cu^+ was in part companied with Eqs. (1) and (2), as shown in the presence of PEG-400 in Fig. 1. Fig. 1a shows the reflectance peaks of Cu_2O and tiny Cu when 7.0 mmol of NaOH was added into the reaction system, only the reflectance peaks of pure phase cubic Cu_2O appear in Fig. 1b or c, which corresponds to the reaction in the proceeding with 8.0 mmol of NaOH or more, 8.5 mmol of NaOH, respectively. It was found difficult to obtain phase-pure Cu_2O in the absence of appropriate organic additives in the liquid phase reduction of metal salt [16]. Organic additives play a crucial role in the appearance of pure phase of Cu_2O . XRD patterns

of the samples (A–L) prepared in the presence of EG, PEG-200, PEG-400, PEG-10000, PEG-20000 or PVP K-30, respectively, are shown in Fig. 2. All reflectance peaks are indexed to a cubic Cu_2O phase (JCPDS 5-669). The peaks at 2θ values of 29.523° , 36.391° , 42.333° , 61.598° , 73.787° and 77.580° correspond to 110, 111, 200, 220, 311, 222 phases of standard crystalline Cu_2O , respectively. Single crystals or polycrystals of certain morphologies can be prepared through the use of the suitable organic additives. For example, Fig. 3 shows the TEM and selected area electron diffraction (SAED) micrographs of sample E prepared in the presence of PEG-20000. A hexagonal shape of a crystal of sample E in Fig. 3a shows a quadrilateral shape (Fig. 3c) when it is rotated 30° . Electron diffraction of the freshly prepared Cu_2O (Fig. 3b) reveals that sample E is a single crystal cubic Cu_2O . Fig. 4 shows the TEM and SAED micrographs of sample C prepared in the presence of PEG-400 and reveals a spherical morphology. The ring-like SAED (Fig. 4b) implies

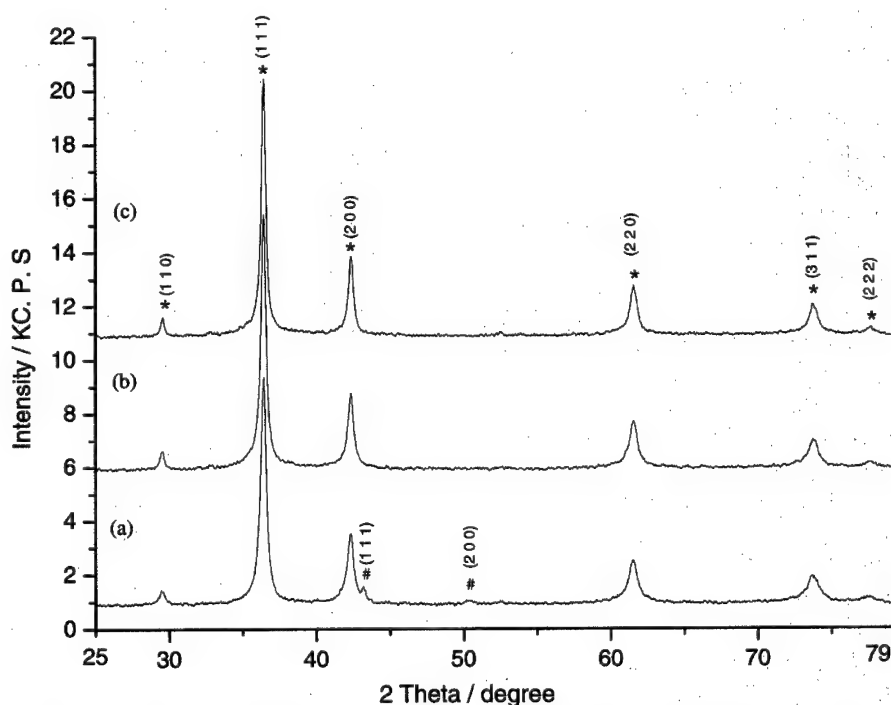


Fig. 1. The XRD patterns of Cu_2O produced in the presence of PEG-400 with (a) 7.0 mmol, (b) 8.0 mmol and (c) 8.5 mmol of NaOH (*), Cu_2O (#), Cu.

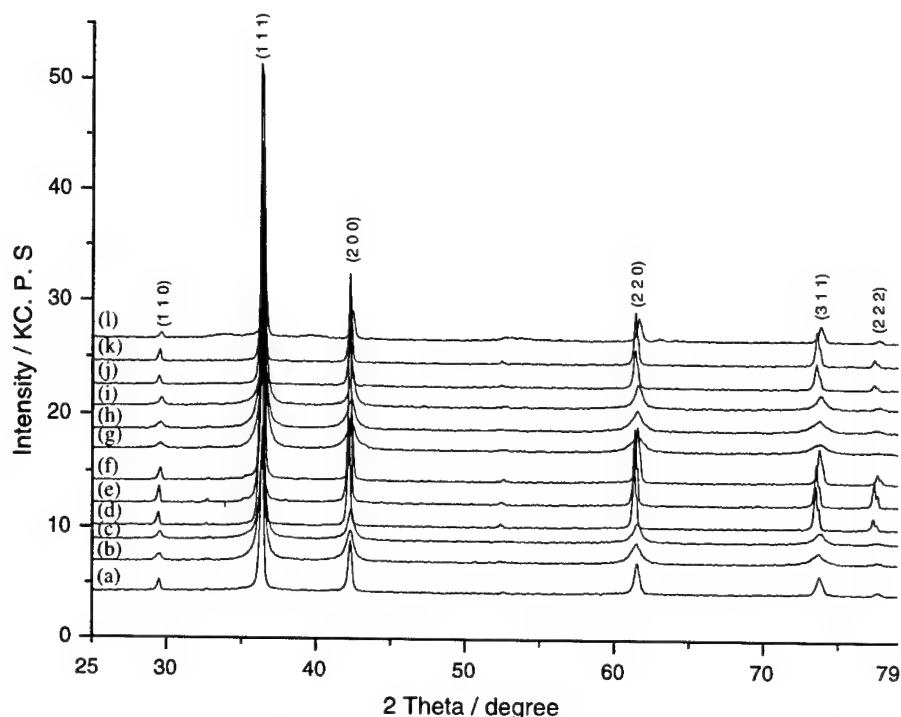


Fig. 2. The XRD patterns of Cu_2O samples (A–L) denoted by a–l, respectively, in the presence of six kinds of different organic additives, are obtained at different time as shown in Table 1.

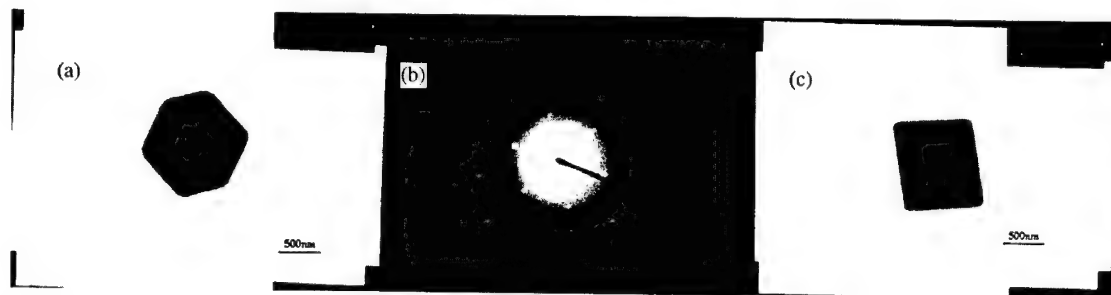


Fig. 3. The TEM and selected area electron diffraction (SAED) micrographs of Cu_2O (sample E) prepared in the presence of PEG-20000: A hexagonal shape of the sample crystal appears in (a) whose quadrilateral shape is shown in Fig. 3c when it is rotated 30° , (b) shows electron diffraction of the as-prepared Cu_2O , which reveals that it is a cubic Cu_2O single crystal.

that the spherical particle of sample C is polycrystal.

A diffusion mechanism [19,20] could be used to explain the formation of monodispersed single crystals. A monodispersed precipitation process is kinetically controlled, resulting in a short nucleation burst once a critical supersaturation of particle forming species is reached. The nucleation stage is then followed by diffusion of constituent

complexes onto these primary particles until the supply is exhausted. The aggregation mechanism [21,22] could be used to explain the formation of monodispersed polycrystals. This mechanism indicates that uniform particle formation usually proceeds in several stages. In the initial induction stage, solutes are formed to yield a supersaturated solution, leading to nucleation. The nuclei then grow by diffusive mechanism to form the

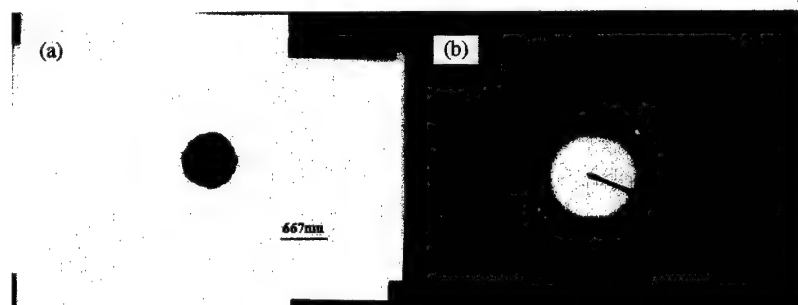


Fig. 4. The TEM (a) and SAED (b) micrographs of Cu_2O (sample C), which reveal that it is a spherical polycrystal morphology, are produced in the presence of PEG-400.

Table 1

Comparison of results from the reaction system in the presence of six different organic additives as modifiers

Sample no.	Modifier	Reaction time (t)	NaOH (mmol)	Product	Morphology	Particle size (nm)
A	EG	1 h	8.0		Spherical	54
G		12 min				50
B	PEG-200	1 h	8.0		Spherical	25
H		25 min				23
C	PEG-400	1 h	8.0		Spherical	32
I		25 min				29
D	PEG-10000	1 h	10.0	Cu_2O	Cubic	123
J		12 min				76
E	PEG-20000	1 h	10.0		Cubic	76
K		12 min				68
F	PVP K-30	1 h	8.0		Cubic	102
L		12 min				56

The particle sizes were calculated from Scherrer's equation based on the Cu_2O (111) diffraction peak.

crystalline subunits, which in turn aggregate to form the larger polycrystalline assemblages.

Differences in two mechanisms have been discussed recently. These two mechanisms are believed to coexist in influencing the morphologies of the Cu_2O particles under competitive condition. In other words, the nucleation process is accompanied with diffusion as well as aggregation. In the presence of a modifier in the solution system, single crystals may form through primarily diffusion process. In the presence of another modifier under almost the identical condition, polycrystals could be produced because the aggregation becomes a dominating route. Figs. 3 and 4 show two

examples of diffusion mechanism and aggregation mechanism, respectively. In the presence of PEG-20000 as a modifier, the nucleation was controlled by the diffusion process, and single crystals of Cu_2O were produced. When PEG-400 was used as a modifier under almost the same condition, the nucleation was dominated by aggregation and polycrystals of Cu_2O were formed.

The samples were collected at two different periods of their growth processes, in the presence of six organic additives as modifiers. These experiments were conducted to elucidate the mechanism of the growth of Cu_2O single crystalline and polycrystalline solids. These results are

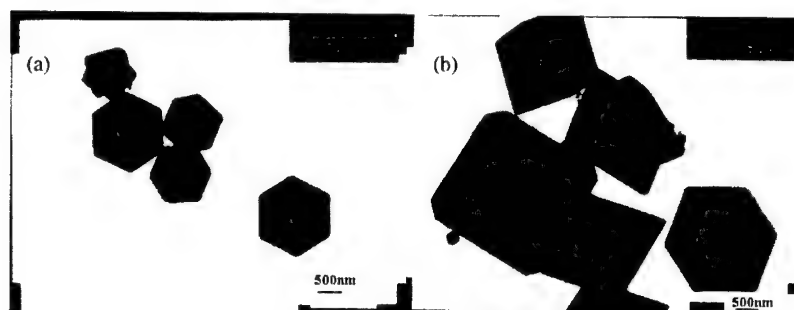


Fig. 5. The TEM micrographs of the Cu_2O in the presence of PEG-20000 at 12 min (sample K) and 1 h (sample E).

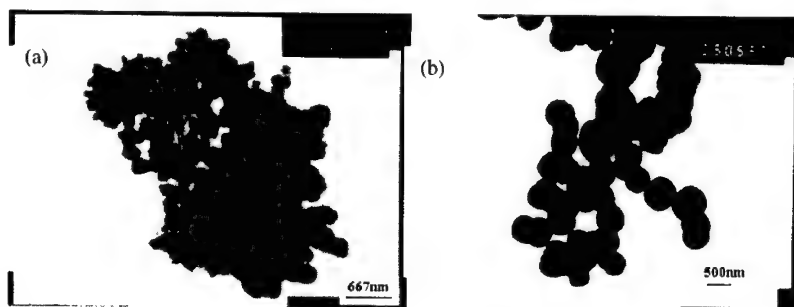


Fig. 6. The TEM micrographs of the Cu_2O in the presence of PEG-400 at 25 min (sample I) and 1 h (sample C).

shown in Table 1. The TEM micrographs of samples E and K prepared with PEG-20000 as well as C and I prepared with PEG-400 (Figs. 5 and 6), were considered as examples of solids from the two growth mechanisms. Small cubic single crystals of sample in Fig. 5a were obtained at the end of the reaction. However, after 1 h, larger cubic single crystals, showing no aggregation, were produced. Diffusion might be a dominating process in the formation of these single crystals. In contrast, Fig. 6a shows small spherical polycrystals of sample I at the end of reaction. After 1 h, some larger spherical polycrystals were obtained. They were yielded through aggregation. In the reaction process, the nucleation is mainly followed by aggregation. Furthermore, Table 1 indicates small organic additives as modifiers are helpful for diffusion, while larger organic additives promote aggregation. However, their role in the reaction and foundation of crystals is unclear. Perhaps larger organic additives cover tightly the particle surfaces and thus block aggregation of particles.

However, small organic additives may not be able to cover the surfaces and block the particle aggregation. FT-IR spectra of the as-prepared Cu_2O are observed a major peak at 628 cm^{-1} , assigned to Cu_2O [23]. This is consistent with the XRD and TEM results.

4. Conclusions

Cu_2O was prepared in the presence of different organic additives as modifiers, which was found to play a key role in determining the morphologies and crystallinity of Cu_2O . Diffusion and aggregation could be used to explain the morphologies of the Cu_2O solids from the current reaction. In the presence of PEG-10000, PEG-20000 or PVP K-30 as modifiers, diffusion became a dominating factor which was apt to single crystals. When EG, PEG-200 or PEG-400 were used as modifiers under almost identical conditions, aggregation was the main route, giving polycrystals.

Acknowledgements

This work was supported by Major State Basic Research Development Program (G200077500) and Distinguished Overseas Young Fund from the Natural Science Foundation of China (No. 20028101).

References

- [1] I. Grozdanov, Mater. Lett. 19 (1994) 281.
- [2] M.Y. Shen, T. Yokouchi, S. Koyama, T. Goto, Phys. Rev. B 56 (1997) 13066.
- [3] W. Shi, K. Lim, X. Liu, J. Appl. Phys. 81 (1997) 2822.
- [4] R.N. Briskman, Sol. Energy Mater. Sol. Cells 27 (1992) 361.
- [5] L.C. Olsen, F.W. Addis, W. Miller, Sol. Cells 7 (1982) 247.
- [6] M. Hara, T. Kondo, M. Komoda, S. Ikeda, K. Shinohara, A. Tanaka, J.N. Kondo, K. Domen, Chem. Commun. (1998) 357.
- [7] S. Ikeda, T. Takata, T. Kondo, G. Hitoki, M. Hara, J.N. Kondo, K. Domen, H. Hosono, H. Kawazoe, A. Tanaka, Chem. Commun. (1998) 2185.
- [8] P.E. de Jongh, D. Vanmaekelbergh, J.J. Kelly, Chem. Commun. (1999) 1069.
- [9] P.E. de Jongh, D. Vanmaekelbergh, J.J. Kelly, Chem. Mater. 11 (1999) 3512.
- [10] J.K. Barton, A.A. Vertegel, E.W. Bohannon, J.A. Switzer, Chem. Mater. 13 (2001) 952.
- [11] L.M. Huang, H.T. Wang, Z.B. Wang, A. Mitra, D.Y. Zhao, Y.S. Yan, Chem. Mater. 14 (2002) 876.
- [12] S. Deki, K. Akamatsu, T. Yano, M. Mizuhata, A. Kajinami, J. Mater. Chem. 8 (1998) 1865.
- [13] R.V. Kumar, Y. Mastai, Y. Diamant, A. Gedanken, J. Mater. Chem. 11 (2001) 1209.
- [14] H. Yanagimoto, K. Akamatsu, K. Gotoh, S. Deki, J. Mater. Chem. 11 (2001) 2387.
- [15] S. Ranz, C. Mitra, Mater. Sci. Eng. A 304–306 (2001) 805.
- [16] Y.J. Dong, Y.D. Li, C. Wang, A.L. Cui, Z.X. Deng, J. Colloid Interface Sci. 243 (2001) 85.
- [17] S.I. Stupp, P.V. Braun, Science 277 (1997) 1242.
- [18] C.Y. Wang, Y. Zhou, Z.Y. Chen, B. Cheng, H.J. Liu, X. Mo, J. Colloid Interface Sci. 220 (1999) 468.
- [19] V.K. La Mer, R.H. Dinegar, J. Am. Chem. Soc. 72 (1950) 4847.
- [20] V.K. La Mer, Ind. Eng. Chem. 44 (1952) 1270.
- [21] S.H. Lee, Y.S. Her, E. Matijević, J. Colloid Interface Sci. 186 (1997) 193.
- [22] V. Privman, D.V. Goia, J. Park, E. Matijević, J. Colloid Interface Sci. 213 (1999) 36.
- [23] H. Klug, L. Alexander, X-ray Diffraction Procedures, Wiley, New York, 1962, p. 125.



**Essential
Research
Resource**

SCIENCE @ DIRECT®

More **Choice** in...

- Content
- Navigation
- Functionality
- Platforms

**For the Scientists
of Today**

Journal Collections

1,200 scientific, medical and technical journals

A&I Databases

Intuitive navigation across 30 million
abstracts from over 10,000 journals from
multiple publishers

Open Linking Technologies

CrossRef... plus robust internal linking to
3 million full-text articles and abstracts

Journal Backfiles

Access to deeper historical research

Scirus.com

World's most comprehensive scientific
Web search engine

www.sciencedirect.com

New York
+1 212 462 1978
usinfo@sciencedirect.com

Amsterdam
+31 20 485 3767
nlinfo@sciencedirect.com

Singapore
+65 434 3727
sginfo@sciencedirect.com

Tokyo
+81 3 5561 5035
jpinfo@sciencedirect.com

Rio de Janeiro
+55 21 509 5340
brinfo@sciencedirect.com



find



submit



track



alerts



personalise

authorGATEWAY

from Elsevier Science

[illegible]

The integrated online entry point for all your submission needs

- ➡ Find your journal - search by title, keyword or editor; browse by subject area or title.
- ➡ Submit your paper - access comprehensive instructions about getting published, including online submission where available.
- ➡ Track your paper - track the status of your paper from acceptance to publication (this service was formerly known as OASIS)
- ➡ Set up alerts for your favourite journals - receive tables of contents by email from ContentsDirect.
- ➡ Personalise your homepage - create your own unique homepage with quick links to your papers, journals and email alerts.

<http://authors.elsevier.com>
helping you get published

helping you get published

For more information about the Author Gateway contact Author Support at: authorsupport@elsevier.com

AUTHORS

**If you want to make the best of your artwork
send it in the correct digital format**

All articles accepted for publication in Elsevier Science journals are processed using electronic production methods. Authors should therefore ensure that their artwork conforms to the following guidelines:

- **Colour and greyscale images** should be supplied as **TIFF** or **EPS** files (resolution 300 dpi).
- **Line drawings (black & white or colour)** should be supplied as **EPS** files

*If you need help to create files in these formats, go to
www.elsevier.com/locate/authorartwork/formats*

Please also note:

- We still need a good quality hard copy of each figure in case the electronic file cannot be used. The hard copy and electronic file must match exactly.
- We can use floppy disks, ZIP disks or CD-ROM. Artwork files should be on a separate disk or CD to article text files.
www.elsevier.com/locate/authorartwork/media
- Only standard fonts should be used, for example:
Times, Times New Roman, Helvetica, Arial, Symbol
www.elsevier.com/locate/authorartwork/formats
- Lines should be a minimum width of 0.5 pt.
www.elsevier.com/locate/authorartwork/linewidth
- Only standard colours should be used.
www.elsevier.com/locate/authorartwork/colours
- Lettering should be a consistent size and appropriate to the size of the figure.
www.elsevier.com/locate/authorartwork/sizing
- An image which looks acceptable on a computer may not reproduce well, so it is important to ensure that these guidelines are followed.

*Our Author Artwork website has all the information you need on
how to submit your artwork correctly. Visit it today at:*

www.elsevier.com/locate/authorartwork



ELSEVIER



NORTH
HOLLAND



PERGAMON

Solution growth; industrial, biological and molecular crystallization

Surface imaging of a natural mineral surface using scanning-probe microscopy

D.G. Bokern, W.A.C. Ducker, K.A. Hunter and K.M. McGrath

139

A new phase of cadmium titanate by hydrothermal method

H. Wang, X. Zhang, A. Huang, H. Xu, M. Zhu, B. Wang, H. Yan and M. Yoshimura

150

Growth, spectroscopic and thermal behavior of $\text{Cd}(\text{SCN})_2(\text{DMSO})_2$

X.Q. Wang, D. Xu, D.R. Yuan, M.K. Lu, X.F. Cheng, J. Huang, G.W. Lu, S.Y. Guo and G.H. Zhang

155

Sonochemical preparation of lead sulfide nanocrystals in an oil-in-water microemulsion

H. Wang, J.-R. Zhang and J.-J. Zhu

161

Solvothermal preparation of Cu_2O crystalline particles

S.-J. Chen, X.-T. Chen, Z. Xue, L.-H. Li and X.-Z. You

169

Journal of Crystal Growth

Instructions to Authors (short version)

Submission of papers

Manuscripts (one original + two copies) should be sent to a member of the Editorial Board or preferably to an appropriate subject Associate Editor. For addresses, see preliminary pages of each issue or the website of the journal: <http://www.elsevier.com/locate/jcrysgr>. You may suggest 4 to 6 names of preferred referees. However, we cannot guarantee that any referees suggested will be used. News or announcements should be submitted through the Principal Editor.

Types of contributions

Original research work

As a guideline: experimental papers should not be longer than 16 doublespaced typed pages and 8 figures + tables; for theoretical papers a maximum of 20 pages and 10 figures + tables is suggested.

Priority communications

For reporting important new results only (must be accompanied by a statement regarding the "prime novelty"). Priority communications should not be longer than 5 double-spaced typed pages, and 3 figures + tables. Priority communications should be submitted to editor L.F. Schneemeyer.

Letters to the editor

For matters of urgency only (including comments on papers published in this journal). Letters to the editor should not be longer than 5 double spaced typed pages.

Original material

Contributions are accepted on the understanding that the authors have obtained the necessary authority for publication. Submission of an article must be accompanied by a statement that the article is original and unpublished and is not being considered for publication elsewhere.

Preparation of manuscript

All manuscripts should be written in good English. Both hard copy (for refereeing) and electronic (for printing) versions of the manuscript are required. More information on the electronic text can be found in the section entitled "Electronic text of manuscripts" below. The paper copies of the text should be prepared with double line spacing and wide margins, on numbered sheets.

Structure Please adhere to the following order of presentation: Title, Author(s), Affiliation(s), Abstract, Keywords, Main text, Acknowledgements, Appendices, References, Figure captions, Tables.

Corresponding author The name, complete postal address, telephone and fax numbers and the e-mail address of the corresponding author should be given on the .rst page of the manuscript. **Keywords/PACS codes.** Please supply one or more PACS-1998 codes and up to six keywords from the keyword list, published in the last issue of every volume, and put them below the abstract. Each keyword should be accompanied by the capital letter denoting the category from which the keyword has been selected, e.g. **Keywords:** A1. Biocrystallization, A3. Topotaxy, B1. Nanomaterials. If the keywords from the list are not relevant, authors may choose their own keywords, but each of these should also be accompanied by the capital letter denoting the category into which it falls. Both PACS codes and keyword list are available on the journal homepage: <http://www.elsevier.com/locate/jcrysgr>. **References.** References should only be given to published material; references are not allowed to be footnotes and references to not readily accessible reports should be avoided.

Illustrations

Illustrations should also be submitted in triplicate: one master set and two sets of copies. The *line drawings* in the master set should be original laser printer or plotter output or drawn in black india ink, with careful lettering, large enough relative to the size of the figure, to remain legible after reduction for printing. *Photographs* should be originals, with somewhat more contrast than is required in the printed version. They should be unmounted unless part of a composite figure. Any scale markers should be inserted on the photograph itself, not drawn below it.

Colour plates. Colour plates are possible but the extra costs involved are charged to the author. Further information is available from the publisher (for contact details see below).

Electronic text of manuscripts

The publisher requires an electronic version of your accepted manuscript. If there is not already a copy of this (on diskette) with the journal editor at the time the manuscript is being refereed, you will be asked to send a file with the text of the revised manuscript. All major text processing packages can be handled. As to formats, both MS-DOS and Macintosh formatted disks can be handled. Please note that no deviations from the version accepted by the editor of the journal are permissible without the prior and explicit approval by the editor. Such changes should be clearly indicated on an accompanying printout of the file. In case discrepancies between hardcopy and electronic text are found by the publisher, the hardcopy version of the manuscript will be followed in all cases.

Electronic graphics for manuscripts

The publisher welcomes electronic graphics accompanying accepted manuscripts. Besides the need to always submit a high quality original hardcopy of every figure included with the manuscript, authors should send also send electronic versions, *on a separate disk*. Especially for halftones (micrographs (AFM, STM, TEM, SEM etc.) and images) better results can be achieved when reproducing from electronic files. Authors may use any of the following media: floppy, CD-ROM or Zip-disk. For a full version of instructions for submitting electronic graphics contact our web-site: <http://www.elsevier.com/locate/authorartwork>

After acceptance

Notification. The corresponding author will be notified by the editor of the acceptance of the article and urged to supply an electronic version of the accepted text, if this is not already available (usually this request is made at revision stage). Also an electronic version of illustrations will be requested. **Copyright transfer.** In the course of the production process you will be asked to transfer copyright of the article to the publisher. This transfer will ensure the widest possible dissemination of information.

Page proofs. Page proofs are made and sent out to authors, in order to check that no undetected errors have arisen in the typesetting (or file conversion) process. No changes in, or additions to, the edited manuscript will be accepted.

OASIS

Elsevier operates a system called OASIS which enables authors to get information on the status of their accepted manuscript in the production process. Entrance is on the basis of user name/password, where the corresponding author's surname acts as the former and the reference code of the article as the latter. The reference code is given on the acknowledgement letter every corresponding author receives upon receipt of the accepted article at Elsevier.

Author benefits

No page charges. Publishing in Journal of Crystal Growth is free.

Free offprints. The corresponding author will receive 25 offprints free of charge. An offprint order form will be supplied by Elsevier for ordering any additional paid offprints.

Discount. Contributors to Elsevier Science Journals are entitled to a 30% discount on all Elsevier Science books.

Author enquiries

For enquiries relating to the submission of articles (including electronic submission where available) please visit the Author Gateway from Elsevier Science at <http://authors.elsevier.com>. The Author Gateway also provides the facility to track accepted articles and set up e-mail alerts to inform you of when an article's status has changed, as well as detailed artwork guidelines, copyright information, frequently asked questions and more. Status Information System (OASIS), author Frequently Asked Questions and any other enquiries relating to Elsevier Science, please consult <http://www.elsevier.com/locate/authors/>. For specific enquiries on the preparation of electronic artwork, consult <http://www.elsevier.com/locate/authorartwork/>. Contact details for questions arising after acceptance of an article, especially those relating to proofs, are provided after registration of an article for publication.

Abstracted/Indexed in: Aluminium Industry Abstracts; Chemical Abstracts; Current Contents: Physical, Chemical and Earth Sciences; EI Compendex Plus; Engineered Materials Abstracts; Engineering Index; INSPEC; Metals Abstracts

CONTENTS

Classical semiconductors

Temperature control in InGaAs-based quantum well structures grown by molecular beam epitaxy on GaAs (100) and GaAs (111)B substrates

J. Hernando, J.M.G. Tijero and J.L. Sánchez de Rojas 1

Atomic depth distribution and growth modes of Sn on Si(111)-4I-In and α -33-Au surfaces at room temperature

T. Yamanaka and S. Ino 9

Enhanced impurity incorporation by alternate Te and S doping in GaAs prepared by intermittent injection of triethylgallium and arsine in ultra high vacuum

Y. Oyama, K. Tezuka, K. Suto and J.-I. Nishizawa 15

Defect-selective etching of GaN in a modified molten bases system

G. Kamler, J.L. Weyher, I. Grzegory, E. Jezierska and T. Wosiński 21

N-type doping behavior of $\text{Al}_{0.15}\text{Ga}_{0.85}\text{N}:\text{Si}$ with various Si incorporations

C.-R. Lee 25

On mass transport and surface morphology of sublimation grown 4H silicon carbide

D. Schulz, J. Doerschel, M. Lechner, H.-J. Rost, D. Siche and J. Wollweber 31

A global thermal analysis of multizone resistance furnaces with specular and diffuse samples

I. Pérez-Grande, Damián Rivas and V. de Pablo 37

The role of growth conditions on the p-doping of GaN by plasma-assisted molecular beam epitaxy

E. Haus, I.P. Smorchkova, B. Heying, P. Fini, C. Poblenz, T. Mates, U.K. Mishra and J.S. Speck 55

A new phenomenon in the floating-zone (FZ) growth of Si nanowires

Q. Hu, G. Li, H. Suzuki, H. Araki, N. Ishikawa, W. Yang and T. Noda 64

Structural characterization of epitaxial lateral overgrown GaN on patterned GaN/GaAs(001) substrates

X.M. Shen, Y. Fu, G. Feng, B.S. Zhang, Z.H. Feng, Y.T. Wang and H. Yang 69

Temperature dependence of stresses in GaN/AlN/6H-SiC(0001) structures: correlation between AlN buffer thickness and intrinsic stresses in GaN

J. Keckes, G. Koblmüller and R. Averbeck 73

Electronic materials

Crystal structure and ferroelectricity of nanocrystalline barium titanate thin films

M.-C. Wang, F.-Y. Hsiao, C.-S. Hsi and N.-C. Wu 78

Preparation of high-quality anthracene crystals using double run selective self-seeding vertical Bridgman technique (DRSSVBT)

A. Arulchakkaravarthi, C.K. Lakshmanaperumal, P. Santharaghavan, K. Sivaji, R. Kumar, S. Muralithar and P. Ramasamy 85

Relationships between DTA and DIL characteristics of nano-sized alumina powders during θ - to α -phase transformation

F.S. Yen, J.L. Chang and P.C. Yu 90

Characteristics and crystal structure of the $\text{Ba}(\text{Zr}_x\text{Ti}_{1-x})\text{O}_3$ thin films deposited by RF magnetron sputtering

M.-C. Wang, C.-Y. Chen, C.-S. Hsi and N.-C. Wu 99

Directional CdS nanowires fabricated by chemical bath deposition

H. Zhang, X. Ma, J. Xu, J. Niu, J. Sha and D. Yang 108

Thermal stability and interfacial reaction of TiB_x films deposited on (100)Si by dual-electron-beam evaporation

Y.-K. Lee 113

Growth and characterization of $\text{Pb}_{1-x}(\text{Mg}_{1-x}\text{Sr}_x)_x\text{S}$ thin films prepared by hot-wall epitaxy

S. Abe and K. Masumoto 121

Investigation of interfacial microstructures of MBE-grown NdF_3/Si (111) heterostructures

N.T. Cho, J.M. Ko, K.B. Shim and T. Fukuda 127

CrN single-crystal growth using Cr-Ga-Na ternary melt

M. Aoki, H. Yamane, M. Shimada and T. Kajiwara 133

Contents continued on final page

